THE UNIVERSITY *of* EDINBURGH

Perovskites under extreme conditions: pushing the limits of neutron diffraction

Mara Capone

THE UNIVERSITY *of* EDINBURGH

Doctor of Philosophy
The University of Edinburgh
June 2020

Lay Summary

ISIS is the Neutron and Muon spallation source located at Harwell campus, Oxfordshire, United Kingdom. It has been a centre of scientific research since the 1980s, where a broad range of experimental techniques have been developed and practised. The work in this thesis was carried out primarily on the PEARL diffractometer, the instrument dedicated to perform high-pressure neutron-diffraction experiments. On PEARL neutron diffraction is the method used to investigate atomic structures of materials and their physical properties, particularly under extreme conditions of pressure and temperature.

An important aspect of the work reported in this thesis is to use high-pressure neutron diffraction to obtain accurate and unique information on the material structures investigated. In particular, this work has studied perovskite compounds. These are a family of compounds exhibiting an extraordinarily flexible crystal structure, which can be modified by acting externally by chemical substitution, application of pressure or temperature variation.

High-pressure neutron-diffraction techniques are in continuous development. Another important part of this research is the deployment of new pressure capabilities on the PEARL instrument. The main goals are to extend the accessible pressure range on sample materials and to overcome the requirement of large sample volumes (typical in neutron diffraction experiments). This is achieved by the integration of diamond anvil cells, which simultaneously can reach very high pressures and measure very small sample volumes. This enables the study of materials on PEARL, such as perovskite compounds produced with high-pressure techniques, which cannot provide material sizes big enough for standard high-pressure neutron diffraction presses.

This new development allows us to extend the pressure range accessible in neutron-diffraction experiments. Study of materials under high pressure enables

us to reproduce conditions of materials which can be found in the inner Earth or planetary bodies and study their structures under laboratory conditions. By comparing how structural, electrical, magnetic or optical properties change across a range of pressure not before achievable, we can improve our understanding of these materials either for fundamental studies or technological applications.

Abstract

The application of hydrostatic pressure and temperature are effective methods for manipulating and correlating crystal structures and physical properties of materials. Volume, interatomic distances, chemical bonds, local atomic coordination are all strongly altered by pressure and temperature, which can either distort or symmetrise the structure and cause the alteration of the crystal symmetry with huge consequences on the physical properties. High Pressure (HP), in particular, can induce significant structural and physical changes and can be used to explore structural-property relationships in a huge variety of materials. Perovskite compounds are excellent candidates for HP investigations owing to remarkable changes in their structural, electrical and magnetic properties in response to a variation of the chemical composition x or volume of the material. Diverse crystal structures and physical properties are found in the perovskite family, which can be controlled by the application of pressure and/or temperature. Among the broad spectrum of experimental techniques, neutron-powder diffraction offers several advantages for *in situ* investigation under extreme conditions of perovskite materials. Neutron diffraction provides the ability to map the relative positions of atoms and their structural changes down to the nanometre length-scale. The complex dependence of the coherent neutron scattering cross section σ^{Coh} on the atomic number Z of the scattered material enables diffraction comparison between neighbouring elements in the periodic table and isotopes, and a higher sensitivity to light elements such as hydrogen or oxygen in the presence of heavier atoms.

The primary aim of this thesis investigates perovskite oxides and focuses on their structural and physical characterisation under the application of hydrostatic pressure and/or temperature. Perovskites exhibit physical properties utilised in several technological fields, from the magnetoresistence of lanthanum manganites, to the catalytic activity of cobalt-based compounds or to the antiferromagnetism

of lanthanum ferrite materials. This thesis reports a pressure and temperature-dependent neutron-diffraction study of the lanthanum cobaltite $LaCoO_3$. The present study gives insight into the unique pressure and temperature-dependent electronic properties of $LaCoO_3$ and aims to deepen the understanding of structural-electronic correlations in this material. Neutron-diffraction data were collected at 120, 290 and 480 K in the 0–6 GPa pressure range and used to report the equation of state of the sample at each temperature and to accurately determine chemical bonds and structural parameters. A similar investigation reports details of the structural and physical properties of the lanthanum ferrite $LaFeO_3$ material. Neutron-diffraction data were collected at 110 and 290 K in the 0–6.5 GPa and 0–16.2 GPa ranges, respectively. This work analyses the equation of state of the sample and changes within its structure under extreme conditions. This study also monitors the magnetic behaviour of $LaFeO_3$ and how its magnetic moment varies under the application of hydrostatic pressure. In addition, high-pressure Raman spectroscopy data were collected at 290 K in the 0–7.6 GPa pressure range, and the structural-spectroscopic relationships of $LaFeO_3$ analysed.

Chemical doping is a further strategy to alter the structure of materials and tune their physical properties. Specific doping elements are used to produce subtle distortions in crystal structures and to regulate changes in their physical properties. This thesis describes the effect of selective doping on the $LaCoO_3$ oxide, which is the parent compound of several material series of the type $LaCo_xB_{1-x}O_3$ (where B is a different transition-metal ion). High-pressure neutron-diffraction experiments were performed in the 0–6 GPa range at 290 K on the $LaCo_{0.9}Mn_{0.1}O_3$ material. This study analyses the effect of the low manganese doping on the crystal structure of $LaCoO_3$ and reports changes in the equation of state, structural parameters and chemical bonds. The introduction of manganese ions also influences the magnetic properties of this material. DC magnetometry measurements were performed on $LaCo_{0.9}Mn_{0.1}O_3$ in the 0–4 GPa pressure range and used to determine the Curie temperature of the sample, which shows a strong dependence not only on the chemical doping, but also on the applied pressure.

The aforementioned high-pressure neutron-diffraction experiments were performed on the PEARL diffractometer, the instrument dedicated to performing high-pressure diffraction measurements at the ISIS Neutron and Muon Source. The PEARL instrument has been running for nearly three decades and diverse pressure tools are used to carry out high-pressure experiments and different

sample environments have been developed in the past. Another important part of the work presented in this thesis focuses on extending the pressure range, which can currently be applied as part of the user programme on the ISIS diffractometer, by the development of new pressure cells for neutron diffraction, such as diamond anvil cells (DACs). DACs have been designed and developed for the PEARL instrument and their integration has already started. These new pressure cells will provide the ability to remarkably reduce the sample volume during experiments, hence resulting in an increased accessible pressure range.

Declaration

I declare that this thesis has been composed by myself and that it has not been submitted, in whole or in part, in any previous application for any degree or professional qualification. Except where otherwise acknowledged, the work presented is entirely my own.

Parts of this work have been published in:

[1] M. Capone, C. J. Ridley, N. P. Funnell, M. Guthrie, and C. L. Bull. *Phys. Status Solidi A*, 216(6):1800736, 2019;

[2] M. Capone, C. J. Ridley, N. P. Funnell, G. B. G. Stenning, J. S. Loveday, M. Guthrie, and C. L. Bull. *J. Phys. Condens. Matter*, 30(3):035402, 2017 .

(*Mara Capone, June 2020*)

Acknowledgements

Firstly, I would like to thank my supervisor Dr. Craig Bull, at the ISIS STFC facility. A thousand words would not be enough to describe my gratitude for his thoughtful comments and recommendations on this dissertation. I am sincerely grateful for all the time he has dedicated to me and to this project, for his everyday support, help and guidance. His motivation and passion for this job has been inspirational, and pushed me to achieve results I could have never imagined. Huge thanks go to my supervisor Dr. Malcolm Guthrie, at the European Spallation Source. His help has always been extremely valuable, and I am very grateful for his helpful feedbacks and comments on this manuscript. I would like to express my gratitude to the funding institutes of my PhD studentship, ISIS STFC and ESS. This project was born from the collaboration between my supervisors, and I am extremely grateful I had the opportunity to be part of it.

Many people have been working by my side during these four years and their help has been precious. I would particularly like to thank Dr. Christopher Ridley, who has shared with me all his knowledge, with patience and generosity. I am very grateful for all the time he has dedicate to me and for all the times he has come to my help when I needed. Sincere thanks go to Dr. Nicholas Funnell for his valuable scientific contribution to this project and help throughout the past four years, but also for his everyday kind presence. I would like to thank Dr. John Loveday for the academic support at the University of Edinburgh. I am sincerely grateful to Dr. Stephen Hull, leader of the crystallography group at the ISIS facility, for his kind and precious support. Huge thanks go to all the people of the crystallography group, which made me feel part of them during my stay at the ISIS facility. My gratitude goes to Dr. Gavin Stenning and Dr. Daniel Nye, who have helped me in various experiments, at the Material Characterisation Laboratory at the ISIS facility.

I would like to thank my family, my parents and my brother. You have always been and still are my strongest supporters. Although far, your care and support have always been strong during these years. Lastly, I would like to thank Kevin, who has been by my side during all these years. All this would have never been possible without all the help I received from you.

Contents

List of Figures

List of Tables

Glossary

$\boldsymbol{\mu_B}$	Bohr magneton, unit of magnetic moment (SI $9.274 \times 10^{-24}\,\mathrm{J\,T^{-1}}$)
$\boldsymbol{h}$	Plank constant (SI $6.626\,070\,04 \times 10^{-34}\,\mathrm{J/s}$)
$\hbar$	Plank constant (SI $1.054\,571\,817 \times 10^{-34}\,\mathrm{J/s}$)
$\boldsymbol{m_N}$	Neutron mass (SI $1.674\,927\,498\,04(95) \times 10^{-27}\,\mathrm{kg}$)
$\boldsymbol{r_e}$	Classical electron radius (SI $2.82 \times 10^{-15}\,\mathrm{m}$)
$\boldsymbol{k_b}$	Boltzmann constant (SI $1.380\,649 \times 10^{-23}\,\mathrm{J\,K^{-1}}$)
$\boldsymbol{e}$	Electron charge (SI $1.602\,176\,62 \times 10^{-19}\,\mathrm{C}$)
$\boldsymbol{c}$	Speed of light (SI $2.997\,92 \times 10^{8}\,\mathrm{m/s}$)
$\boldsymbol{\pi}$	PI (3.141592)
$\boldsymbol{\Phi_0}$	Magnetic quantum flux (SI $2.0678 \times 10^{-15}\,\mathrm{Tm^2}$)

Introduction

The application of extreme conditions of pressure and temperature on materials is a versatile way to generate changes in structural, physical and chemical properties. Temperature and pressure are two distinct variables, which affect matter differently and provide complementary information. Temperature directly varies the kinetic energy of a system, with consequences in thermodynamic and vibrational properties. On the other hand, increasing pressure, for example on a crystal, compresses the volume of the system and affects the energy of the atomic bonds. Increasing pressure provides information on atomic interaction and chemical bondings, and correlates material structures and their physical properties. Pressure modifies the electron density of a system and in crystal structures can promote metal-insulator, spin-state, magnetic and structural transitions.

This is especially true for perovskite materials, which are a class of compounds with a crystal structure extremely flexible and modifiable in a controlled way by pressure and/or temperature. On this hinges an astonishing variety of physical properties which can be altered in favour of many technological applications. A great interest is thus devoted to the potential understanding of physical and chemical properties under extreme conditions in these materials.

Among the broad range of experimental techniques, neutron-powder diffraction is a technique for *in situ* investigation under extreme conditions. Neutron diffraction provides the ability to study and map the relative positions of atoms and their structural changes down to the nanometre length-scale providing unique information on material structures compared to other diffraction techniques, such as X-ray diffraction. Neutrons are directly scattered by interaction with the nuclei, which means the neutron form factor is independent of the momentum transfer in the scattering process. The scattering magnitude has a complex dependence on the atomic number Z and is isotope dependent. This allows us

to distinguish neighbouring atoms in the periodic table, light atoms like oxygen in the presence of heavier atoms such as metals, and isotopes such as hydrogen and deuterium. Neutrons have an intrinsic magnetic moment and are sensitive to long-range magnetic order. They can be used to directly determine the atomic magnetic moments and also measure their relative orientation. Neutron diffraction can be used to ascertain unique signatures of crystal structures and their properties. It is the technique of choice for studying materials made of a mix of light and heavy atoms. This is especially convenient for perovskite compounds, where light and heavy atoms are arranged in space, and a flexible diffraction contrast is a fundamental necessity.

Combining high-pressure and neutron-diffraction experiments provides the ability to study a wide range of materials and to probe the inter-atomic bond interactions with an accuracy which cannot be achieved by other techniques. High-pressure neutron-diffraction technology is thus in continuous development at neutron source facilities around the world such as the ISIS, STFC Neutron and Muon Source, UK. Considerable efforts have been made to extend the accessible pressure range, which is still lower than in X-ray diffraction experiments, due to high instrumentation costs and technical issues arising from the weak neutron fluxes available. Despite the challenges, the development of high-pressure diffraction techniques is extremely worthwhile in light of the unique information neutrons can give on a wide variety of materials.

Chapter 1

Perovskites

The work presented in this thesis focuses on the structural and physical study of perovskite-oxide materials under extreme conditions of pressure and temperature. This chapter provides an overview of the structural, electrical and magnetic properties of perovskite compounds. Through various examples, the main structural and physical characteristics and their correlations are described and tools for a quantitative description of the crystal structure will be introduced.

A perovskite material is historically defined as a compound showing the same chemical structure as the calcium titanium oxide $CaTiO_3$ [3], the first discovered mineral perovskite compound. This crystal structure is characterised by the general chemical formula ABX_3, where A and B are cations with different ionic radius (such as transition metals, rare-earth and alkaline atoms) and X are negatively charged anions. Although the majority of perovskite compounds are oxides or fluorides, other forms like heavier halides [4], sulphides [5], cyanides [6], oxyfluorides [7] and oxynitrides [8] are also reported. The perovskite structure can accommodate a wide variety of different elements in the periodic table as A, B or X. Different chemical combinations produce distinct crystal structures, with diverse electrical, magnetic and optical properties. This chemical flexibility and the strong correlation between the structure and physical properties make these types of materials important.

1.1 Physical properties of perovskite materials

Since its discovery, the perovskite structure has raised great interest in several fields such as geology. For example, the most abundant solid-phase minerals in the Earth's lower mantle belong to the magnesium-silicate-based compound series (Mg,Fe)SiO_3 [9–15], which adopt a perovskite structure. Insight in the lower mantle constituents can be achieved by the analysis of the high-pressure and high-temperature form of this compound series, whose structural stability under extreme conditions is still an object of debate.

Perovskite materials have attracted attention due to their varied physical properties. In the 1940s, ferroelectricity was discovered in the perovskite-structured barium titanate $BaTiO_3$ [16]. The ability to reverse the electrical dipole moment by an applied external electric field opened its use in electrical devices such as transducers and capacitors. Since this discovery, considerable efforts have been made to enhance the ferroelectric behaviour of $BaTiO_3$. This led to a major development in perovskite material synthesis in order to tune the ferroelectricity of $BaTiO_3$. Several compounds have been synthesised such as the A-site doped (Ba,Sr)TiO_3, in which by tuning the ratio Ba^{2+}/Sr^{2+} the temperature of paraelectric to ferroelectric transition can be shifted towards lower or higher values [17]. $PbTiO_3$, $PbZrO_3$, $BiFeO_3$ and related compound families such as (Pb,Ca)TiO_3 or (Ba,Ca)(Sn,Ti)O_3 solid solutions, all show ferroelectric properties [18–21] and have applications in data storage, capacitors or non-linear optical devices. These materials are also extensively used for their piezoelectric properties, that is the ability to convert mechanical stress into energy [22].

Ferroelectricity is one of many physical properties which perovskites may exhibit. Long-range magnetic correlation can also occur in these materials. One of the interesting related phenomena observed in perovskites is giant and colossal magnetoresistance (GMR, CMR), that is large changes in electrical resistance when an external magnetic field is applied. Manganese-based perovskites, such as $Ln_{1-x}A_xMnO_3$ (Ln is a trivalent rare-earth and A an alkaline earth metal) like the $La_{1-x}Sr_xMnO_3$ series, are oxides extensively used in spintronic applications such as in magnetic field sensors, electric field devices and many more [23–34].

Many multiferroic materials are also found in the perovskite family. These materials not only exhibit ferroelectricity but also magnetic order and are capable of switching their magnetisation by the application of an external magnetic field.

Several series have been studied, including the manganites $RMnO_3$ (where R is a rare-earth atom), the tetragonal double perovskite $(Ca,Mn)Ti_2O_6$ [33, 35] and the $BiFeO_3$ compound [36, 37]. Orthorhombic $RMnO_3$ and the $CaMnTi_2O_6$ perovskites have attracted attention for technological applications. However, the magnetic ordering occurs at temperatures typically much lower than the liquid nitrogen temperature of 77 K, and their practical use is very limited. $BiFeO_3$ has driven attention for the much higher transition temperature and hence the potential use as room temperature multiferroic material in electronic devices such as batteries or memory storage systems.

Catalytic activity is also a common property found in perovskites [38–42]. Most modern catalytic devices contain mixed metal oxides, for example low manganese doped cobalt-based perovskite oxides are good catalysts for exhausted substances of vehicle particulate [43].

Perovskite systems are also extensively applied as novel high-temperature superconducting materials. Both cuprate-based and non-cuprate based systems can adopt the perovskite structure [44–46] and exhibit a superconducting temperature higher than the 77 K boiling temperature of liquid nitrogen. The YBaCuO oxide family for example shows a superconducting transition temperature around 93 K [44, 45].

New generation solar cells and opto-electronic devices utilise perovskite oxides or halide perovskites [4, 47–58]. Perovskites gained interest as a long stable photovoltaic device with enhanced power conversion efficiency and as new components of light-emitting diodes (LEDs) or laser. As in the case of organic–inorganic lead halide perovskite ($CH_3NH_3PbI_3$) solar cells, a power conversion efficiency (PCE) of 23.7% has been reached approaching the high conversion performance of single-crystalline silicon solar cells. This high performance in addition to the low-cost device fabrication processes are making perovskites emerge in both photovoltaic technology and optoelectronic devices.

There is a strong correlation between the crystal structure of perovskites and their physical properties. This means that, by making fine adjustments to the structure, electrical, mechanical and magnetic properties can be modified in a controlled way and be tuned in light of enhancing the various technological applications listed above and many more. This can be achieved by chemical substitution or pressure and temperature variation. This topic will be deeply discussed throughout this thesis.

1.2 Perovskite crystal structure: the cubic symmetry

The ideal perovskite structure ABX_3 (aristotype) exhibits a cubic symmetry and is characterised by the $Pm\bar{3}m$ space group[1]. It is found at ambient temperature and pressure in materials such as the strontium titanate $SrTiO_3$ [59] or the fluoride $KMgF_3$ [60]. A representation of the cubic $SrTiO_3$ crystal structure is depicted in Figure 1.1. The A, B and X atoms are depicted as green, light blue and red spheres, respectively. Black lines show A–X and B–X bonds.

[1]Primitive lattice with a mirror plane orthogonal to x, y and z directions, a 3-fold axis orthogonal to the body diagonal and a mirror plane orthogonal to the face diagonal.

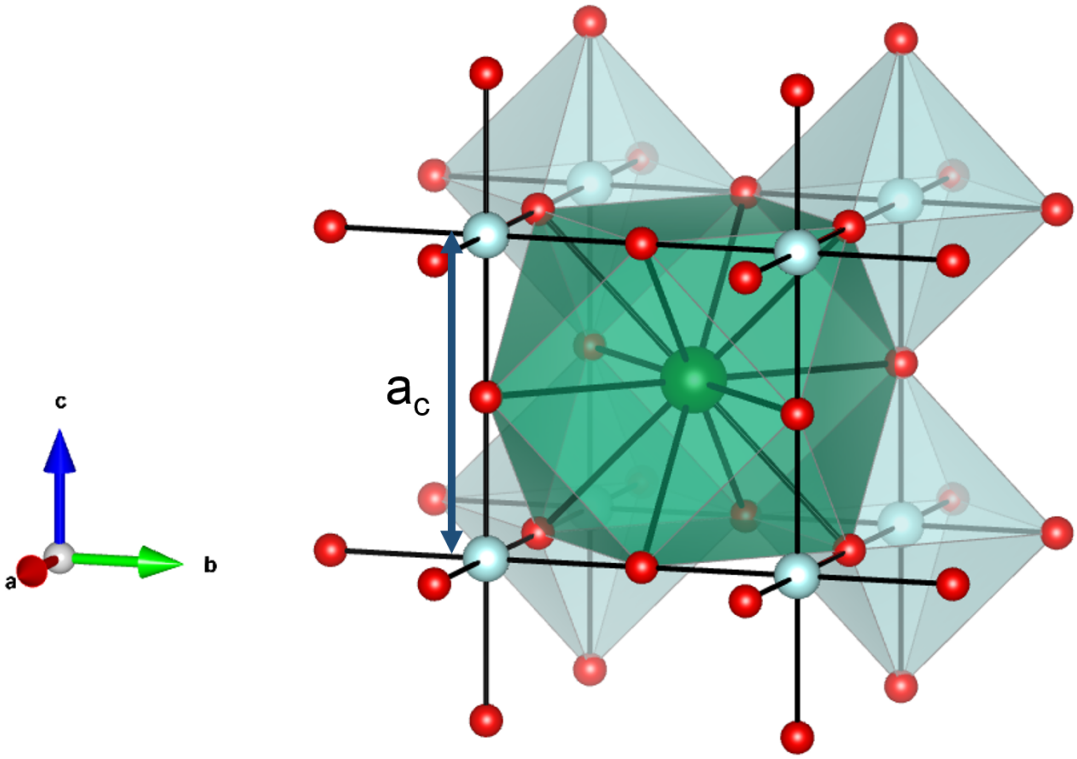

Figure 1.1 *Crystal structure of cubic $Pm\bar{3}m$ $SrTiO_3$. The structure consists of corner-sharing TiO_6 octahedra, with Ti cations in the centre of the 6-fold coordinated polyhedron in Wyckoff positon 1a (0,0,0). The Sr atom is located in interstitial sites in Wyckoff position 1b $\left(\frac{1}{2},\frac{1}{2},\frac{1}{2}\right)$ coordinated by twelve oxygen atoms in Wyckoff position 3d $\left(\frac{1}{2},0,0\right)$. Strontium, titanium and oxygen atoms are depicted as green, light blue and red spheres, respectively. Black lines depict the chemical bond lengths. The cubic unit cell coincides with the Ti–O bond lengths and the lattice parameter a_c is indicated by the dark blue arrow.*

The structure is characterised by alternate layers of TiO_6 octahedra, with the B (Ti) cations sitting in the centre at the origin of the unit cell. The larger A cation (Sr) is located in interstitial sites coordinated by twelve anion atoms in a cube-octahedral geometry. Axes formed by the Ti–O bonds coincide with the crystallographic cubic axes and are parallel to each other. The lattice parameter a_c is equal to double the Ti–O bond distance as highlighted in Figure 1.1. The octahedra are regular with six equal Ti–O bond lengths and with flat O–Ti–O intra-octahedral angles of 180°. Strontium atoms are at the centre of the unit cell in a regular cube-octahedral geometry. An alternative approach to look at the perovskite structure is to translate the origin of the unit cell to the A-site position as shown in Figure 1.2. Under this view the titanium atom is located at the centre of the unit cell coordinated by six oxygen atoms in face-centred position respect to the cubic unit cell.

Cubic symmetry is rarely adopted by either mineral or synthetic perovskites, most of which exhibit lower symmetry structures. The $CaTiO_3$ perovskite itself is

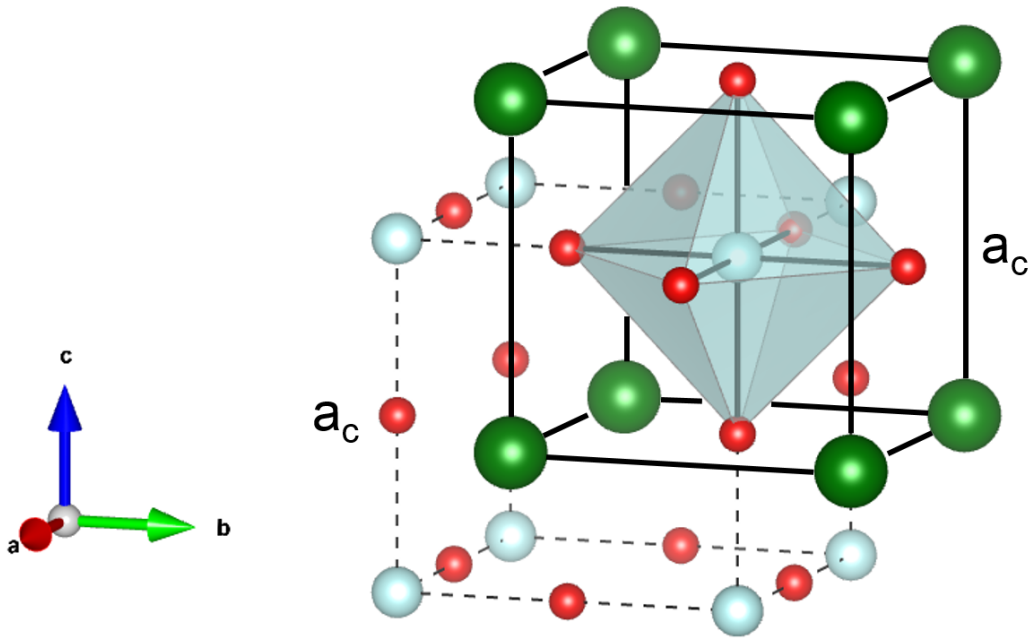

Figure 1.2 *Crystal structure of cubic $Pm\bar{3}m$ $SrTiO_3$. The crystallographic axes are translated so that the A-site cation is located at the origin of the unit cell in Wyckoff position 1a (0,0,0). The titanium is at the centre of the unit cell coordinated by six oxygen atoms in face-centred positions, Wyckoff site 3c $(\frac{1}{2}, \frac{1}{2}, 0)$. Dashed black line depicts the A-centred unit cell, while solid black line indicates the B-centred unit cell. Sr–O bonds are not shown for clarity.*

found at ambient conditions in orthorhombic symmetry [3]. The crystal symmetry which will be adopted by a perovskite compound depends on the relative size of its own constituent elements. Approximating the perovskite structure to a pure ionic solid, it is possible to define the so-called Goldschmidt's tolerance factor t [61, 62]:

$$t = \frac{r_A + r_X}{\sqrt{2}(r_B + r_X)} \tag{1.1}$$

where r_A, r_B and r_X are the effective ionic radii of A, B and X ions. The tolerance factor t roughly predicts the stability of the perovskite phase. The perovskite system will form for values of t close to 1. The tolerance factor can be used to approximately classify perovskite distortions:

- An upper limit of the tolerance factor is approximately 1.04.
- For a value of $0.9 < t < 1$ the cubic phase is expected.
- For $t > 1$ perovskites are expected to be tetragonal or hexagonal.
- For $0.75 < t < 0.9$ structures are found to be either orthorhombic or trigonal.
- Values of $t < 0.75$ give structures with a 6-coordination A–site such as the ilmenite structure of $FeTiO_3$ [63].

As t decreases, the stability of the perovskite phase decreases and eventually it will not form. The anion element may be a sulphur, oxygen, fluorine or halide such as chlorine or iodine, or many more. The ionic radius varies with the coordination number of the ions. For the B-site the ionic radius for octahedral coordination must be used, for the X-site the linear coordination and for the A-site, whose coordination number varies according to the symmetry, the 12-coordination value must be used. The radius of the A cation is typically between 1.0 and 1.9 Å, whereas the usual radius of the B cation ranges from 0.5 to 1.2 Å [64]. The A and B cations can also show different oxidation states. For example, in cubic $SrTiO_3$ or in orthorhombic mineral $CaTiO_3$, the Sr/Ca cation is divalent and the Ti cation is tetravalent, while in trigonal $LaCoO_3$ or orthorhombic $LaFeO_3$ the rare-earth La and the transition-metals Co/Fe are both trivalent.

1.3 Distortions in perovskites

Three different distortion mechanisms have been found to occur in perovskites: cation displacement, octahedral distortion and tilting of the octahedra [65, 66]. These structural distortions are of interest because they can have important effects on physical properties of perovskite compounds, particularly electrical and magnetic properties. By controlling these distortions it is possible to alter the electronic configuration of the perovskite materials and tune their electrical and magnetic properties [67–71]. The imbalance between the A and B cation sizes lowers or raises the tolerance factor t and does not allow most crystals to adopt the high-symmetry cubic phase. For most crystal symmetries a quantitative description of the structure is not as straightforward as for the cubic ideal aristotype. A helpful method to describe these structures is to visualise them as distorted from the cubic aristotype. To accommodate the imbalance of the A and B cation sizes, the cubic perovskite undergoes structural distortions and a lower symmetry perovskite phase is stabilised. It is common to redefine the unit cell in terms of a pseudo-cubic unit cell with lattice constant a_{pc}, in the case of the cubic phase $a_{\mathrm{pc}} = a_{\mathrm{c}}$. Different structural distortions drive different low-symmetry crystal structures.

1.3.1 Cation displacement

Cation displacement takes place when the B cation is too small for its 6-fold octahedral site. The B atom moves off-centre within the octahedron along one of its symmetry directions. Perovskites which show cation displacement usually crystallise in tetragonal, orthorhombic or trigonal symmetry dependent on the magnitude and direction of the displacement. Displacement of the cation from the centre of the octahedron generates a permanent electric dipole and is responsible for the ferroelectric and piezoelectric response found in many perovskites. The most conventional example of a perovskite which shows cation displacement and ferroelectricity is the barium titanate $BaTiO_3$. At room temperature $BaTiO_3$ crystallises in the tetragonal $P4mm$ space group[2] and displays ferroelectric properties [72]. At 2 GPa [73] or at 393 K [72], it undergoes a transition to cubic $Pm\bar{3}m$ and no ferroelectric response is observed.

[2]Primitive lattice with a 4-fold symmetry axis parallel to z, a mirror plane respect to x and y-axes, and a mirror plane with respect to both of the diagonals between the x and y-axes.

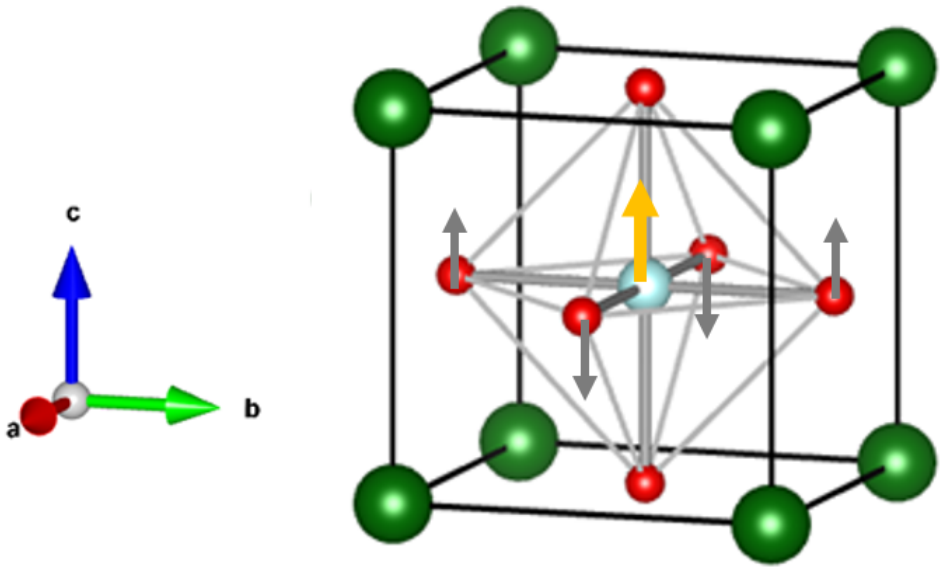

Figure 1.3 *Cation displacement in tetragonal P4mm $BaTiO_3$. Yellow arrow indicates the direction of displacement of the Ti cation (light blue sphere), while gray arrows show the direction of displacement of oxygen atoms (red spheres) from the ideal cubic position. Green spheres are barium atoms, whose bonds are not shown for clarity.*

The tetragonal to cubic transition is driven by cation displacement, the Ti^{4+} cations shift to the centre of the octahedra in the cubic phase and this turns off the ferroelectricity.

$BaTiO_3$ is tetragonal in the 268–393 K temperature range. Starting from the ideal cubic situation and cooling down the barium titanate the cubic cell expands along the *c*-axis and slightly contracts along *a* and *b*-directions to create the tetragonal unit cell. The change in symmetry is driven by the displacement of the Ti cation along the *c*-axis as shown in Figure 1.3. In octahedral symmetry the *c*-crystallographic direction is characterised by a 4-fold rotational symmetry axis. The Ti–O bonds parallel to the displacement direction are not equivalent, but a longer and shorter bond will be observed. This also drives a displacement of the equatorial oxygen atoms in the same and opposite direction to the *c*-axis.

1.3.2 Octahedral distortion

Octahedral distortion occurs when the A–X and/or B–X bonds have electrical instability, for example in the presence of Jahn-Teller distortion or charge

disproportion. The Jahn-Teller effect describes the tendency of a crystal with a symmetrical atomic configuration and a degenerate electronic ground state to remove the energetic degeneracy. The crystal structure is more stable in a more distorted environment. This distortion affects electrons in the *3d*-orbitals of the B cation. When Jahn-Teller effect takes place, an octahedron distorts by elongation or contraction of the octahedral edges along one of the fourfold symmetry axes. The BX_6 octahedron will show either four shorter B–X bonds and two longer B–X bonds if elongated, or four longer B–X bonds and two shorter B–X bonds if compressed. Charge disproportion also causes distortion of the octahedra. The presence of B cations with different oxidation states will influence the surrounding anions giving rise to a distortion of one or both of the cation-centred octahedra, resulting in two different octahedra of different size.

The Jahn-Teller distortion can be altered by application of pressure. For example, potassium trifluorocuprate $KCuF_3$ perovskite fluoride shows Jahn-Teller distortion due to the $3d^9$ electron-shell configuration of Cu^{2+} cations [74]. This lowers the symmetry from the typical cubic $Pm\bar{3}m$ of most KMF_3 fluorides [74, 75] (where M = Mg, Zn, Co, and Ni) to tetragonal *I4/mcm*. Pressure strongly suppresses the Jahn-Teller distortion in the $KCuF_3$ perovskite, as reported in a high-pressure neutron diffraction study up to 8 GPa [76], where the Jahn-Teller effect is suggested to disappear around 18 GPa and the structure to transform into cubic.

1.3.3 Octahedral tilting in perovskites

The tilting of the BX_6 octahedra is the most common distortion observed in perovskites and is related to the imbalance between the size of the cations. If the A cation is too small for its cube-octahedral environment the BX_6 octahedra will tilt to reduce the volume of the A-site cavity, hence reducing the symmetry of the A-site cation coordination environment, whilst leaving the B cation octahedral geometry nearly unchanged. Depending on the various tilting combinations, a different change in the A–X bond lengths will occur.

By considering the various tilting systems it is possible to derive the corresponding lowered symmetry and associated space group. The most popular classification of perovskites according to their tilting system (respect to the aristotype) has been proposed by Glazer [77] and is widely used in the academic literature. Glazer notation classified the various tilt combinations into twenty-three different tilting

systems, described in terms of component tilts around the axes of the cubic aristotype. When an octahedron is tilted about one of the cubic directions, consecutive octahedra in the plane normal to the tilt axis are constrained to tilt in opposite directions. However, the octahedra directly above and below are not so constrained and can tilt in one of two ways. Glazer developed the notation: $a^{+/-}b^{+/-}c^{+/-}$, in which the literals refer to tilts around the [100], [010] and [001] directions of the aristotype, and the superscript +/- takes the value 0, + or - to indicate no tilt around an axis or tilts of successive octahedra in the same or opposite way. Letters are repeated to indicate equal tilts around the different pseudo-cubic axes. The cubic $Pm\bar{3}m$ space group which exhibits the ideal undistorted octahedra geometry is referred to in Glazer notation as $a^0a^0a^0$. By the application of the twenty-three tilt systems to the cubic aristotype, the various space groups which characterise perovskite systems are obtained. However, the number of independent tilt systems has been reviewed and is lower than twenty-three [66, 78]. This will be discussed in more detail in Section 1.5.

1.4 Crystal symmetries in perovskites

By the application of the aforementioned structural distortions, the perovskite ABX_3 chemical structure can adopt different crystal symmetries and express a wide range of physical properties. In the following sections some of most important crystal symmetries found in the perovskite structure will be described through various examples.

1.4.1 Tetragonal symmetry

Tetragonal symmetry is the second highest symmetric crystal structure found in the perovskite family. When the A cation is too large for its cube-octahedral coordination shell, the B–O octahedral bond distorts and the unit-cell stretches along the c-axis. A characteristic group is the tetragonal $I4/mcm$ space group[3] observed in the low-temperature phase of $SrTiO_3$ [59]. Its crystal structure is depicted in Figure 1.4.

[3]Body-centred lattice with a mirror plane orthogonal to the 4-fold symmetry axis respect to the z-crystallographic axis, a mirror plane orthogonal to the x and y axis and a mirror plane orthogonal to the body diagonal.

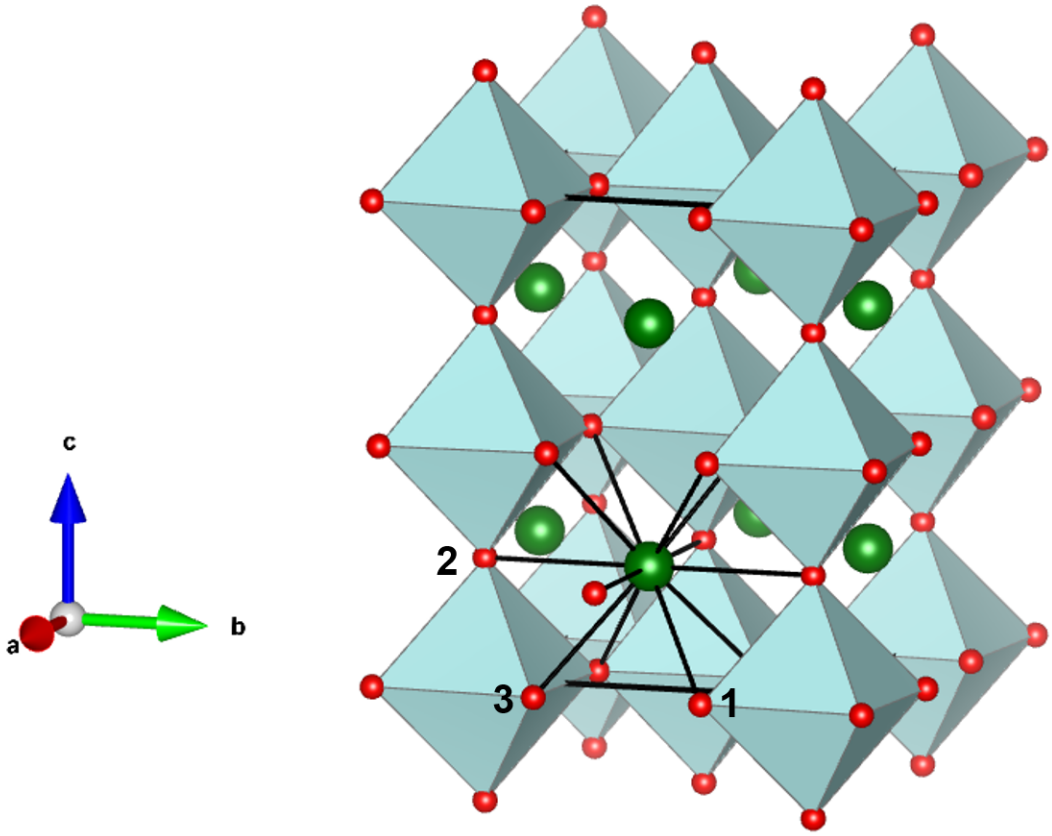

Figure 1.4 *Tetragonal I4/mcm $SrTiO_3$ crystal structure. The tilting system reduces the symmetry of the cube-octahedron SrO_{12} with respect to the cubic symmetry and leads to three groups of equivalent bonds: four short Sr–O1, four intermediate Sr–O2 and four long Sr–O3, shown for only one Sr atom for clarity. Strontium and oxygen atoms are depicted as green and red spheres, respectively. Black line shows the tetragonal unit cell.*

The *I4/mcm* space group is obtained by out-of-phase rotation of the octahedra around the [001] axis of the cubic aristotype, denoted in Glazer notation as $a^0a^0c^-$ and depicted in Figure 1.5.

The oxygen atoms belonging to the TiO_6 octahedra move from the cubic position, whilst maintaining their corner-shared links. The rotation of the octahedra redefines the cubic aristotype into a tetragonal unit cell, whose lattice vectors, which are still perpendicular to each other, now have dimensions $a = b \sim \sqrt{2}a_{\mathrm{pc}}$ and $c \sim 2a_{\mathrm{pc}}$. The octahedra are still regular, that is characterised by four equivalent Ti–O bond distances, while the symmetry of the Sr-site is reduced to three distinct 4-degenerate Sr–Oi (i = 1, 2, 3) bonds: four short Sr–O1, four intermediate Sr–O2 and four long Sr–O3 bonds.

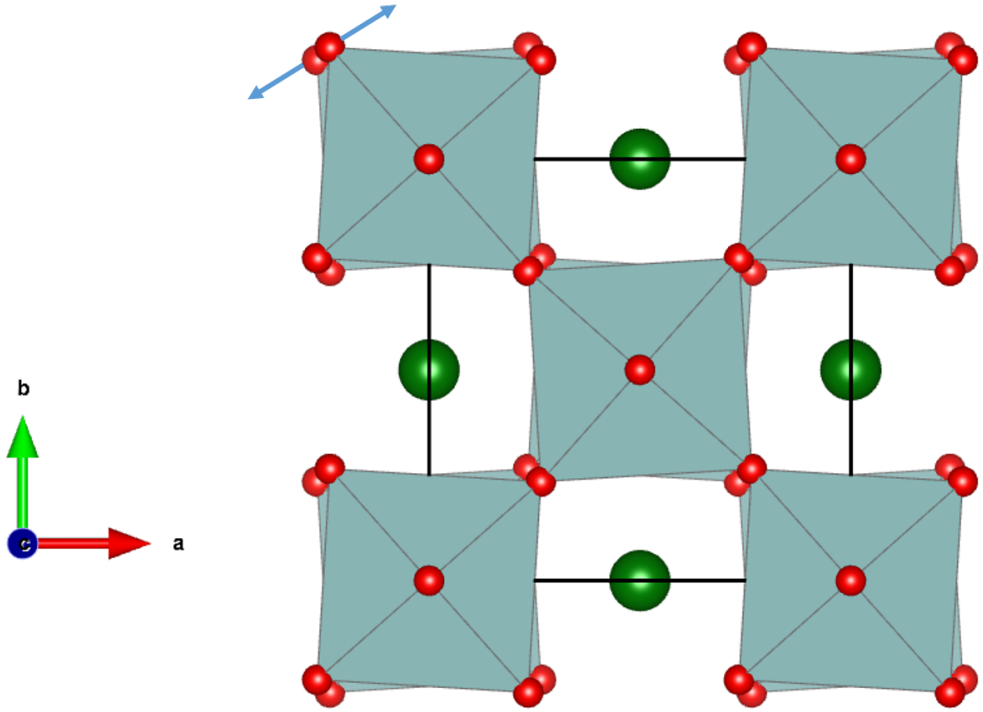

Figure 1.5 *Crystal structure of tetragonal $SrTiO_3$ viewed along the c-axis direction. Blue arrows represent the out-of-phase octahedral tilting around the c-crystallographic direction of the cubic aristotype. Strontium and oxygen atoms are depicted as green and red spheres, respectively. Black line shows the tetragonal unit cell.*

Another typical tetragonal compound is ferroelectric $BaTiO_3$, which exhibits the *P4mm* space group, Glazer notation $a^0a^0a^0$. As already discussed in Section 1.3.1, the tetragonal distortion is driven in $BaTiO_3$ by displacement of titanium cations along the *c*-crystallographic axis, which differently from octahedral tilting, leads to irregular octahedra with two different Ti–O bonds along the displacement direction and no octahedral tilt about the parent cubic axes.

1.4.2 Orthorhombic symmetry

The orthorhombic crystal lattice is obtained by stretching the cubic lattice so that the a, b, and c lattice parameters acquire distinct values. The three lattice vectors remain mutually orthogonal. Figure 1.6 shows the orthorhombic *Pbnm* space group[4] ($Z = 4$) as observed in the mineral $CaTiO_3$.

[4]Primitive lattice with a b-glide plane perpendicular to the x-axis, an n-glide perpendicular to the y-axis, and a mirror plane perpendicular to the z axis.

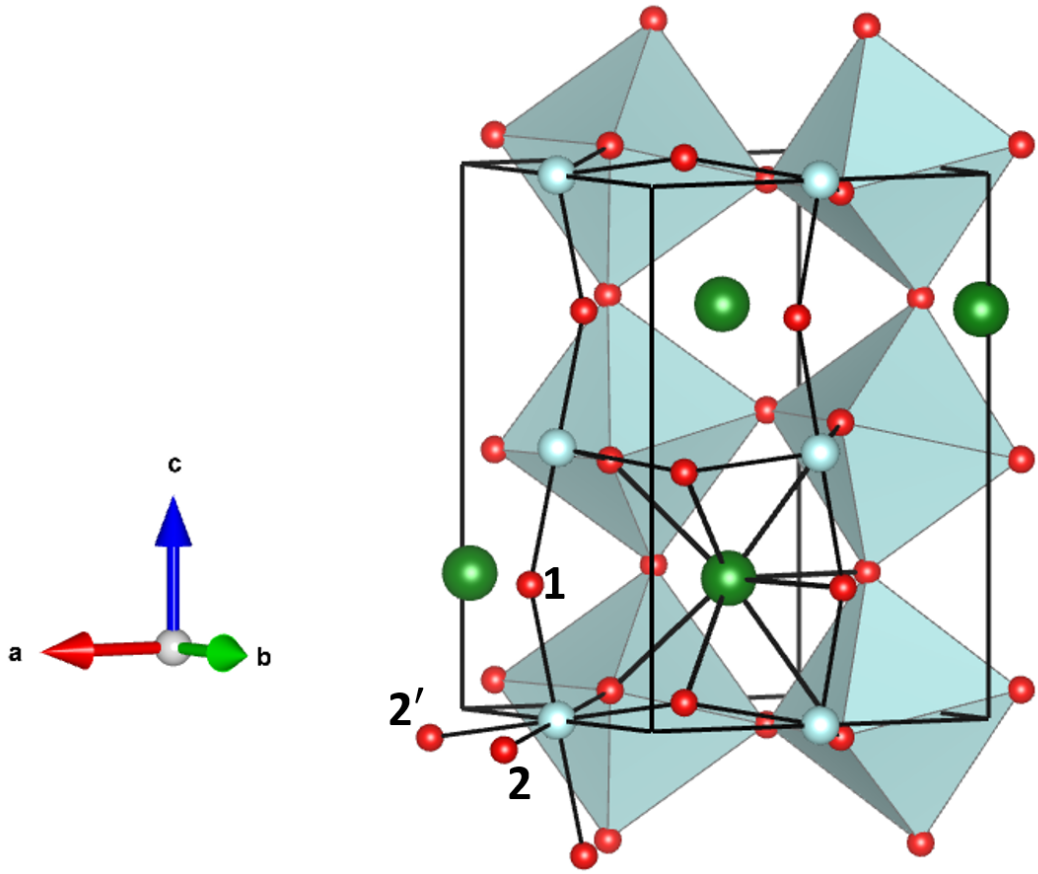

Figure 1.6 *Crystal structure of orthorhombic Pbnm $CaTiO_3$. The Ti cation is located in Wyckoff position 4b $\left(0, \frac{1}{2}, 0\right)$. The Ca atom is in interstitial points in Wyckoff site 4c $\left(x, y, \frac{1}{4}\right)$, coordinated by eight oxygen atoms occupying two distinct Wyckoff sites 4c $\left(x, y, \frac{1}{4}\right)$ and 8d (x, y, z). The orthorhombic unit cell is redefined so that the lattice parameters are equal to $a \sim b = \sqrt{2}a_{pc}$ and $c = 2a_{pc}$. Ca, Ti and O atoms are depicted as green, light blue and red spheres, respectively. Solid black line depicts the orthorhombic unit cell. Front octahedra and Ti–O bonds are not shown for clarity.*

The orthorhombic symmetry is described by ten variables: five fractional coordinates corresponding to the oxygen positions, two fractional coordinates correspondent to the A cation, and three lattice parameters defining the size of the orthorhombic unit cell. All of which must be specified in order to completely describe the crystal structure. The orthorhombic distortion leads to a decrease in the coordination number of the A-site from twelve to eight and to two distinct crystallographic sites for the O anions: four oxygen atoms in position O1 in Wyckoff site 4c $\left(x, y, \frac{1}{4}\right)$ and eight in general positions 8d (x, y, z). The orthorhombic symmetry is characterised by three distinct couples of equivalent bonds: two equivalent Ti–O1, two Ti–O2 (short) and two Ti–O2' (long) bonds.

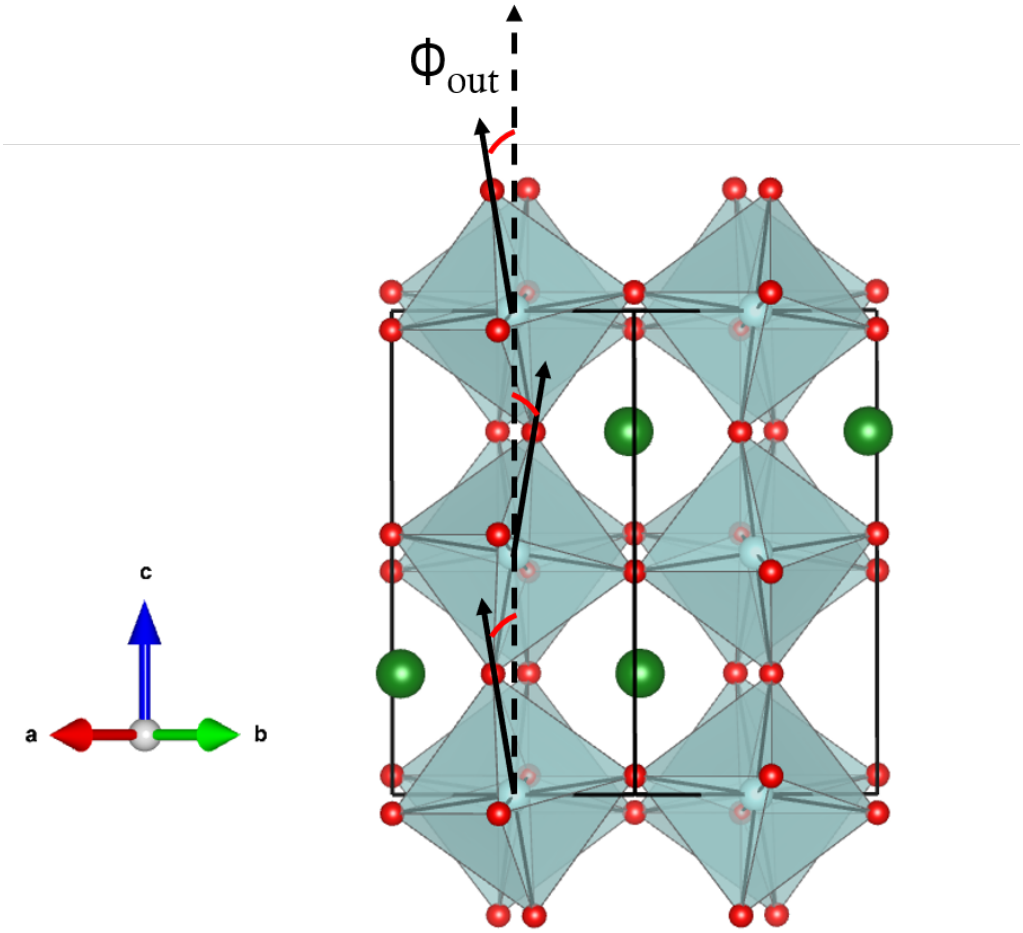

Figure 1.7 *Representation of the out-of-phase tilting angle ϕ_{out} in orthorhombic Pbnm $CaTiO_3$. The structure is viewed along the [110] crystallographic direction. Solid black arrow shows the oxygen displacements from the cubic positions, which lie along the dashed black arrow. Ca, Ti and O atoms are depicted as green, light blue and red spheres, respectively.*

The small size of the A cation causes the TiO_6 octahedra to tilt around the cubic crystallographic axes. In *Pbnm* space-group, the octahedra tilt in-phase around the *c*-crystallographic direction and out-of phase around the *a* and *b*-axes [79] ($a^-a^-c^+$ in Glazer notation). A schematic representation of the out-of-phase and in-phase tilting angles in *Pbnm* is shown in Figures 1.7 and 1.8.

The tilting of the octahedra can be calculated from the lattice parameters as [79]:

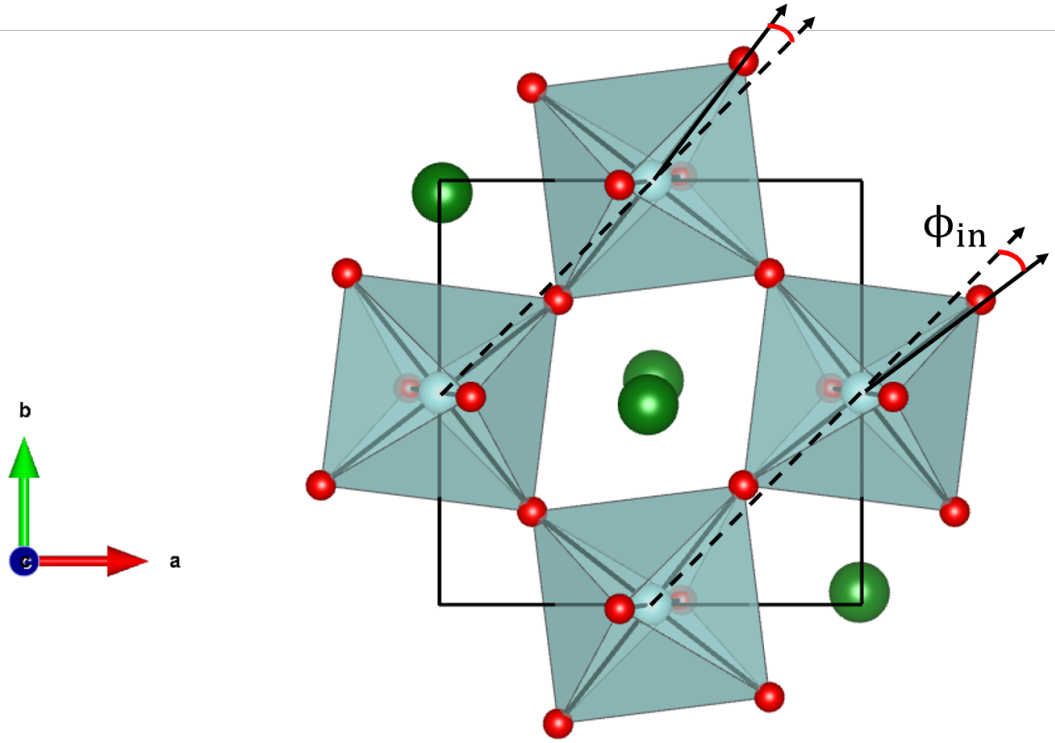

Figure 1.8 *Representation of the in-phase tilting angle ϕ_{in} in orthorhombic Pbnm $CaTiO_3$. The structure is viewed along the [001] crystallographic axis. Solid black arrow shows the oxygen displacements from the cubic positions, which lie along the dashed black arrow. Ca, Ti and O atoms are depicted as green, light blue and red spheres, respectively.*

$$cos\phi_{\text{in}} = \frac{a}{b} \tag{1.2}$$

$$cos\phi_{\text{out}} = \sqrt{2}\frac{a}{c} \tag{1.3}$$

However, the above equations are valid for ideal symmetric octahedra. A more accurate method is to consider the X anions displacement from the cubic crystallographic position. For a *Pbnm* space group the displacement of the O2 atom $\left(\frac{1}{4}-u, \frac{1}{4}+v, w\right)$ from the cubic positions is used to determine the in-phase tilting around the [001] cubic crystallographic axis and the out-of-phase tilting around the [110] axis by [80, 81]:

$$tan\phi_{\text{in}} = 4\frac{u+v}{2} \tag{1.4}$$

$$tan\phi_{\text{out}} = 4\sqrt{2}w \tag{1.5}$$

which account for the deformation of the octahedral edges and avoid over/under estimation of the tilting angle parameters. Orthorhombic symmetry is one of the most adopted by the perovskite structure. Various compounds show an orthorhombic lattice, such as the lanthanide $LaFeO_3$ [82], perovskite material studied in this work, or $LaMnO_3$ [83], which is the parent compound of a perovskite family showing magnetoresistence properties.

1.4.3 Trigonal symmetry

The second most common and stable space group observed in perovskites is the trigonal $R\bar{3}c$ space group[5]. A representation of its crystal structure is shown in Figure 1.9.

[5]Rhombohedral lattice with a 3-fold rotation axis parallel to the z-axis and a c-glide plane parallel to x and y-axes

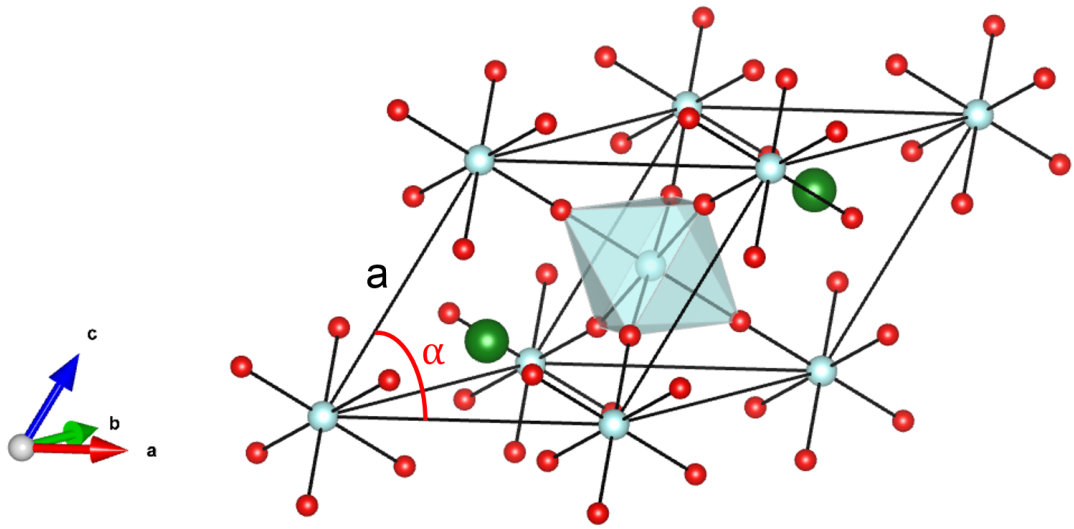

Figure 1.9 *Rhombohedral $R\bar{3}c$ unit cell. Black line shows the rhombohedral unit cell described by the lattice parameter a and the rhombohedral unit-cell angle α. A, B and X atoms are shown as green, light blue and red spheres, respectively.*

The $R\bar{3}c$ space group can be derived from the parent $Pm\bar{3}m$ structure by a cooperative anti-phase rotation of the cubic-phase BX_6 octahedra [65, 66, 77], $a^-a^-a^-$ in Glazer notation. Such tilting pattern reduces the A-site cavity volume as shown for the trigonal $LaCoO_3$ perovskite in Figure 1.10 and leads to three distinctive A–X bonds: three A–X1 short bonds; six A–X2 intermediate bonds and three A–X3 long bonds. This space group has a single crystallographic site for each of the A, B, and X ions. As discussed in detail in the work of Megaw [65], it is possible to quantify the structural distortion of rhombohedral perovskites compared to the cubic aristotype. The equations are based on the choice of the rhombohedral setting for the trigonal crystal lattice. The magnitude of this distortion can be expressed by the anion displacement parameter e from the ideal cubic crystallographic position, as indicated by yellow arrows in Figure 1.10.

Using the relationship $O_x = 0.25 - 2e$, where O_x is the refined oxygen fractional coordinate, it is possible to determine the tilt angle parameter (ω) by the geometrical relation [65]:

$$tan(\omega) = 4\sqrt{3}e \tag{1.6}$$

which quantifies the combined effect of the BX_6 unit rotations about the <100> symmetry axes of the parent cubic unit cell. A value ω tending to 0 indicates the transition to the cubic higher symmetry $Pm\bar{3}m$, where the octahedra are characterised by an ideal undistorted geometry.

Another distortion that characterises trigonal perovskites is the simultaneous elongation or compression of the octahedron along the triad axis of the pseudo-cubic aristotype. Such deformations can be quantified with the value ζ, where ζ is the octahedral strain parameter defined for the $R\bar{3}c$ space group in [65] as:

$$cos(\alpha_{pc}^{obs}) - cos(\alpha_{pc}^{calc}) = \frac{2}{3}\zeta\left(1 - \frac{2}{3}sin^2(\omega)\right)^{-1} \tag{1.7}$$

where α_{pc}^{obs} and α_{pc}^{calc} are the observed and calculated interaxial angles related to the parent pseudo-cubic unit cell as defined in [65]. A value $\zeta > 1$ indicates that the octahedra are elongated along the threefold rotation axis, $\zeta < 1$ indicates compression, and $\zeta = 1$ if the octahedra are perfectly regular, as in the cubic aristotype. Many perovskites adopt the same trigonal symmetry as $LaCoO_3$ [2, 68, 84], such as important and well-known compounds of the lanthanide-oxide

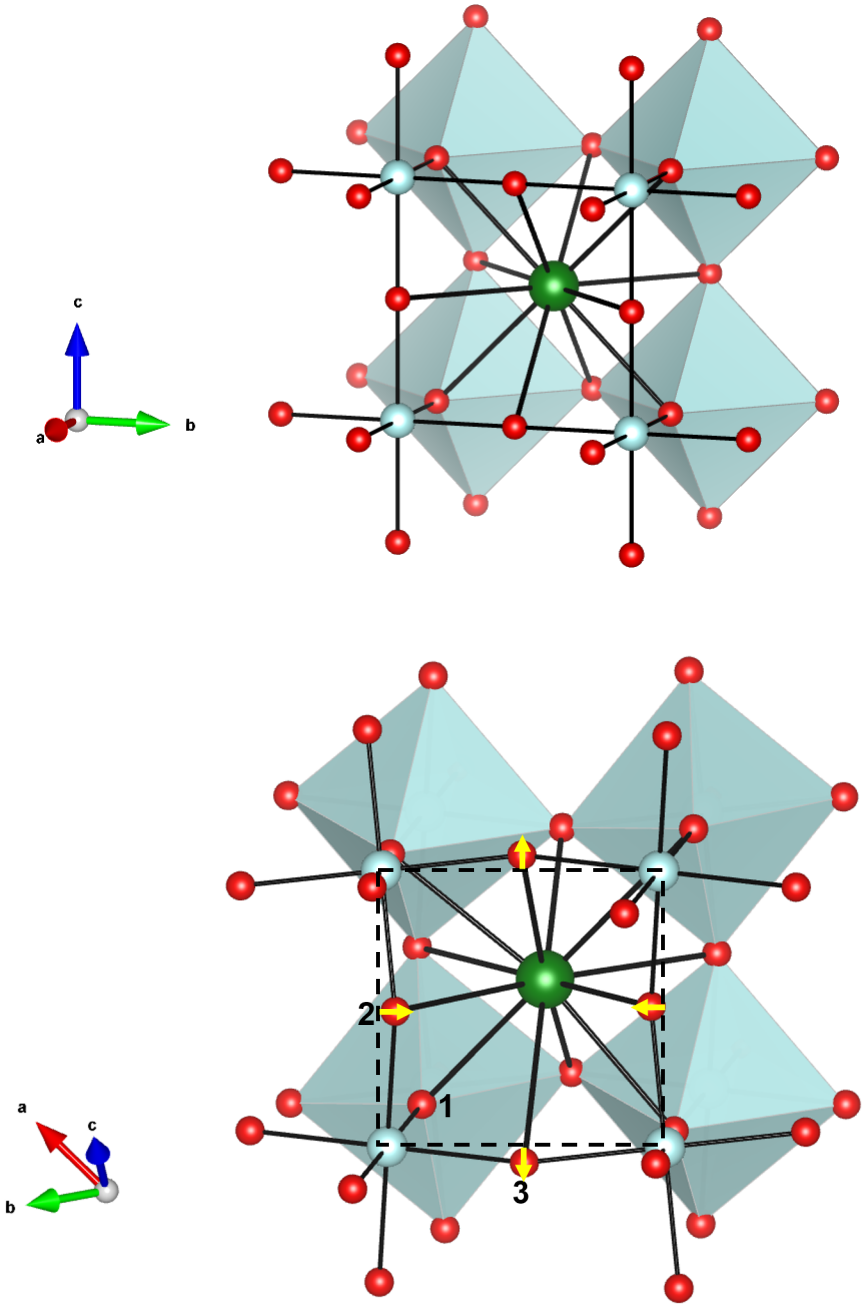

Figure 1.10 *Representation of the octahedral tilting distortion in rhombohedral $R\bar{3}c$ $LaCoO_3$. Top crystal structure shows the $Pm\bar{3}m$ cubic symmetry for comparison. The trigonal $R\bar{3}c$ perovskite shown at the bottom is characterised by successive layers of octahedra rotated of the same magnitude in opposite direction about the $\langle 100 \rangle$ symmetry axes of the cubic aristotype. Oxygen atoms (red spheres) are displaced from the cubic 3d Wyckoff positions (lying along the dashed line) to the 6e site $\left(2e + \frac{1}{4}, \frac{1}{4} - 2e, \frac{3}{4}\right)$ as indicated by the yellow arrows. Green and light blue spheres depict lanthanum and cobalt cations, respectively.*

family like $LaNiO_3$ [85] or the doped $La_{0.7}Sr_{0.3}MnO_3$ [86]. Trigonal symmetry is also found in $LaAlO_3$ [87], and for example in the lithium-based $LiNbO_3$ [88], which display the polar $R3c$ space group.

1.4.4 Monoclinic symmetry

The monoclinic symmetry is a high distorted phase which can be found in perovskite systems. In this symmetry an angle of the unit cell is free to vary, a, b and c lattice parameters have different lengths, and all these structural parameters are necessary to describe the unit cell. A representative monoclinic perovskite is shown in Figure 1.11.

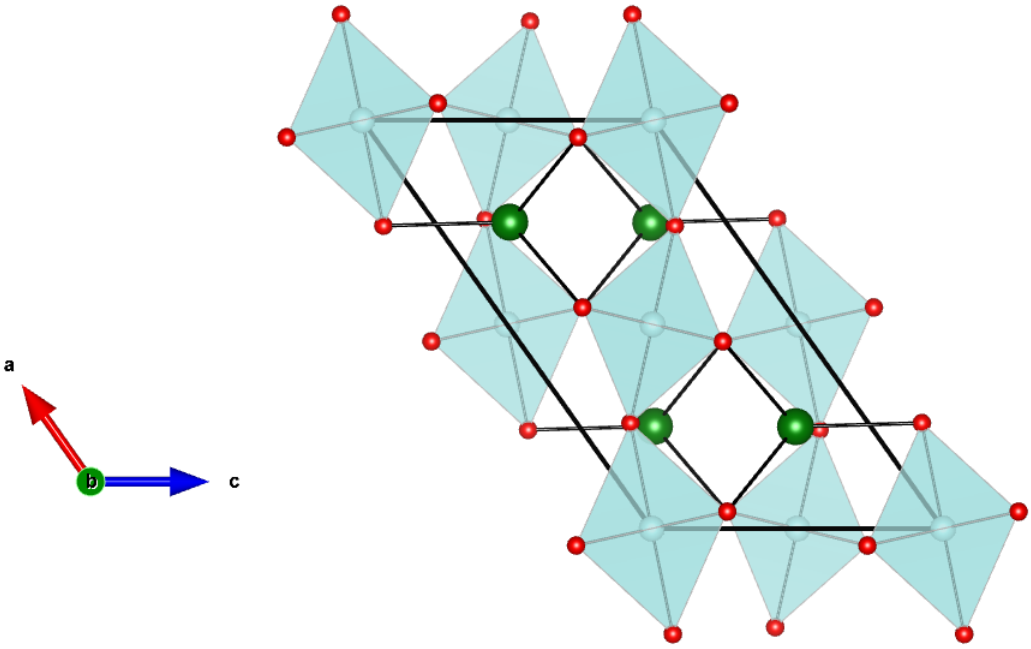

Figure 1.11 *Representation of monoclinic C2/m $LiMnO_3$. The unit cell is distorted so that one of the unit-cell angles deviates from the ideal value of 90°. Solid black line shows the monoclinic unit cell. Li, Mn and O atoms are shown as green, light blue and red spheres, respectively.*

It depicts the $LiMnO_3$ oxide, which adopts a monoclinic $C2/m$ space group [89]. The unit cell is now stretched so that the angle $\beta \sim 109.4°$. The monoclinic $C2/m$ space group is driven by out-of-phase tilting around the [010] and [001] cubic directions with different magnitudes, and is referred to as $a^0b^-c^-$ in Glazer notation. Other typical examples of monoclinic structures include the $BaPbO_3$ and $BiMnO_3$ oxides [90, 91], or B-site ordered double perovskites, such as

La_2NiMnO_6 and La_2MnCoO_6. These perovskite structures show a monoclinic $P2_1/n$ space-group [92, 93]. The $P2_1/n$ space group is described in Glazer notation as $a^-a^+c^-$, that is the result of out-of-phase tilting around the [101] cubic direction with different magnitude and in-phase around the [010] direction. In these materials, the monoclinic distortion is very low. The β angle diverges from the ideal value of 90° by less than 0.1°. The stability of the monoclinic structure is due to cation order of the B-site atoms.

The double perovskite, such as La_2NiMnO_6 and La_2MnCoO_6 [92], is a specific structure which shows 1:1 cation ordering on the B site. This geometry gives rise to structures of the type $A_2BB'O_6$. The 1:1 cation order can also occur on the A site, producing structures of the type $AA'B_2O_6$ such as in the multiferroic double perovskite $CaMnTi_2O_6$ [33, 35]. Three different types of 1:1 order of B cations are identified in double perovskites: rock salt, columnar and layered, which are dependent on the magnitude of disproportion between the cations in size and charge. The most commonly adopted atomic arrangement by B-site ordered perovskites is the rock salt, in which B and B′ are kept at the maximum possible distance between each other in alternating layers of BO_6 and $B'O_6$ octahedra.

1.5 Structural phase transitions

An alternative approach to study the stability of crystal structures and phase transitions is by the application of group representation [78]. Distortions from the cubic aristotype can be described by the parametrisation of the atoms fractional coordinates in terms of an appropriate set of symmetry-adapted basis-vectors of the aristotype phase. The displacements of the A-site cations and the X anions can be expressed as linear combinations of the magnitudes of an appropriate set of symmetry-adapted basis-vectors of the aristotype phase. The idea is to consider the cubic perovskite symmetry and see how its space-vectors transform under the application of specific group operations, which are related to specific atoms displacements and will promote the lower-symmetry structure. By the analysis of the amplitude of these displacement modes it is possible to quantify the structural stability and degree of distortion of a non-cubic perovskite. Considering in-phase or out-of-phase tilting and the magnitude of the tilt angle, there are six basic component tilt systems $a^{+/-}b^0c^0$, $a^0b^{+/-}c^0$, $a^0b^0c^{+/-}$. The tilt systems for perovskites are a linear combination of the six component tilts. Considering a repeat pattern of no more than two neighbouring octahedra, the

Table 1.1 *Independent fifteen tilting system combinations as determined by Howard and Stokes [78]. Examples of perovskite compounds and correspondent space groups are also reported.*

Tilting system	Space Group	Symmetry	Example
$a^0a^0a^0$	$Pm\bar{3}m$	Cubic	$SrTiO_3$ [59], $KMgF_3$ [60]
$a^0a^0c^-$	$I4/mcm$	Tetragonal	low T $SrTiO_3$ [59]
$a^0a^0c^+$	$P4/mbm$	Tetragonal	$KCuF_3$ [94]
$a^0b^-b^-$	$Imma$	Orthorhombic	$BaPbO_3$ [90]
$a^-a^-a^-$	$R\bar{3}c$	Trigonal	$LaCoO_3$ [84], $LaAlO_3$ [87]
$a^-a^-c^+$	$Pbnm$	Orthorhombic	$LaFeO_3$ [82], $LaMnO_3$ [83]
$a^+a^+a^+$	$Im\bar{3}$	Cubic	$Ca_{0.25}Cu_{0.75}TiO_3$ [95]
$a^0b^+b^+$	$I4/mmm$	Tetragonal	Not known examples
$a^+b^+c^+$	$Immm$	Orthorhombic	$Ba_{0.6}K_{0.4}BiO_3$ [96]
$a^0b^+c^-$	$Cmcm$	Orthorhombic	$SrZrO_3$ (973 K) [97]
$a^+a^+c^-$	$P4_2/nmc$	Tetragonal	$CaFeTi_2O_6$ [98]
$a^-b^-b^-$	$C2/c$	Monoclinic	Not known examples
$a^0b^-c^-$	$C2/m$	Monoclinic	low T $BaPbO_3$ [90]
$a^+b^-c^-$	$P2_1/m$	Monoclinic	$GaLiI_3$ [99]
$a^-b^-c^-$	$P\bar{1}$	Triclinic	WO_3 (230–300 K) [100, 101]

number of possible tilt systems is reduced compared to Glazer's classification. The group-theoretical analysis describes the tilting mode by a specific vector in a representation space and identify the required space group which leave the associated vectors invariant. Eight of Glazer's tilt systems are found to be redundant due to the fact they impose a higher symmetry than is required by the space-group symmetry. Table 1.1 reports the fifteen tilt systems that can occur in real crystals and its correspondent space groups.

From the work proposed by Howard and Stokes [78], the oxygen displacements from the cubic $Pm\bar{3}m$ aristotype associated to the in-phase and out-of-phase tilting of the octahedra can be decomposed into two distinctive modes, which transform as the irreducible representation *irreps* M_3^+ and R_4^+ respectively [78, 102]. The group-subgroup relationships are schematically depicted in Figure 1.12. According to this approach for example, the orthorhombic symmetry as in the standard *Pnma* space group is derived from the cubic aristotype by anti-phase tilting of octahedra along the [101] directions and in-phase tilting along the cubic [010] direction [77].

There are different ways in which a cubic $Pm\bar{3}m$ system can transform into orthorhombic *Pnma*. It is more likely that the transformation proceeds through a higher intermediate symmetry before the orthorhombic space group is adopted.

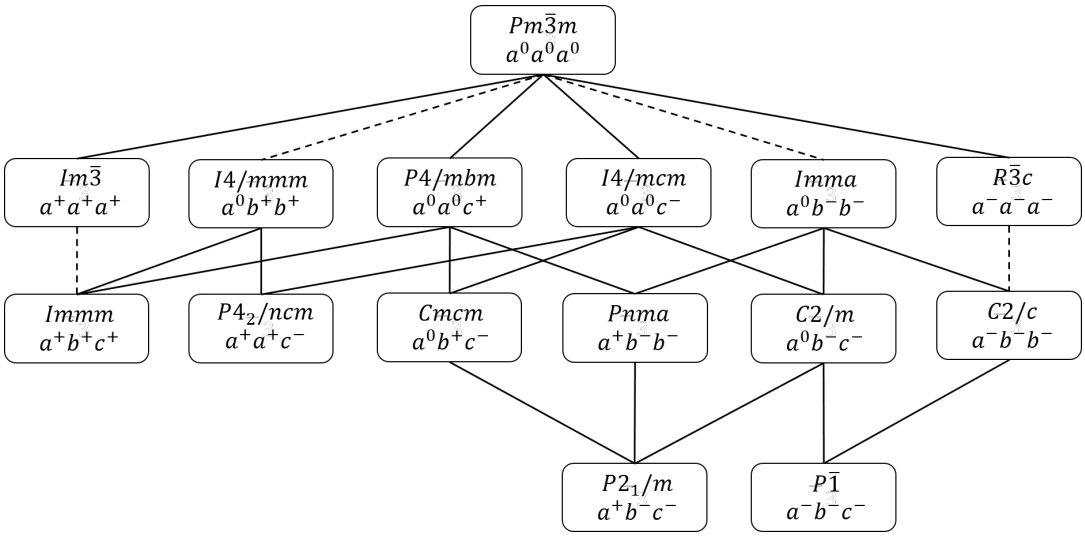

Figure 1.12 *Diagram indicating the group–subgroup relationships among the fifteen space groups of Table 1, re-adapted from Howard and Stokes [78]. The dashed line indicates that the transition must be first order.*

From Figure 1.12 the cubic symmetry will undergo either a transition by an in-phase tilting around one of its crystallographic directions or out-of-phase tilting around two crystallographic directions. After this intermediate state which will be either a tetragonal *I4/mcm* system or an orthorhombic *Imma* space group the structure will transform into the orthorhombic phase. Controlling how the amplitudes of such displacement modes evolve upon pressure or temperature variation is indicative of the route of transformation that crystal symmetry is going to. A further example is given by the trigonal symmetry. As discussed by Glazer and Howard [77, 78] the transitions from $Pm\bar{3}m$ to $R\bar{3}c$ space group is driven by the octahedral anti-phase tilting mode of equal magnitude around the <100> crystallographic directions of the parent cubic structure. The oxygen displacements connected to the anti-phase tilting for the trigonal $LaCoO_3$ are associated to the irreducible representation R_4^+ [78]. A decrease in the pressure/temperature or compositional variation dependence of this amplitude mode is indicative of a possible phase transition from the trigonal symmetry to the cubic aristotype.

The out-of-phase and in-phase tilting angles are then defined as order parameters of the phase transitions. In general, the order parameter correspond to a physical parameter, such as octahedral tilting and strain or the magnetic moment, which drives the distortion of the parent structure by atomic displacements or cation/magnetic orderings. The order parameter is zero in the undistorted $Pm\bar{3}m$

structure. By inducing changes in the structure, for example by variation of pressure and temperature, the order parameter evolves according to the associated representation. For instance the out-of-phase tilting angle order parameter transforms as R_4^+. The order parameter is then a vector, whose magnitude and direction promote structural phase-transitions. This vector is three dimensional, and the most general order parameter direction is R_4^+(a,b,c) which indicates displacements of different magnitudes along different crystallographic directions, leading to a structure with space group symmetry $P\bar{1}$. Higher-symmetry directions R_4^+(a,0,0), R_4^+(a,a,0), R_4^+(a,a,a), R_4^+(a,b,0), and R_4^+(a,a,b) are possible, leading to tetragonal, orthorhombic, rhombohedral and two monoclinic space groups, respectively. The order parameter can evolve either continuously or discontinuously, this defines a transition as of II or I order. For example the temperature-driven ferromagnetic to paramagnetic transition is a II order transition in which the magnetic moment continuously decreases to zero by increasing temperature up to the transition temperature.

The BX_6 octahedra are also potentially deformed from the cubic structure by modes that transform as the *irreps* X_5^+, M_2^+ and R_5^+. Displacements associated to the A-site cations can also be decomposed. These displacements of the A cation along the cubic crystallographic axes, are described by the sum of two basis-vectors, which transform as the irreducible representations R_5^+ and X_5^+.

It is possible to numerically determine the various mode amplitudes by the use of the software ISODISTORT [103]. ISODISTORT is a tool for exploring the structural distortion modes of crystalline materials induced by irreducible representations of the parent space-group symmetry.

1.5.1 Pressure and temperature effects on the perovskite structure

Structural changes and phase transitions of perovskite materials have been largely studied under high pressure or temperature. The cubic aristotype distorts to lower symmetry phases according to the ionic radii of its constituents as well as the conditions of temperature and pressure. By increasing temperature perovskites typically tend to higher-symmetry structures. For example, orthorhombic $LaFeO_3$ becomes trigonal at $\sim$1228 K [104], trigonal $LaAlO_3$ transforms into cubic at 813 K [105] or ferroelectric tetragonal $BaTiO_3$ becomes cubic at temperatures

higher than 393 K [72]. In contrast, under the application of pressure both transitions from lower to higher-symmetry and from higher to lower-symmetry are observed [106–111]. For example, orthorhombic (*Pnma*) $LaGaO_3$ transforms to a rhombohedral ($R\bar{3}c$) structure at 2.5 GPa [112], ferroelectric $BaTiO_3$ becomes cubic at ∼2 GPa [73] or orthorhombic $NdNiO_3$ transforms into rhombohedral at 4 GPa [106]. On the other hand, several iso-structural transitions are reported for orthorhombic perovskites. $GdMnO_3$ orthorhombic perovskite undergoes an iso-structural transition around 50 GPa [110], $LaFeO_3$ is suggested to become body-centred *Ibmm* around 20 GPa [113], or $PbRuO_3$ is reported to undergo an orthorhombic *Pbnm* to orthorhombic $Pbn2_1$ transition [111]. The behaviour under high pressure of perovskite fluorides of the KMF_3 family, where M is a divalent cation, is also interesting. For example, the cubic $Pm\bar{3}m$ structure of $KMgF_3$ remains stable up to 50 GPa as reported by high-pressure X-ray diffraction [75], or $KMnF_3$ undergoes a symmetry lowering from $Pm\bar{3}m$ at ambient conditions to tetragonal *I4/mcm* at an applied pressure of 3.1 GPa [114]. Phase transitions as a function of pressure have thus attracted a large interest and a full understanding of the effect of pressure on chemical structures is still to be achieved.

1.6 3d orbitals in octahedral environment

A transition-metal ion in free space is characterised by five degenerate $3d$-orbitals. In the BX_6 octahedral environment the presence of the six oxygen atoms breaks the orbital degeneracy according to the ligand-metal bond strengths. The $3d$ orbital degeneracy is thus removed by electrostatic interaction between the anion electrons and the B cation electrons in the $3d$ energetic levels according to the geometry of the complex.

The $3d$ electronic orbitals can be pictorially depicted as lobes lying along or in-between the x, y and z directions. The d_{xy} lobes lie in-between the x and y axes; the d_{xz} in-between the x and z axes; the d_{yz} in-between the y and z axes. The $d_{x^2-y^2}$ lobes lie on the x and y axes, while the d_{z^2} are two lobes on the z axes and a toroidal shape ring on the xy plane around the two lobes. In an octahedral complex, there are six ligands attached to the central transition metal, which interact with the positive cation along different directions. Not all the d-orbitals interact directly or with the same energy. In octahedral geometry, ligands approach the metal ion along the x, y, and z axes. Therefore, electrons in the d_{z^2}

and $d_{x^2-y^2}$ orbitals (which lie along these axes) experience greater repulsion.

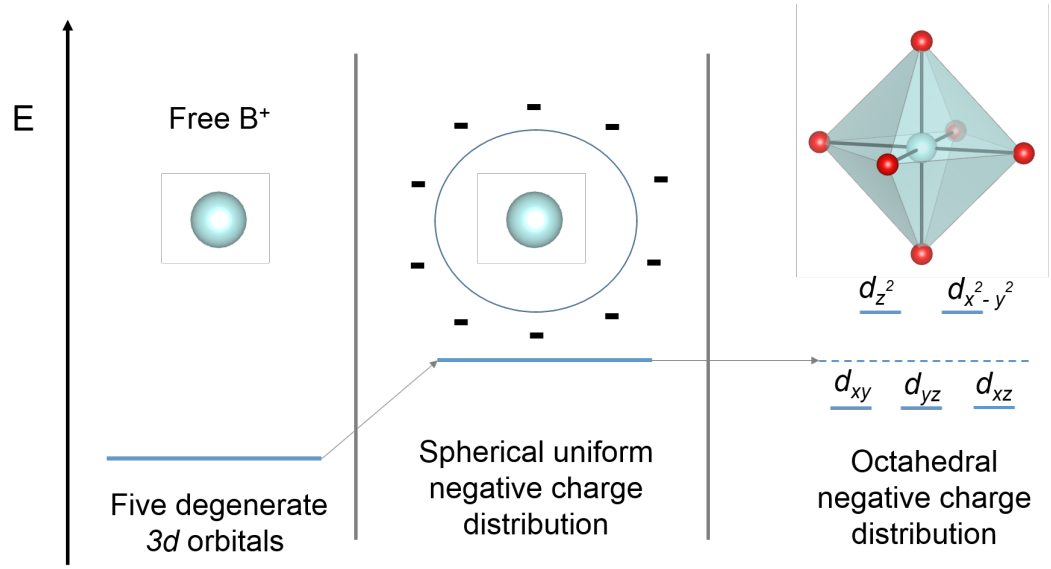

Figure 1.13 *Representation of 3d-orbitals energy-level variation for a cation (B^+) in free space (left), in negative spherical charge distribution (centre), and in negative octahedral charge distribution (right). Black arrow (E) indicates increasing energy direction.*

It requires more energy to have an electron in these two orbitals than in one of the other orbitals. This causes a splitting in the energy levels of the d-shell denoted as the crystal-field splitting (Δ). As shown in Figure 1.13 the energies of the d_{z^2} and $d_{x^2-y^2}$ orbitals (referred to as double-degenerate e_g orbitals) increase due to greater interactions with the O ligands. The d_{xy}, d_{xz}, and d_{yz} orbitals (referred to as triple degenerate t_{2g}) decrease with respect to this normal energy level and become more stable (Figure 1.13). The magnitude of the splitting Δ depends on several factors, such as the oxidation of state of the B cation or the bond strengths between the anion and cation. The higher the oxidation state is or the stronger the bond, the larger the splitting is. The crystal-field splitting Δ determines optical and magnetic properties of transition-metal oxides. The energy required to promote an electron from t_{2g} to e_g (that is Δ) determines the radiation wavelength absorbed by the transition-metal oxide and hence its colour (complementary to the absorbed radiation). Following the Aufbau principle and Hund's rule, electrons are filled from lower to higher energy and in order to have the highest number of unpaired electrons. For example, in the case of Co^{3+}, which has electronic configuration [Ar]$3d^6$, there are six electrons to be placed in the d-orbitals. By Hund's rule three electrons will occupy the d_{xy}, d_{xz}, and d_{yz} with spin parallel to each other. When adding the fourth electron two configurations are possible: to fill a higher energy orbital (d_{z^2} or $d_{x^2-y^2}$) or pair with an electron

on the d_{xy}, d_{xz}, or d_{yz} orbitals. This pairing of the electrons also requires an expense of energy (spin-pairing energy Δ_{ex}). If Δ_{ex} is lower than the crystal-field splitting energy Δ, the electrons (remaining two of the six) will fill the d_{xy}, d_{xz}, or d_{yz} orbitals due to stability. This situation allows for the least amount of unpaired electrons, and is known as low spin (LS). If Δ_{ex} is higher than Δ, the electrons will fill the d_{z^2} or $d_{x^2-y^2}$ orbitals as unpaired electrons. This situation allows for the most number of unpaired electrons, and is known as high spin (HS). As an example, the low, intermediate and high electronic configurations for Co^{3+} are schematically depicted in Figure 1.14.

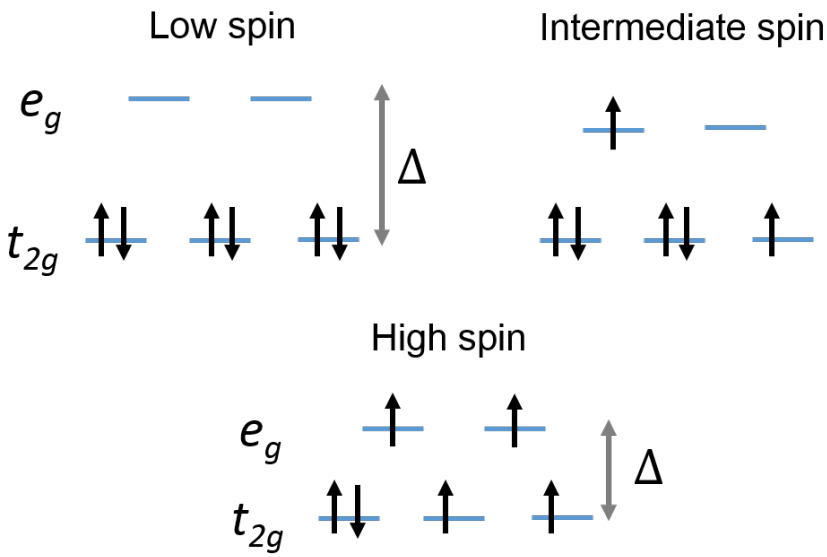

Figure 1.14 *Low ($t_{2g}^6 e_g^0$), intermediate ($t_{2g}^5 e_g^1$), and high-spin ($t_{2g}^4 e_g^2$) electronic configurations of the trivalent cobalt cation with electronic configuration* [Ar]$3d^6$ *in octahedral geometry.*

The magnetism of the compound is also dependent on the intensity of the energy splitting and the competition between Hund's rule of orbital filling and Pauli's exclusion principle. If there are unpaired electrons, the material will show magnetic behaviour; if all electrons are paired, the complex is non-magnetic and will not give rise to any magnetic order.

1.7 Elements of magnetism

Long-range order of magnetic moments is liable to occur in crystal structures such as the perovskite. The alternating layers of BX_6 octahedra allow coupling between close cations. Diverse types of coupling can occur, in which the magnetic

moments of neighbouring cations align parallel or antiparallel depending on a complex mechanism of interactions. The magnetisation of a material, M, is the physical quantity which describes the effect of an external magnetic field H on a system. It is defined by:

$$M = \chi_m H \tag{1.8}$$

where χ_m is the bulk magnetic susceptibility which indicates the behaviour of a material under a magnetic field. Materials can be classified in terms of their magnetic behaviour depending on their bulk magnetic susceptibility.

1.7.1 Paramagnetism

Paramagnetic compounds are materials which show randomly oriented magnetic moments in absence of an external magnetic field. When a magnetic field (H) is applied, the magnetic moments slightly align to the magnetic field direction and a low magnetisation, M, is generated in the same direction as H. The paramagnetic susceptibility assumes values $0 < \chi_m \ll 1$.

By increasing the compound temperature, the increased thermal agitation of the magnetic moments will make harder the alignment of such moments to the magnetic field with a consequent decrease in magnetic susceptibility. This is referred to as the Curie law, which is expressed as:

$$\chi_m = \frac{C}{T} \tag{1.9}$$

where C is a material-specific constant called the Curie constant, T the temperature of the material and χ_m its bulk susceptibility. Not all paramagnetic materials obey the Curie law, but only materials with non-interacting localised magnetic moments. The Curie law is a specific case of the more general Curie-Weiss law which is given by:

$$\chi_m = \frac{C}{T - \Theta} \tag{1.10}$$

where Θ is referred to as the Weiss constant and accounts for the interaction of

neighbouring magnetic moments. If $\Theta = 0$ the Curie-Weiss law reduces to the Curie law. If $\Theta \neq 0$ there is interaction between magnetic moments and the material will be paramagnetic only above a specific transition temperature. The Curie-Weiss law is only valid when the material is in the paramagnetic state. A plot of $\frac{1}{\chi_m}$ as a function of temperature is known as a Curie-Weiss plot. Ideally, it should be linear if the Curie-Weiss law is obeyed. From this plot the Curie constant can be determined as the inverse of the slope and the Weiss constant as the x-intercept.

1.7.2 Ferromagnetism

If $\Theta > 0$, in Equation 1.10, the material is defined as ferromagnetic. Ferromagnetic compounds are materials in which the atoms are arranged (for example in a lattice) so that the atomic magnetic moments can interact and align parallel to each other. The ferromagnetic susceptibility assumes values $\chi_m \gg 1$. This effect is explained in classical theory by the presence of a molecular field within the ferromagnetic material, which was first postulated by Weiss in 1907. Weiss postulated the presence of magnetic domains within the material, which are regions where the atomic magnetic moments are aligned. The movement of these domains determines how the material responds to a magnetic field and as a consequence the susceptibility is a function of the applied magnetic field. In a ferromagnet $\Theta = T_{\mathrm{C}}$, which represents the Curie temperature of the material, that is the transition temperature from the ferromagnetic to the paramagnetic state. As ferromagnetic materials are heated, the thermal agitation of the atoms increases and the degree of alignment of the atomic magnetic moments decreases. Eventually the thermal agitation becomes so great that the material becomes paramagnetic. Above T_{C} the susceptibility ideally varies according to the Curie-Weiss law.

1.7.3 Antiferromagnetism

If $\Theta < 0$, in Equation 1.10, the material is antiferromagnetic. Antiferromagnetic compounds are very similar to ferromagnetic materials but the interaction between neighbouring atoms leads to the anti-parallel alignment of the atomic magnetic moments. Therefore, the magnetic field cancels out and the compound appears to behave in the same way as a paramagnetic material. Similarly to fer-

romagnets these materials become paramagnetic above a transition temperature, known as the Néel temperature, T_N. However, the value of T_N is unrelated to the Weiss constant. The antiferromagnetic susceptibility assumes values $0 < \chi_m \ll 1$.

In the perovskite structure different types of magnetic order can be found across the crystal lattice. These are referred to as: A-type, if layers of parallel moments are antiparallel to adjacent layers of parallel moments; C-type, if columns of parallel moments are antiparallel to adjacent columns of parallel moments; and G-type, if a magnetic moment located in a lattice point is antiparallel to all nearest neighbours' moments. The B-type refers to the ferromagnetic alignment, in which all spins are parallel throughout the crystal lattice.

1.7.4 Ferrimagnetism

Ferrimagnetism is only observed in compounds which have a complex crystal structures, such as in the presence of charge disproportion (for example in perovskites with different cation oxidation states). Within these materials the interactions between magnetic moments lead to parallel alignment in some of the crystal sites and anti-parallel alignment in others. However, the opposing moments are unequal and a net magnetisation remains. The material breaks down into magnetic domains as a ferromagnetic material. The magnetic behaviour is also very similar, although ferrimagnetic materials usually have lower saturation magnetisations.

1.7.5 Diamagnetism

Diamagnetic compounds are materials which show no net magnetic moment in absence of an external magnetic field. When a magnetic field, H, is applied the electrons precess producing a magnetisation, M, in opposite direction with respect to H. All materials have a diamagnetic effect, however, it is often masked by the larger paramagnetic or ferromagnetic term. The diamagnetic susceptibility is independent of temperature and assumes the values: $-1 < \chi_m < 0$.

1.8 Goodenough Kanamori Anderson rules

The superexchange interaction theory was developed by Kramers, Anderson, Goodenough and Kanamori [115–117]. Kramers in 1934 proposed the idea that a magnetic interaction between two magnetic ions such as Fe cations can occur by mediation of a non magnetic ion such as oxygen atoms. This model was further developed by Anderson in 1950. In the same year, Goodenough and Kanamori proposed some semi-empirical rules for superexchange interaction between these ions, which are called Goodenough-Kanamori-Anderson (GKA) rules. These guidelines predict a strong antiferromagnetic (AF) order between the transition metal d electrons when the ion-anion-ion angle is 180° with partially filled d-shells, and weak ferromagnetism (FM) when the angle is 90°. The GKA rules are based on the symmetry relations and electron occupancy of the overlapping atomic orbitals and can be used to predict whether the interaction is ferromagnetic or antiferromagnatic, that is if the spins of unpaired electrons align parallel or antiparallel across the structure. Electrons in the *2p* orbitals can form two types of covalent bond, a stronger bond denoted as σ symmetrical with respect to rotation about the bond axis, and a weaker bond referred to as π, when the orbital overlap occurs laterally and anti-symmetrical respect to rotation about the bond axis. Orbitals involved in such types of bonds are conventionally denoted as p_σ and p_π. When two ions have orbital lobes pointing towards each other to have a good overlap integral as schematic represented in Figure 1.15, the exchange is antiferromagnetic.

According to the direction of approach of the different ions some different cases can be distinguished:

- When the lobes are d_{z^2} orbitals at 180°, pointing directly towards a ligand and each other as in Figure 1.15, they interact by p_σ. The large orbital overlap gives rise to strong antiferromagnetism.
- When d_{yz} orbitals are in 180° position to each other, they can interact via p_π orbitals on the ligand and there is an antiferromagnetic coupling, but weaker than the one arising from σ bonds.
- At 90° if a lobe is d_{z^2} and one ion contributes to the overlap with a d_{xy}, and hence interacting by p_σ and p_π orbitals respectively, a reasonably strong overlap is obtained and AFM coupling occurs.

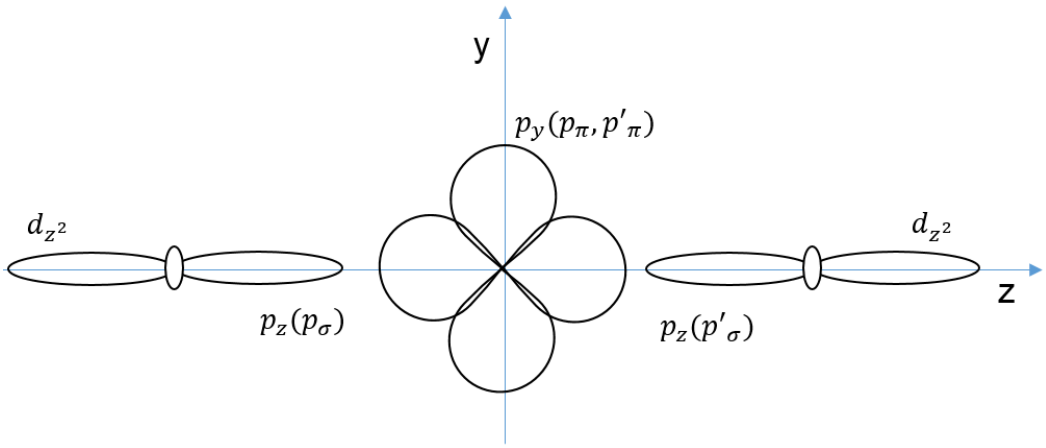

Figure 1.15 *Schematic representation of the superexhange interaction between d_{z^2} orbitals mediated by 2p electrons at $\theta = 180°$. The symbol $p_{\sigma/\pi}$ indicates the type of bond along the bond axis. Symbols in brackets indicate how the d-orbital interacts with p-orbitals along the bond axis (without apostrophe), and with p-orbitals orthogonal to the bond axis (with apostrophe).*

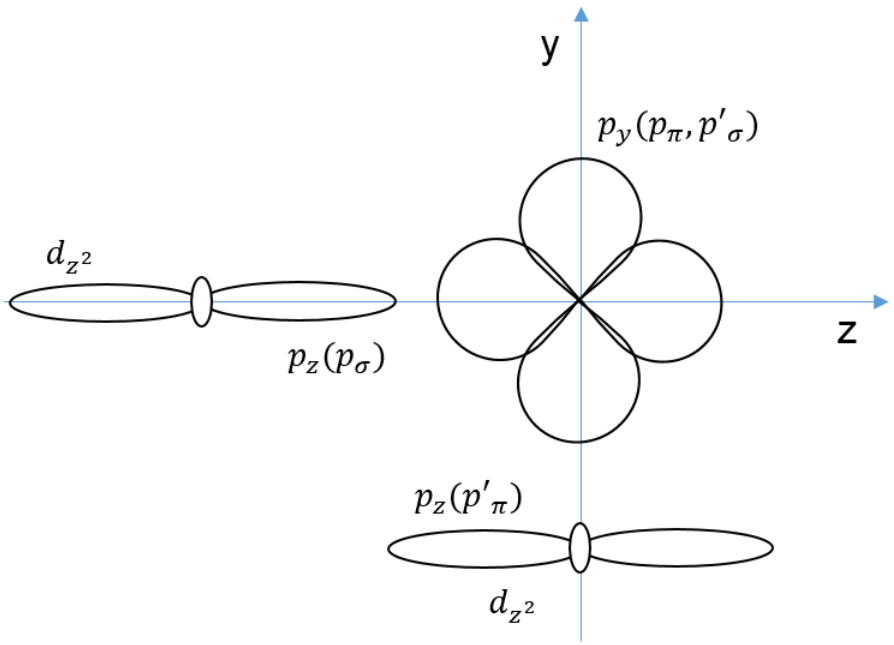

Figure 1.16 *Schematic representation of the superexchange interaction between d_{z^2} orbitals placed at an angle $\theta = 90°$ mediated by 2p electrons. Symbols in brackets indicate how the d-orbital interacts with p-orbitals along the bond axis (without apostrophe), and with p-orbitals orthogonal to the bond axis (with apostrophe).*

If the ions have contact but no overlap integral, for example a d_{z^2} and a d_{xy} at 180° or another d_{z^2} at 90° as illustrated in Figure 1.16, the interaction is weak and gives ferromagnetic interactions. The coupling between electronic spins are

then rooted in the overlap of electrons and in Pauli's principle. The exchange interaction between neighbouring atoms will force individual spins into parallel or antiparallel alignment. The idea can be illustrated with a few representative examples. Consider a Fe^{3+}–O^{2-}–Fe^{3+} system lying along the same axis as to form an ideal angle $\theta = 180°$. The Fe^{3+} ions, characterised by the electronic configuration $[Ar]3d^5$, interact by the mediation of the *2p* electrons of the non-magnetic O^{2-} anion as depicted in Figure 1.17a.

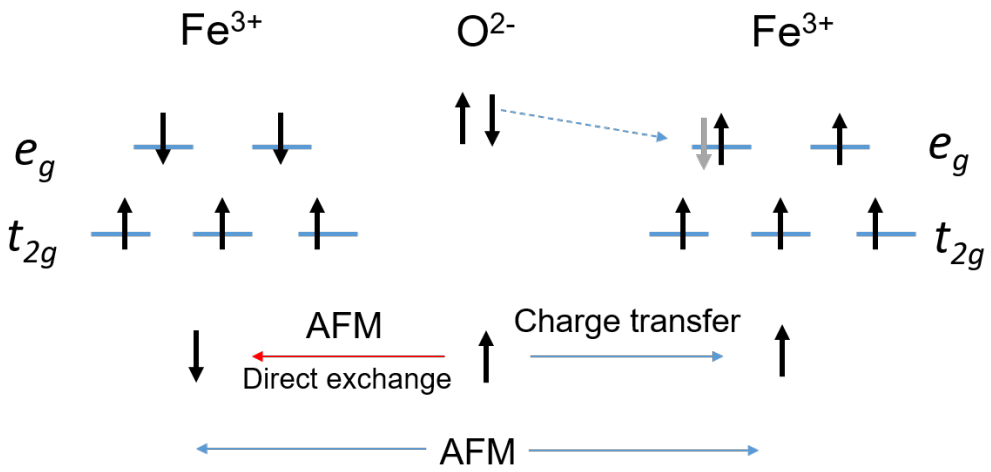

(a)

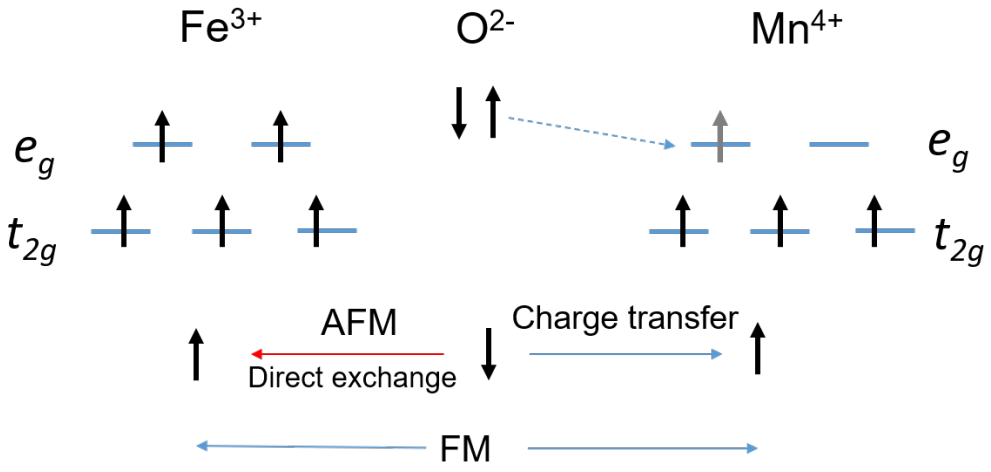

(b)

Figure 1.17 *1.17a Representation of the antiferromagnetic superexchange interaction in the Fe^{3+}–O^{2-}–Fe^{3+} system at $\theta = 180°$. 1.17b Representation of the ferromagnetic superexchange interaction in the Mn^{4+}–O^{2-}–Fe^{3+} system at $\theta = 180°$. Red arrows indicate AFM direct exchange interaction between electrons in non-orthogonal 3d and 2p orbitals.*

Along the axis direction the p orbitals are orthogonal to the t_{2g} ($d_{xy,yz,xz}$) orbitals

which lie in-between the x, y and z-axes, but are not orthogonal to the e_g orbitals lying along the axes. As a consequence of orbital overlapping one electron from the oxygen, the spin down electron according to Pauli's principle, will hop to one of the e_g orbitals. The remaining electron will undergo direct exchange with the second iron atom, and the large overlap between the two orbitals will promote an antiferromagnetic coupling. Direct exchange operates between atoms close enough to overlap their wavefunction. Strong interaction, but short range and decreases rapidly with separation of the atoms. The resulting interaction between the trivalent iron cations will be antiferromagnetic as in the orthorhombic lanthanum ferrite $LaFeO_3$.

If the first trivalent iron is replaced with tetravalent manganese (electronic configuration $[Ar]3d^3$) as in Figure 1.17b, only three electrons will fill by Hund's rule the t_{2g} orbitals. Hund's rule itself imposes the up-spin electron to hop from the *2p* orbital to the trivalent cation. The direct exchange between the remaining electron and the trivalent iron will again be antiferromagnetic, whereas the overall superexchange interaction between the transition metal cation will be ferromagnetic. In the $\theta = 90°$ interaction configuration the p_σ orbitals will acquire the p_π orbital character. If we consider again the case of Fe^{3+}–O^{2-}–Fe^{3+}, we will still observe charge transfer of the down-spin electron to the first trivalent iron, however the p_σ orbital has now a p'_π character and is orthogonal to the d-orbital and thus a weak ferromagnetic coupling is predicted by direct exchange with a resulting ferromagnetic interaction, as shown in Figure 1.18a. Equivalently, considering at $\theta = 90°$ the interaction between two transition metal cations in the case of Mn^{4+}–O^{2-}–Fe^{3+} (Figure 1.18b), charge transfer of the up-spin electron will occur, but now the remaining electron will couple by direct exchange with the orthogonal d_{z^2} orbital and a resulting antiferromagnetic superexchange is predicted. Direct exchange is ferromagnetic if the orbitals are orthogonal, if not the magnitude of the overlapping integral provide a measure of the covalency of the bond and an antiferromagnetic coupling is expected.

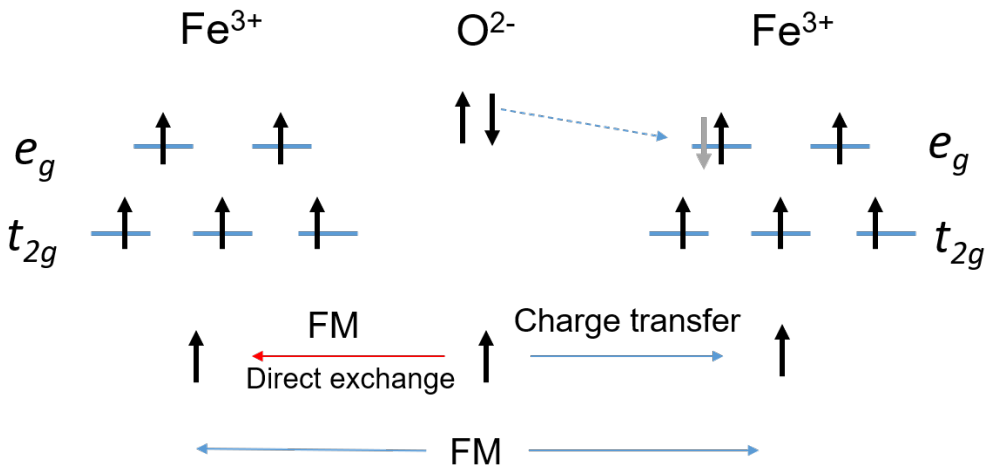

(a)

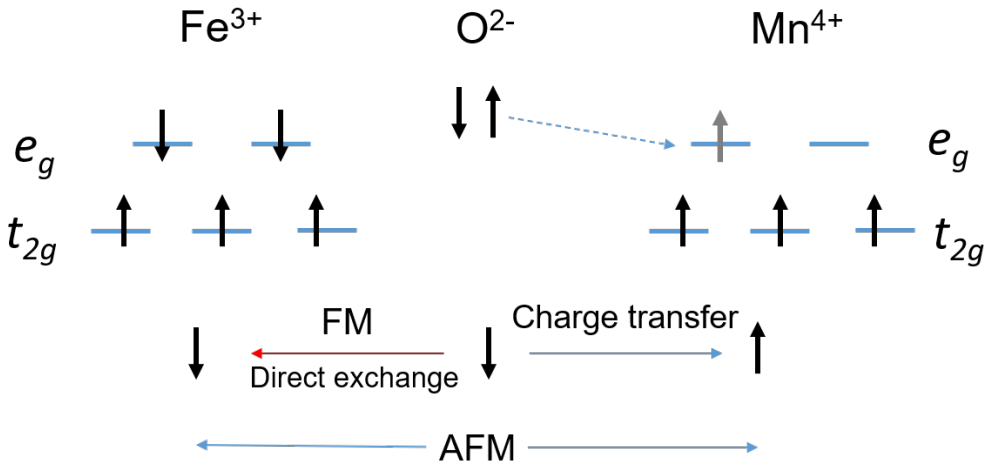

(b)

Figure 1.18 *1.18a Representation of the ferromagnetic superexchange interaction in the Fe^{3+}–O^{2-}–Fe^{3+} system at $\theta = 90°$. 1.18b Representation of the antiferromagnetic superexchange interaction in the Mn^{4+}–O^{2-}–Fe^{3+} system at $\theta = 90°$. Red arrows indicate FM direct exchange interaction between electrons in orthogonal 3d and 2p orbitals.*

1.9 Structural-physical property relationships

The study of structural distortions in perovskite materials is of interest not only from a crystallographic point of view. Structural distortions are strictly related to physical properties of perovskites, and by acting on these distortions these properties can be advantageously tuned. Physical properties of the perovskite structure are related to the electronic configuration of the material, which depends on the number of $3d$ electrons, the Hund's rule, the crystal-field splitting, Jahn-Teller splitting of the $3d$ electron states and to exchange energies. Hopping and superexchange of electrons in unfilled *3d* orbitals take place via oxygen sites due to the overlap of the respective wave-function and may lead to long-range magnetic order. Physical properties and phase diagrams of a perovskite strongly depend on the chemical composition and even more on tilting or distortions of the BX_6 octahedra. Understanding structural-physical property relationships in perovskite systems is thus crucial in light of tuning the physical features and enhancing the performance of perovskite compounds in their various technological applications. Nowadays, this is achievable by chemical substitution, application of hydrostatic pressure or temperature variation.

For example, cobalt-based perovskites are studied for their spin-state transitions and are model systems for investigating electronic-structural correlations. In the $LaCoO_3$ perovskite [68, 118–124], which exhibits the crystal structure as shown in Figure 1.10, all three spin states of Co^{3+} ($3d^6$) LS, IS and HS are close to degenerate. As these states correspond to slightly different ionic radii, upon pressure or temperature variations a change in the populations from high spin, intermediate spin to low spin of the trivalent cobalt can be promoted. Acting on the structure by hydrostatic pressure or temperature variation has been demonstrated to activate spin-state transitions in this compound [68, 119, 120, 122, 123]. The $LaCoO_3$ perovskite has been extensively studied in this thesis and a detailed analysis is reported in Chapter 3.

1.9.1 Electric and magnetic properties

An important example of structural-property relationship is transition-metal-based perovskites characterised by high dielectric permittivity and ferroelectricity. As discussed for tetragonal $BaTiO_3$ [16], the high permittivity is connected to

polar transition-metal displacement from the centre of the oxygen-coordinated octahedral cages along the z cubic axis and so is the ferroelectric behaviour. Cation displacement within the octahedral site induces a permanent electric dipole moment across the crystal structure, which can be reversed by the application of an external magnetic field. The direction and magnitude of the displacement determines the direction of the resultant dipole moment. Upon cooling from the ambient temperature tetragonal phase $BaTiO_3$ undergoes two further transitions. The first, to an orthorhombic symmetry $Amm2$ is caused by the B cation displacement along the [110] cubic direction [72]. By further cooling $BaTiO_3$ becomes rhombohedral, $R3m$, and the displacement of the cation is seen to occur along the [111] aristotype direction [72]. The three diverse Ti cation displacements within the octahedron are schematically depicted in Figure 1.19.

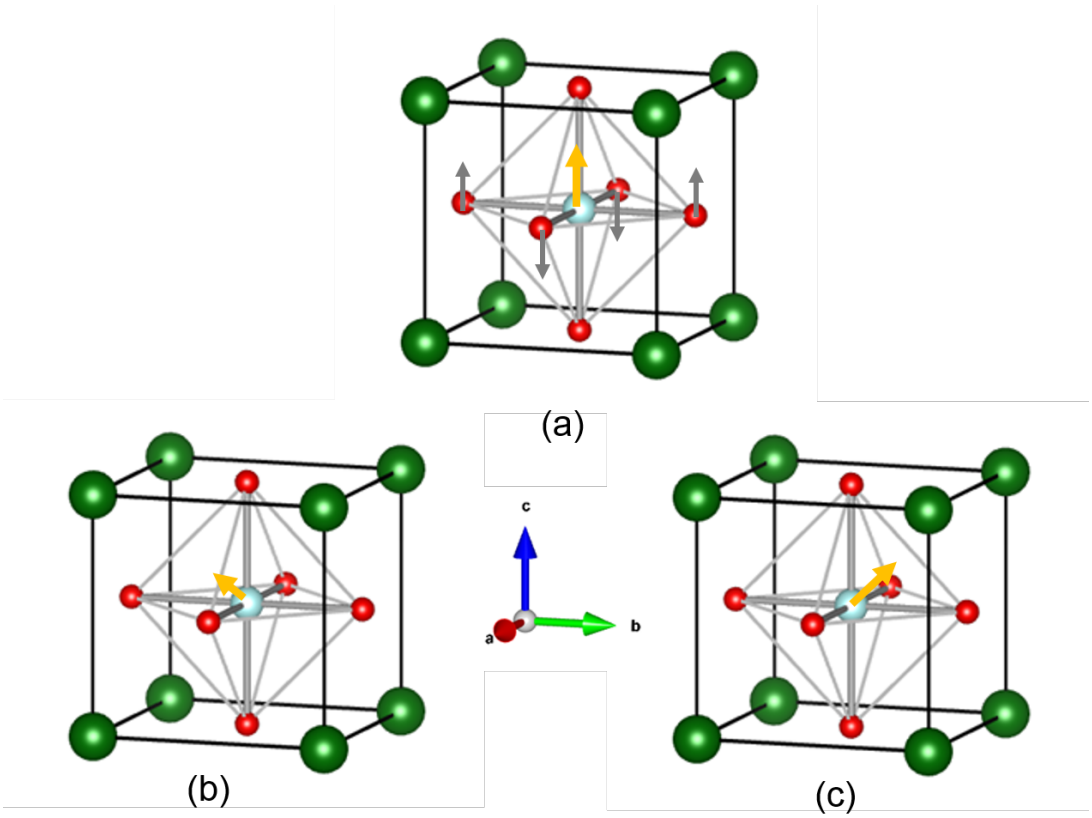

Figure 1.19 *1.18a Cation displacement in tetragonal $BaTiO_3$ along the [001] four-fold octahedral axis. 1.18b Cation displacement in orthorhombic Amm2 $BaTiO_3$ along the [110] two-fold axis. 1.18c Cation displacement in trigonal R3m $BaTiO_3$ along the [111] three-fold axis.*

Multiferroism is also observed in perovskites. These materials show ferroelectric response and simultaneous long-range magnetic order. Non-centrosymmetric

$BiFeO_3$ ($R3c$) has driven attention because it is a candidate for ambient temperature applications [125]. This material shows ferroelectricity and antiferromagnetic order. $BiFeO_3$ becomes ferroelectric at $T_C \sim 1100\,K$ and antiferromagnetic at $T_N = 650\,K$ [126, 127], the paraelectric phase structure is orthorhombic *Pbnm*. If manganese is substituted on the B-site, the $BiMnO_3$ structure crystallises with monoclinic symmetry in the polar $C2$ space group. The material shows ferroelectricity, however ferromagnetic order is observed [128, 129]. $BiMnO_3$ becomes ferroelectric at 450 K and ferromagnetic at T_C 105 K [130]. In both materials the magnetic ordering is due to the B-site cation electronic configuration. In $BiFeO_3$ AFM arises from Fe^{3+}–O^{2+}–Fe^{3+} superexchange interaction, while ferromagnetism in $BiMnO_3$ comes from the FM ordering of high-spin Mn^{4+} ions. The ferroelectric response has its origin from the A-site electronic configuration. The main driving force of the ferroelectric phase in both materials seems to be the stereochemical activity of the Bi *6s* lone-pair, which is responsible for displacement of Bi and O sublattices, hence driving the generation of a permanent dipole moment. The Fe and Mn cations have also been shown to be slightly displaced and their displacement also contributes to the total electric polarisation [125, 129, 131].

Under an applied external electric field polar perovskites have shown to provide a strong response. If an external magnetic field is applied various perovskites show a further interesting effect that is a strong variation, either positive or negative, of the electrical resistance. This effect is called magnetoresistance and has been discovered in the $Ln_{1-x}A_xMnO_3$ (Ln = rare earth; A = divalent ion), such as in the $La_{1-x}Sr_xMnO_3$ material series. By doping the perovskite with different concentrations of Sr^{2+} cations, a mixture of Mn^{3+}/Mn^{4+} ions will be induced on the B-site. This corresponds to the number of Mn sites with a single occupied e_g orbital (Mn^{3+}) and empty e_g orbitals (Mn^{4+}). Double exchange between the different valent Mn ions can occur, and direct hop of electrons from neighbouring cations takes place. The magnetoresistance effect arises from double exchange between Mn^{3+} and Mn^{4+} cations [27, 115, 132]. As a function of chemical composition different magnetic ground states and orbital orders are formed. The colossal magnetoresistance phenomenon is ascribed to the strong coupling among cation charges, orbital overlapping and electronic spin-states. The external magnetic field reorients the ferromagnetic components to an aligned state, generating a magnetic disorder-order transition. The change in electrical resistance is due to the contribution of the scattering of electrons by the non-aligned ferromagnetic components when there is no applied field.

1.9.2 Optical properties

Perovskite materials such as halide perovskites have recently begun to be utilised in the photovoltaic and optoelectronic industry especially as components of new generation solar cells and light-emitting-diodes [4, 47–57].

This new attention, especially on photovoltaic applications, is related to the possibility to improve the photovoltaic response of perovskites, that is the generation of a voltage across the structure by illumination. Tin and lead iodide perovskite semiconductors candidate for high-efficiency low-cost photovoltaics, in part because they have band gaps, that is the energy difference between the electronic valence and conduction band, that can be tuned over a wide range by chemical substitution. It is possible to increase or decrease the band-gap by controlling the tilting distortion in the material [133, 134] and this is easily achievable by the application of pressure or temperature. Increasing the octahedral tilting and thus the A-site volume leads to an increase of the band-gap. Reducing the size of the A-site cation can distort the perovskite lattice in two distinct ways: by tilting the BX_6 octahedra or by simply contracting the lattice isotropically. The former effect tends to raise the band gap, while the latter tends to decrease it [134].

In this way it is possible to control the absorption wavelength of the materials and thus the electron-hole recombination energy. In halide perovskites it is dependent on the ratio of halides (X) present in the structure such as I, Br or Cl. This is exploited in optoelectronic devices where the application of an electric field changes the optical response of a material. Cesium lead halide perovskites $CsPbX_3$ are an example of perovskite materials utilised in optoelectronic devices. By tuning the composition of the halide element X, a long carrier diffusion and carrier life-time can be obtained [50, 52–54]. Moreover, absorption wavelength can be freely tuned and set it in the visible spectral range by mixing I and Br or Cl and Br, and forming mixed-halide solid solutions [53, 57].

1.9.3 Ionic and electrical conductivity

Perovskite systems are also exploited for their electrical and ionic conductivity [135–139]. The perovskite halides, $CsPbCl_3$, $CsPbBr_3$ and $KMnCl_3$ or oxygen deficient perovskite oxides such as $(La,Ca)AlO_{3-\delta}$ or $Ca(Ti,Al)O_{3-\delta}$, and other

oxides are excellent ion conductors and applied in energy storage devices such as batteries or fuel cells [135, 137]. Two main phenomena of conduction can occur in perovskites, which arise from either electron or ion transport. The ionic conductivity effect consists of the moving of cations and/or anions throughout the perovskite structure by the application of an external electric field. The ion transport is dependent on the presence of vacancies in the chemical composition of the perovskite material. Ionic conductivity is commonly enhanced by inducing vacancies by chemical substitution such as in the oxygen deficient families (La,Ca)$AlO_{3-\delta}$ or Ca(Ti,Al)$O_{3-\delta}$ [135, 137]. The oxygen ions conduction takes place via an interstitial mechanism, in which the interstitial ion moves into a normally occupied site while simultaneously displacing the resident ion into an adjoining interstitial position. An activation potential for the conduction phenomenon can be defined, which depends on the interlink of the octahedra and thus on the octahedral tilting. The conduction barrier was observed to decrease by increasing the octahedral distortion. As the tilting distortion is sensitive to temperature and pressure variation, the migration process can be promoted or reduced by deviation from room conditions. Moreover, as a function of pressure it has been reported that tensile strain lowers the potential barrier, while compressive strain increases it [138, 139].

An important requirement for ionic conductivity is the constraint to have ions within the A and B site with the same oxidation state. If there are transition-metal ions with different valence, electrons transport will also occur. Electron conduction is a more intense phenomenon than ionic conduction, whose intensity is easily overcome and its contribution to the total conductivity of the material becomes negligible.

1.10 Thesis outline

The research carried out in this thesis concerns the structural-physical property characterisation of perovskite oxides. The strong structural-physical property relationships are key aspects of these materials. Chemical, electrical, magnetic, optical and transport properties can be finely adjusted by externally acting on the structure, and the application of pressure is a straightforward method to achieve it. In this work, perovskite oxides are investigated by a combination of several techniques, in particular by high-pressure neutron diffraction, whose methods and equipment will be deeply discussed. The following chapter, Chapter 2, gives an

overview of the physical background behind the experimental techniques utilised in this work. Elements of neutron and X-ray diffraction, Raman spectroscopy and magnetometry are discussed. Detailed descriptions of methods and equipments for high-pressure experiments are also reported.

Following three chapters show experimental results on the perovskites $LaCoO_3$ (Chapter 3), $LaFeO_3$ (Chapter 4), and $LaCo_{0.9}Mn_{0.1}O_3$ (Chapter 5). These chapters report the high-pressure structural characterisation performed on the samples primarily by neutron diffraction. Details on the structural compression are discussed in terms of evolution of the unit-cell parameters, chemical bonds and the distortion parameters, such as the octahedral tilting angle and strain previously introduced in this chapter. These results are complemented with details in the chemical synthesis and preliminary phase characterisation as well as further high-pressure Raman spectroscopy or magnetisation characterisation. This thesis shows experiments carried out at the ISIS, Neutron and Muon Facility, STFC. In particular, high-pressure neutron diffraction experiments were performed on the PEARL instrument. Chapter 6 describes details of the PEARL diffractometer and reports recent instrument capability developments. These are aiming at integrating diamond anvil cells for neutron diffraction at the ISIS facility with the final goal to reduce the usable sample volume and extend the pressure range during experiments.

Chapter 2

Methods

This chapter provides an overview of the various experimental techniques and equipment utilised in this work. Structural properties of materials have been studied primarily by neutron-diffraction. X-ray diffraction has also been used after material synthesis for a preliminary structural characterisation of powder samples, which were synthesised by solid state reaction methods. Spectroscopic and magnetic properties of materials have also been studied in this work by Raman scattering and DC magnetisation measurements. High-pressure neutron-powder-diffraction measurements were carried out on the PEARL diffractometer, at the ISIS Neutron and Muon facility. Magnetisation and Raman experiments have also been performed at high-pressure by the use of specially designed pressure cells at the ISIS facility. This chapter gives an overview of the fundamentals of these various techniques and describes the different pressure-generating devices utilised in pressure-dependent experiments.

2.1 Diffraction

Diffraction is the phenomenon which describes the interaction of a wave, such as X-ray radiation, with a scattering obstacle or a slit. Neutrons can be associated to a wavelength by the De Broglie relation $\lambda = \frac{h}{m_n v}$, where h is the Planck constant, m_n the neutron mass and v its velocity. Neutrons can diffract/scatter[1] materials as a wave.

[1] In classical physics diffraction refers to the interaction of a wave with an element, while scattering is the term used to refer to the interaction between a particle and an element.

Consider a wave or a particle incident with wavevector $\vec{k_i}$ and angular frequency ω_i on a scattering object. The resultant scattering phenomenon will alter the momentum $\vec{p}$ and energy E of the incident ray/particle. The momentum transfer can be expressed as $\vec{p} = \hbar\vec{Q} = \hbar(\vec{k_i} - \vec{k_f})$ and the transferred energy as $E = \hbar(\omega_i - \omega_f)$. In the case of elastic scattering there is no transfer of energy and the modulus of the wavevector remains unchanged after the scattering process $|\vec{k_i}| = |\vec{k_f}|$. The scattered radiation emerges at an angle 2θ respect to the incident beam direction. The magnitude of the scattering vector can be calculated from the wavelength λ and the scattering angle 2θ and is given by:

$$Q = \frac{4\pi}{\lambda} sin\theta \tag{2.1}$$

A scattering experiment consists in the measurement of the scattered intensity distribution as a function of the scattering angle 2θ, hence as a function of the scattering vector $\vec{Q}$ [140].

2.1.1 Bragg's law

Diffraction, either by neutron or X-ray radiation (with λ in the order of the Ångstrom, approximating the atomic spacing of atoms), enables us to map the relative position of atoms in materials and is one of the basic techniques to investigate structural properties of compounds. The measurement principle of diffraction is based on interference (constructive) and the Bragg relation [141, 142]:

$$2d_{h,k,l} sin(\theta) = n\lambda \tag{2.2}$$

where λ is the wavelength of the incoming and scattered (elastic scattering) radiation, 2θ is the angle between incoming and scattered radiation and d is the distance between atomic planes identified by $\{hkl\}$ Miller indices. In Equation 2.2 n is an integer determined by the diffraction order which indicates if constructive interference occurs for a path difference equal to $n\lambda = 1\lambda, 2\lambda, 3\lambda...$ Figure 2.1 schematically depicts the Bragg's scattering phenomenon. Parallel monochromatic waves of wavelength λ scatter a crystal lattice with inter-planar spacing d.

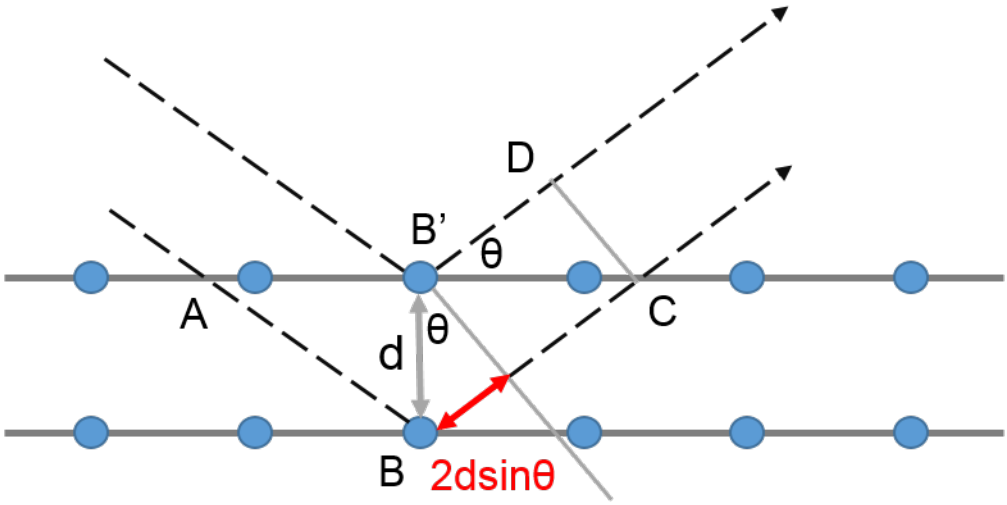

Figure 2.1 *Schematic representation of Bragg's law. Incoming and scattered radiation is shown as dashed black arrows, while the red arrow highlights the path difference between two parallel waves. The angle θ is equal to half the angle between the incident and scattered wave. d indicates the inter-planar spacing between adjacent crystallographic planes.*

If the scattering is elastic, the scattered waves will emerge at an angle 2θ with the same wavelength as the incident radiation. However, there will be a path difference between waves scattered from different lattice points. Bragg diffraction occurs when waves of wavelength comparable to the atomic spacings are scattered in-phase by the atoms in the crystal and undergo constructive interference. This will occur if the path difference is equal to a multiple integer of the radiation wavelength $n\lambda$. By geometrical relationships in Figure 2.1, the path difference can be calculated in terms of half the scattering angle θ and the inter-planar spacing d, which leads to Equation 2.2. The inter-planar distance d_{hkl} is related to the unit-cell structural parameters by:

$$\frac{1}{d_{hkl}^2} = h^2a^{*2} + k^2b^{*2} + l^2c^{*2} + 2hka^*b^*cos\gamma^* + 2hla^*c^*cos\beta^* + 2klb^*c^*cos\alpha^* \quad (2.3)$$

where $a^* = \frac{bcsin\alpha}{V}$, $cos\alpha^* = \frac{cos\beta cos\gamma - cos\alpha}{sin\beta sin\gamma}$ and correspondent permutations for b^*, c^*, $cos\beta^*$ and $cos\gamma^*$. The diffraction peak position represents the average of the atomic distances in the crystal. Bragg's law describes the condition for constructive interference from successive crystallographic planes of the crystalline lattice. Scattered waves from different lattice points will contribute to the

diffraction pattern if they arrive in-phase to the detector. If waves are scattered out-of-phase disruptive interference will occur, hence a loss in the scattered signal. Not all lattice points satisfy Bragg's law and contribute to the scattered signal, but lattice points generating a momentum transfer, which is equivalent to a lattice vector in reciprocal space. This is referred to as the Laue condition.

2.1.2 The Ewald sphere

The Ewald sphere is a geometrical construction used in crystallography to relate the transferred momentum $\vec{Q}$, to the scattering angle and the reciprocal lattice [143]. Draw a lattice in reciprocal space, for example in 2D the reciprocal of a square lattice is a square lattice. Consider elastic scattering of an incident wavelength on a point, the scattered radiation will be emitted at angle 2θ as shown in Figure 2.2.

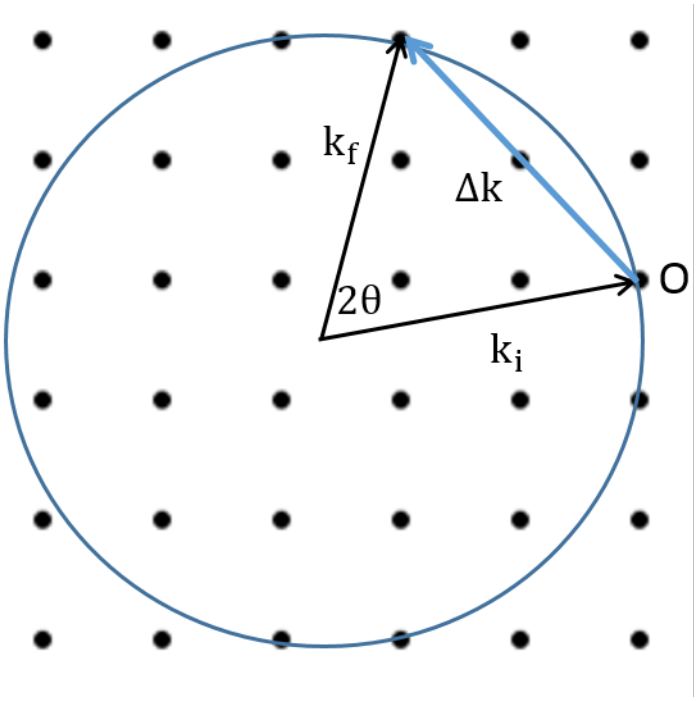

Figure 2.2 *Schematic representation of the Ewald sphere in 2D (blue circle). Black points indicate a squared reciprocal lattice with origin at O. Black arrows show the incoming and scattered wavevectors of the scattering probe, which are the vectors spanning the Ewald sphere. Δk (blue arrow) denotes the momentum transfer of the diffraction, which if scattering is elastic $|\vec{k}_i| = |\vec{k}_f|$, will lie on the Ewald surface (in 2D a circumference). The Ewald sphere denotes lattice points giving constructive interference. Only points that belong to the Ewald surface (circumference) satisfy Bragg's law.*

The scattering is elastic, hence initial and final wavevectors have the same magnitude, and the exchanged momentum $\vec{Q} = \Delta\vec{k}$ lies on a sphere of radius $\frac{2\pi}{\lambda}$ spanned by the two equal wavevectors, which is the Ewald sphere. The Laue condition states that to have constructive interference in reciprocal space the vector $\vec{Q}$ must be a lattice vector of the reciprocal space. This implies that, if the origin of the reciprocal lattice O is placed at the edge of the incoming wavevector, only lattice points lying on the surface of the Ewald sphere will undergo constructive interference and satisfy Bragg's law.

2.2 The scattering cross section

A diffraction experiment measures the fraction of scattered particles, which emerge along different directions and are detected under a solid angle $d\Omega$ by the detectors, $\frac{d\sigma}{d\Omega}$. If neutrons or X-ray photons form a steady flux Φ, that is number of particles N per unit time and unit area, the rate of arrival dR within the angle $d\Omega$ into a detector can be written as [140]:

$$\frac{d\sigma}{d\Omega} = \frac{1}{N\Phi}\frac{dR}{d\Omega} \tag{2.4}$$

The photons or neutrons incoming beam can be expressed by a plane wave of the type $\psi_i = \psi_0 e^{ikz}$ when propagating along z towards a single fixed atom. After elastic scattering occurs, the particles will be emitted radially in respect to the scattering centre, their wavevector will be parallel to the propagation direction, and the scattered waves/particles per unit area will fall with the distance r. The scattered particles can be expressed in a spherical distribution as [140]:

$$\psi_f = \psi_0 f(Q)\frac{e^{ikr}}{r} \tag{2.5}$$

where $f(Q)$ is the atomic form factor of the scattered element. Since the scattered radiation emerges radially from the scattering object, $\vec{k}$ is parallel to $\vec{r}$, and Equation 2.5 depends only on the modulus of Q. This function describes the possibility to have scattered particles with transfer momentum Q, that is at a wavelength λ and at an angle θ. If the scattering rate from an atom, summed over all directions, is dR when the incident flux is Φ, then this is equivalent to the hit-rate of a classical target with an area of $\sigma = \frac{dR}{\Phi}$ perpendicular to the incoming

beam. The number of particles of wavelength λ deflected in the direction of 2θ and ϕ, per unit time and area, is given by the squared modulus of ψ_f:

$$\mid \psi_f \mid^2 = \frac{\Phi}{r^2} \mid f(Q) \mid^2 \tag{2.6}$$

where $\Phi = \psi_0^2$. The scattering rate can be expressed as:

$$dR = \int\int \mid \psi_f \mid^2 d\Omega \tag{2.7}$$

and thus the cross section can be expressed as [140]:

$$\sigma(\lambda) = \int\int \mid f(Q) \mid^2 d\Omega \tag{2.8}$$

where the relation between the solid angle of acceptance of detectors Ω and the scattering angle 2θ is given by $d\Omega = 2r^2 sin2\theta d2\theta d\phi$, which is related to Q by Equation 2.1. The case can be generalised to the scattering from multiple atoms. Consider the scattering of a beam of wavelength λ by an assembly of N particles at positions R_j, with $j = 1,...\ N$. The direction of any scattering wave will be defined by its scattering vector Q, with $\vec{Q} = \vec{k}_f - \vec{k}_i$ and $|\vec{k}_f| = |\vec{k}_i|$ for elastic scattering, but it will be scattered at an angle 2θ related to the incoming beam direction. The Q range for constructive interference is limited by the Ewald sphere as $Q = \frac{4\pi}{\lambda} sin(\theta)$. The amplitude and wave of this scattered wave will be the vector sum of the scattered waves from the N atoms of the unit cell. In our case $\psi_f(Q) = \sum_j^N f_j(Q) e^{-i\vec{Q}(\vec{R}_j)}$, where f_j is the atomic form factor of the j-th atom. The scattering rate will be given by:

$$dR = \mid \psi_s(Q) \mid^2 = \Phi\delta\Omega \mid \sum_j^N \mid f_j(Q) e^{i\vec{Q}\vec{R}_j} \mid^2 \tag{2.9}$$

and the scattering cross-section by normalising the intensity as:

$$\frac{d\sigma}{d\omega} \propto \sum_j^N \mid f_j(Q) e^{i\vec{Q}\vec{R}_j} \mid^2 \tag{2.10}$$

In crystallography, a F_{hkl} factor called the scattering factor is used, and valid only

for crystals. The value F_{hkl} accounts for the amplitude and phase of the diffracted beam by the $\{hkl\}$ planes of a crystal in relation to a single scattering unit at the vertices of the primitive unit cell. In particular, F_{hkl} gives the amplitude and its squared modulus the scattering intensity. The structure factor is the squared modulus of the Fourier transform of the crystal lattice. The value of the scattering factor is the same for each lattice point, but varies due to changes in the form factor f and Q. For a perfect crystal the lattice gives the reciprocal lattice, which determines the positions of the diffracted beam and hence the angles. The Laue condition imposes that the transferred wavevector Q must create a vector in reciprocal space, so that a reciprocal vector of the type $\vec{Q} = \vec{G} = h\vec{a} + k\vec{b} + l\vec{c}$ can be replaced in Equation 2.10. The structure factor F_{hkl} determines the amplitude and phase of the diffracted beams, and is expressed as the vector sum of all waves scattered in the direction of the $\{hkl\}$ reflection with N atoms in the unit cell:

$$F_{hkl} = \sum_{j}^{N} f_j(Q) e^{-2\pi i(hx_j + ky_j + lz_j)} \tag{2.11}$$

where the sum is over all the atoms in the unit cell, x_j, y_j, z_j are the positional coordinates of the j-th atom, and f_j is the atomic scattering factor of the j-th atom. The positional coordinates have the same directions and dimensions as the lattice vectors (a, b, c), $\{hkl\}$ are the Miller indices denoting lattice planes in real space. The atomic form factor $f_j(Q)$ has already been introduced in the definition of the structure factor F_{hkl} as a function related to the crystal lattice. It accounts for the scattering of the probe from a single component, and it gives information on the type of atom, size and composition. The form factor is hence related to the scattering of a wave/particle from an isolated atom. The form factor also depends on the type of scattering, that is on the nature of the incident radiation such as X-ray and neutrons. Consider an infinitesimal volume $\mathrm{d}\,V$ at position $\vec{r}$, which acts as a point source and scatters isotropically. The form factor becomes the Fourier transform of the spatial density distribution of the scattering object:

$$f(Q) = \int \rho(\vec{r}) e^{i\vec{Q}\vec{r}} d^3\vec{r} \tag{2.12}$$

where $\rho(\vec{r})$ is the spatial density of the scattered object and $\vec{Q}$ the momentum transfer. The broader the distribution $\rho(\vec{r})$ is the narrower $f(Q)$ is, that is faster the form factor will decay with increasing Q.

2.3 X-ray diffraction

X-rays are electromagnetic waves with an associated wavelength λ in the range 10^{-8}–10^{-11} m, or equivalently beams of photons with associated energies $E = \frac{hc}{\lambda}$. The expression of the form factor $f(Q)$ for the scattering of X-rays by an atom is very different to those for neutrons. This is a consequence of the different type of interaction which occurs between X-rays and atoms, and neutrons and atoms. X-ray radiation scatters materials in particular crystalline solids because their wavelength is of the same order of the inter-planar crystallographic distance. X-rays scatter the electron cloud of atoms. The scattering proceeds by long-range electromagnetic interaction. For X-ray radiation $\rho(\vec{r})$ is the electronic distribution of the outer shell of the scattered object, which can be approximated to a spherical charge distribution.

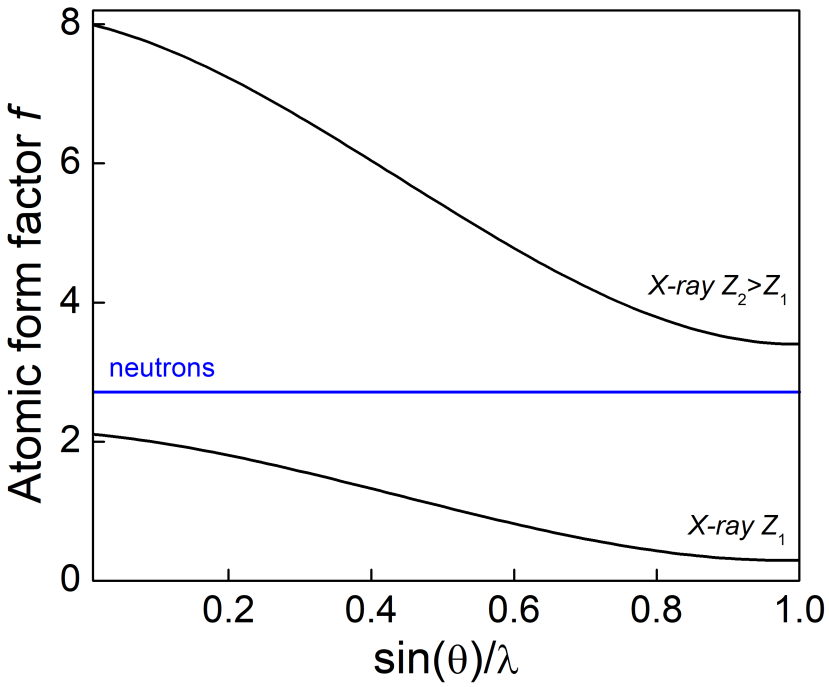

Figure 2.3 *Qualitative representation of the X-ray form factor f as a function of* $Q \propto \frac{sin\theta}{\lambda}$ *and increasing Z. Blue line anticipates the neutron-diffraction form factor, which is constant in Q.*

As X-ray scattering occurs primarily by interaction with the electrons that surround an atom, the strength of the scattering depends on the number of electrons, so that the X-ray scattering power of an atom increases with atomic

number. In contrast, since the spatial extent of the electron cloud around an atom is roughly the same as the X-ray wavelength, the X-ray scattering factor falls off with increasing $\vec{Q}$ as shown in Figure 2.3. By increasing Z the dimension of the X-ray radiation and the electron cloud is comparable and consequently a loss of scattering energy occurs. In X-ray diffraction the scattering factor decays as 1/Å.

X-ray diffraction is rarely the technique of choice to study materials such as the perovskite oxides investigated in this work of thesis. The nature of the interaction causes a lack of sensitivity to neighbouring atoms across the atomic table (for example Co and Mn, which differ by only two electrons), to light atoms in the presence of heavier atoms (such as O and La), and a complete insensitivity to isotopes.

2.3.1 X-ray production

In this work, X-ray powder diffraction measurements are used for a preliminary characterisation of synthesised samples using X-ray tube source based diffractometers. The X-ray tube is a vacuum tube, containing a cathode and a high voltage anode. The cathode (negative pole) is connected to a high voltage circuit and contains a heater filament. The anode (positive pole) is located at the opposite end of the tube and consists of a heavy (usually Cu or Mo) metallic disk. The cathode filament is heated by application of a current and emits electrons. Electrons are accelerated by the high voltage towards the anode where they hit the metal disk. On scattering the target electrons of sufficient energy excite electrons of the metallic disk from the inner shell referred to as the K-shell to an upper-shell energy level. The excited states are strongly unstable and the promoted electrons relax into the vacant states emitting electromagnetic radiation of energy equal to the energy level difference, the X-ray radiation, as shown in Figure 2.4 for a copper target.

The X-ray radiation is not monochromatic, copper has characteristic X-ray emission at $K\alpha_{1,2} = 1.54056\,Å$, $1.54439\,Å$, and $K_\beta = 1.39222\,Å$, but the most intense $K\alpha_1$ emission can be selected by the use of a monochromator and filters. The monochromator is a set of consecutive crystal planes which behaves as a diffraction grating in optics. When properly oriented with respect to the incident polychromatic beam, it will diffract only the wavelength that satisfies Bragg's law. An X-ray background radiation is also emitted, which is Bremsstrahlung

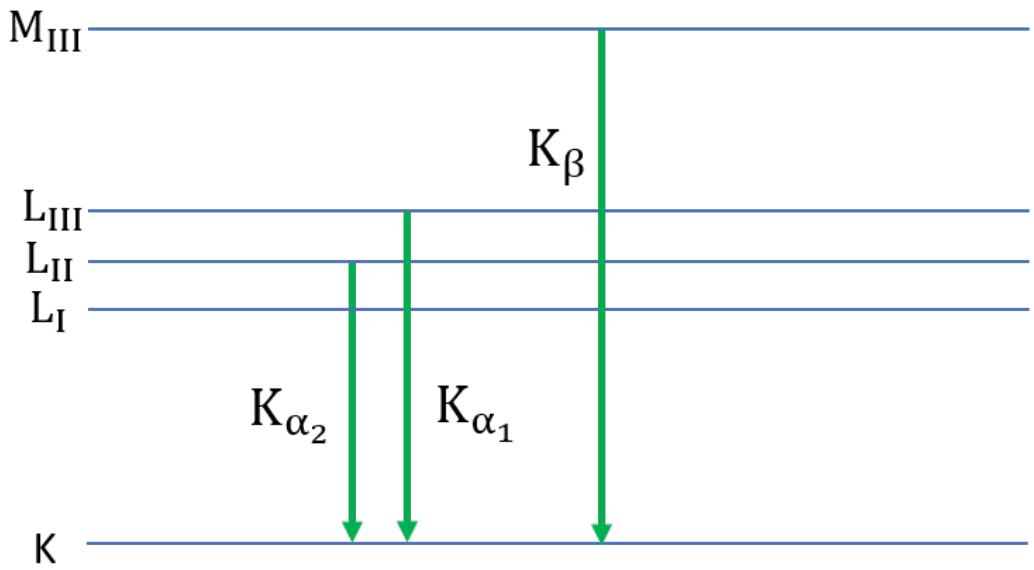

Figure 2.4 *K_{α_1} = 1.54056 Å, K_{α_2} = 1.54439 Å, and K_β = 1.39222 Å X-ray emission of a copper source. K, L and M indicate different electron shell energies. Their emission intensity is roughly in the ratio 100:50:25.*

radiation arising from the deceleration of electrons when hitting the target. The emitted X-ray radiation wavelength is specific for each disk material.

X-rays can also be produced by the use of particle accelerators such as synchrotrons. In this type of accelerator, electrons are accelerated and bent in a circuit of consecutive straight and curved sections. When electrons are bent by the magnets they lose kinetic energies which is released by conservation of energy as electromagnetic radiation referred to as Bremsstrahlung radiation. This is a continuous spectrum of energies emitted in tangential direction. The synchrotron radiation is a powerful continuous light including the region from hard X-rays to soft X-ray, which is selected by filters and diffraction gratings. The produced flux is very intense and provides the ability of performing ultra-fast measurements at a very high resolution. This is ideal both for diffraction and spectroscopic experiments.

2.3.2 X-ray characterisation

XRD patterns are collected at ambient temperature by a D2 Bruker Advance diffractometer equipped with a Cu-K$\alpha_{1,2}$ radiation source, working in the standard Bragg-Brentano geometry $\theta/2\theta$. In this geometry, the X-ray source is

kept fixed, the sample is rotate of θ/min and the detector is rotated of $2\theta/min$. Temperature dependent X-ray measurements are also carried out in this work. A SMARTLAB Miniflex Rigaku diffractometer at the Material Characterisation Laboratory at the ISIS facility, is used either equipped by a furnace or a cryostat system. The diffractometer uses a monochromatic Cu-Kα (1.5404 Å) radiation source, selected by a Si(220) monochromator. An Anton Paar HTK 1200N high-temperature oven chamber is used to collect diffraction patterns in the temperature range 293–1200 K, whereas an Anton Paar TTK 450 low-temperature chamber is utilised to collect data in the low temperature region 15–300 K.

2.4 Neutron diffraction

Neutrons are neutral subatomic particles discovered in 1932 by English physicist James Chadwick. Neutrons have no electric charge and a rest mass equal to $1.6749\,10^{-27}$ kg (equivalent energy 939.56 MeV), and are bound to protons in the nucleus of atoms by nuclear force. Neutron diffraction is a complementary probe to X-ray to study the structural composition of materials. The scattering process takes place between the neutron and the nuclei, and it is mediated by the nuclear short-range interaction. In neutron crystallography the wavelength associated to the incident neutrons must be in the same order as the crystal lattice and thus in the Ångstrom region. Typically thermal neutrons of several Ångstrom or cold neutrons of tens of Å are used in crystallography. However, the nucleus order of magnitude is in the *fm* region, and it is seen from neutrons as a point, which scatters neutrons in radial directions. The spatial distribution density $\rho(\vec{r})$ is the spatial distribution of the nucleus which is a point scatterer and expressed as a Dirac delta function [140, 144]:

$$f(Q) = \int \delta(\vec{r}) e^{i\vec{q}\vec{R}} d^3\vec{r} \tag{2.13}$$

and remembering that the Fourier transform of a Dirac delta in the overall space is equal to:

$$\frac{1}{(2\pi)^{3/2}} \int \delta(\vec{r}) e^{i\vec{q}\vec{R}} d^3\vec{r} = 1 \tag{2.14}$$

the form factor in neutron scattering is constant, and the scattering amplitude is independent of the momentum transfer Q.

The neutron form factor is scaled by the amplitude of the spherical wave and it is referred to as scattering length b. The scattering length varies randomly across the periodic table and isotopes of the same element and are usually determined experimentally. Hence, for elastic neutron scattering with nuclei the form factor becomes a constant and equal to the scattering length b, ($f(Q) = -b$ for convention). The magnitude of b determines the strength of the scattering, whereas its sign indicates whether the incident and scattered waves are in or out-of-phase. The scattering interaction quantified by the constant b depends on the constituents of the nucleus and the orientation of its spin (if not zero) relative to that of the neutron, making them isotope specific and complexly varying with the atomic number Z. Neutron diffraction is sensitive to different isotopes, such as hydrogen and deuterium, or different nuclear spin state of the scattered atom. Neutrons, differently from X-rays, can also provide good contrast between adjacent atoms in the period table. Considering the independence of the form factor of Q, $f(Q) = -b$, the scattering cross section of Equation 2.8 becomes [140, 144]:

$$\sigma = 4\pi \mid b \mid^2 \tag{2.15}$$

where 4π emerges from the integral over the solid angle Ω. The scattering length b is dependent on the nuclear spin of scattering nuclei, which shows a different value according to the possible nuclear spin configuration of the scattering object. In addition, b is isotope dependent, and a compound can naturally contain a percentage of different isotopes. To take this into account, b is identified by means of an average value and a standard deviation:

$$b =< b > +\Delta b \tag{2.16}$$

and the scattering cross section can be reformulated as:

$$\sigma = 4\pi < b^2 >= \sigma_{Coh} + \sigma_{Inc} = 4\pi < b >^2 +4\pi(\Delta b)^2 \tag{2.17}$$

which are referred to as the coherent and incoherent cross-section. To understand

this consider a hydrogen atom, which can be characterised by both a triplet or singlet spin ground state. The b scattering lengths determined for the two different magnetic configurations are different, and an average value $< b >$ and a standard deviation $(\Delta b)^2 =< b^2 > - < b >^2$ is given [140]. Δb gives rise to the so-called incoherent scattering, which is observed in a neutron-diffraction pattern as an additional background. Quantitative information on the structure derives from the coherent scattering cross section.

A neutron also possesses nuclear spin and hence, magnetic moment and can magnetically interact with unpaired electrons in the scattering material. The spatial distribution is this time the spatial distribution of unpaired electrons around the nucleus. These orbitals have comparable size to the incident neutrons and the form factor resembles the X-ray form factor. However, because neutrons are scattered only by the outer electrons the form factor decays quite rapidly. The magnetic form factor is not isotope dependent but depends on the oxidation state of the material.

The structure factor F_{hkl} defined for crystals can be rewritten for coherent scattering as:

$$F_{hkl} = \sum_{j}^{N} < b_j > e^{iQR_j} e^{-W_j} \tag{2.18}$$

where e^{-W_j} has been introduced, as the Debye-Waller temperature contribution, $< b_j >$ is the mean nuclear scattering length of the j-th atom, and $\vec{Q}$ is a vector in reciprocal space. The Debye-Waller factor accounts for how thermal fluctuation of atoms extinguish the intensity of the scattering process, hence the intensity of the Bragg peaks. This especially happens for high Q peaks. The lost scattering intensity appears in the form of diffuse scattering, because thermal fluctuation of atoms from their equilibrium position generates a non-perfect lattice.

The squared modulus of the structure factor is proportional to the measured intensity, which can be finally rewritten for neutron scattering as:

$$|F_{hkl}|^2 = |F_N|^2 + |F_m|^2 =| \sum_{j}^{N} b_j e^{iQR_j} e^{-W_j} \; |^2 + | \sum_{j}^{N} p_j q_j e^{iQR_j} e^{-W_j} \; |^2 \tag{2.19}$$

where F_m is the magnetic structure factor, p_j is the magnetic scattering length and q is the magnetic scattering vector, introduced because only the component of the moment perpendicular to the scattering vector will result in magnetic scattering. As with the nuclear structure factor, the magnetic structure factor gives the Fourier transform of the magnetisation distribution in the lattice.

Unfortunately, the determination of the spatial density distribution is not easily achievable because a loss of information on the phase of the probe occurs after the diffraction measurement. In X-ray and neutron-diffraction experiments the phase of the scattered signal must be retrieved to enable a quantitative solution of the crystal structure from experimental data [145]. The diffraction data without phase information only provide a measurement of the Fourier transform amplitude of the scattering object spatial density $\rho(\vec{r})$. For a crystal the Fourier transform to be determined is given by:

$$\rho(r) = \frac{1}{V} \sum_{hkl} |F(hkl)| e^{[(hx+ky+lz)-\phi(hkl)]} \tag{2.20}$$

where $\phi(hkl)$ are phases related to the structure factor F_{hkl}, which represents the resultant diffracted beams of all atoms contained in the unit cell in a given direction. h, k ,l are the Miller indices of the diffracted beams (the reciprocal points) and V the unit-cell volume. Several methods have been developed to solve the phase problem. To date with high-performing computers, the most common method is to select and test a big number of initial phases.

2.4.1 Neutron generation: reactors and spallation sources

Neutrons for scattering experiments are produced either in nuclear reactors or spallation sources. The produced neutron energy spectra are different, with reactors producing continuous neutron beams, and spallation sources producing pulsed beams of more high-energy neutrons.

Reactor sources produce a continuous neutron flux by nuclear fission. By absorption of a neutron, a large nucleus, such as of uranium-235, splits into two or more smaller nuclei with release of kinetic energy and emission of gamma rays and free neutrons. A portion of these neutrons is absorbed by other fissile atoms and triggers further fission events, creating a self-sustained reaction chain. Typically, neutrons of energies in the order of meV are required to maintain

such self-sustained reaction. This is related to the absorption cross section of a neutron from fissile nuclei, which is extremely high for neutrons in the meV region. However, neutrons produced during the fission events are in the MeV energy region, which in contrast are characterised by a very low absorption cross section. They are made to lose kinetic energy through collisions with light atoms, since the exchange is most efficient between particles of similar mass, to create the right conditions for the chain reaction. This is obtained with use of neutron moderators, usually graphite or heavy water (D_2O), which cool down the high energy neutrons to the moderator temperature, which is kept to correspond to the meV energy range (25.85 meV$\sim$300 K).

In a reactor, neutron so produced are then in the thermal energy region, which corresponds to the energy range where their wavelength is comparable to the interatomic distance of atoms (12 meV–100 meV/2.6–0.9 Å), and thus are suitable for diffraction experiments. However, monochromation of the neutron beam is necessary to obtain a neutron radiation at a specific wavelength, which can be then related to the atomic spacing by Bragg's law. Neutrons are produced in a reactor at the Institute Laue Langevin (ILL, France), where the most intense continuous neutron flux in the world is produced in the moderator region $1\,10^{15}$ neutrons/(s cm^2).

An alternative way to produce neutrons is by spallation reactions. The term spallation refers to the process of emission of nucleons from a heavy nucleus after being hit by high-energy particles. Such neutron sources use particle accelerators to accelerate light elements, such as electrons or protons. The accelerated particles hit a heavy target, typically tungsten, tantalum or uranium. On scattering, the high energy particles excite the heavy target nuclei, which decay emitting gamma rays and neutrons. Differently from the reactor source, a wide polychromatic spectrum of neutrons is produced, however no monochromation is needed. This is related to the pulsed nature of the neutron flux, which permits to identify the neutron wavelength by the time-of-flight technique. Spallation sources are nowadays replacing nuclear reactors in research. This is mainly because the target materials do not need to be a fissile element, and there is no danger of a runaway chain reaction, or meltdown, as the spallation process stops when power is cut off to the accelerator.

2.4.2 The ISIS spallation source: the time-of-flight technique

ISIS is a neutron source which produces neutrons by spallation reactions. Neutrons are produced at ISIS from the scattering of protons accelerated up to 800 MeV onto a tantalum target by the combined use of a LINAC and a synchrotron. On hitting the target each proton produces 25–30 fast neutrons. ISIS operates at 50 Hz, that is it generates a pulse of polychromatic neutrons every 20 ms. The momentum and wavelength of the neutron are related by the De Broglie relation, so large wavelengths correspond to slow neutrons. Neutrons so generated are too energetic for crystallographic investigations and need to be cooled down to the thermal region. Different types of moderators are used according to the energies required in experiments. For example, a methane moderator at a temperature of 110 K is used in diffraction experiments. After the moderator, the neutron energy distribution follows a Maxwellian distribution peaked around the moderator temperature given by:

$$N_f(v) = 4\pi N \left(\frac{m_N}{2\pi k_B T}\right)^{\frac{3}{2}} v^2 e^{-\frac{m_N v^2}{2k_B T}} \tag{2.21}$$

where v is the neutron velocity, m_N the neutron mass, T its temperature and k_B the Boltzmann constant. After passing through the liquid methane moderator, the neutron pulse is roughly 30 μs wide and reaches the instruments after a flight path of length L_0. Neutrons are diffracted according to Bragg's law and detected after an additional flight path L_D to the detector position in a total time-of-flight t. The De Broglie relation $\lambda_N = \frac{h}{m_N v} = \frac{ht}{m_N(L_0+L_D)}$ yields a relation between the time-of-flight t (which is the measured quantity) and the neutron wavelength. Combining the De Broglie equation and Bragg's law the inter-planar distance d is calculated by:

$$2dsin(\theta) = \frac{ht}{m_N L} \tag{2.22}$$

where m_N is the neutron mass, t is the time-of-flight (measured), L the total flight path (known), θ half the scattering angle (measured), and d the calculated d-spacing.

Neutrons can also be exploited in spectroscopic experiments. The main difference from a diffraction experiment is that in this case there is a change in the scattered

energy and the scattered vector differs from the incoming one, $|\vec{K}_i| \neq |\vec{K}_s|$. Spectroscopic experiments are generated by inelastic scattering of neutrons with materials and probe the dynamic, optical, phononic properties of the scattering object and many more. At ISIS neutron spectroscopy is routinely performed in parallel to diffraction experiments. Inelastic neutron scattering requires to resolve the energy transfer during the scattering. This is done by two main methods. For a beam of neutrons created at the same time and travelling in the same direction, the higher their kinetic energy is the shorter their wavelength is (by De Broglie law). A specific wavelength is selected by the pulsed polychromatic beam either after the scattering of a well-defined wavelength by a device such as a monocrystal (Bragg diffraction principle) or a chopper system (ToF method). The final energy is determined by measuring the time-of-flight between the sample and the detectors. Alternatively, the sample can be illuminated by the wide polychromatic beam, the incident energy at the sample position is determined by the measurement of the time-of-flight and the final energy is measured by a monocrystal (inverse geometry).

2.4.3 Comparison between neutrons and X-rays

Neutron and X-ray diffraction are two possible ways to map the crystal structure of materials. Neutron scattering is the technique of choice of the current thesis. The collected data are presented in the Results chapters by neuron-diffraction, in particular under extreme conditions of temperature and pressure. Neutrons are a non-invasive probe and carry a few advantages:

- The main characteristic is the form factor independence of the moment transfer Q. This enables us to distinguish between isotopes and neighbouring atoms. For example, the scattering length of hydrogen is $b_H = -0.3739 \times 10^{-14}\,\mathrm{m}$, while deuterium has $b_D = 0.6671 \times 10^{-14}\,\mathrm{m}$, where a negative sign indicates neutrons scattered out-of-phase with respect to the incident radiation.
- The interaction between neutrons and atoms is nuclear, while the interaction between X-ray and matter is electromagnetic.
- Neutrons have high-penetration and low absorption (for most elements).
- Neutrons posses magnetic moment, which interacts by inelastic neutron scattering with materials.

A few disadvantages can be found. First of all neutron sources are very expensive to build and maintain, and this expenditure has often discouraged the building and the upgrade of neutron facilities. Secondly, neutron fluxes are remarkably lower than X-ray synchrotron radiation. The low flux has several disadvantages, for example it limits neutron detection of rapid time dependent processes, and it requires the use of large sample volumes, not always available. Further, sample environment capabilities for neutron experiments are typically very expensive and more complex than in X-ray diffraction.

2.5 Powder diffractogram and the Rietveld refinement method

This thesis shows neutron-diffraction data from powder samples, which have been analysed by the use of the General Structure Analysis System (GSAS) software [146] and Rietveld refinement method [147, 148]. GSAS is an open source Python project for determination of crystal structures using both powder and single-crystal diffraction and with both X-ray and neutron probes. The basic idea behind the Rietveld method is to calculate the entire powder pattern using a variety of refinable parameters and to improve a selection of these parameters by minimizing the weighted sum of the squared differences between the observed and the calculated powder pattern using least squares methods. The weighted R-factor provides a quantification of how well the proposed model fits the data and can be expressed as [149]:

$$wR_p = \sqrt{\frac{\sum_j^N w_j(y_j^{obs} - y_j^{calc})^2}{\sum_j^N w_j(y_j^{obs})^2}} \tag{2.23}$$

where the sum is over the j independent observations, y_j^{obs} is the measured intensity, y_j^{calc} the calculated intensity and w_j the weight.

Assuming a zero background the equation:

$$y_j^{calc} = s \sum_k^{k_j} m_k L_k |F_{hkl}|^2 G_j \tag{2.24}$$

expresses the calculated intensity at a point j. In Equation 2.24 s is the overall scale factor, L_k is the Lorentzian factor (which defines the angular dependence of the integrated intensity), $|F_{hkl}|$ the structure factor, and G_j a function describing the peak shape. The sum is over the multiplicity of the reflection m_k. In powder diffraction a Bragg reflection arises from the contribution of atoms located in symmetry equivalent positions, which can be expressed by a value referred to as multiplicity. The Rietveld method calculates the intensity of a single reflection, that is generated by a single lattice point, and then multiplies it for its multiplicity.

At ISIS, a powder diffractogram displays the scattered intensity as a function of the time-of-flight and contains a number of peaks, that is the Bragg reflections which are characterised by their position, intensity and profile. The position depends on the periodic arrangement of the atoms in the crystal structures, and gives information on lattice parameters and phase analysis. The intensity is mainly related to the structure factor, which depends on the crystal symmetry, on the type of atoms scattered in a specific site and the amount of material. The shape of the reflection, such as the peak profile and its width, depends on the atomic thermal motion, that is the Debye-Waller factor, lattice distortions such as micro-strain or crystallite site, or can be instrument originated. Other parameters are the background, the instrumental information, such as detector flight paths and angles, sample absorption and extinction. In order to be able to carry out a refinement, the space group of the material must be known. A starting diffraction pattern must be calculated from a suitable phase. It is important to adopt a good starting model, which can be selected *a priori* by symmetry considerations and complementary optical studies. In summary, the Rietveld procedure:

- calculates a diffraction pattern from a model;
- compares the calculated pattern to the observed data;
- minimises the difference between the observed and calculated patterns by varying parameters in the model through a least squares method.

When the calculated and experimental diffraction patterns match, the selected

structural model may reflect the sample crystal structure. The Rietveld method is a structure refinement method, which does not find a structural solution, but the best model compatible with experimental data.

2.5.1 Instrument calibration parameters

A diffractometer requires subtle corrections of Equation 2.22, which account for instrument and sample related effects. This is performed with the GSAS software [146], which converts the measured time-of-flight into d-spacing according to the empirical equation:

$$t = \mathrm{DIFC}d + \mathrm{DIFA}d^2 + \mathrm{ZERO} \tag{2.25}$$

The parameters are determined before the start of every beam-cycle and calibrated to the instrument and its experimental geometry by measuring a standard material of known d-spacing. DIFC relates the time-of-flight to the inter-planar spacing. Equation 2.22 can be re-written as:

$$t = \frac{2m_N L}{h} sin(\theta)d = \mathrm{DIFC}d \tag{2.26}$$

so that $\mathrm{DIFC} = 2\frac{m_N}{h}Lsin(\theta)$, t is expressed in microseconds (μs) and d is in Ångrstrom (Å). The DIFC parameter depends on half the scattering angle (θ) and varies by changing detector bank. During the Rietveld refinement DIFC is typically kept fixed, but could be refined if necessary, for example in case of simultaneous refinement of different detector banks.

The DIFA parameter contains information on neutron absorption effects from the sample material. The neutron absorption cross-section of an atom is wavelength dependent. Short wavelengths (low t) are less absorbed than longer ones (long t). This affects the average penetration into the sample, and hence the total flight path L and scattering angle 2θ, which vary with the neutron wavelength. The resulting time-of-flight associated to Bragg reflections may be different from that predicted by considering the only DIFC term especially at long d-spacing. An addition correcting term is then defined as DIFA, which corrects possible peak shift due to neutron absorption from the sample. The DIFA quadratic dependence on d in Equation 2.25 was empirically found to give the best fit to the peak shift

correction.

The ZERO parameter is instrument-dependent and must be fixed during the Rietveld refinement. The ZERO accounts for differences between timing signals in the ISIS accelerator and instrument data acquisition. It also corrects for the finite time response of detectors.

2.5.2 The magnetic unit cell and magnetic refinement

Perovskite materials are characterised by a regular B–X–B network of bonds, in which the magnetic moments of the B cations can create long-range magnetic order in form of ferromagnetic or antiferromagnetic arrangement. This defines a magnetic unit cell which satisfies specific symmetry operators according to the type of magnetic coupling. In the case of ferromagnetic ordering the symmetry corresponds to the crystal symmetry, since all spins are parallel to each other. In the case of antiferromagnetic order the symmetry of the magnetic unit cell may either coincide or differ from the crystallographic symmetry. For example, in case of an A-type antiferromagnetism the magnetic unit cell is double with respect to the crystallographic unit cell, alternatively antiferromagnetic symmetries may resemble rock salt, layered and columns orders. The long-range magnetic order manifests in the powder diffactogram with the appearance of extra reflections purely magnetic in nature referred to as superlattice reflections. These peaks usually overlap with the nuclear structure of the system, but strongly affect the intensities of the measured reflections.

Elastic neutron diffraction can be used to study the magnetic ordering in perovskite materials. The structure factor given in Equation 2.19 consists of two non-interacting components. The first term is the nuclear structure factor related to the crystal structure, while the second term arises from magnetic scattering. The nuclear and magnetic scattering intensities are summed to give the total measured intensities during the diffraction experiment. This allows us to describe the structure by two separate crystalline phases. One accounts for the arrangement of the atoms in the crystal structure and is described with a unit cell and space group. The other phase contains the magnetic atoms in an equivalent or different unit cell with a magnetic space group which describes the atoms and magnetic moments arrangement. Both phases must describe the same atomic arrangement so that the positions of the magnetic ions will be linked by constraints between the phases. A starting magnetic phase with initial

parameters such as electronic spin orientations, and magnetic moment intensities is to be given to the GSAS software, which is chosen according to literature or complementary experiments.

2.6 High-pressure studies

Pressure is an alternative thermodynamic variable to temperature which allows us to infer on structural and physical properties in materials. Pressure modifies the atomic arrangement in compounds and their electron density. This can promote structural, electrical, mechanical and magnetic transitions. Such structural and physical transitions can be detected experimentally by neutron or X-ray diffraction, optical spectroscopy, or electrical and magnetisation measurements. This makes high-pressure studies of materials important in several fields from fundamental studies to technology. Considerable interest is for example found in geophysics. The application of pressure permits us to explore in laboratory materials in the Earth's mantle, where most of the matter is in a state of very high-pressure and temperature. Neutron-diffraction high-pressure experiments, for example, can identify structural and physical properties of materials such as the perovskite $(Mg,Fe)SiO_3$ series introduced in Chapter 1, which is the most abundant solid-phase mineral in the Earth's lower mantle [9–15]. Not only compounds in the interior of our planet but also materials found in planetary bodies are at different conditions of pressure and temperature with respect to Earth's minerals. In this context, high-pressure studies, such as by neutron diffraction, have reached great impact results. For example, high-pressure researchers have focused for decades on ices of ammonia, water and methane, which are materials found in bodies of the outer solar system and their high-pressure behaviour is relevant to the modelling of Titan, Uranus and Neptune [150–152]. Strong technological interest is also found, for example in high-pressure material synthesis. Several synthesis procedures rely on the application of pressure such as in the synthesis of novel perovskite compounds. Temperature is the typical thermodynamic variable which is altered during the chemical synthesis to change the reagents and/or the speed of reaction. Pressure is also important because allows the exploration of a different part of the phase space and can promote the synthesis of materials which are not obtainable at ambient conditions.

The study of materials under the application of hydrostatic pressure is the main

focus of this thesis. In this work, neutron diffraction, optical and magnetisation measurements are shown under pressure on perovskite oxides to study structural-physical property correlations and how they evolve under the application of pressure.

2.6.1 The equation of state

The equation of state (EoS) is a relation between the pressure P, volume V and temperature T of a physical system. The equation of state is a fundamental characteristic of a gas, liquid or solid and allows the application of principles of thermodynamic theory to investigate samples. A relation $P = f(V, T)$ can be constructed so that the pressure of a system can be expressed in terms of its temperature and volume.

In high-pressure diffraction studies, especially for solid materials or perovskites several equation of states have been developed [153–156]. The Birch-Murnaghan (B-M) equation of state is the mostly used in the high-pressure community and it is also the EoS applied to materials investigated in this thesis. The B-M equation is an isothermal EoS, which expresses the strain energy of a solid as a Taylor series in the finite Eulerian strain [157]. The expansion to the third order in the strain yields:

$$P(V) = \frac{3B_0}{2}\left[\left(\frac{V_0}{V}\right)^{\frac{7}{3}} - \left(\frac{V_0}{V}\right)^{\frac{5}{3}}\right]\left[1 + \frac{3}{4}(B_0' - 4)\left(\left(\frac{V_0}{V}\right)^{\frac{2}{3}} - 1\right)\right] \tag{2.27}$$

where V is the material volume, B_0 the bulk modulus expressed in GPa, and B' the bulk modulus pressure derivative. For a homogeneous, isotropic, non-viscous solid, the isothermal bulk modulus is formally defined as:

$$B_0 = -V\frac{dP}{dV} \tag{2.28}$$

It represents the ratio between an infinitesimal pressure increase and the relative infinitesimal volume change. B_0 is compound-specific, and quantifies how resistant a material is to compression. The higher B_0 is, the less compressible the material is. For example, the highest known bulk modulus of a mineral material

is associated to the diamond with a value of $B_0 = 443\,\text{GPa}$ at 4 K. This means that the diamond volume compresses of the 1% when a pressure of ∼4.43 GPa is applied to it. The bulk modulus can be determined by powder diffraction experiments under high pressure. In the following Results chapters, the Birch-Murnaghan equation of state is applied to the perovskite oxides studied in this thesis and their bulk moduli are calculated by high-pressure neutron diffraction experiments.

2.7 High-pressure neutron-diffraction at ISIS

Experimental work has been carried out on the PEARL instrument, at the ISIS Neutron and Muon facility, UK. PEARL is the diffractometer dedicated to performing high-pressure experiments [158]. The instrument is optimised for neutron-diffraction measurements under extreme conditions by means of Paris-Edinburgh presses [159], which will be discussed in detail in Section 2.7.1. A schematic drawing of the PEARL instrument is shown in Figure 2.5.

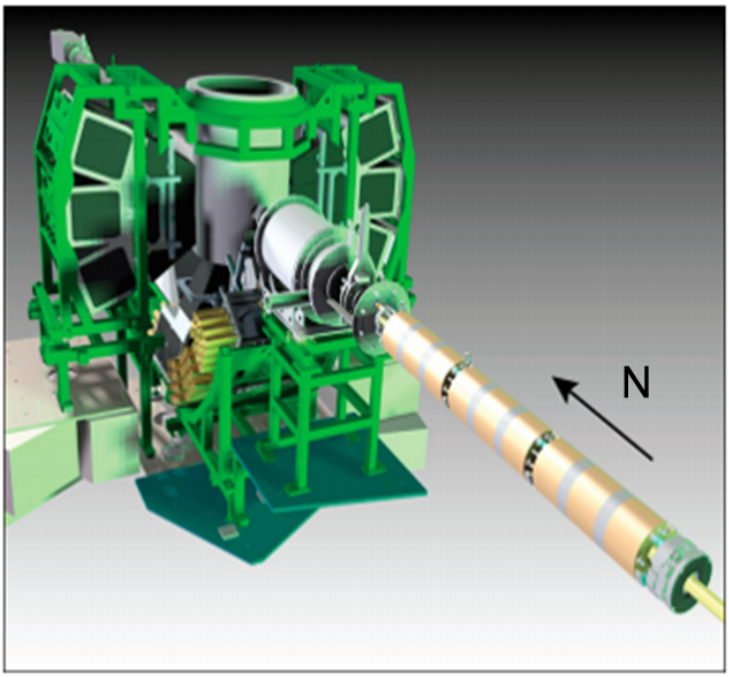

Figure 2.5 *Schematic representation of the PEARL instrument [158]. Black arrow indicates the direction of incoming neutrons, which hit the sample placed at the centre of the instrument and are collected at 90° by the transverse detector banks.*

The pressure cell is held by a metal frame and placed inside an evacuated sample

tank at the centre of the instrument. The polychromatic radiation of the ISIS pulsed source enables us to work in transverse scattering geometry, with fixed pressure cell and detector banks. The incident neutron beam incoming along the direction of the black arrow in Figure 2.5 hits the sample and the diffracted neutrons are collected at 90°. The transverse geometry enables us to cover a d - spacing range of 0.5–4.1 Å. The pressure cell can be rotated by 90° to acquire access to the longitudinal banks. The pulsed nature of the neutron beam from a spallation source permits us to measure a longer d - spacing range in the 90° scattering geometry. The pulsed beam sends four 20 ms pulses to the PEARL instrument, but the fourth pulse can be counted up to 40 ms. The slower neutrons extend the measurable d - spacing range up to $\sim$ 8 Å. Unfortunately, the counting statistics are reduced because only a quarter of the neutron pulses contain neutrons with the required energies, and the neutron flux at longer wavelengths is significantly reduced as a result of moderator performance. On the other hand, this is compensated by diffracted long-wavelength neutrons, which produce stronger Bragg reflections with a peak intensity proportional to λ^4. This approach aids the indexing of new phases and investigation of magnetic reflections. A detailed description of the PEARL diffractometer and its experimental capabilities will be given in Chapter 6.

2.7.1 The Paris-Edinburgh press

Paris-Edinburgh (PE) presses are compact hydraulic presses with a capacity ranging from 50 to 500 tonnes, which compress sample volumes typically of the order of 33–1000 mm^3. The PE press was developed in the 1990s by a collaboration between the Universities of Edinburgh and Paris [159] to improve high-pressure neutron-powder-diffraction experiments in the 0–10 GPa range. PE presses are available in two different geometries: the historical four column V-type [159] and a more recent two-column VX-design [160].

In a neutron spallation source where data are collected at a constant diffraction angle, the 4-column V-design model is conventionally used, such as the V3 type shown in Figure 2.6a, which is routinely used on the PEARL diffractometer. Diverse capacities are available to be chosen according to the load required in experiments. The V3-type press of Figure 2.6a has a load capacity of 250 tonnes and a mass of about 50 kg. Figure 2.6b shows a cross section of the V-type press. Hydrostatic fluid (typically oil) is injected through an inlet (1) and pushes on

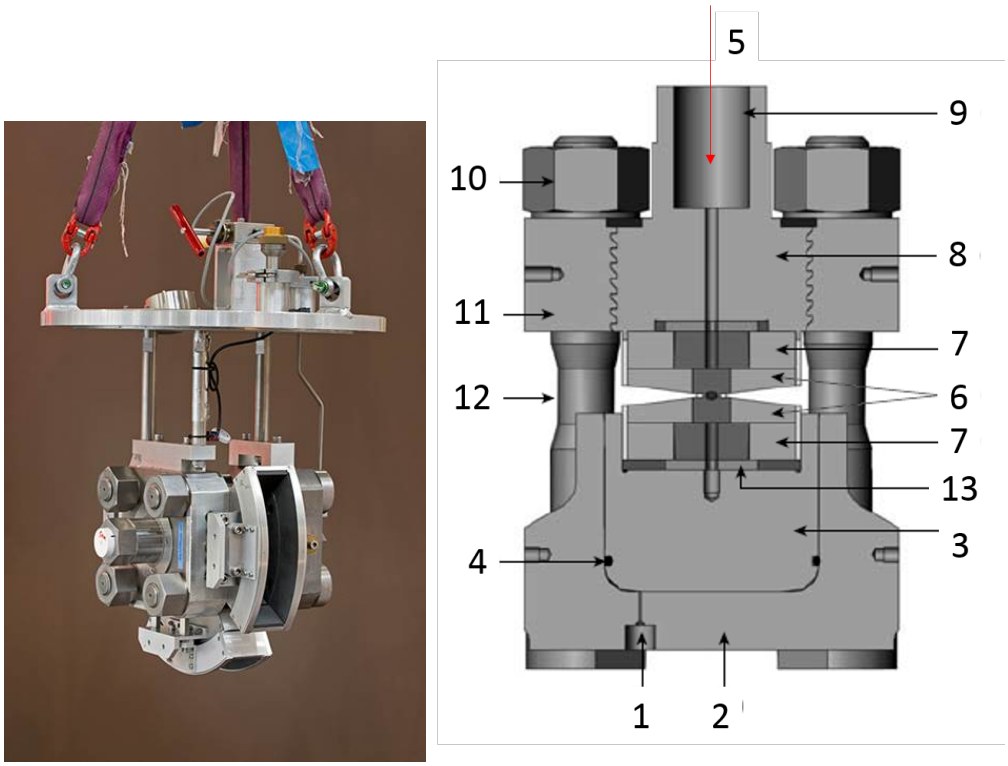

(a) (b)

Figure 2.6 *2.6a: V3 model Paris-Edinburgh press adopted on PEARL for high-pressure ambient-temperature diffraction measurements [158]. 2.6b Cross section of the V-design PE-press. (1) Hydraulic fluid inlet; (2) cylinder; (3) piston; (4) O-ring; (5) incoming neutron direction; (6) anvils; (7) anvil seats; (8) breech; (9) collimator; (10) nut; (11) top platen; (12) tie rod and (13) backing disc [161].*

a piston (3) of known section[2]. The piston pushes on the anvil steel-supported WC seat (7), which transmits the generated force onto the anvil (6). The upper part of the cell is made of a breech (8) screwed into the top platen (11). The incident neutron beam passes along the direction of red arrow (5) from left to right when the press is oriented as in Figure 2.6a, and is collimated by a boron nitride (white) insert with a central 5 mm hole. On PEARL the PE press is oriented so that the neutron beam passes through the anvils from right to left and the component scattered at 90° is collected by the detector banks. The press position is controlled by a motorised sliding mechanism that can translate the press along the length of the beam path. This ensures that the sample is always situated at the defined instrument centre. The transverse scattering geometry is suitable for spallation sources because of the fixed 2θ and the variable wavelength of the

[2]For a V3-type the piston section is $\sim$100 cm^2, so that an applied oil pressure of 1 kbar generates a load of 100 tonnes on the press piston.

incoming neutrons. It also provides an efficient shielding from background noise. However, the transverse mode shows the disadvantage that the polychromatic beam has to cross nearly 6 mm of anvil material and is strongly distorted by the wavelength-dependent absorption effect, which needs correction to obtain reliable intensities of collected data.

2.7.2 Anvils and gaskets

The PE press generates load using opposed anvils made of various sintered materials. Common materials are tungsten carbide (WC), zirconia-toughened-alumina (ZTA), sintered diamond (SD) or boron nitride (BN). The choice of the type of anvils depends on the parameters of the measurements to be performed, for example the scattering geometry, the sample pressure required, or to avoid overlapping of Bragg reflections between the anvil materials and samples. Typical choices of anvils are the ZTA or WC for measurements up to 10 GPa or SD anvils in case higher pressures are needed. In case of a longitudinal scattering geometry, where the beam gets in and out along the same path, BN or sintered diamond anvils are preferable in order to reduce the contamination of the diffraction pattern by anvil reflections.

Anvil geometries are characterised by two types of profile: single and double-toroidal, shown in Figure 2.7. The former can operate at a maximum pressure of ∼13 GPa (WC anvils [161]), while the latter can generate pressures up to 28 GPa using a much smaller sample volume [158]. The anvil geometry adopted in most neutron-diffraction experiments is the single-toroidail profile, which is made of a central Bridgman-profiled cup with a 6–10 mm diameter and an outer ring which accommodate the toroidal-shaped sample chamber [162].

Tungsten-carbide anvils have been the preferable anvil material for decades owing to their remarkable toughness and low price. However, WC anvils strongly attenuate the polychromatic neutron radiation and provide a relatively high signal-to-noise ratio. Currently, the most used anvil material for experiments in the 0–8 GPa range is the ceramic ZTA shown in Figure 2.7a. The ZTA material is characterised by a much higher transparency to neutrons compared to other anvil types. This transparency is reduced with shorter wavelengths but is still significantly higher than that of the WC anvils. ZTA anvils easily operate in the 0–8 GPa range over a temperature range of 80–500 K [158].

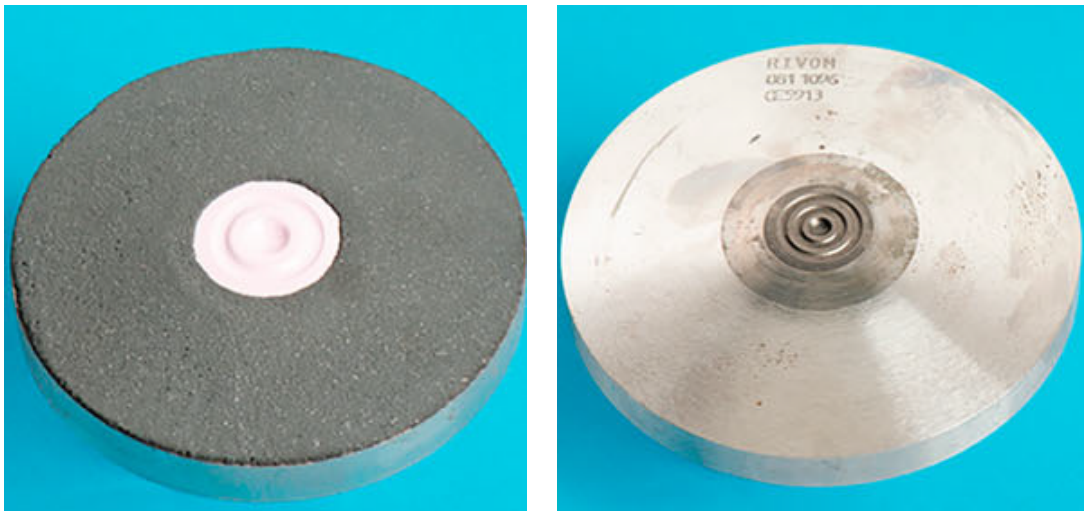

(a) **(b)**

Figure 2.7 *2.7a Single-toroidal zirconia-toughened-alumina (ZTA) ceramic anvil, and 2.7b sintered diamond (SD) double-toroidal profile anvil. Figure is re-adapted from Bull et al [158].*

Sintered diamond anvils (Figure 2.7b) provide a decreased level of background scattering and reduced attenuation of the beam than WC anvils, but higher than ZTA ones. Sintered diamonds sustain a much higher load than the other types of materials and are the anvils of choice when pressures higher than 8 GPa are required in the experiment. With a single-toroidal profile, SD anvils generate pressures up to 12 GPa, and with the use of a double-toroidal profile pressures of 28 GPa can be reached. These very high pressures limit the sample volume, hence data collection times are increased to obtain equivalent counting statistics. Unfortunately, SD anvils are extremely expensive, and reaching a pressure of 28 GPa is usually at the expense of the anvil integrity. This issue is addressed in detail in Chapter 6.

Powder samples are placed into an encapsulated metallic holder (gasket), which is placed between the anvils in a sample chamber of 6 mm in diameter. The most widely used gasket material is the null-scattering alloy TiZr (68%:32%, $b = 0.0$ fm). The gasket consists of two parts: an outer ring and two hemispherical dishes as shown in Figure 2.8. Powder samples are packed within the two hemispherical disks. Pressure on loaded materials is determined by including in the sample volume a calibrating compound with a known equation of state.

The encapsulated gasket allows us to encapsulate the sample and to introduce a pressure transmitting medium, which guarantees homogeneous hydrostatic pres-

Figure 2.8 *Unmounted single-toroidal encapsulated TiZr gasket routinely used on the PEARL instrument. The powder sample is packed inside the two hemispherical disks, which are placed within the supporting metallic ring.*

sure transmission throughout the sample. The most used pressure transmitting medium in neutron diffraction is the perdeuterated 4:1 methanol-ethanol fluid [163]. Pressure transmitting media and the importance of hydrostatic pressure is discussed later in this work in Chapter 6.

2.7.3 Pressure calibration

The hydraulic ram of the PE press transmits load to the anvils which compress the loaded material placed inside the gasket. The applied load needs to be converted into a real thermodynamic variable of pressure, P, which is hydrostatic across the sample. This is fundamental to compare the experimental results with theory. In the PE press this is achieved by including in the sample volume a pressure calibrator [161]. The pressure calibrator is a marker element of well-know equation of state. By the determination of the pressure-marker material volume as a function of the applied load, equation of states can be applied to calculate the correspondent pressure value. Most commonly used pressure markers are lead [164], MgO [165] or NaCl [166]. This is especially necessary when studying materials with not-known equation of state, or liquid and glasses which do not show Bragg scattering. The use of a pressure marker carries the problem of pressure gradients, which might occur between the sample and the pressure marker. In case of the study of materials with well-known EoS the most accurate way is to apply the equation of state itself previously determined by other techniques such as X-ray diffraction.

2.7.4 High T, low T setup

High-pressure temperature-dependent measurements can also be performed on the PEARL diffractometer. Figure 2.9 shows the PE press model used to perform temperature-dependent measurements in the 110–500 K temperature range [158].

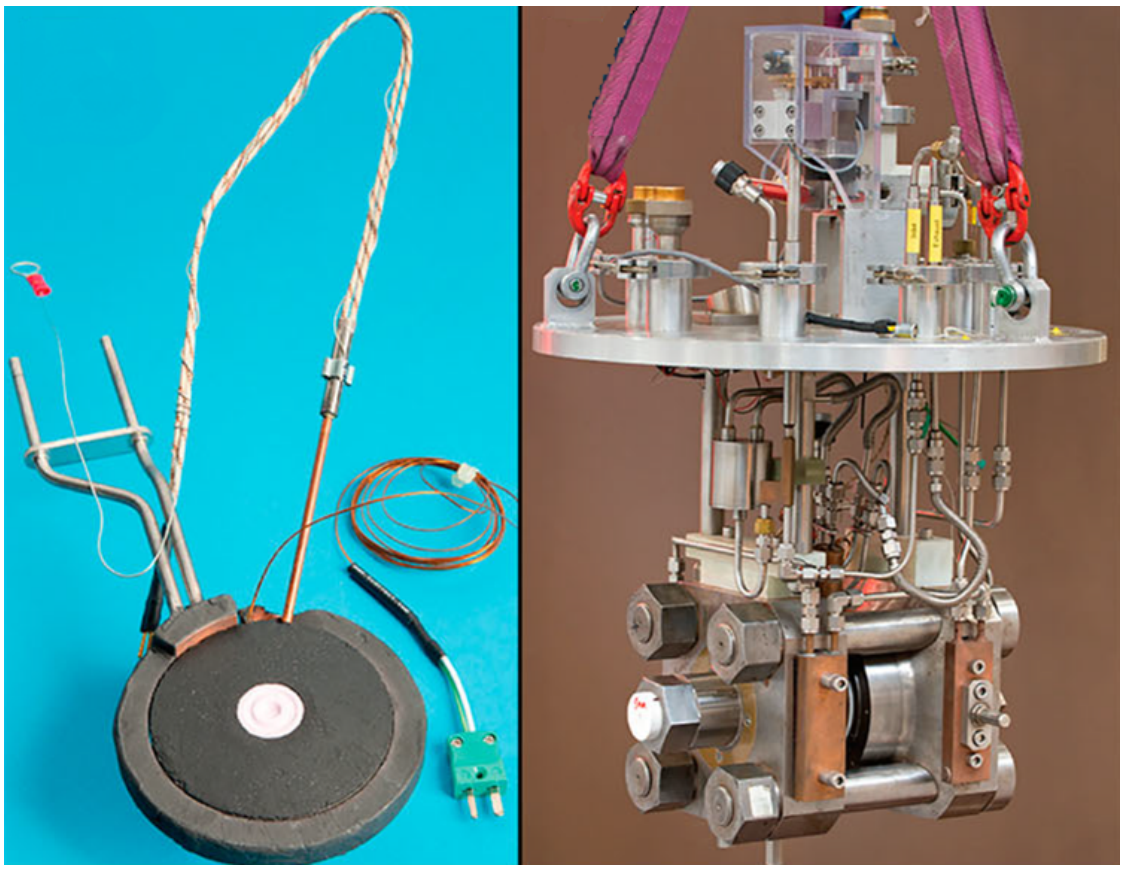

Figure 2.9 *Temperature-dependent PE press setup and anvils. Left panel: ZTA anvils with cooling ring and built in heaters. Right panel shows the PE press V3 model temperature-dependent variant [158].*

The sample is locally heated or cooled. The anvils (left panel of Figure 2.9) are surrounded by a ring in which liquid nitrogen can flow. In-built heaters, eurotherm controlled, are used to locally warm up the sample and counteract the liquid nitrogen stream. By tuning the liquid nitrogen flow and the heater power, the temperature of the sample is locally controlled with a nominal stability of ±1 K. The overall cell body is kept at ambient temperature by a water bath which allows the hydraulic press and the oil inlet to operate as in ambient temperature experiments.

2.8 The diamond anvil cell

Diamond-opposed-anvil cells (DACs), in which two single-crystal diamonds apply the force onto the sample, are one of the leading pressure-generating devices in all high-pressure research fields [167]. First developed in the late 1950s at the NBS laboratories in Washington [168, 169] (now the National Institute of Standards and Technology, NIST), DACs revolutionised high-pressure research. Diamond is a very strong material and is also transparent to many types of electromagnetic radiation, such as gamma rays, X-rays, visible light, and much of the infrared and ultraviolet region. The diamond cell enabled for the first time high-pressure researchers to visually observe the effects of pressure on samples. Nowadays, specially designed diamond anvil cells exist for a wide range of techniques, primarily X-ray diffraction, high-pressure material synthesis, infrared, UV and Raman spectroscopy, Mössbauer spectroscopy, magnetometry and many more. Laser heating of diamond-cell samples has extended accessible pressure-temperature conditions in laboratory which equal those in most of the solid inner Earth [170, 171].

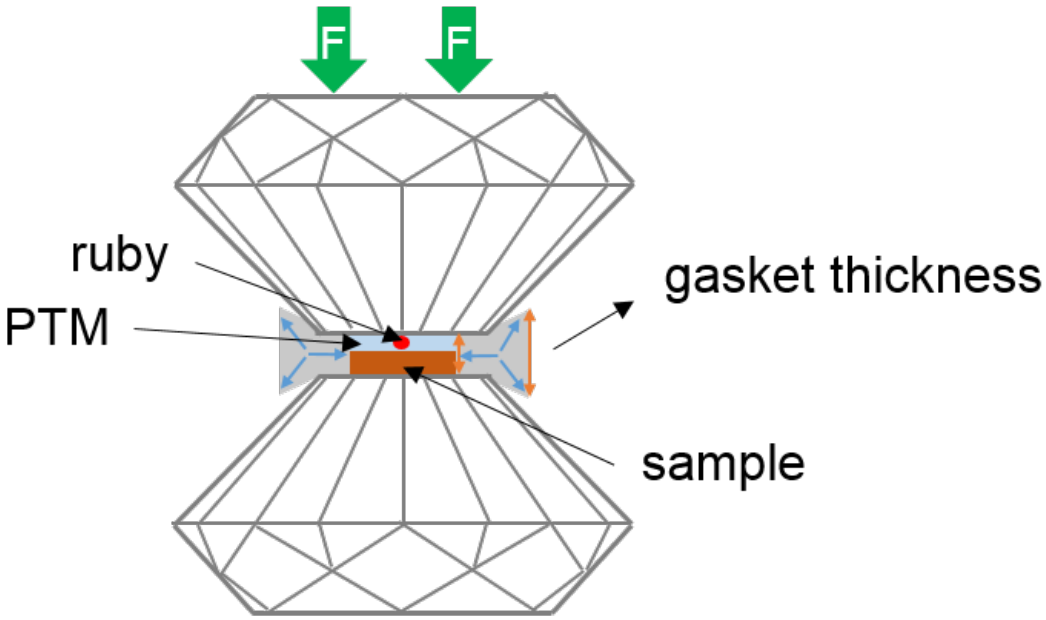

Figure 2.10 *Schematic drawing and main elements of a diamond anvil cell device. Blue arrows indicate the force distribution across the gasket, which is transmitted onto the sample loaded with a small ruby (red sphere) as pressure marker. Big green arrows indicate the direction of application of the force (F) to the top anvil.*

The real revolution owes to the idea of placing a drilled thin metal foil (gasket)

between the diamond anvils to act as pressure chamber with the two diamond culets [172]. The drilled gasket enabled the loading of liquids and fluids, and to pressurise samples in hydrostatic conditions by the insertion of a pressure transmitting fluid. Figure 2.10 shows a schematic representation of a diamond anvil cell and its main elements. The bottom diamond is attached at the bottom seat and fixed during the pressure generation. The upper diamond is free to move towards the opposite anvil. A drilled metallic disk is placed between the diamond faces (culets) to form a cylindrical sample chamber. Common gasket materials include stainless steel, rhenium, tungsten, beryllium, copper-beryllium, boron and a few more. The gasket material choice depends on the pressure required in experiments. Rhenium or tungsten are typically used if pressures higher than 50 GPa must be generated, whereas T-301 stainless steel is chosen for most experiments below 40 GPa. The maximum pressure reachable during the compression depends on the initial indentation thickness of the gasket. Thinner gaskets produce higher pressures, but allow us to load less sample. Be or CuBe are primarily used in X-ray diffraction because both these compounds are X-ray transparent. However, machining beryllium is extremely dangerous and can cause terminal disease.

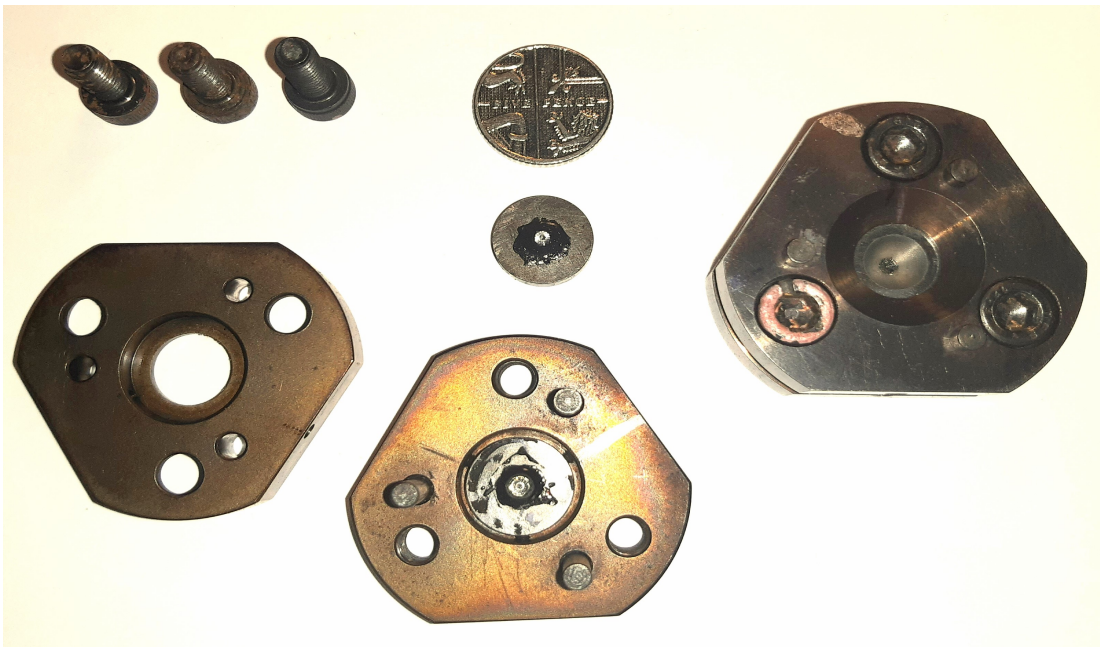

Figure 2.11 *Merrill-Basset diamond anvil cell. The cell is shown both assembled and unmounted. The load is generated by turning the three top screws. Diamonds are glued to the diamond seats, which are aligned at the centre of the cell and between each other.*

A typical example of a diamond anvil cell used in spectroscopic or X-ray

diffraction experiments is shown in Figure 2.11. This type of cell is based on the Merrill-Basset design [173], in which the load is mechanically generated by a three-screw system, which compresses the material placed inside the gasket. Materials are carefully packed with a pressure transmitting medium to transmit pressure hydrostatically throughout the chamber. The determination of pressure generated on samples is typically performed by the ruby fluorescence method [174, 175].

2.8.1 The ruby fluorescence method

High-pressure research lived its major innovation with the design and deployment of diamond anvil cells. This would have not been possible without the development in 1972 of the ruby fluorescence pressure determination method [174]. Scientists of the high-pressure group at NBS laboratories studied the pressure-dependence of several fluorescence materials to find an alternative way to measure pressure *in situ* to the study of equation of states.

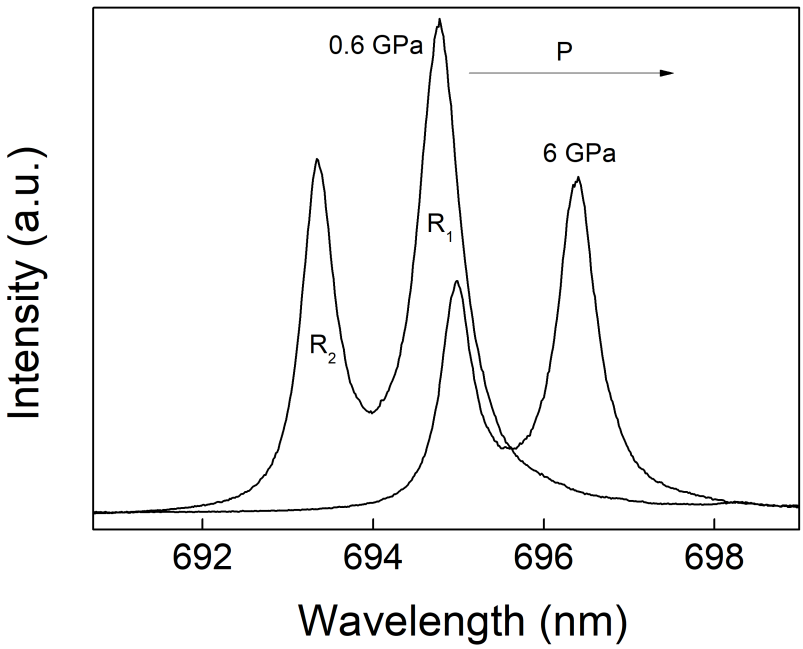

Figure 2.12 *R_1 and R_2 fluorescence lines of ruby Al_2O_3 as a function of pressure. Fluorescence spectra were collected in a Merrill-Bassett-type diamond anvil cell with an in-house optical setup at the ISIS facility.*

Among these, ruby (Al_2O_3) showed the most characteristic behaviour under the

application of pressure. Ruby main fluorescence lines (the $R_{1,2}$ doublet lines) are intense and sharp, and the lines shifts towards the red end of the spectrum with increasing pressure as shown in Figure 2.12. A further advantage is the high intensity of the fluorescence signal, which can be detected with a ruby chip so small as to occupy a negligible portion of the sample chamber volume. Finally, the ruby is chemically inert and can be included in samples without interacting with loaded materials. After the selection of ruby as pressure marker, the R_1-line behaviour upon increasing applied pressure was calibrated. The calibration of the R_1-line was achieved by the study of the equation of state of NaCl and relating this to the measured shift in the wavelength of the ruby R_1-line [176]. Intensive work has been devoted in the past decades to improve the accuracy of the ruby pressure-scale calibration, and nowadays very precise ruby-pressure scales are available [175, 177, 178].

2.9 Raman spectroscopy

Raman scattering is also used to characterise the spectroscopic properties of samples, and in some cases high-pressure Raman experiments are also performed. Raman spectroscopy refers to the phenomenon of inelastic scattering of light with an object. When a monochromatic wave scatters an object, the emerging radiation will include an elastic component, Rayleigh scattering, but also a small amount of radiation scattered at higher and lower frequencies as schematically shown in Figure 2.13.

The inelastic peaks appear at frequencies which differ from the incident/Rayleigh one by a constant quantity, $\Delta\nu$, called relative Raman shift which is independent of the excitation frequency. The band emitted at lower energy is referred to as Stokes, while the inelastic band emitted at higher energy is referred to as anti-Stokes. A Raman spectrum consists of a plot of inelastic peaks collected intensity as a function of their energy expressed by the relative Raman-shift given in cm^{-1}. Raman scattering has a lower intensity than the Rayleigh component, approximately 1 photon is scattered inelastically per 10 million scattered elastically. The frequency variation of the scattered photon provides chemical and structural information about the sample. The incident wave interacts with electrons in the system, which displace from their equilibrium position. This generates a variation in the electric dipole moment d proportional to a quantity referred to as polarisability and conventionally denoted as α.

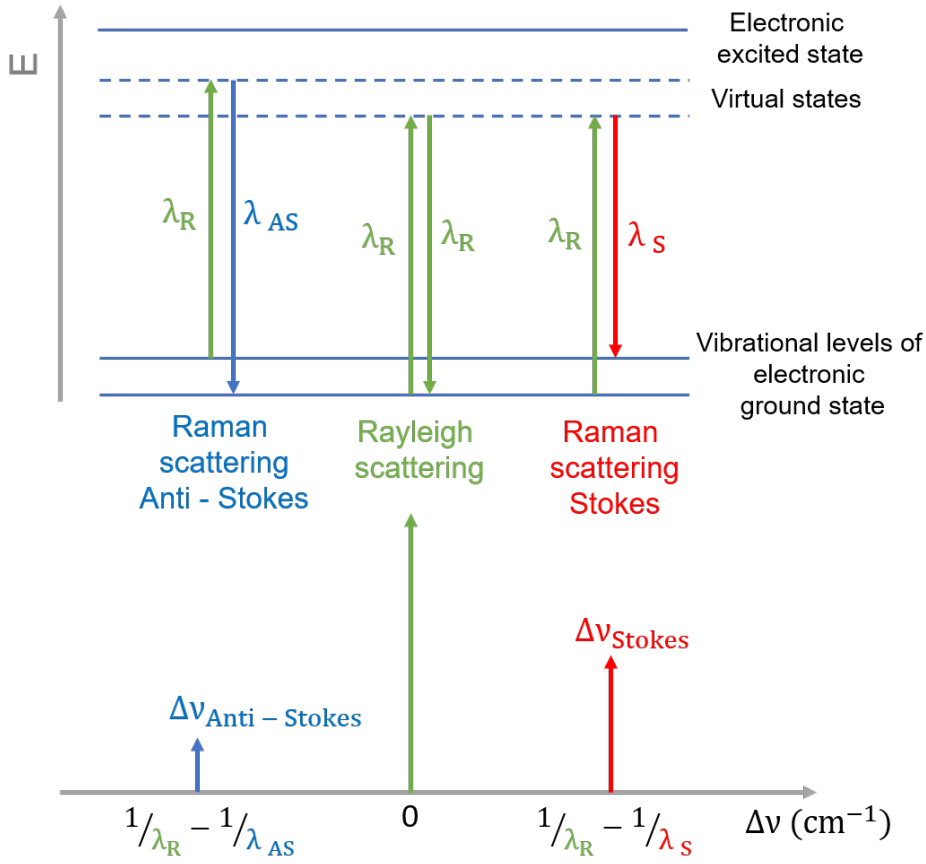

Figure 2.13 *Diagram showing the elastic Rayleigh scattering λ_R (green arrow) and the inelastic Raman scattering emission as a function of increasing energy (E). The Raman scattering gives rise to the emission of radiation at $\lambda_S < \lambda_R$ and $\lambda_{AS} > \lambda_R$, red and blue arrow, respectively. At the bottom is shown a schematic representation of a typical Raman spectrum. This is a plot of the scattered intensity as function of the relative Raman shift, which is independent of the excitation frequency.*

The polarisability is also dependent on the internal molecular vibrations of the scattering system, that is on the normal vibrational modes. The polarisability of a molecule decreases with increasing electron density, increasing bond strength, and decreasing bond length. The molecular vibration modulates the polarisability and an inelastic response is only obtained if the first derivative of the polarisation with respect to the normal vibrational mode is different from zero when calculated at the equilibrium position.

2.9.1 Vibrational modes in perovskites

The current work uses Raman spectroscopy to characterise the vibrational property of perovskite oxides. Various vibrational modes are at the origin of Raman spectra of perovskite oxides, such as vibration of the A-site and B-site (in case of non centrosymmetric structures). However, what is mostly interesting in light of this thesis is that Raman modes can be associated to oxygen displacements and hence to the tilting of the octahedra [179–182]. The following symbols (Mulliken symbols) are used to classify symmetries of point groups of molecular vibrational modes.

- A, Symmetric with respect to principal axis of symmetry;
- B, Antisymmetric with respect to principal axis of symmetry;
- E, Doubly degenerate, two-dimensional irreducible representation;
- T, Triply degenerate, three-dimensional irreducible representation;
- g, Symmetric with respect to a centre of symmetry;
- u, Antisymmetric with respect to a centre of symmetry;
- 1 (subscript), Symmetric with respect to a C2 axis that is perpendicular to the principal axis. Where there is no such axis the subscript indicates that reflection in a vertical plane of symmetry is symmetric;
- 2 (subscript), Antisymmetric with respect to a C2 axis that is perpendicular to the principal axis. Where there is no such axis the subscript indicates that reflection in a vertical plane of symmetry is antisymmetric.

A Raman mode assigned as A_1 can be either a totally symmetric stretch or bend with respect to the principal axis of symmetry in a molecule without a center of symmetry. A band designated A_g can also be either a totally symmetric stretch or bend, and here the subscript g informs us that the molecule is centrosymmetric. The g and u subscripts are used to indicate if the system is symmetric or antisymmetric by rotation about the principal symmetry axes. A Raman mode assigned as B_2 indicates a stretching or bending mode, which is antisymmetric with respect to the principal axis of symmetry and antisymmetric with respect

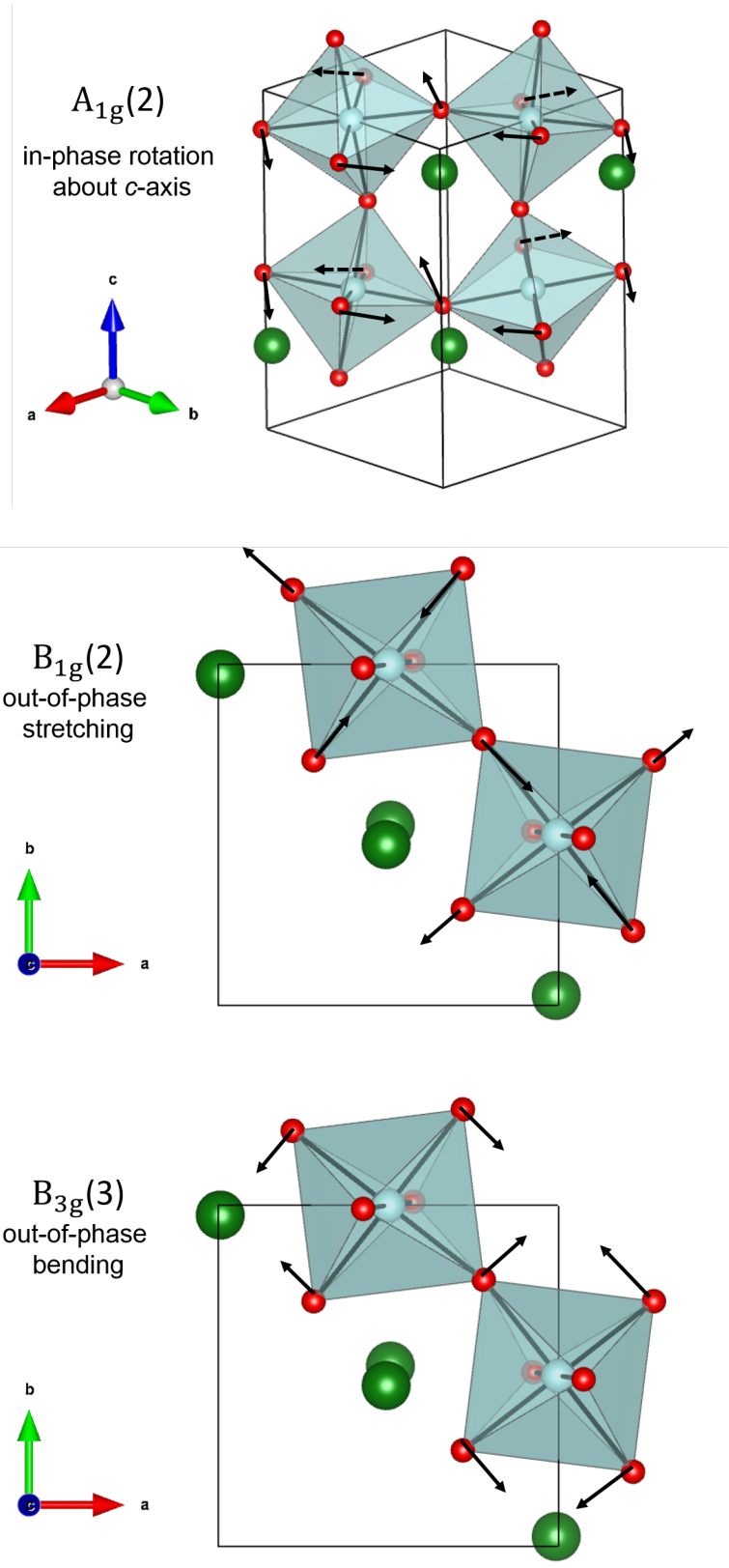

Figure 2.14 *Selected vibrational modes (black arrows) of the BX_6 octahedra in Pbnm space-group. The unit cell (thin black line) and lanthanum atoms (green spheres) are shown for clarity. Dashed arrows are used to indicate atomic vibrations which lie behind the octahedra.*

to either a vertical reflection plane or a C2 axis perpendicular to the principal axis of symmetry.

Figure 2.14 depicts selected molecular vibrations in octahedral geometry referred to as $A_{1g}(2)$, $B_{1g}(2)$ and $B_{3g}(3)$ (black arrows). The presented octahedra belong to the orthorhombic *Pbnm* structure described in Section 1.4.2. The A_{1g} mode relates to in-phase octahedral rotations around the crystallographic c-axis and is associated to the tilting system $a^0a^0c^+$ [182]. Vibrations referred to as $B_{1g}(2)$ and $B_{3g}(3)$ indicate out-of-phase stretching and bending of oxygen atoms, respectively. Raman scattering is a tool for identifying structural phases and phase transitions, since vibrational modes provide a unique signature of the crystal structure and of its correlated structural, electronic and optical properties.

2.9.2 High-pressure Raman spectroscopy

Raman spectroscopy experiments were also carried out at the ISIS facility, using an in-house Raman spectroscopy setup equipped with a Princeton Instrument SP2500i spectrometer and a diode laser with excitation wavelength $\lambda = 532.23\,\text{nm}$. A 1800 g holographic blaze grating has usually been used during the measurements. The light was collected in back-scattering after passing through a Mitutoyu objective lens.

A Merrill-Basset-type diamond anvil cell [173] has been used as high-pressure cell, which was shown and described in Figure 2.11. Gaskets were usually pre-indented from an initial thickness of 250 μm to 110 μm, and the drilled gasket hole typically ranged from 300 to 400 μm. A small ruby sphere was used as pressure marker and the pressure on the sample determined by ruby fluorescence measurements [175]. Hydrostatic pressure was generated by the use of a 4:1 methanol-ethanol solution as pressure transmitting medium.

2.10 SQUID DC magnetisation measurements

SQUID DC magnetometry is one of the techniques to detect the magnetic moment of materials. An advantage of SQUID magnetometry is the high sensitivity to small magnetic flux changes, detecting variations in the order of $10^{-14}\,\text{T}$. In a SQUID device, two superconducting materials are connected in parallel by two

Josephson junctions as to form a superconducting loop [183, 184]. Two properties of superconducting materials are at the base of the SQUID device: the Josephson effect and the quantisation of the magnetic flux enclosed in a superconducting loop. The Josephson effect predicts the tunnelling of Cooper pairs between two superconducting materials separated by a thin insulating layer (Josephson junction) without generating any voltage at the junctions. Superconducting loops can enclose a magnetic flux, which must be a multiple of a flux quantum Φ_0 given by:

$$\Phi_0 = \frac{2\pi\hbar}{2e} = 2.0678\,10^{-15}\,Tm^2 \tag{2.29}$$

If a constant current I_b is applied to a SQUID, the current will split into the two branches of the loop. Tunnelling of the Cooper pairs through the junctions will occur. If a magnetic field H is then applied to the system, by electric induction an opposite current I_s is generated into the superconducting ring to counteract the effect of the magnetic field H. In the two branches $I_c = \frac{I_b}{2} \pm I_s$ will flow, which generates a phase difference at the two junctions. If the biasing current is maintained constant, the measured voltage oscillates with change in the magnetic flux enclosed in the superconducting ring. The phase oscillations are proportional to the flux change which has occurred. The current I_c is also related to the phase difference between the superconducting materials. The current decreases as the external field is increased, is zero when the flux is exactly Φ_0, and again reverses direction as the external field is further increased. Thus, the current changes direction periodically, every time the flux increases by an additional half-integer multiple of the quantum flux. By measuring I_c, the phase difference hence the voltage between the superconductors can be measured. A small variation in the voltage corresponds to a variation in the enclosed magnetic flux. If the current is increased, to respect the quantisation of the magnetic flux the SQUID device will increase the total flux, instead of counteracting it. The SQUID magnetometer measures the variation of the magnetic flux by variation in the voltage at the edges of the Josephson junctions:

$$I = \frac{\Delta\Phi}{L} - - > \Delta V = \frac{R}{L}\Delta\Phi \tag{2.30}$$

where L is the self-inductance of the superconducting ring, $\Delta\Phi$ is the magnetic flux variation, and R (Ω) is its resistance.

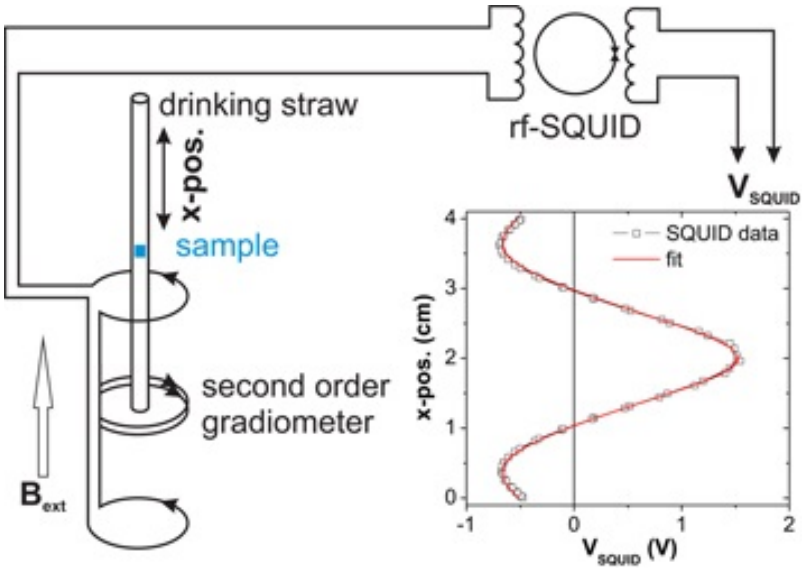

Figure 2.15 *Schematic representation of the MPMP - XL SQUID magnetometer circuit setup [184]. Inset shows the SQUID response V_{SQUID} as a function of sample position.*

In a SQUID device the sample is place in a non-magnetic sample holder and located as shown in Figure 2.15 in a superconducting coil. The sample oscillates through the device generating a variation in the voltage. SQUID magnetometers detect the change of magnetic flux created by mechanically moving the sample through the superconducting coil, which induces a current by electromagnetic induction.

DC magnetometry measurements presented in the current thesis were performed using an MPMS-XL SQUID (Superconducting Quantum Interference Device) magnetometer, at the Material Characterisation Laboratory, at ISIS Neutron and Muon Facility. The MPMS magnetometer is equipped with a superconducting magnet which enables measurements in an applied magnetic field up to 7 T, with a field uniformity of 0.01 T over 4 cm. Magnetisation measurements can be made as a function of both temperature and applied magnetic field over a temperature range of 2 to 400 K. Temperatures up to 800 K can be achieved by using an optional furnace insert, but the sample must be mounted in an alumina sample holder to withstand the higher temperatures, which increase distortion of the dipole signal and therefore the background noise on the measurement. When calibrated to a sample of known mass, the SQUID response can be fitted to obtain the magnetic moment of the sample in electromagnetic units (emu).

2.10.1 High-pressure SQUID magnetisation measurements

High-pressure SQUID magnetisation measurements were also used in the work reported in this thesis. Measurements were performed by the use of a Turnbuckle-type diamond anvil cell (TM-DAC) specially developed for MPMS SQUID devices [185].

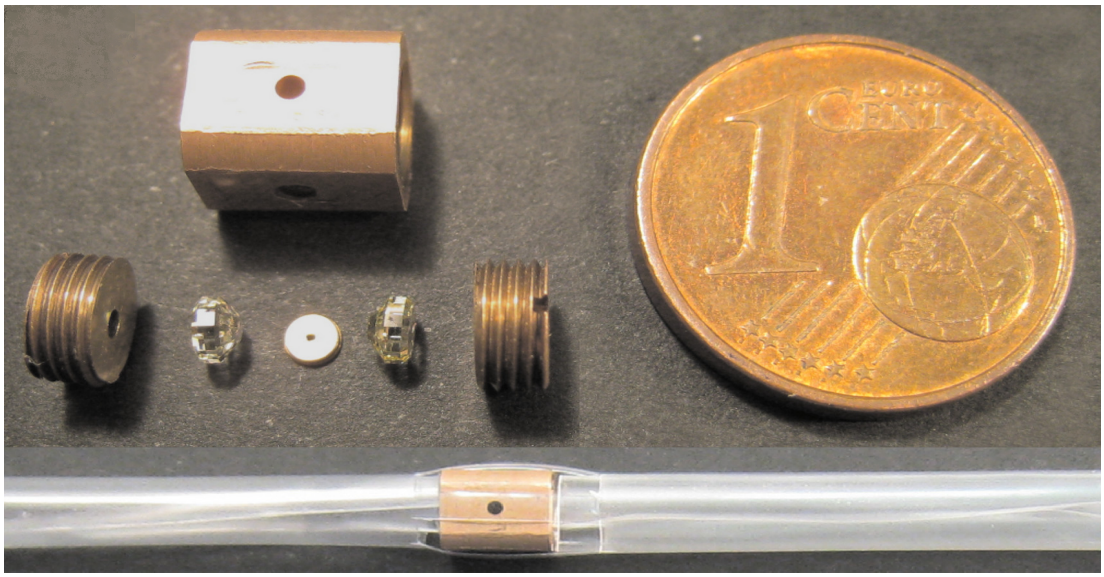

Figure 2.16 *Turnbuckle-type diamond anvil cell (TM-DAC) specially developed for SQUID magnetisation measurements. The pressure cell is made of fully hardened copper-beryllium alloy. The cell is shown assembled at the bottom inside the plastic straw holder of an MPMS SQUID device [185].*

The TM-DAC is shown in Figure 2.16. The body of the cell is a cylinder 7 mm long and 7 mm in diameter. Four holes are machined in the sides for viewing the anvils and the gasket. The two end-nuts have four guiding drilled holes at one side and the diamond anvils attached at the other end. The sample is packed in a metallic gasket pre-indented at a thickness typically around 120 μm. If a gasket hole of 350 μm in diameter is drilled typical sample volumes are in the order of 10^{-2}mm^3. A specially designed bracket is attached with four pins at the four holes in both end-nuts. The pins so attached can only slide up and down, when the body of the cell is rotated. A small initial pressure is generated by rotating the cell. Higher loads are generated by placing the TM-DAC in a manual hydraulic press. Ruby fluorescence technique is typically used to determine the pressure generated on samples.

The magnetisation as a function of temperature scans of the loaded material is

inevitably altered by the magnetic contribution coming from the copper-beryllium cell. The measured signal must be carefully corrected for this background contribution. The magnetisation of the empty pressure cell as a function of different magnetic fields and temperatures is preliminary recorded, and used for background corrections [185].

2.11 Material synthesis

This thesis investigates polycrystalline powder oxides, whose material synthesis is achieved using solid state reaction methods. Polycrystalline samples were synthesised by the nitrate decomposition route [186, 187], at the chemistry laboratory at the ISIS Facility.

The sample preparation requires high purity precursors and subsequent steps. Firstly, nitrate reagents in relative molar ratio are mixed in distilled water in a ceramic pot. The pot is placed and left in an ultra-sonic bath for a few minutes to favour a homogeneous mix of the reagents. The aqueous solution is dried in oven at 100 °C and further boiled on a hot plate, preheated to about 300 °C and heated to 550 °C to evaporate excess water. The resulting gel is heated under air in a furnace at 700 °C until the nitrates start to decompose, as detected by the evaporation of brown smoke. The furnace is further heated to 900 °C for 24 h and gradually cooled down to ambient temperature at a rate of 2°C/min. The nitrates have to decompose uniformly and a gradual heating and cooling of the compound during the synthesis avoids formation of strain or oxygen vacancies. The residual powder is finely ground and pelletised using an uni-axial dye. The pellet is then thermally treated in a furnace at 1100 °C for 24 h. Pelletisation increases the contact surface among particles and favours a quicker and more uniform synthesis. The powder is repeatedly ground, pelletised and annealed at 1100 °C. Consecutive pelletisation, grinding and annealing is fundamental for producing homogeneous samples, and the process is usually repeated a few times before a phase pure sample is obtained.

The $LaFeO_3$ perovskite material is one of the samples synthesised and characterised in the current thesis. A stoichiometric amount in the molar ratio 1La:1Fe of $La(NO_3)_3 6H_2O$ and $Fe(NO_2)_3 9H_2O$ (99.999% Sigma-Aldrich) was mixed to form 3 g of material. Figure 2.17 shows selected XRD patterns of $LaFeO_3$ at three different steps of the synthesis route.

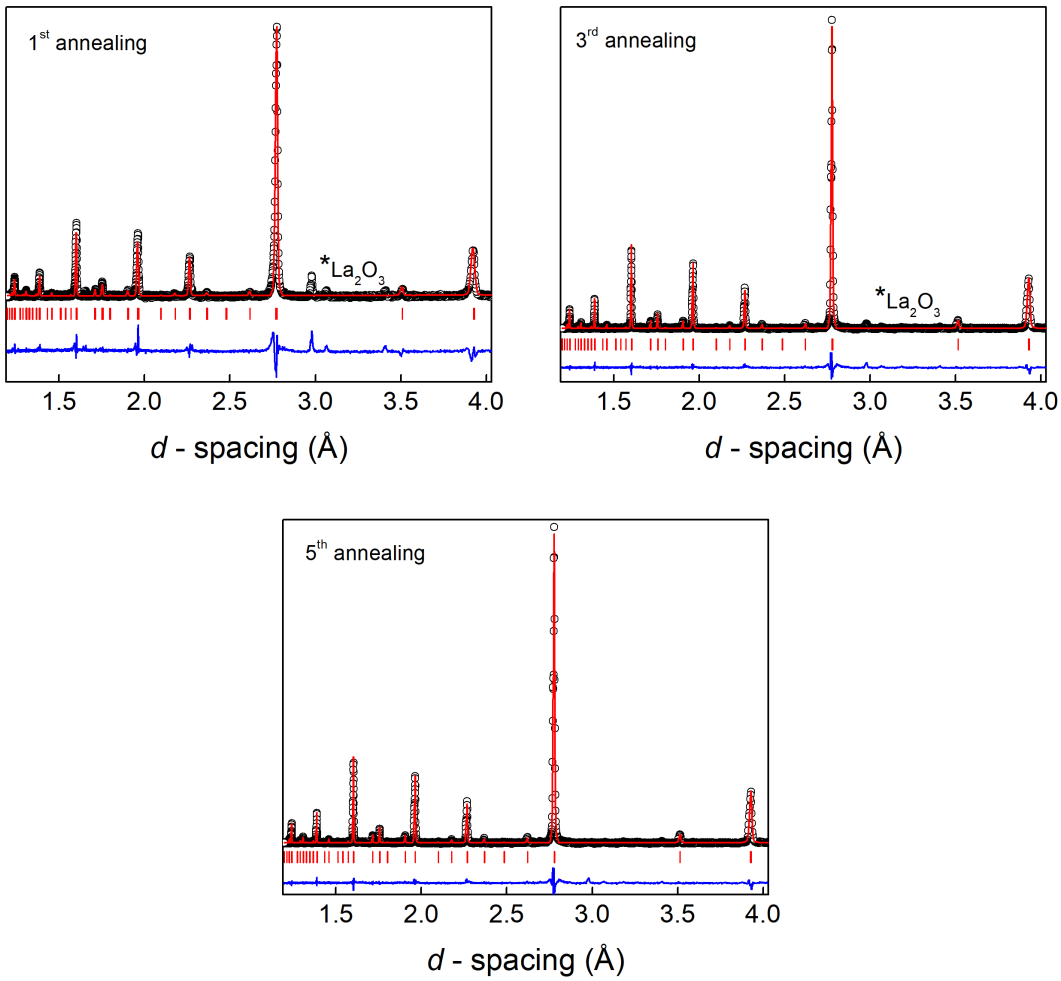

Figure 2.17 *XRD patterns of $LaFeO_3$ at three different cycles of the synthesis route. Experimental data (open circles) were collected with a D2 Bruker diffractometer equipped with a Cu-K$\alpha_{1,2}$ radiation source. Red solid lines show fits to the data with a Pbnm space group. Vertical tick marks indicate calculated reflections from the sample phase and bottom blue lines show the residual of the Rietveld fits.*

Impurities of La_2O_3 are observed in the first stages of the annealing route. By consecutive pelletising, grinding and annealing, the impurities gradually disappear until a phase pure sample is produced. Phase purity of the perovskite samples must be verified not only by X-ray diffraction, but advanced neutron diffraction characterisation is necessary to confirm the phase purity of samples. The oxygen atoms could form oxide impurities, which might not be detected by X-ray diffraction.

2.12 Conclusions

This chapter sought to introduce the fundamentals of the various experimental techniques and instruments utilised in this work for material characterisation. Basic elements of X-ray and neutron diffraction theory are used to introduce Bragg's law and fundamental parameters in crystallography research such as the inter-planar spacing d, the scattering cross-section σ and the structure factor F_{hkl}. Not only structural information, but spectroscopic and magnetic properties have been studied by using Raman scattering and magnetisation measurements, with the aim to find correlation between physical and structural properties. Several pressure tools have been used to perform high-pressure experiments on powder samples, from the Paris-Edinburgh press for neutron diffraction to specially designed diamond anvil cells for optical or magnetisation measurements. The following chapters discuss main results on perovskite materials obtained by the use of the aforementioned experimental capabilities.

Chapter 3

High-pressure studies of $LaCoO_3$

This chapter presents the high-pressure structural characterisation carried out on the $LaCoO_3$ perovskite. High-pressure neutron-diffraction experiments are shown at temperatures of 120, 290 and 480 K in the 0–6 GPa pressure range. The equation of state of the sample is determined at each temperature and accurate measurements of structural parameters are reported at pressures higher than previously reported by neutron diffraction. The major interest of the current work is to explore the structural-electronic property relationships of $LaCoO_3$ under high-pressure and obtain precise measurements of the Co–O and La–O bond distances. The low and high temperatures have been selected according to the previously reported magnetic transition temperatures of $LaCoO_3$ [68, 119] with the aim to compress the $LaCoO_3$ sample in different starting electronic configurations. The precise structural parameters determined in this work of thesis may be indicative of the nature of spin-state transitions in this compound.

3.1 Background

$LaCoO_3$ is a material attracting attention owing to its spin-state transitions, which are strongly dependent on temperature and/or pressure [68, 84, 118, 119, 122, 188–193]. However, there is still a lack of consensus within the academic literature on the structural-magnetic changes of this compound under extreme conditions. $LaCoO_3$ exhibits electronic configurations strongly dependent on temperature [68, 188, 191, 193, 194]. This is caused by the small crystal-field

splitting between the t_{2g} and e_g orbitals of the cobalt cations, which allows electrons to be thermally excited from the t_{2g} to e_g energy levels. At low temperatures (<50 K) $LaCoO_3$ is a diamagnetic insulator characterised by the Co^{3+} atoms in the low-spin state (LS) $t_{2g}^6 e_g^0$ (total spin number $S = 0$) [68, 84]. At T∼100 K the material undergoes a magnetic transition to a paramagnetic state interpreted as a higher spin-state configuration being gradually populated with increasing temperature [68, 84]. Great interest has been devoted to the higher spin state and some controversy still exists on its nature. Both intermediate-spin $t_{2g}^5 e_g^1$ ($S = 1$) (IS) and high-spin (HS) $t_{2g}^4 e_g^2$ ($S = 2$) state of the trivalent cobalt have been suggested to be populated after the transition temperature. A consensus has been reached on the importance of all three spin states, low spin, intermediate spin, and high spin for $LaCoO_3$ [68, 188, 191, 193, 194]. The low-temperature transition from LS to IS states and the high-temperature transition from intermediate to high-spin states would both be thermally activated after the transition temperature. With further increase of temperature the formation of a long-range-ordered superstructure of Co_{HS} and Co_{LS} has been suggested to occur [188]. In this superstructure the cobalt cations in the high-spin and low-spin state occupy distinct crystallographic sites, hence lowering the symmetry of the crystal structure from $R\bar{3}c$ to $R\bar{3}$. However, neutron-diffraction studies have not observed, yet, the lower symmetry required for the ordered Co_{HS} and Co_{LS} superstructure [68, 84], and a mixture of both IS and HS state has been suggested after the transition temperature. Around 500 K a further anomaly in the magnetic susceptibility has been observed [194] and explained as an insulator-metal transition, where the electrons in the e_g orbitals become mobile and break the superstructure. Above 648 K charge transfer between Co cations takes place and disproportionation of the cobalt cation to Co^{2+} and Co^{4+} has been observed [195]. The pressure behaviour of the electronic configuration of $LaCoO_3$ has also been an object of study. At room temperature, a pressure-driven transition occurs around 4 GPa as reported from anomalies in photoemission measurements [196] and further supported by magnetic measurements under hydrostatic pressure [120]. In the latter work, pressure is observed to increase the crystal-field splitting of the *3d* orbitals and a depopulation of the e_g orbitals is promoted, driving a high-spin to low-spin electronic transition.

$LaCoO_3$ crystallises at ambient temperature and pressure in the trigonal symmetry $R\bar{3}c$ space group [84]. Its crystal structure is depicted in Figure 3.1 and extensively described in Section 1.4.3.

The $R\bar{3}c$ space group is derived from the cubic aristotype by anti-phase rigid tilting of the CoO_6 octahedra about the [111] crystallographic cubic axis. The octahedral tilting reduces the La-site volume and leads to three distinct La–O bond distances: La–O1 (short, 3-fold), La–O2 (intermediate, 6-fold), and La–O3 (long, 3-fold), whereas the octahedral environment remains unchanged, with six equivalent Co–O bond lengths. Several attempts have been made to relate the structural properties of $LaCoO_3$ to its various electronic configurations. However, there is a strong literature discrepancy and a clear structural-magnetic property relationship picture has yet to be achieved. Several diffraction studies as a function of temperature were performed to determine the crystal structure of $LaCoO_3$ [68, 69, 84, 187]. In these works a stable $R\bar{3}c$ space group has been reported and a linear increase of the Co–O bond distance has been consistently observed in the 4.2–1200 K temperature range. The degree of distortion is also consistently found to decrease upon temperature, with the CoO_6 octahedra tending to an ideal pseudo-cubic geometrical configuration. In contrast to the Co–O linear evolution, a temperature-dependent neutron diffraction study reported that the La-site shows three anomalies at ∼100, 500, and 800 K, which have

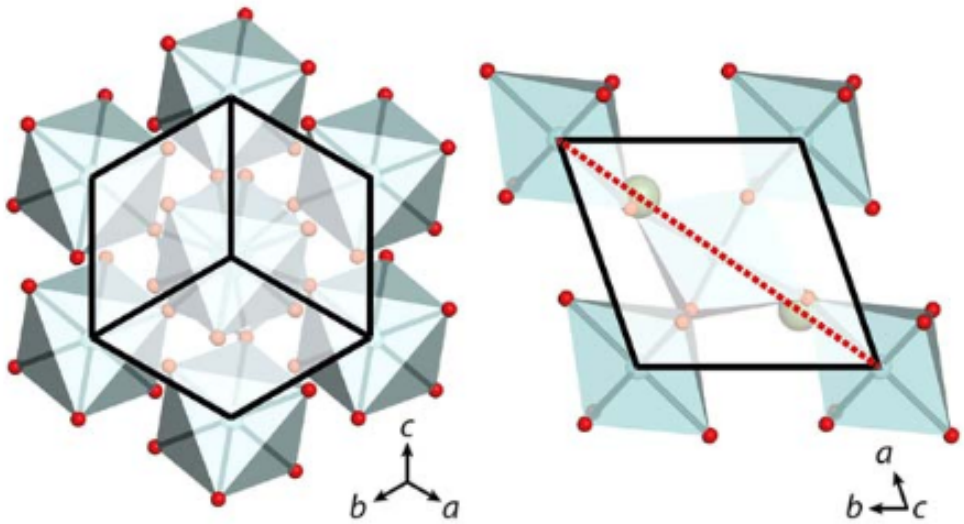

Figure 3.1 *Crystal structure of $LaCoO_3$ viewed down the [111] direction (left panel). The slightly opaque area shows the unit cell, and is outlined by the solid black line. La–O bonds are not shown for clarity. Right panel shows a view of the crystal structure along c-axis. The unit cell is again shown by solid black line and the angle subtended by the two lines is the unit-cell angle. Red dotted line indicates the [111] direction, as viewed in left panel, again, the La–O bonds are not shown for clarity.*

been related to spin-state transitions of the Co cation [68]. As a function of pressure two main structural investigations were performed on $LaCoO_3$. An X-ray diffraction study reports a discontinuity in the compressibility of the Co–O and La–O bond lengths and Co–O–Co angle at 4 GPa [124]. These observed anomalies were explained as a structural signature of the electronic transition from the intermediate-spin to the low-spin state. Neutron diffraction offers a more suitable tool to accurately study transition-metal oxide systems than X-ray diffraction. The Z complex dependence of the scattering process provides the capability to accurately see light atoms such as oxygen atoms in the presence of much heavier atoms such as the La and Co cations. A high-pressure neutron-diffraction study was recently performed up to 4 GPa [123]. This work reports no unusual change in bond distances as a function of increasing pressure and also reports a linear increase of the inter-octahedral Co–O–Co angle, but only four data points have been collected.

The high-pressure neutron-diffraction study reported in this thesis aims to clarify the controversy, which still exists on the structural and magnetic changes of $LaCoO_3$ under extreme conditions.

3.2 Experimental

3.2.1 Material synthesis and preliminary characterisation

The $LaCoO_3$ powder sample was synthesised by a solid-state nitrate decomposition procedure described in detail in Section 2.11. Stoichiometric amounts of $La(NO_3)_3 6H_2O$ and $Co(NO_3)_2 6H_2O$ (Sigma-Aldrich, 99.99%) were completely dissolved in distilled water. The water was removed by evaporation at 350 K over two hours. The resulting gel was decomposed at 870 K overnight and the final grey powder was ground and pelletised. The pelleted sample was annealed in air at 1370 K for 12 h, followed by repeated grinding and annealing until a single-phase material was obtained. The phase purity was verified by X-ray diffraction using a D2 Bruker diffractometer at the Material Characterisation Laboratory, at the ISIS facility. The ground sample was placed on a silicon sample holder and data collected using a $Cu_{k_{\alpha_1,\alpha_2}}$ radiation in the $2\theta = 15°$–$80°$ range. Figure 3.2 shows a representative X-ray diffraction pattern of the synthesised $LaCoO_3$ powder sample in the 1.5–4 Å range.

Raw data are shown as open circles, while red solid line shows a Rietveld refinement to the data with an $R\bar{3}c$ space group. Calculated reflections from the sample phase are also shown. The data were analysed using the GSAS package [146] and Rietveld refinement confirmed the rhombohedral symmetry and phase purity.

Magnetisation measurements were performed on the $LaCoO_3$ sample using a Quantum Design MPMS-XL7 SQUID magnetometer at the Material Characterisation Laboratory. About 120 mg of powder was placed into a gelatine capsule and mounted into a plastic straw. The loaded straw was then placed into the instrument at ambient temperature. Zero field cooling (ZFC) and field

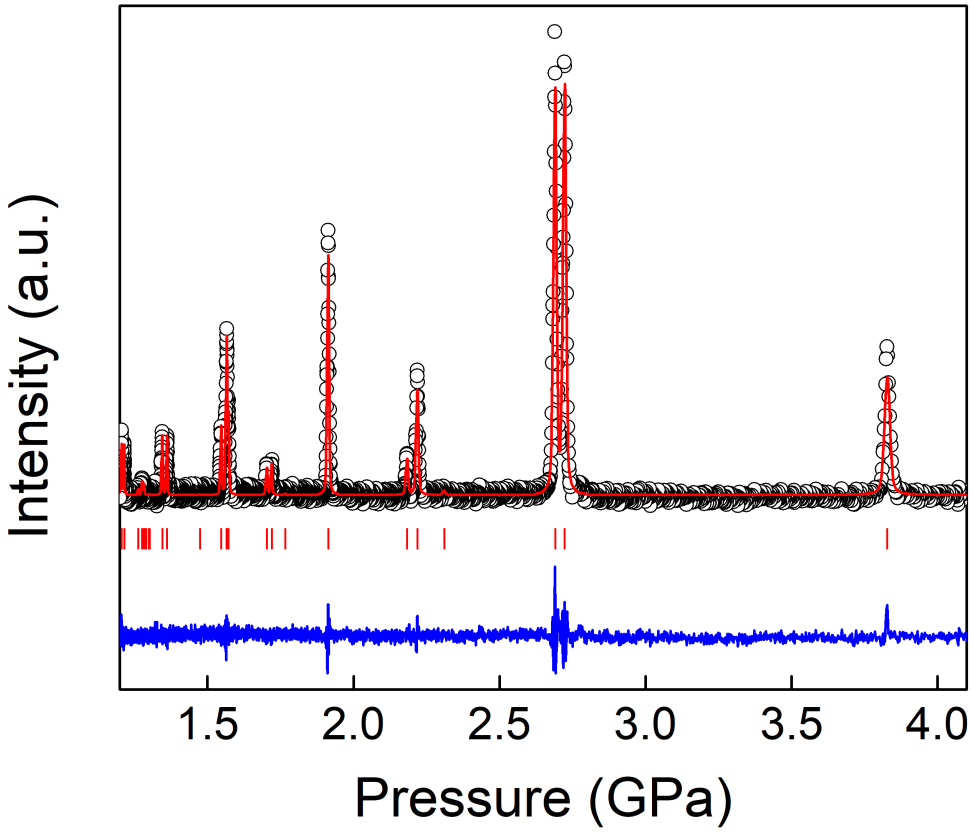

Figure 3.2 *X-ray diffraction pattern of $LaCoO_3$ acquired at ambient temperature and pressure in the 1.5–4 Å range using a D2 Bruker X-ray diffractometer. Experimental data are shown as open circles. The red line is a Rietveld refinement to the data, while the bottom blue trace shows the residual of the refinement. Vertical tick marks represent calculated reflection positions from the $LaCoO_3$ phase.*

cooling (FC) DC magnetisation measurements have been performed in the 2–300 K temperature range upon warming under an applied magnetic field of 100 Oe and a representative example is shown in Figure 3.3.

The magnetisation behaviour is comparable with previously reported magnetisation studies [192, 197, 198]. The well-reported low-spin to intermediate spin transition is found at low temperature as it is observed by the hump in the ZFC curve and by the rapid decrease of the inverse of the FC magnetic susceptibility shown in inset of Figure 3.3. The Curie Temperature T_C was determined as the minimum of the first derivative of the FC static susceptibility curve (not shown). The calculated value of 85.2(5) K is in agreement with the previously reported T_C [192, 197]. A critical temperature of 83 K has been recently proposed for vacant bulk $La_{1-x}Co_{1-x}Co_xO_3$ with induced Co^{4+}/Co^{3+} charge disproportion [198]. In this work, a ferrimagnetic coupling is proposed

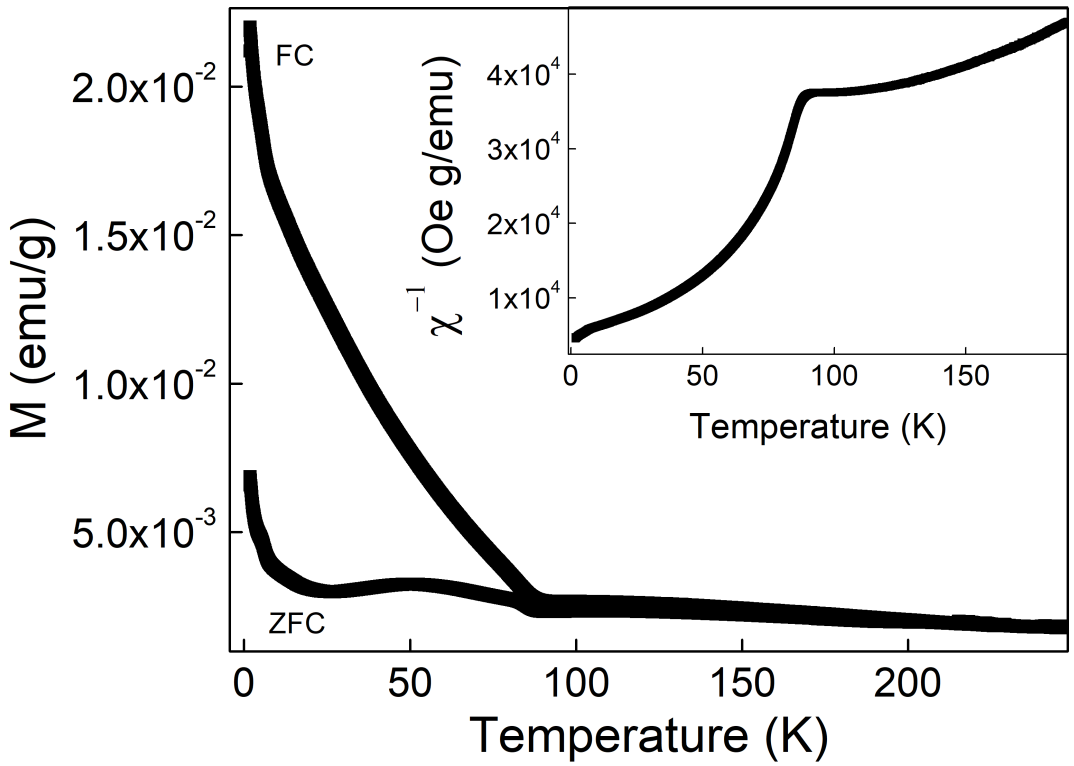

Figure 3.3 *Field-cooled and zero-field-cooled temperature dependent DC magnetisation measurements of $LaCoO_3$ at an applied magnetic field of 100 Oe in the 2–300 K temperature range. The magnetisation M is scaled respect to the sample mass. Inset shows a plot of the inverse static susceptibility χ^{-1} derived from the FC magnetisation curve.*

originating by alternating sublattices of Co^{4+}/Co^{3+} cations, which promote uniaxial compression of the octahedra by Jahn-Teller distortion and the cations align in parallel and antiparallel arrangement. A net magnetisation persists, to which is ascribed the weakly surface ferromagnetism found in $LaCoO_3$ [197]. The inverse of the magnetic susceptibility shows an almost straight line at high temperatures and a sudden drop close to the Curie temperature, which is a characteristic behaviour of a ferrimagnetic arrangement. The FC inverse susceptibility χ^{-1} measured in this work drops at the critical temperature as shown in inset of Figure 3.3, but slower than what reported for the doped Co^{4+}/Co^{3+} compound, where the charge disproportion was induced to enhance the octahedral distortion and thus the ferrimagnetic coupling [198]. In bulk $LaCoO_3$ a lower degree of ferrimagnetic arrangement is also found. This is ascribed to the effect of local Jahn-Teller distortion of the structure [123], which despite the $3d^6$ electronic configuration of the cobalt atoms arises from the gradual population with temperature of an intermediate spin state $t_{2g}^5 e_g^1$.

Attempts to perform high-pressure DC magnetisation measurements were carried out by the use of a miniature Turn-Buckle-type diamond anvil cell (described in detail in Section 2.10.1). However, the magnetic moment of $LaCoO_3$ is not sufficiently high to be measured in this high-pressure magnetisation measurement setup. The magnetic signal from the sample was too weak to be subtract from the cell background.

3.2.2 Raman spectroscopy characterisation

Raman spectroscopy is an efficient way to study vibrational modes and electronic transitions in materials. It is particularly important when dynamic local distortions occur that cannot be detected by a diffraction experiment, such as local site Jahn-Teller distortion of the $3d$ orbitals, which locally lowers the crystal symmetry in perovskite compounds. Raman measurements were used to study the local dynamics of $LaCoO_3$. The sample was placed on a glass substrate and Raman spectra were collected using an in-house Raman system equipped with a Princeton Instruments SP2500i spectrometer with a 1800 g holographic blaze grating. A diode laser ($\lambda = 532.23$ nm) was focused using a 20× Mitutoyu objective lens with a low laser power of 2 mW at the sample position to avoid over-heating of the cobalt surface.

For an $R\bar{3}c$ space group the Raman active modes are $A_{1g}+4E_g$ [200]. The Raman

active modes are associated with the R $\left(\frac{1}{2}, \frac{1}{2}, \frac{1}{2}\right)$ corner point of the cubic-like Brillouin zone of the parent cubic phase. Only few Raman studies have been performed on $LaCoO_3$ [123, 199, 201–204]. The small rhombohedral distortion of $LaCoO_3$ makes Raman scattering extremely weak[1], and laser-induced heating of the cobaltite surface may occur during collection of spectra. Raman spectra previously reported consistently show the presence of additional active bands [123, 199, 204], which may be related to local distortions of the structure (i.e. Jahn-Teller).

A Raman spectrum of $LaCoO_3$ collected at ambient temperature and pressure in the current work is shown in Figure 3.4. The low energy peaks at Raman shift

[1]In the ideal cubic perovskite structure, all lattice sites have inversion symmetry. Therefore, first-order Raman scattering is forbidden.

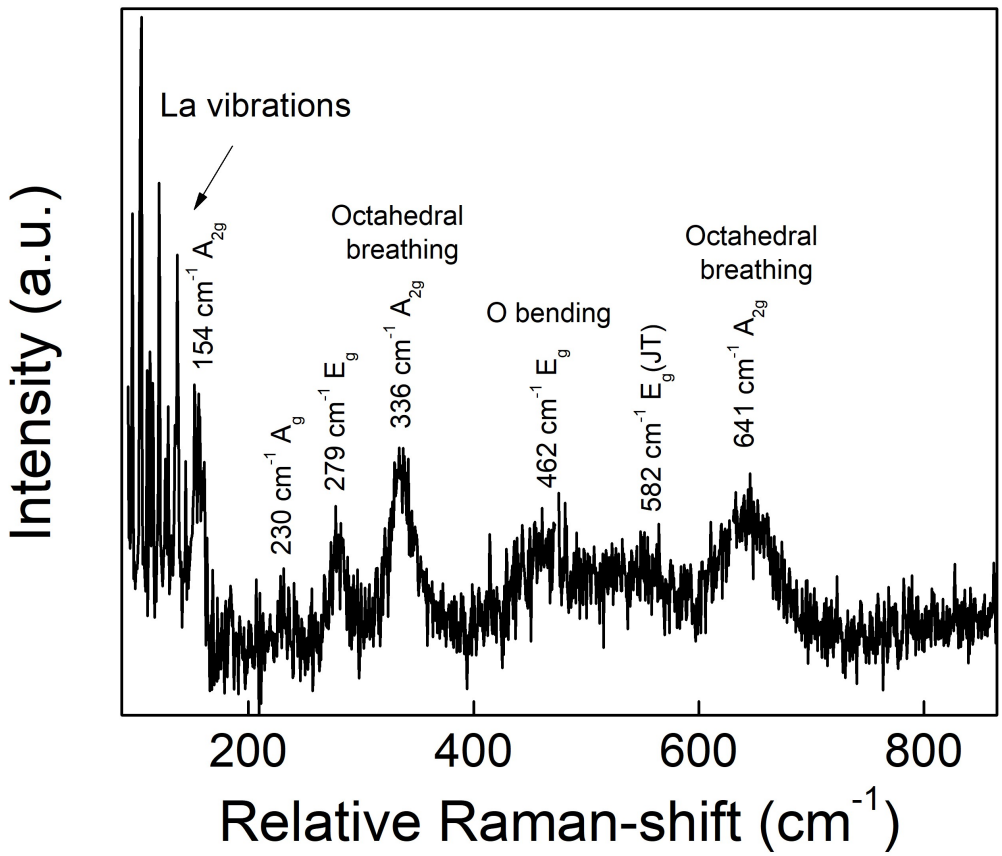

Figure 3.4 *Ambient temperature and pressure Raman spectrum of $LaCoO_3$ collected in the 100–800 cm^{-1} relative Raman-shift range (black line) with a laser power of 2 mW. Raman mode assignment is based on Raman work previously reported [199].*

$<200\,cm^{-1}$ are related to vibrations of lanthanum atoms. The broad peak found at $462\,cm^{-1}$ can be explained as an E_g oxygen bending vibration as assigned in previously reported studies [199, 204]. The peak at $582\,cm^{-1}$ is assigned as a Jahn-Teller E_g mode, and the broad peaks found at 154, 336, and $641\,cm^{-1}$ as A_{2g} breathing modes, in agreement with previously reported Raman studies [123, 199, 204]. These vibrational modes should be forbidden in this space group. The appearance of such modes is confirmed in our characterisation and is related to the local distortion of the structure. The predominance of the intermediate spin configuration for the trivalent cation at ambient temperature over the low and high spin state populations [123, 199, 204] promotes Jahn-Teller distortion of the e_g orbitals, which causes a local lowering of the crystal symmetry not detectable by crystallographic experiments. There is no clear evidence in Figure 3.4 of the A_{1g} mode observed in $LaCoO_3$ in other works at $232\,cm^{-1}$ which is associated to the out-of-phase tilting of the CoO_6 octahedra [199]. However, a weak band is present in the Raman spectrum and a Gaussian curve fit yields a central position of $230\,cm^{-1}$ in agreement with the previously suggested position of the A_{1g} mode.

3.2.3 High-pressure and high-temperature neutron diffraction

Neutron-diffraction experiments were performed in the 0–6 GPa pressure range at temperatures of 120, 290 and 480 K on the PEARL instrument at the ISIS Neutron and Muon Facility [158]. A variant of the V3 Paris-Edinburgh press model [159], which allows temperature control in the 120–500 K range, was used for the high-pressure measurements. The powder sample was loaded in an encapsulated Ti-Zr gasket with a piece of lead, which acted as pressure marker. A 4:1 perdeutareted ethanol-methanol fluid [163] was used as pressure transmitting medium. The gasket was placed between single-toroidal ZTA anvils. The variable temperature experiments were performed by the use of the high T/low T PE-press setup shown in Figure 2.9. The temperature of the sample is locally varied by a coil surrounding the anvils, where liquid nitrogen flows, and by eurotherm controlled in-built heater, while the overall body of the press is maintained at room temperature by a water bath. Neutron-diffraction patterns were collected for 1-2 h. Careful wavelength dependent intensity attenuation corrections have been applied on the collected patterns by the use of the in-house software Mantid [205]. Rietveld refinement of the neutron data was carried out by the use of the GSAS package [146].

3.3 Results

3.3.1 High-pressure neutron-diffraction structural characterisation

Representative neutron diffraction patterns acquired at 120, 290 and 480 K in the 0–6 GPa pressure range are shown in Figures 3.5, 3.6 and 3.7, respectively.

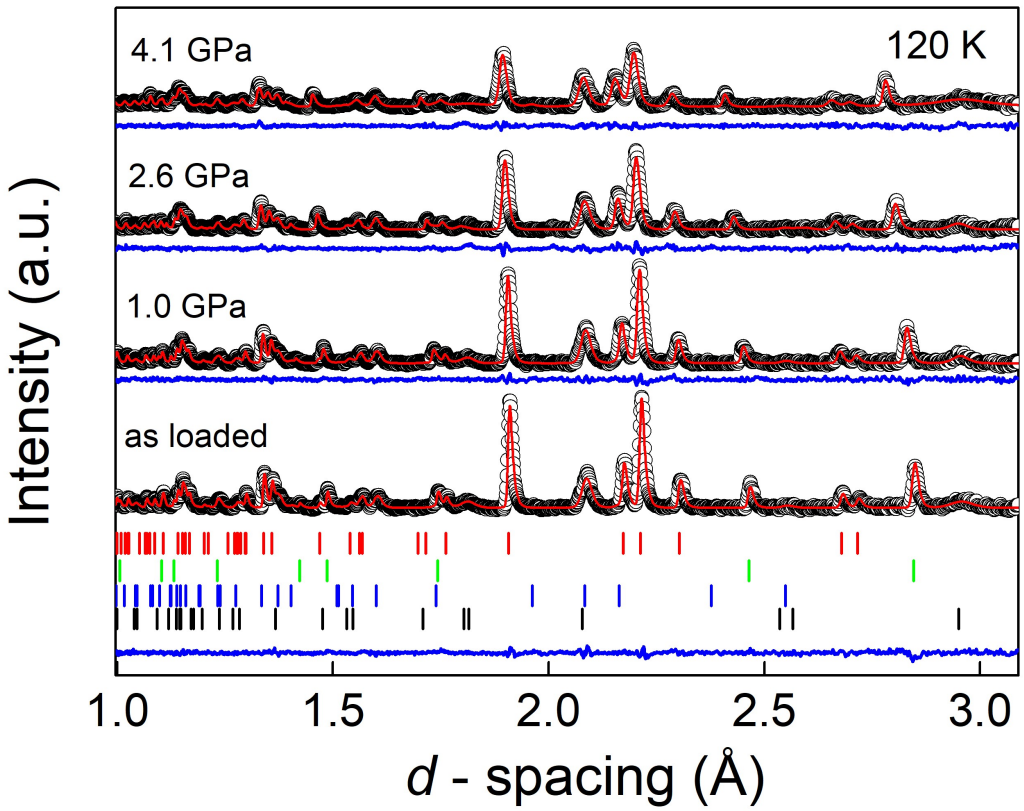

Figure 3.5 *Neutron diffraction patterns collected at 120 K at selected pressure points. Raw data are shown as open circles and the Rietveld refinement curves as solid red lines. Tick marks from sample and sample environment are also shown, from top to bottom: the $LaCoO_3$ sample, the pressure marker Pb, Al_2O_3 and ZrO_2 (from the anvils). Bottom blue lines show residual curves of the Rietveld fits.*

Open circles represent raw data, while red solid lines show Rietveld refinement curves to the neutron patterns. Tick marks from the sample and sample environment phases calculated reflections are also shown: from top to bottom, sample, lead, alumina and zirconia. The bottom blue trace represents the residual

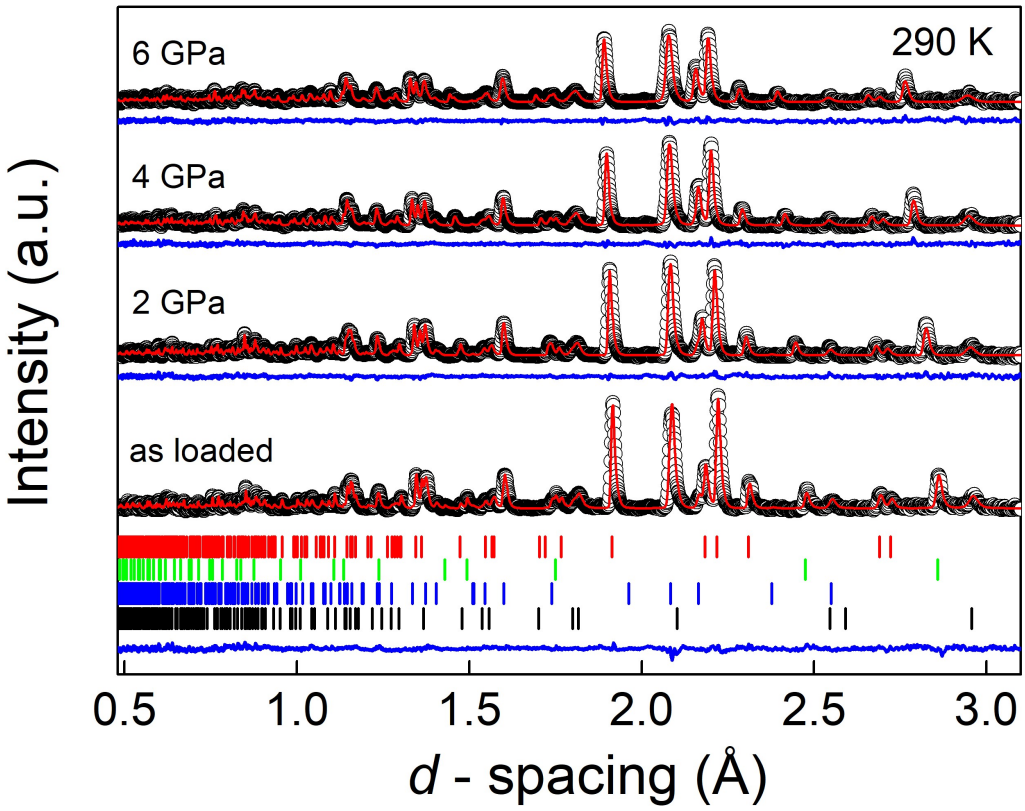

Figure 3.6 *Neutron diffraction patterns collected at 290 K at selected pressure points. Raw data are shown as open circles and the Rietveld refinement curves as solid red lines. Tick marks from sample and sample environment are also shown, from top to bottom: $LaCoO_3$, lead, Al_2O_3 and ZrO_2 (from the anvils). Bottom blue lines show residual curves of Rietveld refinements.*

of the refinement, calculated as difference between the measured and calculated profiles. The structure was refined adopting the trigonal $R\bar{3}c$ space group as previously reported [68, 84] in the rhombohedral setting for each temperature. The atomic positions adopted are: La $2b$ $\left(\frac{1}{4}, \frac{1}{4}, \frac{1}{4}\right)$, Co $2a$ $(0, 0, 0)$, and O $6e$ $\left(x, \frac{1}{2} - x, \frac{3}{4}\right)$. Neutron diffraction data report no evidence of phase transitions and the structure shows a stable trigonal $R\bar{3}c$ space group at each temperature and pressure range investigated. Tables A.1, A.2 and A.3 in Appendix A report refined and determined structural parameters and details of the Rietveld fits. A comparison of selected neutron diffraction patterns acquired at 120, 290 and 480 K at the pressure point of 4 GPa is also shown in Figure 3.8.

Figure 3.9 shows the pressure dependence of the unit-cell volume of $LaCoO_3$, which smoothly compresses at each temperature and no abrupt anomalies are

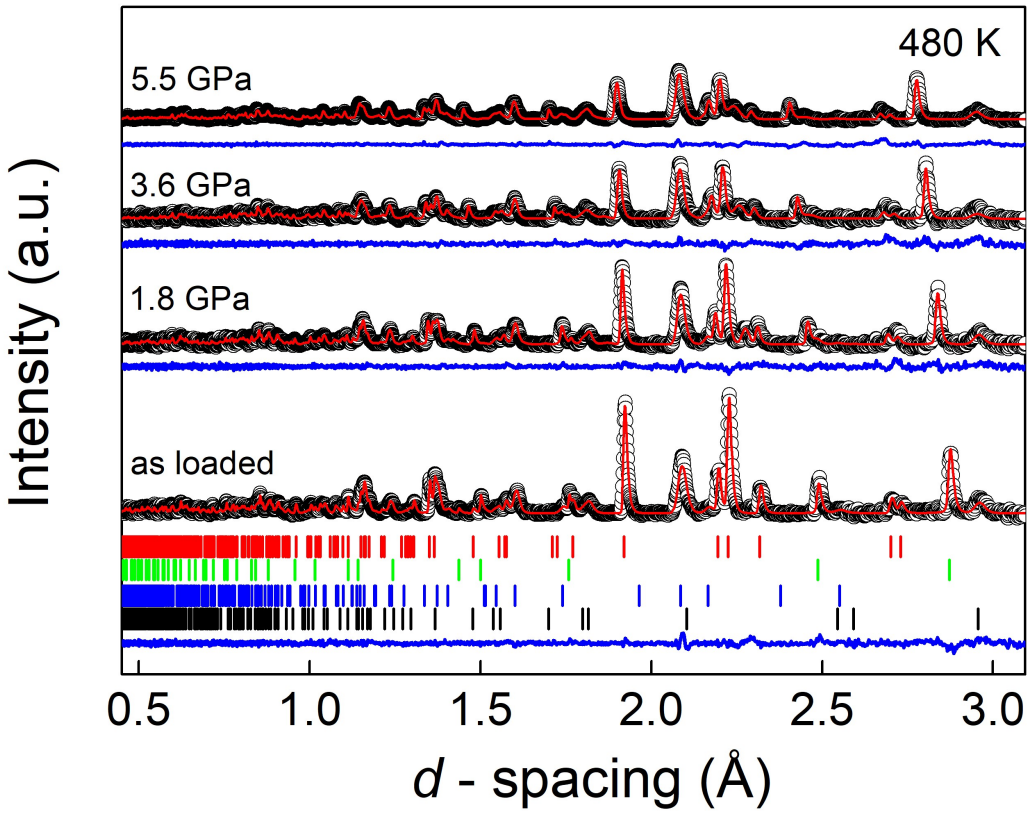

Figure 3.7 *Neutron diffraction patterns collected at 480 K at selected pressure points. Raw data are shown as open circles and the Rietveld refinement curves as solid red lines. Tick marks from sample and sample environment are also shown, from top to bottom: the $LaCoO_3$ sample, the pressure marker Pb, Al_2O_3 and ZrO_2 (from the anvils). Bottom blue lines show the residual curves of the refinements.*

found, hence confirming the stability of the rhombohedral symmetry in this compound.

The bulk modulus of $LaCoO_3$ at the three different temperatures was determined by fitting a second-order Birch-Murnaghan equation of state by the use of the EosFit software [206]. Fitted values are reported in Table 3.1. The fitted ambient temperature values of B_0 are lower than reported from previous studies 165(5) GPa [123], and 150(2) GPa [124], though slightly higher than 122(3) GPa as reported in [79]. The large variation within these values may be a result of the limited number of pressure points collected in these studies. Although a less compressible structure is conventionally expected upon cooling, the bulk modulus of $LaCoO_3$ does not change from the ambient to the low temperature measurements.

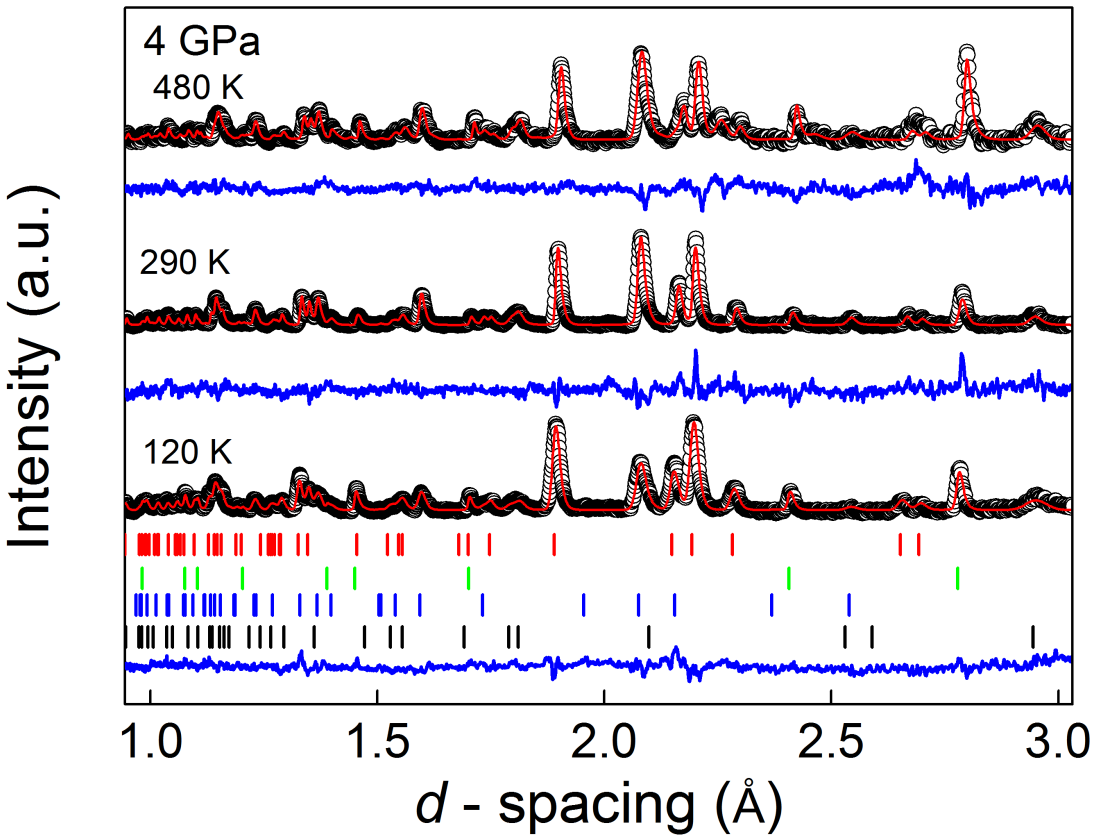

Figure 3.8 *Neutron diffraction patterns of $LaCoO_3$ collected at $P = 4$ GPa at $T = 120$, 290, and 480 K. Experimental data are shown as open circles, the refined profiles as red lines, and the residual difference curves as blue lines. Tick marks from sample and sample environment are also shown, from top to bottom: the $LaCoO_3$ sample, the pressure marker Pb, Al_2O_3 and ZrO_2 (from the anvils).*

Table 3.1 *Bulk modulus (B_0) and ambient pressure volume (V_0) of $LaCoO_3$ determined with a second-order Birch-Murnaghan EoS at the selected temperatures of 120, 290 and 480 K. Fitting curves are shown in Figure 3.9*

T (K)	B_0 (GPa)	V_0 (Å^3)	B_0 (GPa)		
120	134(2)	111.01(2)			
290	135(1)	112.12(1)	150(2)[124]	165(5)[123]	122(3)[79]
480	111(1)	113.38(1)			

Figure 3.10 displays the behaviour of the unit-cell angle at 120 (diamonds), 290 (filled squares) and 480 K (circles) in the 0–6 GPa pressure range.

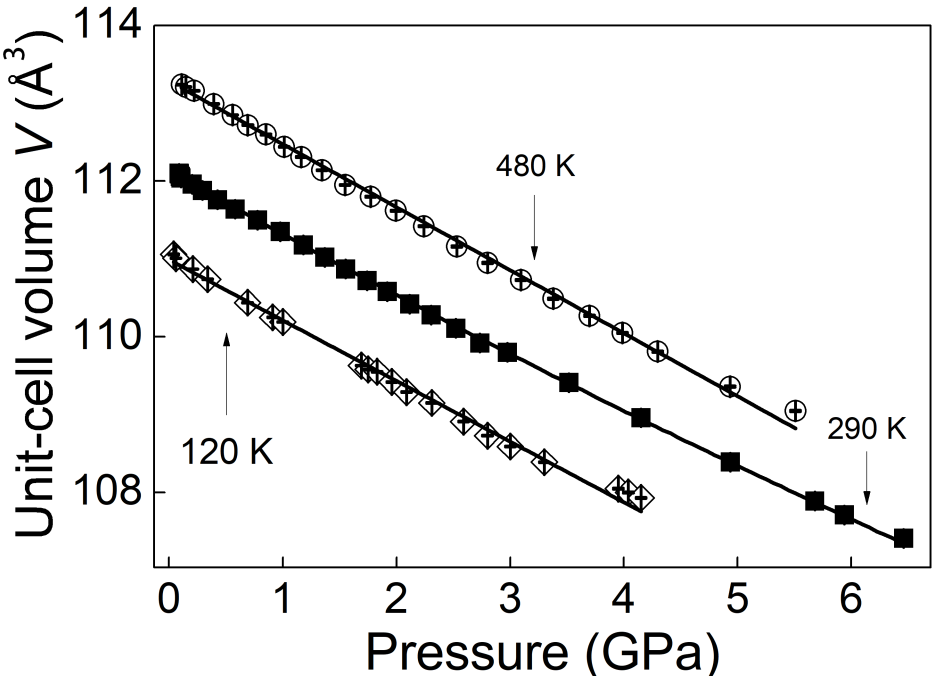

Figure 3.9 *Unit-cell volume as a function of pressure at 120 K (diamonds), 290 K (filled squares) and 480 K (circles). Solid lines show fits to data with a second-order Birch–Murnaghan equation of state. The B_0 and V_0 fitting values are reported in Table 3.1. Error bars are shown but smaller than symbols.*

The extrapolated ambient pressure values are $\alpha_0(120\,K) = 60.89(1)°$, $\alpha_0(290\,K) = 60.80(1)°$ and $\alpha_0(480\,K) = 60.66(1)°$ in agreement with previously reported values for $LaCoO_3$ [68, 187]. As a function of pressure α is seen to increase at each temperature in contrast to the temperature dependent trend previously investigated [68, 187], where the rhombohedral angle is seen to linearly decrease in the 4–1000 K temperature range. The magnitude of increase of the unit-cell angle at low temperature is found higher than at ambient and high temperature. The compression of $LaCoO_3$ at high and ambient temperature is mostly accommodated by the reduction in the unit cell length, while at low temperature is expressed by the unit-cell length and a simultaneous increase in the rhombohedral angle, hence a rhombohedral distortion of the lattice.

The compression of the unit-cell lattice parameter was also analysed at each temperature and is shown in Figure 3.11. At each temperature the lattice constant exhibits a linear decrease in the pressure range investigated. A linear fit to the

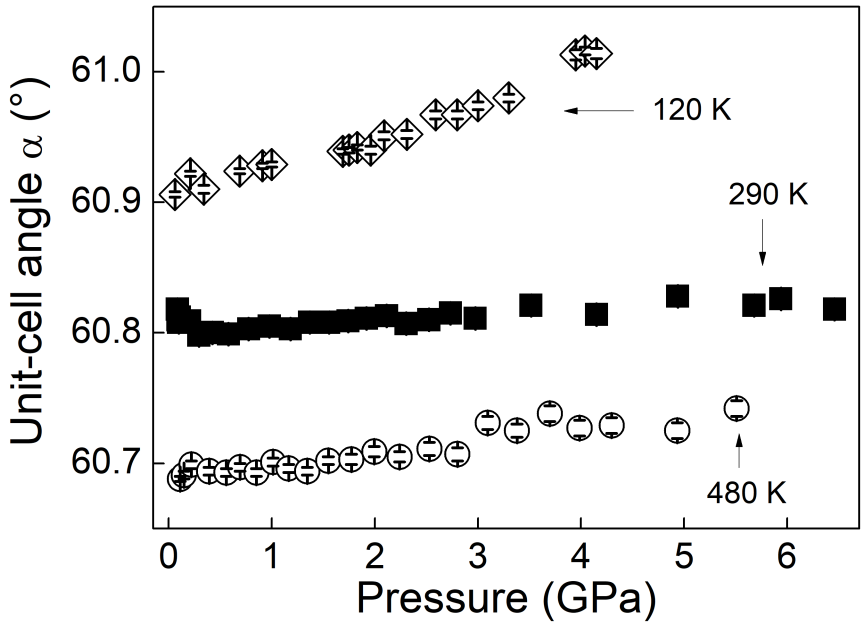

Figure 3.10 *Unit-cell angle of $LaCoO_3$ as a function of pressure at 120 (diamonds), 290 (filled squares) and 480 K (circles). Error bars are also shown.*

data was performed and the rates of compressibility k_a calculated as:

$$k_{\mathrm{a}} = -\frac{1}{a_{P=0}}\frac{da(P)}{dP}. \tag{3.1}$$

Their values are reported in Table 3.3. The rate of compression at ambient temperature is in agreement with what was previously reported [123]. However, k_{a} does not change on warming up or cooling down the sample. At 120 K the lattice parameters reduces with the same magnitude as the softer 480 K structure.

To study the structural-electronic relationships in $LaCoO_3$ an analysis of the bond-distances Co–O and La–O behaviours with increasing pressure was also performed. The bond distances pressure and/or temperature evolution are suggested to be indicative of the spin state transitions in $LaCoO_3$ and several anomalies in the pressure and temperature dependent evolutions have been observed in the bond lengths [68, 124]. Figure 3.12 shows the Co–O bond distance variation as a function of pressure at each temperature determined in the current work. Ambient pressure values were determined by a linear fit to the data and reported in Table 3.2

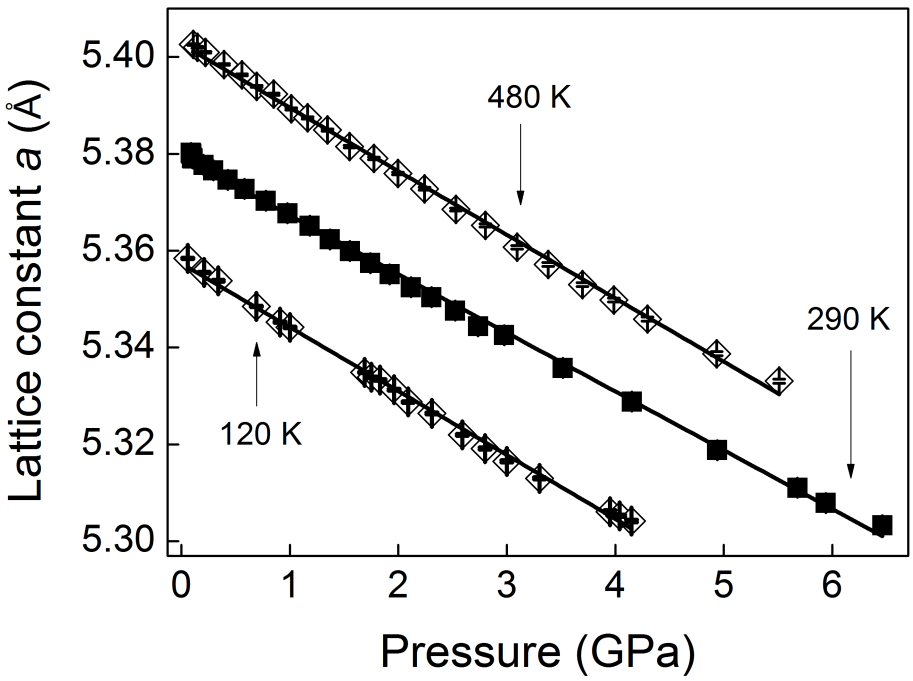

Figure 3.11 *Unit-cell lattice parameter a of $LaCoO_3$ as a function of pressure at 120 (diamonds), 290 (filled squares) and 480 K (circles). Solid lines show linear fits to the data (see main text for details). Error bars are also shown.*

A discontinuity in the pressure behaviour of the Co–O bond distance at 4 GPa and ambient temperature was previously reported by X-ray diffraction [124] and shown in Figure 3.13. This anomaly was interpreted as a manifestation of the pressure-driven depopulation of the trivalent cobalt e_g orbitals. In this work, no anomalies are found in the bond pressure evolution at each temperature and the Co–O bond distances decrease linearly in the pressure range investigated. The rates of compression have been calculated and reported in Table 3.3. The calculated value at ambient temperature $k_{Co–O}$ is in agreement within experimental error with the previously reported value by neutron diffraction of $0.0024(3)\,GPa^{-1}$ [123]. However, the behaviour presented in this current work is different from the previous high-pressure X-ray study at ambient temperature, where $k_{Co–O}$ is shown to exhibit different values before and after the transition pressure of 4 GPa: 0.0045(2) and $0.0012(1)\,GPa^{-1}$, respectively.

In the current $LaCoO_3$ study, the compressibility is also shown to remain unchanged at the investigated temperatures. If the evolution of the Co–O distance is indicative of the Co spin-state, then a larger difference in their rates

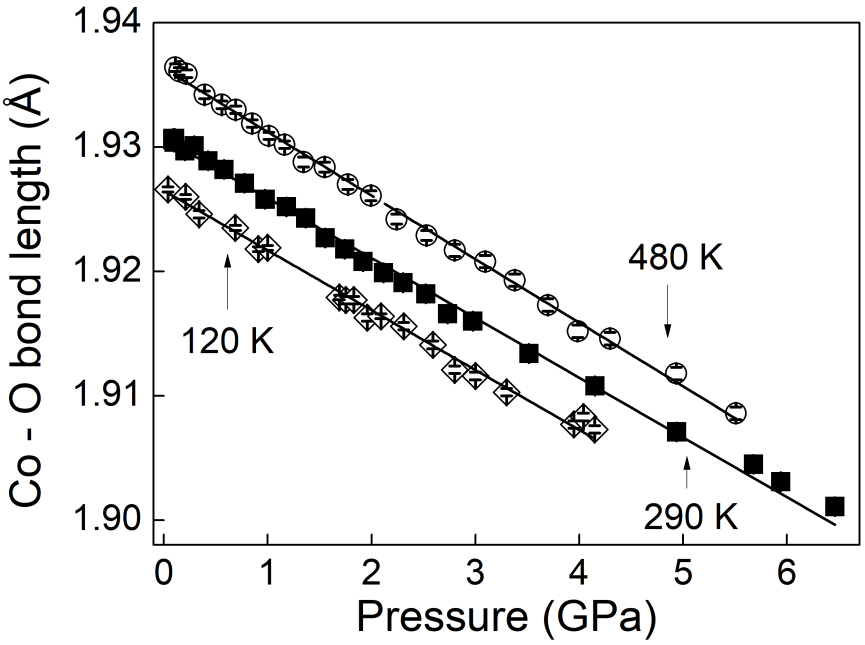

Figure 3.12 *Co–O bond lengths as a function of pressure at 120 K (diamonds), 290 K (filled squares) and 480 K (circles). Black lines indicate linear fit to the data, which yielded intercepts and compressibility rate values reported in Tables 3.2 and 3.3. Error bars are smaller than symbols.*

Table 3.2 *Ambient pressure values of Co–O, La–O1,2,3 bond distances, and Co–O–Co bond angle at 120, 290 and 480 K determined by a linear fit to the data.*

Temperature (K)	120	290	480
$Co–O_{P=0}$ (Å)	1.9262(4)	1.9035(1)	1.9362(1)
$Co–O–Co_{P=0}$ (°)	163.75(6)	164.72(4)	165.15(7)
$La–O1_{P=0}$ (Å)	2.443(1)	2.465(1)	2.479(1)
$La–O2_{P=0}$ (Å)	2.6925(2)	2.7019(2)	2.7128(2)
$La–O3_{P=0}$ (Å)	2.987(1)	2.9788(8)	2.978(1)

of compression may be expected over the three temperatures measured. Figure 3.13 compares the Co–O bond length evolution at 290 K to previously reported neutron-diffraction [123] and X-ray values [124]. Although magnetisation [120], photoemission [196] and electrical measurements [207], show that this spin-state transition is promoted to higher temperatures by the application of pressure, no evidence for this was detected in the average Co–O bond distance in this work. A further confirmation of the structural pressure behaviour proposed in this work comes from the La–site behaviour under pressure. The $R\bar{3}c$ space group

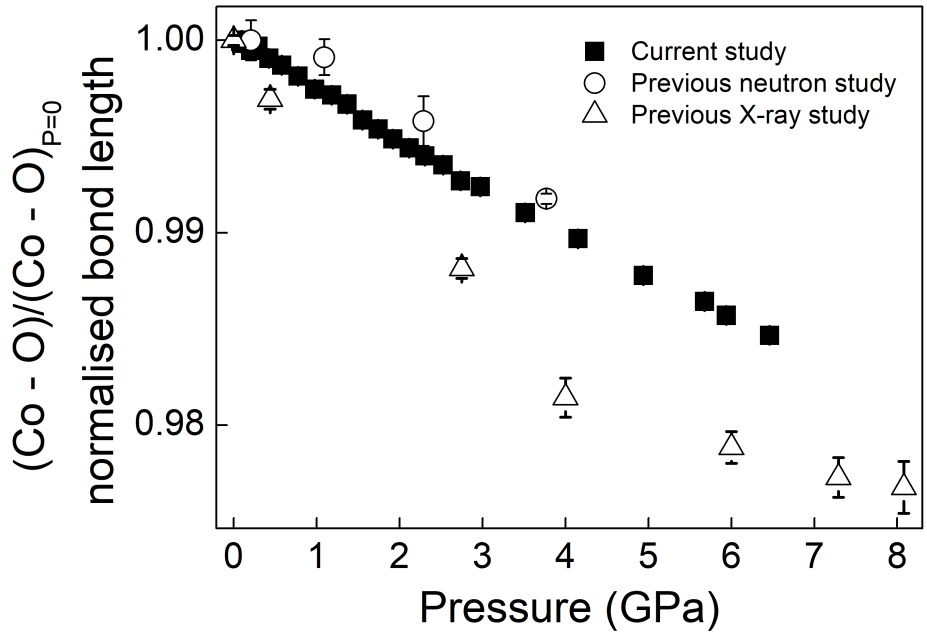

Figure 3.13 *Relative change in Co–O bond distance with pressure at 290 K. Values for the present and previously reported studies [123, 124] are shown for comparison. Error bars are smaller than symbols.*

Table 3.3 *Rates of compressibility of lattice parameter a, Co—O and La—O bond distances of $LaCoO_3$. Last column reports the compressibility rates calculated from the data in reference [124], showing one value for each pressure range 0–4/4–8 GPa where the discontinuity is observed.*

k (GPa^{-1})	120 K	290 K	480 K	290 K [124]
k_a	0.0024(1)	0.0022(1)	0.0024(1)	0.0020(1)
$k_{Co–O}$	0.0025(2)	0.0025(1)	0.0026(1)	0.0045(2)/0.0012(1)
$k_{La–O1}$	0.0012(2)	0.0008(1)	0.0006(2)	0.013(3)/0.010(2)
$k_{La–O2}$	0.0026(1)	0.0024(1)	0.0026(1)	0.0027(2)
$k_{La–O3}$	0.0030(2)	0.0033(2)	0.0037(2)	0.018(3)/0.006(2)

is characterised by a 12-fold coordination shell of the La cation, which comprises three groups of bonds (Figure 3.1): short (3×La–O1), intermediate (6×La–O2) and long (3×La–O3). Vogt *et al* [124] report the La–O bond lengths behaviour with increasing pressure at ambient temperature, and anomalies are reported at the transition pressure of 4 GPa in the La–O1,2,3 distances trends in agreement with the reported Co–O bond evolution. A previous high-temperature study reported three distinctive anomalies in the thermal evolution of La–O3, which were associated to magnetic transitions occurring as a function of temperature in $LaCoO_3$ [68]. Normalised pressure dependence of the short, intermediate and

long bonds determined in the current work are shown in Figure 3.14 at 120, 290 and 480 K. Ambient pressure values were determined by a linear fit to the data and reported in Table 3.2.

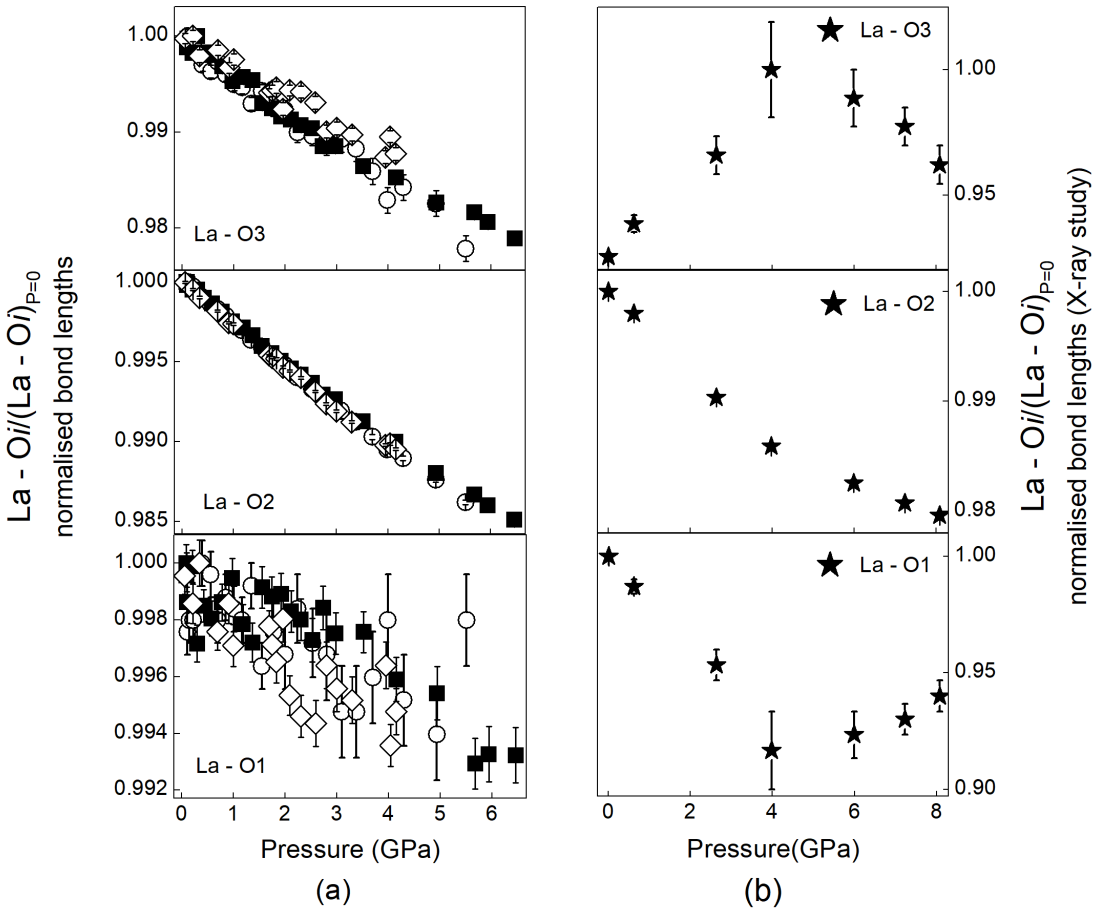

Figure 3.14 *1.14a Pressure dependence of the normalised La–O1,2,3 bond lengths at 120 (diamonds), 290 (filled squares) and 480 K (circles). 1.14b La–Oi normalised bond lengths as a function of pressure determined from values reported by X-ray diffraction [124]. Error bars are also shown, if not visible smaller than symbols. Note the small variation found for the short La–O1 bond from data reported in this work by neutron diffraction.*

The shortest bond La–O1 does not show any significant variation in the pressure

range investigated at each temperature. The intermediate and long bond distance exhibit a linear decrease in the pressure range studied at each temperature and no discontinuities were found in their behaviours under hydrostatic pressure. This behaviour is in contrast with that observed by X-ray diffraction [124], where the La–O3 bond is seen to decrease up to 4 GPa and to increase after the transition pressure. A specular trend is also observed for the short La–O1 bond distance, which is seen to increase up to 4 GPa and to decrease beyond this point, as shown in Figure 3.14b. Calculated rates of compressibility are reported in Table 3.3.

Another indicative parameter of the electronic configuration of $LaCoO_3$ is the inter-octahedral angle Co–O–Co. The ambient temperature X-ray study by Vogt *et al* [124] reports a discontinuous behaviour in the compression trend of the Co–O–Co bond angle at 4 GPa. The inter-octahedral angle is seen to increase up to 4 GPa, whereas it decreases beyond this pressure value.

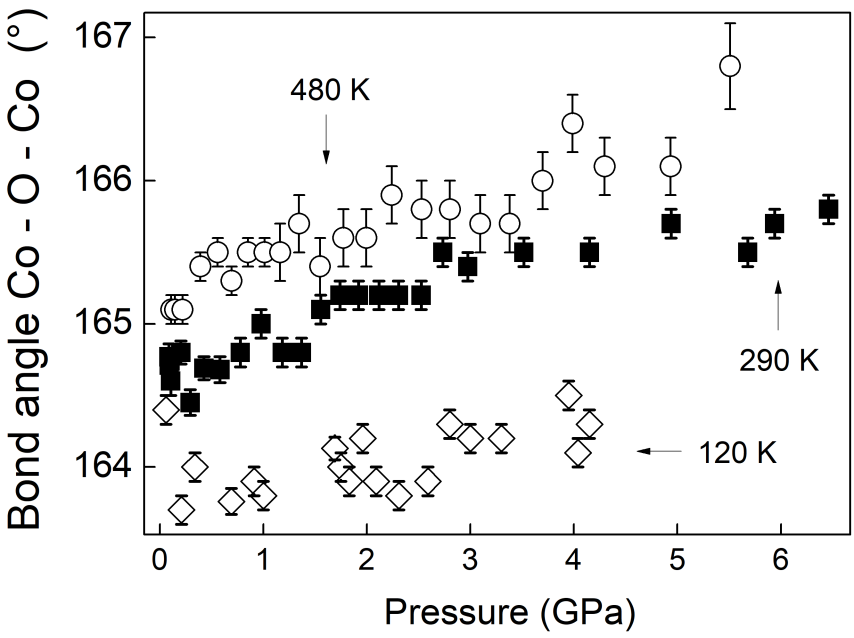

Figure 3.15 *Co–O–Co inter-octahedral bond angle variation as a function of pressure at 120 (diamonds), 290 (filled squares) and 480 K (circles). Error bars are also shown.*

In contrast, the Co–O–Co angle is seen to increase in the 0–6 GPa range at each temperature as shown in Figure 3.15. Ambient pressure values were determined by a linear fit to the data and reported in Table 3.2.

Values of Co–O, La–O1,2,3 bond lengths and Co–O–Co bond angles are reported

in Tables A.1, A.2 and A.3 in Appendix A. The lack of agreement between these two works may be partly related to the sample synthesis history of the perovskite sample, and in the difference in technique used to perform these studies. Neutrons are more sensitive to light atoms, such as oxygen atoms, than X-ray radiation and provide precise determination of the oxygen positions, which is essential to obtain accurate structural parameters such as Co–O and La–O bond lengths. Furthermore, the discontinuity found in the X-ray study [124] may be ascribed to freezing of the pressure transmitting medium during the experiment, which typically affects the hydrostatic compression of a material by a discontinuous decrease in its compression rate.

3.3.2 Octahedral tilt and strain under high pressure

The pressure dependence of the tilting angles at 120, 290 and 480 K calculated according to Equation 1.6 is shown in Figure 3.16.

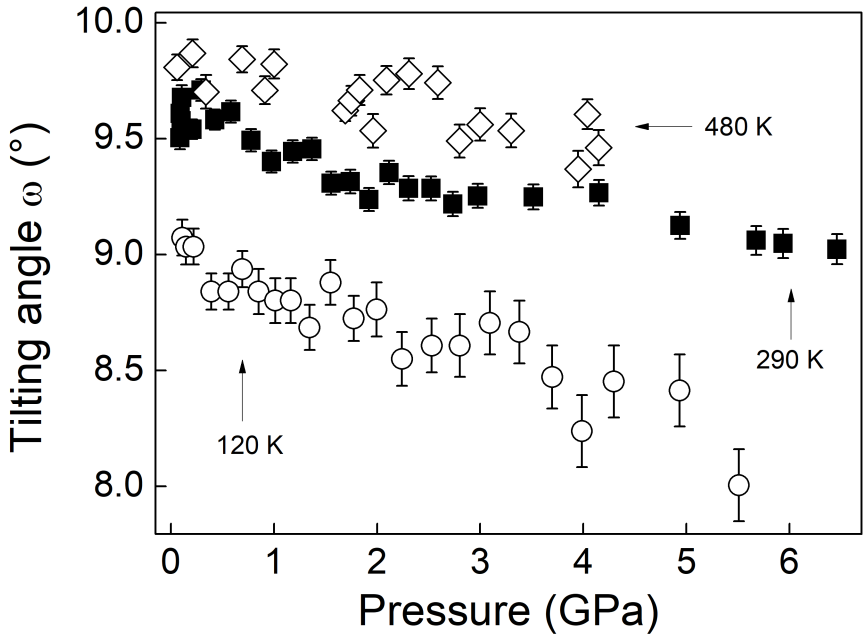

Figure 3.16 *$LaCoO_3$ tilting angle (ω) as a function of pressure at temperatures of 120 (diamonds), 290 (filled squares) and 480 K (circles). Error bars are also shown.*

The fitted ω_0 values are in agreement within experimental error with values previously reported for $LaCoO_3$ [124, 187]. At high temperature the structure

shows the smallest octahedral distortion with a value $\omega \sim 9°$, which is $\sim$0.7/0.8° lower than the tilting calculated at ambient and low temperature. The tilting angle decreases as a function of hydrostatic pressure at each temperature. At high and ambient temperature the tilt decreases significantly more than at low temperature, where the tilting distortion reduces by only $\sim 0.3°$. The structural compression of $LaCoO_3$ proceeds by combined reduction of the unit-cell parameter and tilting angle at 290 and 480 K, while at 120 K the structural compression is mostly driven by the reduction in the unit-cell parameter. The low variation in the tilting angle at 120 K explains the increase of the unit-cell angle to accommodate the structural compression induced by the application of hydrostatic pressure (Figure 3.10).

$LaCoO_3$ is characterised by strain of the octahedra (ζ), which can be quantified for the $R\bar{3}c$ space group along the cubic triad axis by the strain parameter ζ as defined in Equation 1.7. The evolution of the octahedral strain of $LaCoO_3$ as a function of pressure at 120 (diamonds), 290 (squares) and 480 K (circles) is shown in Figure 3.17.

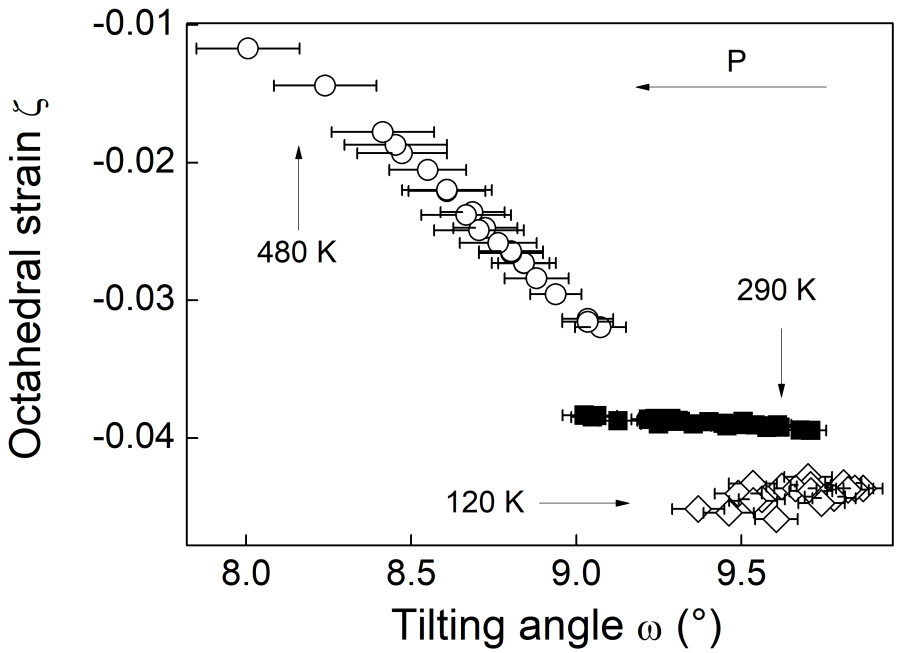

Figure 3.17 *$LaCoO_3$ octahedral strain (along the [111] cubic crystallographic direction) as a function of tilting angle (ω) at temperatures of 120 (diamonds), 290 (filled squares) and 480 K (circles).*

At each temperature the octahedra compress along the [111] crystallographic cubic direction, but their evolution upon pressure is found to be different. At low

temperature the octahedral strain slightly increases upon compression, whereas at ambient and high temperature the strain distortion decreases but at a significantly different rate. At 480 K the strain distortion exhibits a strong dependence on pressure and strongly reduces upon compression. The overall reduction of the tilting angle and strain as a function of pressure suggests that the structure is tending towards the ideal cubic symmetry, with the CoO_6 octahedra tending to an ideal undistorted geometry. However, this is less evident in the structure at 120 K, where both the tilting angle and the rhombohedral unit-cell angle increase in the 0–4 GPa pressure range.

As previously discussed in Chapter 1, an alternative way to describe structural distortions of perovskites is to consider the magnitudes of the orthogonal, symmetry-adapted basis-vectors of the aristotype cubic phase [78]. The anti-phase tilting system, which energetically promotes the rhombohedral symmetry from the parent $Pm\bar{3}m$, is associated to a unique symmetry-adapted mode classified as R_4^+.

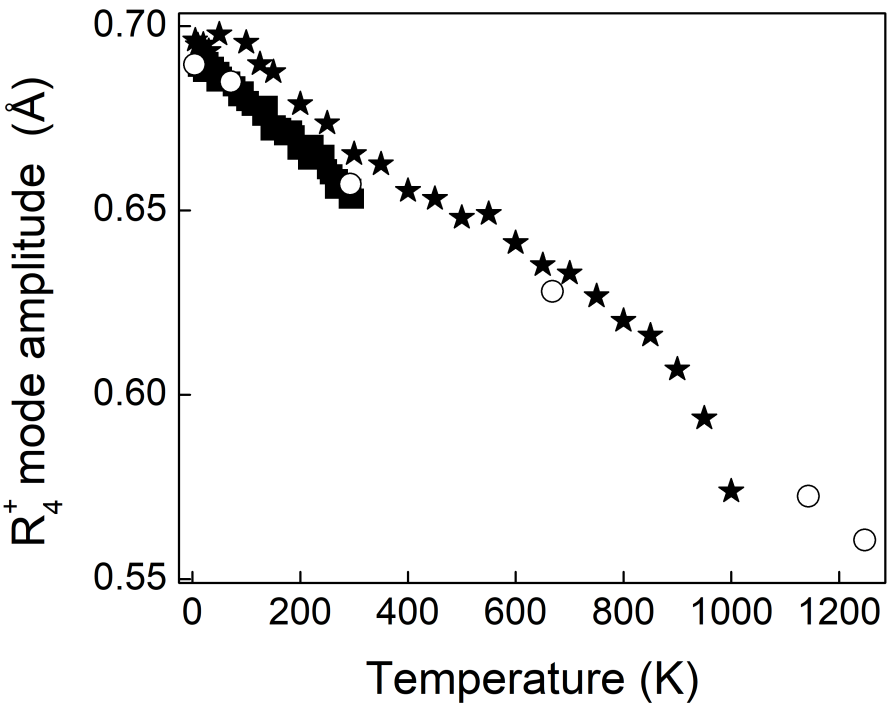

Figure 3.18 *Temperature evolution of the R_4^+ mode amplitude calculated from previously reported temperature dependent crystal structure data: filled squares 4–300 K temperature range [187]; stars 4–1000 K range [68] and circles up to 1248 K [84]*

.

From the neutron-diffraction temperature dependent data of $LaCoO_3$ [68, 84, 187] the amplitude of the R_4^+ mode was determined in the 4–1248 K temperature range by the use of the software ISODISTORT [103], and plotted in Figure 3.18. The trend behaviour calculated from [187] (filled squares) shows a linear decrease in the 4–300 K range and is in good agreement with the behaviour determined from [84] (circles), where the R_4^+ amplitude is found to linearly decrease in the 4–1248 K range, but only six data points were collected. The behaviour reported by Radaelli and Cheong [68] (stars) shows a sudden drop from the linear trend at T >800 K. However, the same anomaly is not found in the work by Thornton (circles) [84]. All trends support the picture of $LaCoO_3$ tending with increasing temperature to an ideal cubic geometry, which will be driven by the decrease of the octahedral tilting distortion.

Low, ambient and high temperature determined lattice parameters and fractional coordinates of $R\bar{3}c$ $LaCoO_3$ were decomposed in the current work as a function of pressure and the R_4^+ mode amplitude variation in the 0–6 GPa pressure range is shown in Figure 3.19.

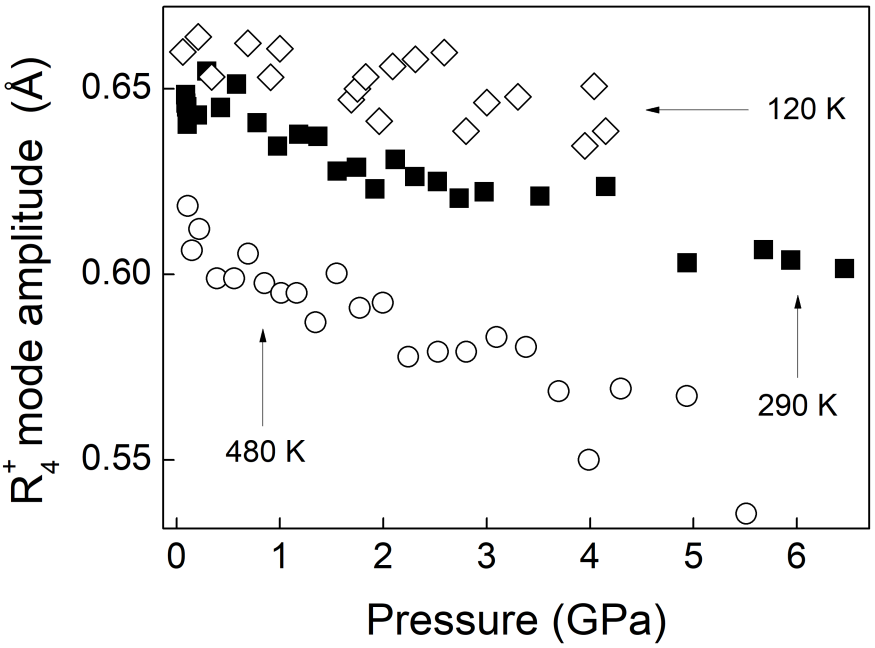

Figure 3.19 *R_4^+ symmetry-adapted-mode amplitude as a function of pressure at temperatures of 120 (diamonds), 290 (filled squares) and 480 K (circles) calculated from neutron-diffraction data of the current work.*

At each temperature the R_4^+ mode amplitude decreases. The high temperature

data show the strongest tilting reduction with increasing pressure. The decreasing rate of the amplitude mode at 120 K is observed significantly lower than at 290 and 480 K. This result is consistent with the tilting angle behaviours shown in Figure 3.16 and with the compression behaviour reported in the current work. The octahedral tilting decreases as a function of hydrostatic pressure and will promote a higher symmetry phase for $LaCoO_3$ at 290 and 480 K..

3.4 Summary and conclusions

The neutron-diffraction study reported in this chapter has investigated the structural properties of $LaCoO_3$ and changes within its crystal structure in response to application of pressure and temperature. The lack of consensus on the structural-magnetic property relationships in $LaCoO_3$ has motivated the current work. The choice of the low and high temperature phase is related to the spin state transitions which were reported in this material as a function of temperature at 100 and 500 K [68].

$LaCoO_3$ preserves a stable rhombohedral $R\bar{3}c$ space group in the 0–6 GPa range at 120, 290 and 480 K. The application of pressure increases the rhombohedral distortion of the lattice as observed by the unit-cell angle behaviour, which increases at each temperature in particular in the low temperature phase. The degree of distortion of trigonal $LaCoO_3$ in terms of tilting angle and octahedral strain was also studied. These distortion parameters decrease under the application of hydrostatic pressure. The CoO_6 octahedra tend to the ideal undistorted geometry characterising the cubic parent structure.

To deepen our understanding of the structural-electronic properties of $LaCoO_3$, the Co–O and La–O1,2,3 bond distances were accurately determined. The chemical bond distances show a linear decrease at each temperature in the pressure range studied. No manifestation of the electronic configuration of $LaCoO_3$ is seen in the structural behaviour in contrast with previously reported works under high pressure [124] or temperature [68]. No structural evidence of the pressure-driven electronic depopulation of the e_g orbitals at 4 GPa is found in the structural parameters variation determined in the current work. The discrepancy with the results reported in the previous X-ray work is caused by the different technique used in the current study. Neutron diffraction provides a better accuracy in the refinement of oxygen positions and determination of related

structural parameters such as the Co–O bond lengths, which can be calculated with a precision that X-ray diffraction cannot guarantee. Furthermore, the X-ray diffraction data behaviour may resemble the typical behaviour manifesting freezing of the pressure transmitting medium, which is typically seen as a discontinuous change in the sample compressibility rate. These elements stress the reliability of the measurements reported in this work.

Chapter 4

High pressure study of $LaFeO_3$

This chapter reports the structural and spectroscopic study under extreme conditions carried out on the $LaFeO_3$ material. Neutron-diffraction experiments were performed at pressures up to 16 GPa at ambient temperature, and up to 6.5 GPa at a temperature of 110 K. The equation of state of the sample is determined at each temperature and changes in the crystal structure are reported as a function of pressure and temperature. Accurate determination of structural parameters, bond lengths and angles, and tilting angles is reported and discussed. The study also reports the magnetic behaviour of the sample as a function of pressure. This structural study is complemented with high-pressure Raman spectroscopy and the vibrational properties of $LaFeO_3$ are discussed in relation to its crystal structure.

4.1 Background

$LaFeO_3$ has attracted interest because it is the parent compound of many iron-based oxide materials, which are extensively used in technological applications such as in fuel cell cathodes, optoelectronic devices, chemical sensors and catalysis [208–215]. This type of material has mainly drawn attention for its long-range G-type antiferromagnetism [208, 216–220], high piezoelectricity [221, 222], and dielectric properties [223, 224].

Structural and spectroscopic studies of $LaFeO_3$ were carried out in the past decades and different phases have been observed as a function of pressure or

temperature. At ambient conditions $LaFeO_3$ crystallises in the orthorhombic *Pbnm* space group [82, 225], and its crystal structure is depicted in Figure 4.1. $LaFeO_3$ is an antiferromagnetic material with a high Néel temperature ~740 K [219]. The long range magnetic order arises from super-exchange interactions between Fe^{3+} cations, in which a high-spin state $t_{2g}^3 e_g^2$ is populated.

As discussed in Section 1.4.2, the orthorhombic *Pbnm* symmetry is obtained by in-phase tilting of the octahedra around the z cubic direction and out-of-phase

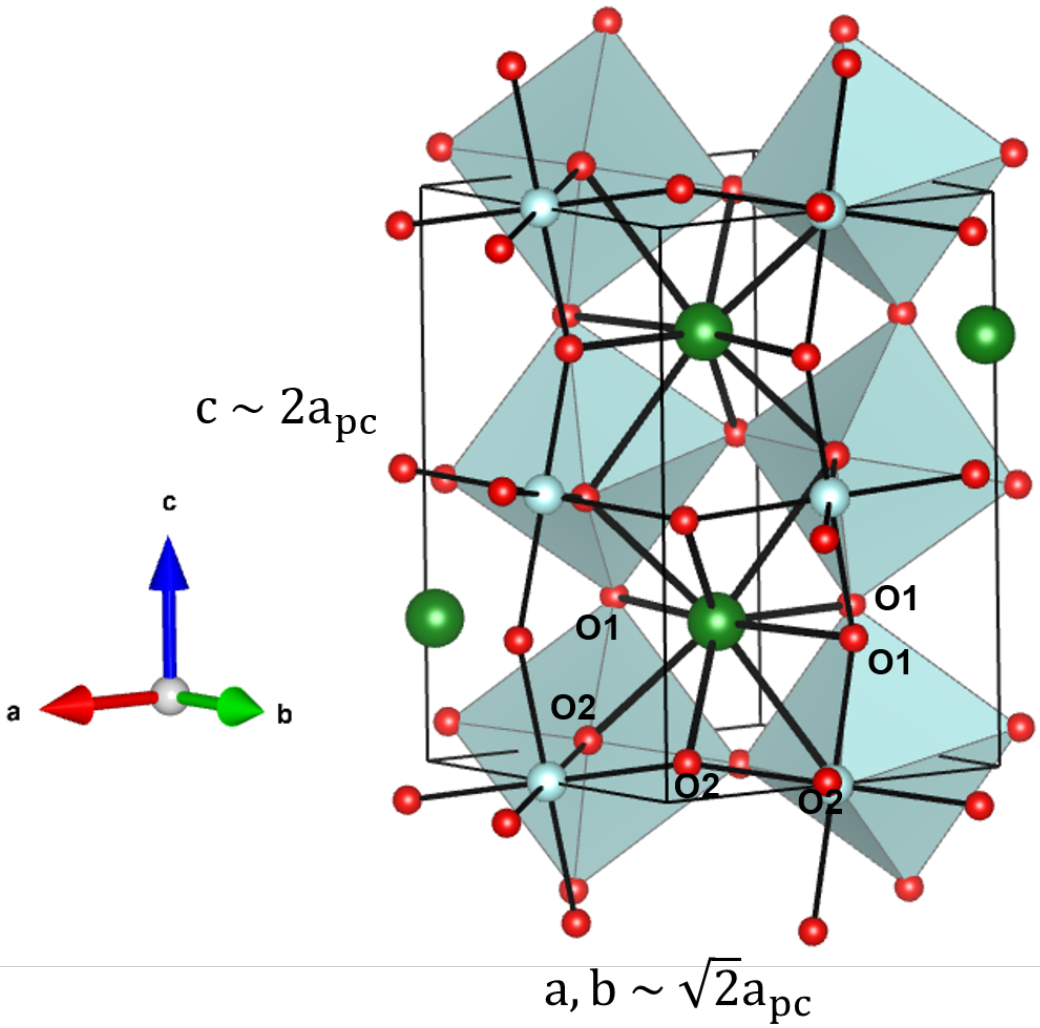

Figure 4.1 *Crystal structure of $LaFeO_3$ at ambient conditions. The unit cell is orthorhombic Pbnm, and is represented by the thin black line. Lanthanum, iron and oxygen atoms are depicted as green, light blue and red spheres, respectively. Atomic positions in the presented crystal structure are: La 4c $\left(x, y, \frac{1}{4}\right)$; Fe 4b $\left(0, \frac{1}{2}, 0\right)$; O1 4c $\left(x, y, \frac{1}{4}\right)$ and O2 8d (x,y,z). Front FeO_6 octahedra are not shown for clarity. Lanthanum atoms are coordinated by nine oxygen atoms, which give rise to three distinct La–O1 bonds, and three distinct double-degenerate La–O2 bonds.*

tilting around the x and y directions of equivalent magnitude. The octahedra are not regular as in the case of $LaCoO_3$ and by symmetry two distinct oxygen crystallographic positions are identified. This gives rise to three independent Fe–O bond distances: two degenerate Fe–O1; two equatorial degenerate Fe–O2 and Fe–O2′, where O2′ indicates the longer and O2 the shorter bond length, respectively. The tilting of the octahedra and non-regularity of the Fe–O distances decrease the La–site coordination in general from twelve to eight: three distinct double degenerate La–O2 bonds and two distinct La–O1 bonds. An X-ray diffraction study of $LaFeO_3$ suggests a higher coordination number for the La–site [225], which is reported to be less distorted than in other $Ln FeO_3$ compounds (Ln = rare-earth atom). This promotes a third La–O1 bond length to form. Upon warming the compound exhibits a first-order transition to $R\bar{3}c$ symmetry at ∼1228 K and to cubic $Pm\bar{3}m$ at 2140 K, as reported by X-ray and neutron diffraction experiments [104, 226].

At high pressure, an X-ray diffraction study reports a second-order structural transition to body-centred *Ibmm* space group at a pressure of 21.1 GPa [113], but no high-pressure neutron-diffraction crystallographic analysis has been performed to-date which could complement such study. In the current thesis the high-pressure structure of $LaFeO_3$ is determined by neutron diffraction and changes within this such as the octahedral tilting and bond distances/angles upon pressure are reported. This study uses neutron diffraction to accurately determine the oxygen fractional coordinates and thereby the octahedral tilting of $LaFeO_3$ under high pressure with the aim to investigate possible phase transitions. This will give insight in the spectroscopic-structural property relationship in this important compound.

4.2 Experimental

4.2.1 Material synthesis and characterisation

A phase-pure sample of polycrystalline $LaFeO_3$ was prepared using the nitrate decomposition method described in Section 2.11. Stoichiometric amounts of $La(NO_3)_3 6H_2O$ and $Fe(NO_2)_3 9H_2O$ (Sigma-Aldrich, 99.99%) were completely dissolved in distilled water. The water was removed by evaporation at 350 K over two hours. The resulting gel was decomposed at 870 K overnight and the

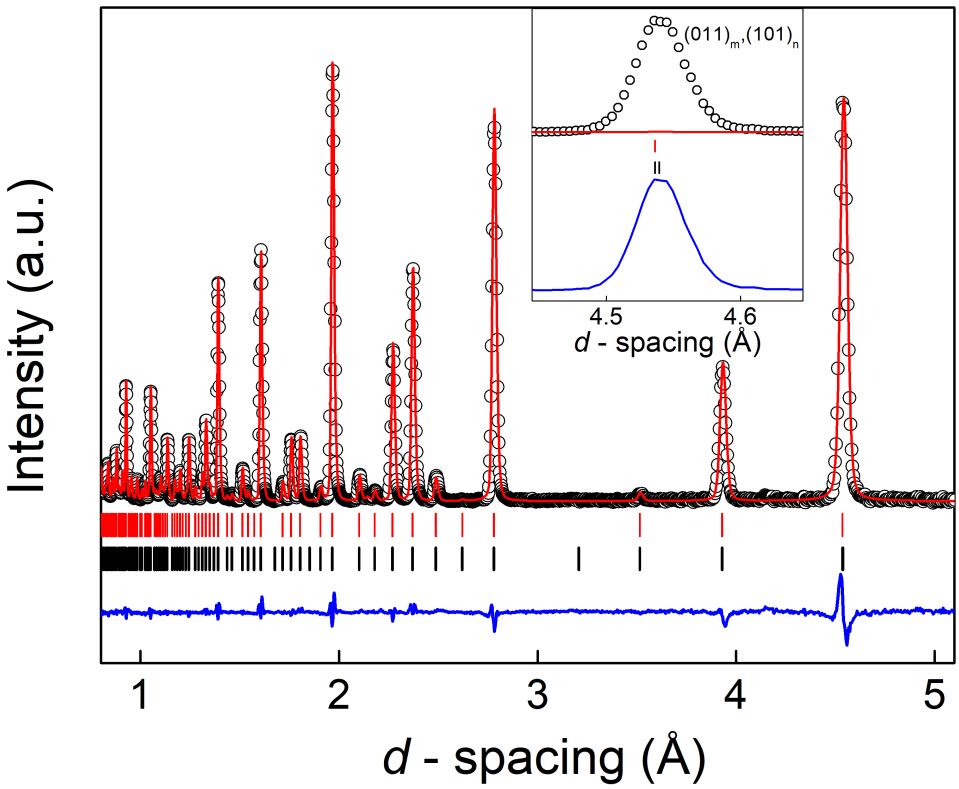

Figure 4.2 *Neutron diffraction pattern of $LaFeO_3$ collected at ambient temperature and pressure on the POLARIS diffractometer (open circles). Red line shows Rietveld refinement of the structure, while bottom blue line denotes the residual of the Rietveld fit. Vertical tick marks indicate calculated positions of nuclear Pbnm (top, red) and magnetic Pb'n'm (bottom, black) phase reflections. Inset shows a zoom of the 4.54 Å reflection when only the nuclear phase of $LaFeO_3$ is used in the Rietveld refinement of the data.*

final grey powder was ground and pelletised. The pelleted sample was annealed in air at 1370 K for 12 h, followed by repeated grinding and annealing until a single-phase material was obtained. The phase purity was initially confirmed by X-ray diffraction characterisation using a D2 Bruker diffractometer. Further neutron-diffraction measurements carried out on the POLARIS diffractometer, at the ISIS facility, have confirmed the phase purity of the sample and enabled the determination of accurate structural parameters, fractional coordinates and magnetic moment of the sample. Approximately 1 g of powder sample was loaded in a 4 mm diameter vanadium can and placed at the instrument sample position. A neutron-diffraction pattern of the sample collected on POLARIS is shown in the 0.5–5 Å range in Figure 4.2 (open circles).

Table 4.1 *Refined and determined structural parameters, atomic fractional coordinates, bond lengths and magnetic moment of $LaFeO_3$ from Rietveld refinement of the neutron-diffraction data collected at ambient pressure and temperature on the POLARIS diffractometer.*

	Parameter	This Work	Previous work [104]
	V (Å^3)	242.765(3)	242.876(9)[113]
	a (Å)	5.55629(5)	5.5544(7)
	b (Å)	5.56208(5)	5.5659(7)
	c (Å)	7.85530(6)	7.8534(8)
Atom			
La	x	0.9937(2)	0.995(5)
	y	0.0294(1)	0.029(9)
	z	0.25	0.25
O1	x	0.0768(3)	0.07(53)
	y	0.4866(2)	0.48(42)
	z	0.25	0.25
O2	x	0.7188(1)	0.72(85)
	y	0.2810(1)	0.28(09)
	z	0.0381(1)	0.05(29)
	$\|\mu\|(\mu_B)$	3.72(1)	
	wR_p %	3.23	
	R_p %	5.25	
	χ^2	3.49	

Parameter	This Work	Previous work [225]
Fe–O1 (Å)	2.0111(4)	2.009(1)
Fe–O2 (Å)	2.002(1)	2.002(3)
Fe–O2'(Å)	2.003(1)	2.007(3)
La–O1 (Å)	3.057(2)	3.041(6)
La–O1 (Å)	2.585(2)	2.591(6)
La–O1 (Å)	2.377(4)	2.416(5)
2×La–O2 (Å)	2.467(2)	2.455(4)
2×La–O2 (Å)	2.667(2)	2.656(4)
2×La–O2 (Å)	2.793(2)	2.805(4)

The structure was refined with a *Pbnm* space group and a *Pb'n'm* magnetic space group with starting magnetic modulus of $4\mu_B$ with spin orientations to reflect a G_x (magnetic moments point along the x crystallographic direction) antiferromagnetic order as previously reported for this oxide [82, 104, 216, 226]. The starting fractional atomic positions used in the present refinement are: La $4c$ $\left(x, y, \frac{1}{4}\right)$; Fe $4b$ $\left(0, \frac{1}{2}, 0\right)$; O1 $4c$ $\left(x, y, \frac{1}{4}\right)$ and O2 $8d$ (x, y, z). Refined and determined structural parameters are consistent with previously determined crystal structures and are reported in Table 4.1.

Orthorhombic $LaFeO_3$ is distorted from the cubic aristotype by two independent octahedral tilts ϕ_{in} and ϕ_{out} as defined in Section 1.4.2 for the *Pbnm* space group. The in-phase and out-of phase tilting distortions of the FeO_6 octahedra were determined according to Equations 1.4 and 1.5, hence considering the displacements of the oxygen atoms from the cubic positions. The calculated values are $\phi_{in} = 7.091(1)^\circ$ and $\phi_{out} = 12.342(1)^\circ$. Attempts to determine the tilting angles by geometrical relations to the unit cell have led to underestimated values. The FeO_6 octahedra are not regular, but characterised by three distinct Fe–Oi distances, which produce a deformation of the octahedral edges, which must be taken into account for an accurate calculation of the tilting angle parameters. The orthorhombic distortion from the cubic symmetry is observed to conventionally reduce the A-site coordination number from twelve to eight. This is in general valid, but lower or higher coordination numbers can be found according to the ionic radii of the A and B elements, and their bond strengths. By the Rietveld refinement carried out in this work, nine first-nearest-neighbours have been found for the lanthanum which yielded: three distinct La–O1 bonds; three (double-degenerate) pairs of La–O2 bonds.

Neutrons possess a magnetic moment and neutron diffraction can probe the magnetic behaviour of the sample if long range magnetic order is present. This is the case of $LaFeO_3$, in which the Fe^{3+} moments are coupled antiferromagnetically across the structure by Fe^{3+}–O^{2-}–Fe^{3+} superexchange interactions as discussed in Section 1.8. This generates the superposition in the diffractogram of reflections, which are generated by the magnetic structure of the sample. The G-type long-range antiferromagnetic order in $LaFeO_3$ contributes strongly to the pattern with additional peaks arising from magnetic scattering. Among these, the intensity of the reflection at ~ 4.54 Å in Figure 4.2 is almost entirely magnetic in nature. This reflection arises from two main contributions: the nuclear (101) Bragg reflection and the magnetic (011) reflection. As shown in inset of Figure 4.2, the nuclear contribution to the intensity is negligible and this reflection can be used to acquire information on the magnetic nature of the sample. The Rietveld fit to the pattern is consistent with the G-type antiferromagnetic model previously reported for $LaFeO_3$ [216, 219, 220] and the refined modulus of the magnetic moment $|\mu| = 3.72(1)$ in Bohr magneton units has its highest contribution along the a direction, while the other magnetic components are negligible.

DC magnetometry measurements were also carried out and are consistent with previous experiments [219]. A 116 mg of sample mass has been loaded in a plastic

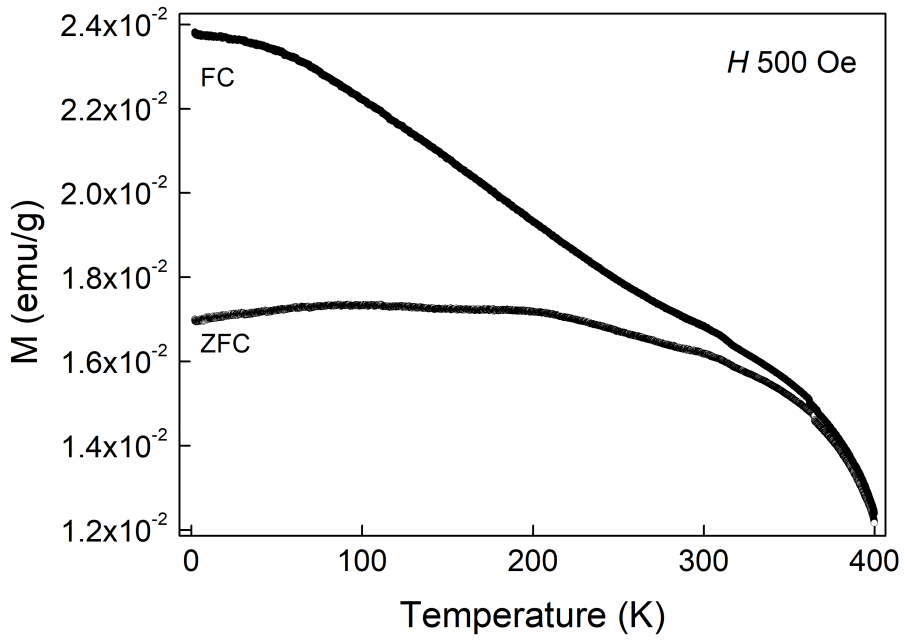

Figure 4.3 *Zero-field-cooling (ZFC) and field-cooling (FC) DC magnetisation measurements of $LaFeO_3$ in the 2–400 K temperature range at an applied magnetic field of 500 Oe.*

straw and placed in a Quantum Design MPMS-XL7 SQUID magnetometer at the Material Characterisation Laboratory at ISIS. Figure 4.3 reports representative zero-field-cooling (ZFC) and field-cooling (FC) DC magnetometry measurements collected in the 2–400 K range in an applied magnetic field of 500 Oe. It is well-know that the magnetisation of $LaFeO_3$ evolves so that a sharp magnetisation peak around 740 K is observed and ascribed as the Néel temperature of the material [219]. However, the low temperature behaviour of $LaFeO_3$ shows a behaviour more similar to a spin-glass-like structure. This is seen in Figure 4.3 where with decreasing temperature the ZFC and FC curves start to diverge around a temperature of 380 K. The FC magnetisation curve shows a sharp rise, while the zero-field-cooling one shows a characteristic broad increase, which resembles a ferromagnetic evolution. The difference in the two curves at low temperature suggests a short-range spin-glass-like magnetic order. This interaction occurs between local ferromagnetic and antiferromagnetic domains present in $LaFeO_3$.

4.2.2 Temperature dependent X-ray diffraction

Temperature dependent X-ray diffraction data were collected using a SmartLab Rigaku X-ray diffractometer at the Material Characterisation Laboratory at the ISIS facility. The diffractometer uses a Cu k_{α_1,α_2} radiation source equipped with a Ge(220)x2 monochromator to select the primary X-ray radiation k_{α_1}.

High-temperature X-ray diffraction data were collected from ambient to 1373 K in temperature steps of 100 K with a typical data collection time of 1 h 30 m. The sample was carefully flattened on an alumina disc holder. X-ray data were collected in the $2\theta = 20° - 80°$ range with a 20 mm×0.3 mm incident and collecting slits. Low temperature X-ray diffraction patterns were collected in the 15–300 K temperature range. The sample was cooled down to 15 K and gradually warmed up in temperature steps of 30 K. The sample was carefully flattened on a silicon disc holder. The same settings of slits, collection time, and $2\theta = 20° - 80°$ acquisition range as for the high temperature experiments were adopted.

4.2.3 High-pressure neutron diffraction

High-pressure neutron-diffraction measurements were performed on the PEARL instrument [158] at temperatures of 110 and 290 K in the 0–16.5 GPa pressure range. A variable temperature PE press V3 model was used for the data collection and the sample temperature controlled as discussed in Section 2.7.4. The sample was loaded in an encapsulated Ti-Zr alloy gasket placed in single-toroidal ZTA anvils for measurements in the 0–6.4 GPa, whereas a double-toroidal gasket in sintered diamond anvils was used for pressure points above 10 GPa at room temperature. Lead was included to act as sample marker in both setups. A perdeuterated 4:1 methanol:ethanol mixture was used as pressure transmitting medium. The interest in detecting the 4.54 Å magnetic reflection of $LaFeO_3$ required long collection time of 3/4 h.

4.2.4 High-pressure Raman spectroscopy

High-pressure Raman scattering measurements were also performed on $LaFeO_3$. $LaFeO_3$ was loaded in a Merrill-Basset-type diamond anvil cell [173], in which load is mechanically generated by a three-screw system. A stainless steel gasket

was pre-indented from an initial thickness of 250 μm to 110 μm. $LaFeO_3$ was loaded in a drilled gasket hole of 300 μm diameter. A small ruby sphere was used as pressure marker and the pressure on the sample determined by ruby fluorescence measurements [175]. Hydrostatic pressure was generated by the use of a 4:1 methanol-ethanol solution as pressure transmitting medium. Raman spectra were collected by using an in-house Raman system equipped with a Princeton Instruments SP2500i spectrometer equipped with a 1800 g holographic blaze grating. A diode laser ($\lambda = 532.23$ nm) was focused using a 20× Mitutoyu objective lens with a low laser power of 5 mW at the sample position to avoid fluorescence from the iron-based sample.

4.3 Results

After the synthesis of the material and verification of its phase purity, $LaFeO_3$ was characterised at extreme conditions of pressure and temperature. The following sections discuss the results obtained by temperature-dependent X-ray diffraction, temperature-dependent high-pressure neutron diffraction, and high pressure Raman spectroscopy.

4.3.1 Temperature-dependent X-ray diffraction structural characterisation

Further characterisation of $LaFeO_3$ was carried out by X-ray temperature-dependent diffraction measurements and changes within the crystal structure were analysed in the 15–1373 K temperature range.

In line with the literature [82, 104] the orthorhombic *Pbnm* to trigonal $R\bar{3}c$ structural transition around 1230 K was observed in the variable temperature X-ray diffraction characterisation performed in the current thesis. Selected X-ray diffraction patterns are shown in Figure 4.4 in the 290–1273 K range. Experimental data are shown as open circles, while red solid lines show Rietveld refinement curves of the data. Vertical tick marks indicate calculated Bragg reflection positions of the sample phase. The structure was refined adopting a *Pbnm* space group up to 1173 K. At 1273 K a structural transition to rhombohedral $R\bar{3}c$ is observed and the structure refined with a rhombohedral $R\bar{3}c$ space group, which yielded refined lattice parameters: $a = 5.63271(7)$ Å and

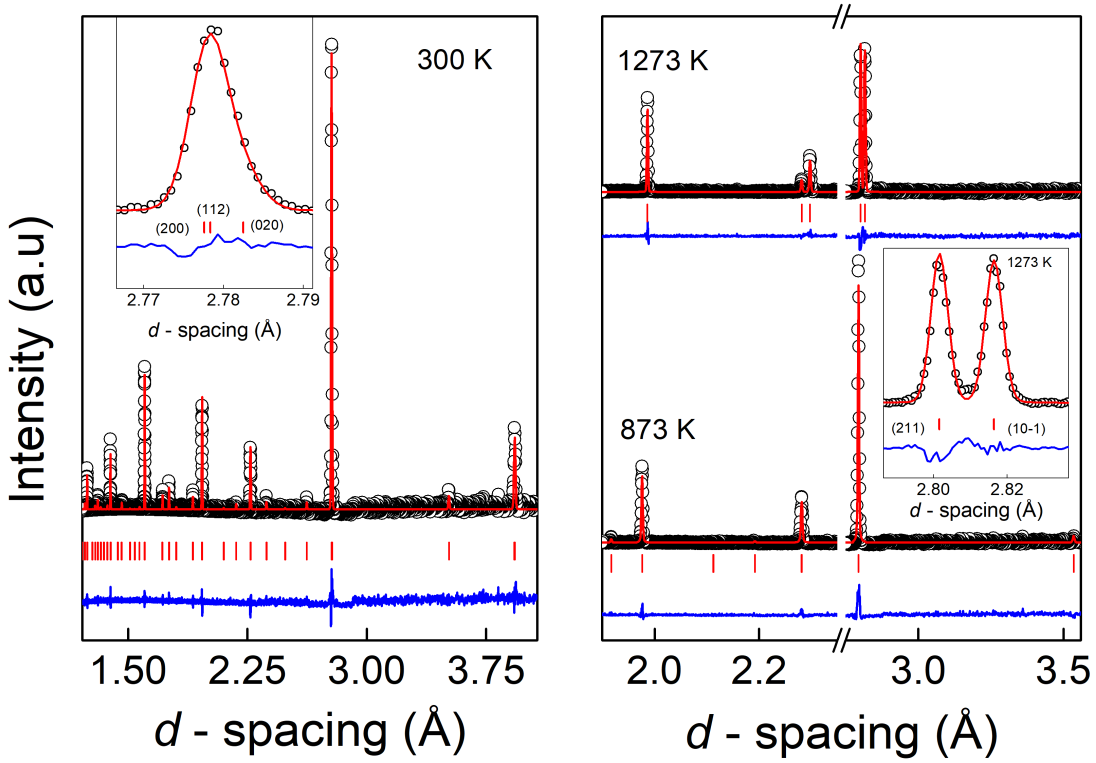

Figure 4.4 *X-ray diffraction patterns of $LaFeO_3$ (open circles) at 300, 873 and 1273 K. Solid red lines show Rietveld fits to the data, while the bottom blue lines show residuals of the Rietveld fits. Vertical tick marks indicate reflections from the orthorhombic Pbnm structural model at 300 K and 873 K, and from the $R\bar{3}c$ space group at 1273 K. The break on the x-axis is to highlight the orthorhombic to rhombohedral reflection splitting. Insets show a zoom in the (200), (112) and (020) Bragg reflections in Pbnm, and the appearance of the trigonal reflections (10-1) and (211) at 1273 K.*

c = 13.6868(2) Å. Insets of Figure 4.4 show a zoom near the 2.8 Å d-spacing position. The (200), (112) and (020) Bragg reflections of $LaFeO_3$ in *Pbnm* at 300 K are replaced by the trigonal reflections (10−1) and (211) at 1273 K. The orthorhombic to trigonal structural transition is related to the A-site cavity volume, which is expanding more rapidly than the B-site octahedra, with a consequent increase of the tolerance factor t [66].

Low temperature X-ray diffraction measurements were also performed and representative patterns are shown in Figure 4.5 in the 15–270 K range. Open circles show the experimental data, while red solid lines indicate Rietveld refinement curves. Vertical tick marks show calculated reflections from the orthorhombic *Pbnm* phase, which is maintained in $LaFeO_3$ over the temperature

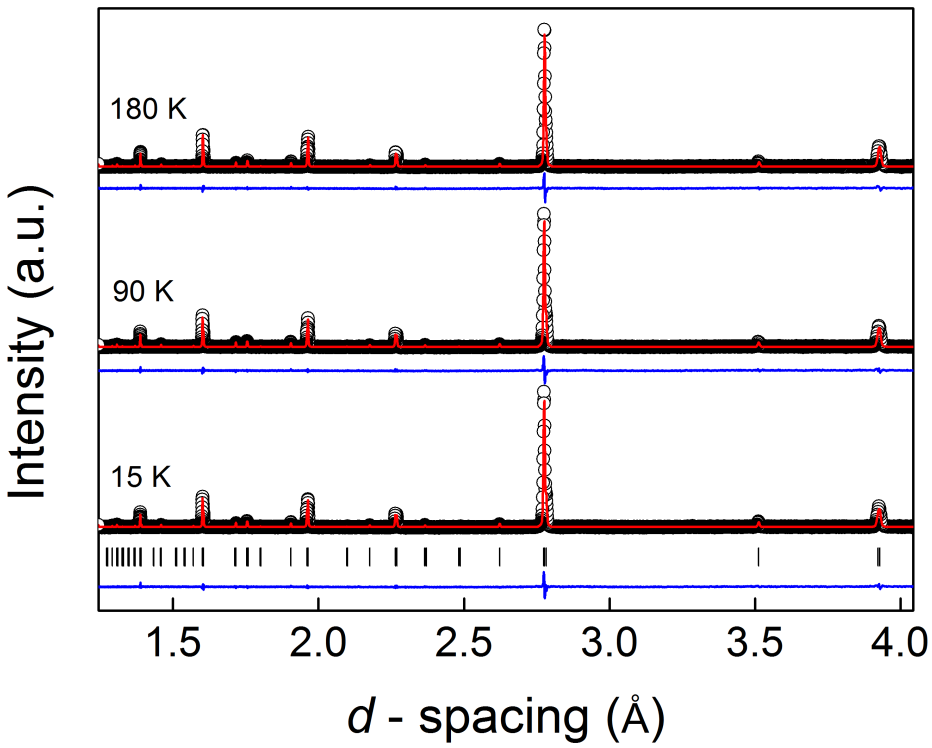

Figure 4.5 *Selected X-ray diffraction patterns of $LaFeO_3$ at temperatures of 15, 90 and 180 K. Experimental data are shown as open circles in the 1.0–4.0 Å range. Red solid lines show Rietveld refinement curves of the neutron data calculated by adopting an orthorhombic Pbnm space group. Vertical black tick marks indicate calculated reflection positions from the sample phase at 15 K. Bottom blue lines show residual curves of the Rietveld fits determined as difference between the observed and calculated intensities.*

range 15–1173 K. Figure 4.6 reports the unit-cell pseudo-cubic lattice parameters variation as a function of temperature calculated from the combined data sets. The cross-over of the a and b lattice constants previously reported by temperature-dependent neutron-diffraction measurements around 770 K is confirmed in the X-ray characterisation carried out in this work, where the a and b parameters are observed to cross around 655 K. The value reported in this work of thesis is lower than that reported by neutron diffraction. However, the same cross-over is also observed in the X-ray characterisation reported by Selbach *et al* [104], and in this work the condition $b < a$ is already observed for $T < 700$ K. This wide range of values may be related to the different experimental technique or to a different thermal history of the samples.

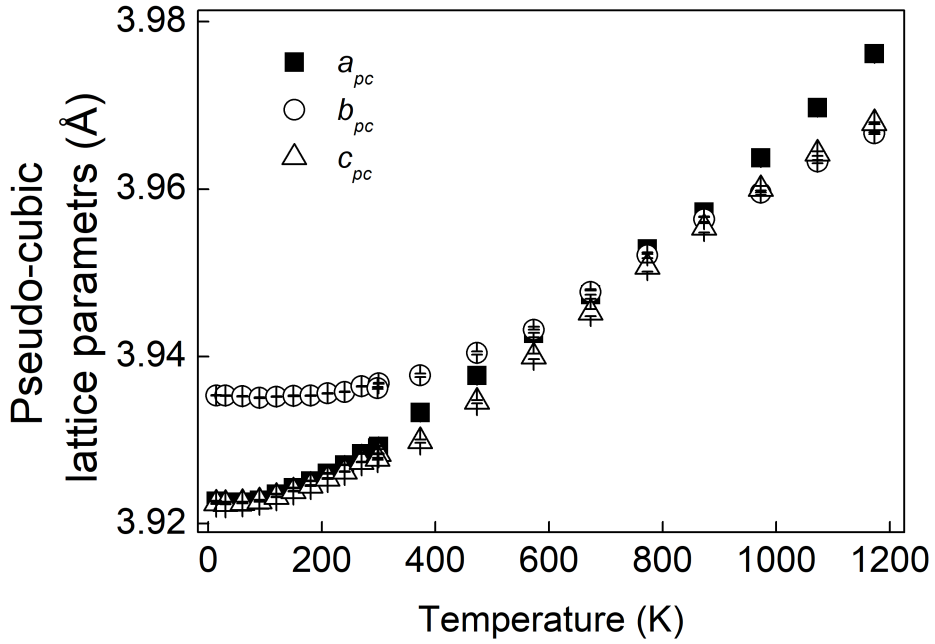

Figure 4.6 *Pseudo-cubic lattice parameters of $LaFeO_3$ as a function of temperature in the 15–1173 K range as determined by Rietveld refinement from XRD low-temperature and high-temperature combined data sets. Pseudo-cubic values were determined using equations: $a = \sqrt{2}a_{pc}$, $b = \sqrt{2}b_{pc}$, and $c = 2c_{pc}$. Error bars are also shown but within symbol size.*

X-ray diffraction does not provide contrast between light oxygen atoms and heavier iron and lanthanum atoms. Rietveld refinement of the fractional coordinates is not performable by X-ray diffraction measurements and attempts to refine the oxygen fractional coordinates led to unphysical values. The ability to accurately distinguish oxygen positions is essential to determine either parameters such as bond distances and angles or structural distortions like the tilting angles. Neutron-diffraction measurements are therefore necessary to deepen the understanding on the crystal structure of $LaFeO_3$. In addition, neutrons also probe the magnetism of materials and can be used to study the magnetic moment behaviour of $LaFeO_3$ under extreme conditions.

4.3.2 High-pressure neutron diffraction

High-pressure neutron-diffraction data at temperatures of 110 and 290 K were collected in the 0–6.5 and 0–5.5 GPa pressure range, respectively. Selected

patterns are shown in Figures 4.8 and 4.7.

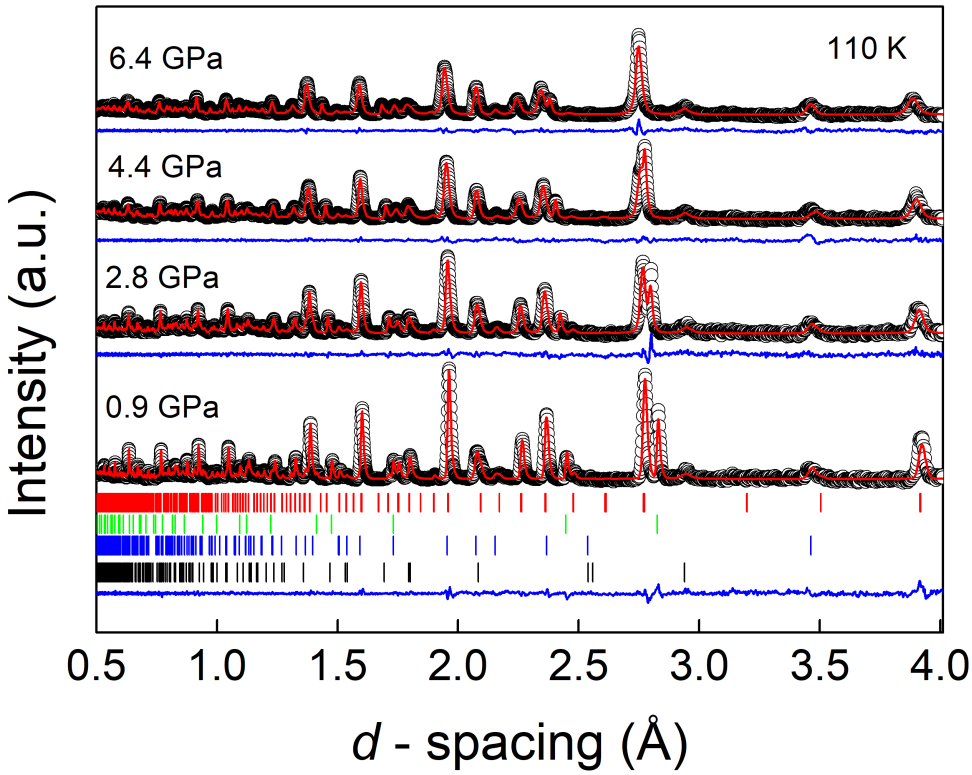

Figure 4.7 *Selected neutron diffraction patterns of $LaFeO_3$ collected at 110 K in the 0–6.4 GPa range (open circles). Solid red lines show Rietveld fits to the experimental data. Vertical tick marks indicate calculated reflection positions, from top to bottom: sample phase, lead marker, alumina, and zirconia. Blue lines show residuals of the Rietveld refinements.*

Experimental data are shown as open circles, while red solid lines show Rietveld refinement curves to the data. Vertical tick marks show calculated reflection positions from the sample (top), lead pressure marker (second top), and the anvil materials alumina and zirconia (third and last from top). The residual of the refinements are also shown as bottom blue lines. Experimental data were fitted according to the *Pbnm* space group for the nuclear phase and with an antiferromagnetic G_x type *Pb'n'm* magnetic space group for the magnetic phase contribution according to Table 4.1. Experimental data in the 0–6.5 GPa pressure range reports no variation from the orthorhombic symmetry *Pbnm* space group at each temperature.

The equation of state of the sample was determined at each temperature by the

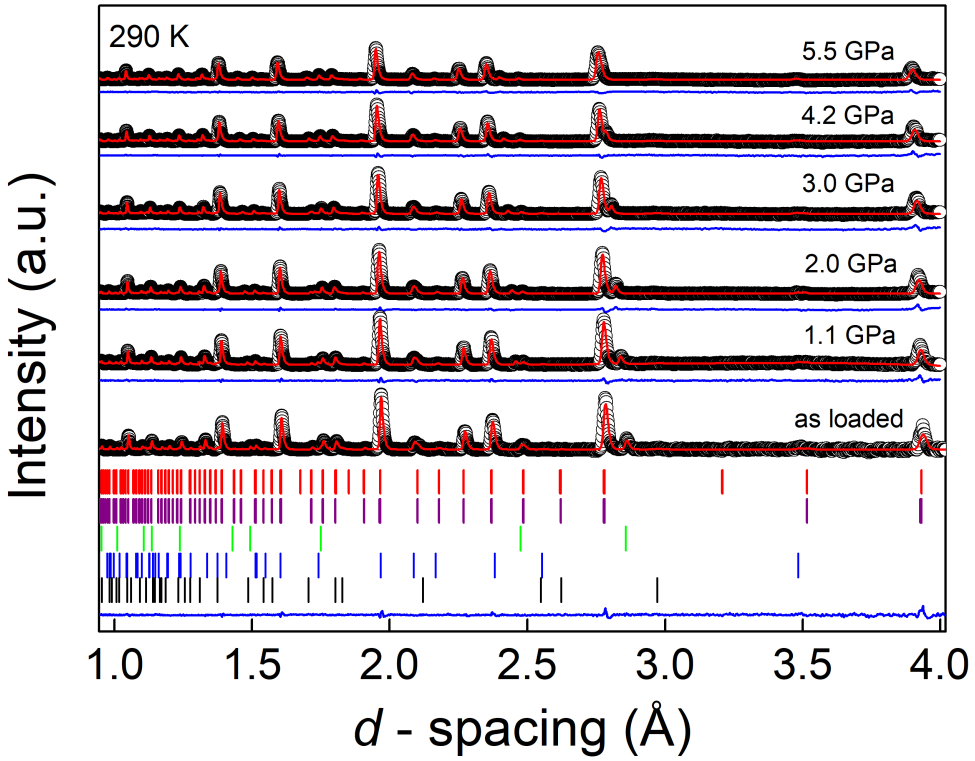

Figure 4.8 *Selected neutron diffraction patterns of $LaFeO_3$ collected at 290 K in the 0–5.5 GPa range (open circles). Rietveld refinement of experimental data are shown as red lines, while blue lines show residuals of the Rietveld fits. Vertical tick marks show calculated reflection positions from top to bottom: magnetic Pb'n'm sample phase, nuclear Pbnm sample phase, lead marker, alumina and zirconia.*

use of the software EoSfit [206]. Figure 4.9 reports the unit-cell volume (V) of $LaFeO_3$ as a function of pressure at temperatures of 110 (diamonds) and 290 K (filled squares). The volume compresses smoothly in the pressure ranges studied and no abrupt anomaly is observed. The orthorhombic *Pbnm* space group is stable up to 6.5 GPa.

Experimental data at 290 K were fitted to a third-order Birch-Murnaghan equation of state and fitted values are reported in Table 4.2. The fitted volume $V_0 = 243.18(3)$ Å^3 is in agreement with values previously reported [82, 113], and the fitted bulk modulus of 175(1) GPa is in agreement with the value recently reported by X-ray diffraction of 172(2) GPa [113] with a third-order Murnaghan equation of state.

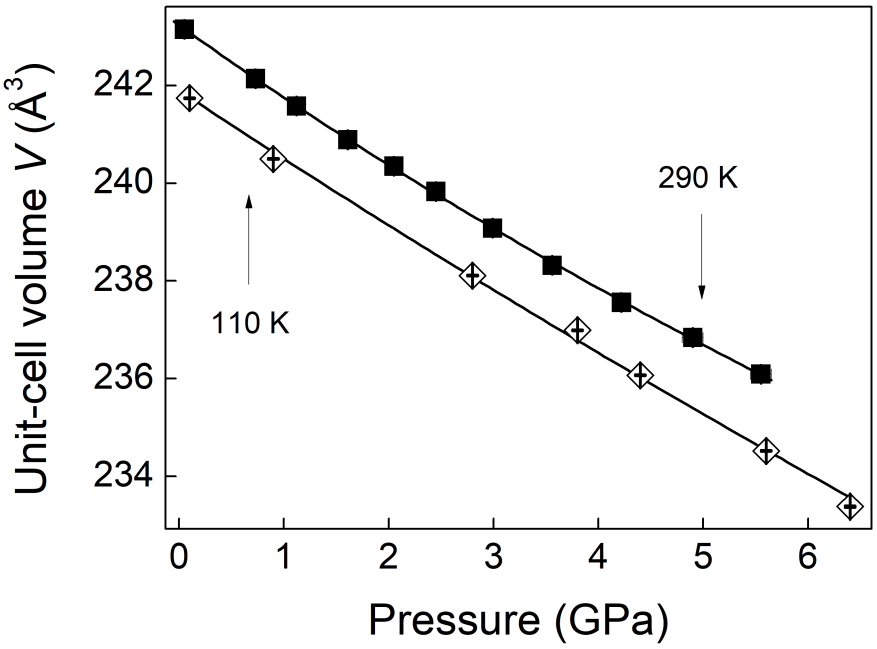

Figure 4.9 *Unit-cell volume (V) of $LaFeO_3$ as a function of pressure at 110 (diamonds) and 290 K (filled squares). Solid lines show a fit to the data by a second (110 K) and third (290 K) order Birch-Murnaghan equation of state, which yielded values reported in Table 4.2. Error bars are also shown but smaller than symbols.*

Table 4.2 *Values of volume V_0, bulk modulus B_0 and first derivative B' of $LaFeO_3$ as determined by Birch-Murnaghan equation of state fits of experimental data shown in Figure 4.9.*

T (K)	V_0 (Å^3)	B_0 (GPa)	B'
110	241.9(1)	170(3)	4
290	243.18(3)	175(1)	7(2)

The bulk modulus at 110 K was calculated by fitting a second-order Birch-Murnaghan equation of state ($B' = 4$). The number of data points at 110 K is not sufficient to allow the use of a third-order EoS, and the fit yields unphysical values. Lattice parameters of $LaFeO_3$ were also analysed and their variation as a function of pressure is reported in pseudo-cubic settings in Figure 4.10. Figure 4.11 also shows the a and b unit-cell parameters variation at 110 and 290 K. Ambient pressure values are in agreement with values previously reported [82, 226]. A cross-over of the a and b parameters is observed around 2.0 GPa in agreement with the previous X-ray pressure dependent study [113], and around 1.7 GPa at 110 K.

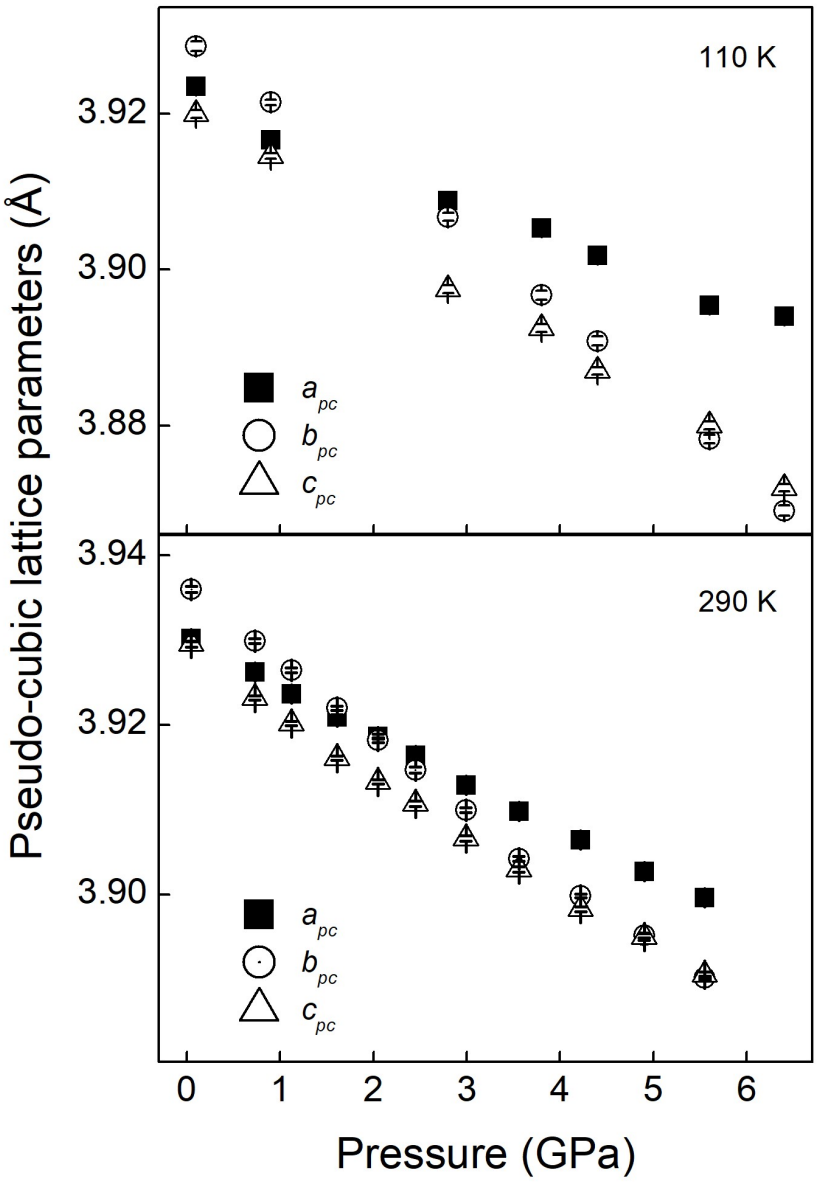

Figure 4.10 *$LaFeO_3$ pseudo-cubic lattice parameters as a function of pressure at 110 (top panel) and 290 K (bottom panel). Pseudo-cubic values were determined using equations: $a = \sqrt{2}a_{pc}$, $b = \sqrt{2}b_{pc}$, and $c = 2c_{pc}$. Error bars are also shown but smaller than symbols.*

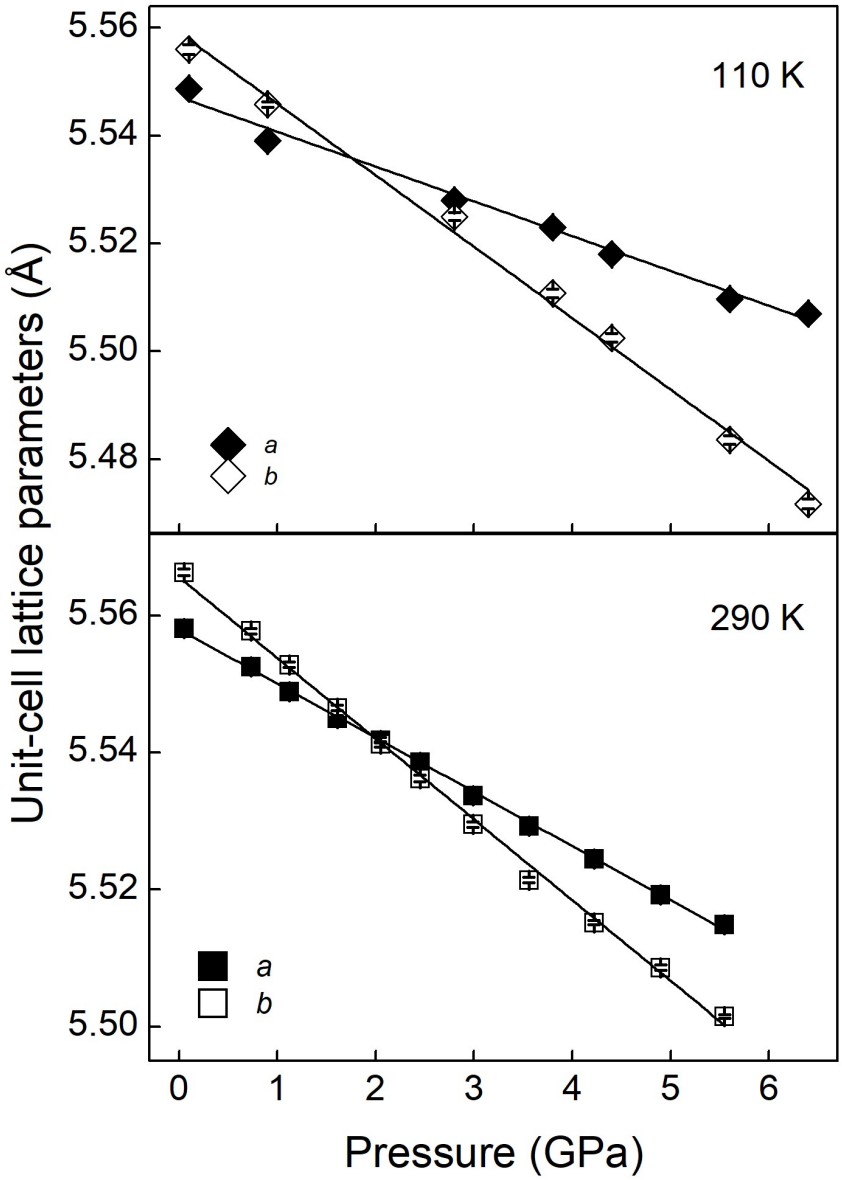

Figure 4.11 *Unit-cell a and b lattice parameters variation as a function of pressure at 110 (open and filled diamonds, top panel) and 290 K (open and filled squares, bottom panel). Solid lines show linear fit to the data used to determine the pressure value at the crossing points. These yielded: P = 2.0 GPa at ambient temperature and P = 1.7 GPa at 110 K. Error bars are also shown but smaller than symbols.*

Table 4.3 *Calculated compressibility rates of a, b and c lattice parameters of $LaFeO_3$ at 110 and 290 K.*

T (K)	k_a (GPa^{-1})	k_b (GPa^{-1})	k_c (GPa^{-1})
110	0.0011(1)	0.0023(1)	0.0019(1)
290	0.0014(1)	0.0021(1)	0.0017(1)

Such cross-over was also observed in temperature dependent X-ray and neutron-diffraction characterisation around 700 K [104, 226] and found in the X-ray characterisation carried out on the current sample. However, this cross-over is not directly associated to any phase transition. Above 2 GPa the a and b lattice parameters are observed to diverge and the orthorhombic symmetry is maintained throughout the pressure range investigated. The compressibility rates were determined for each temperature and values are reported in Table 4.3.

The relationship $a > b$ for the *Pbnm* space group is maintained for regular octahedra, spanned by six equivalent Fe–O bond lengths and intra-octahedral angles, which do not deviate from 90°. However, if the tilted octahedra are not perfectly rigid the crossover $b > a$ may occur [227]. This arises from an intrinsic distortion of the octahedra related to the structural deviation of the intra-octahedral O2–Fe–O2′ angle from the ideal 90° value [228]. The O2–Fe–O2′ angle in $LaFeO_3$ is found in this work of thesis, in agreement with previous temperature dependent neutron-diffraction work [226], to exhibit a value of 91.2° at each temperature and observed to be nearly unchanged upon pressure variation.

The compressibility behaviour of the unit-cell parameters depends also on the Fe–O bond lengths and inter-octahedral Fe–Oi–Fe angles (i = 1,2). As highlighted in Figure 4.12 the Fe–O1 bond distance has its largest component along the c-axis, and the compression of this bond, shown in Figure 4.13, can be seen to be primarily responsible for the change in the c-axis.

In contrast, the Fe–O2 and Fe–O2′ bond lengths have their main components on the a and b-axes, the longer Fe–O2′ (2.012(6) Å at ambient P) has its largest component in the b direction, while the shorter Fe–O2 (1.996(5) Å at ambient P) in the a direction. Changes in the a and b-axes are therefore driven largely by changes in bond lengths and angles or alternatively in tilting angles, when the bond distances do not show a significant change. As shown in Figure 4.14, the compression of the b lattice constant is influenced by the compression of the Fe–O2′ bond, while the little decrease in length of the Fe–O2 bond distance is

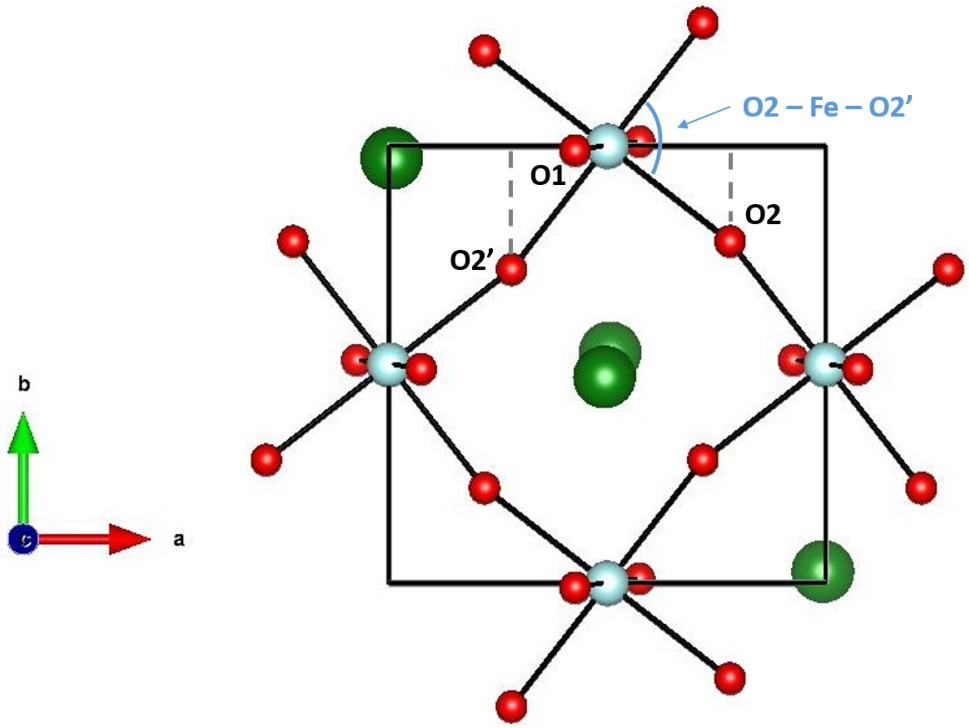

Figure 4.12 *Fe–Oi bond lengths of $LaFeO_3$ shown along the c-axis direction. The Fe–O1 bond has the largest component along the c-axis. The Fe–O2 short and Fe–O2′ long bonds have their largest component in the a and b-axis, respectively. Black solid line represents the orthorhombic unit cell.*

Table 4.4 *Calculated compressibility rates of Fe–Oi bond lengths of $LaFeO_3$ at 110 and 290 K.*

Temperature (K)	$k_{\text{Fe-O1}}$ (GPa^{-1})	$k_{\text{Fe-O2'}}$ (GPa^{-1})	$k_{\text{Fe-O2}}$ (GPa^{-1})
110	0.0017(1)	0.0050(3)	0.0013(3)
290	0.0019(1)	0.0032(2)	0.0050(3)

reflected in the lower compressibility rate of the a lattice parameter: while the Fe–O2′ bond length is seen to decrease in the pressure range studied of about 0.4 Å the Fe–O2 bond remains nearly unchanged. Compressibility rates were determined and reported in Table 4.4.

The FeO_6 octahedra are found to be slightly distorted with the intra-octahedral O2–Fe–O2′ angle deviating from the ideal 90° value.

The inter-octahedral Fe–Oi–Fe ($i = 1, 2$) bond angles as a function of pressure at each temperature are reported in Figure 4.15. Their values remain comparable at the different selected temperatures, and do not affect the geometry of the

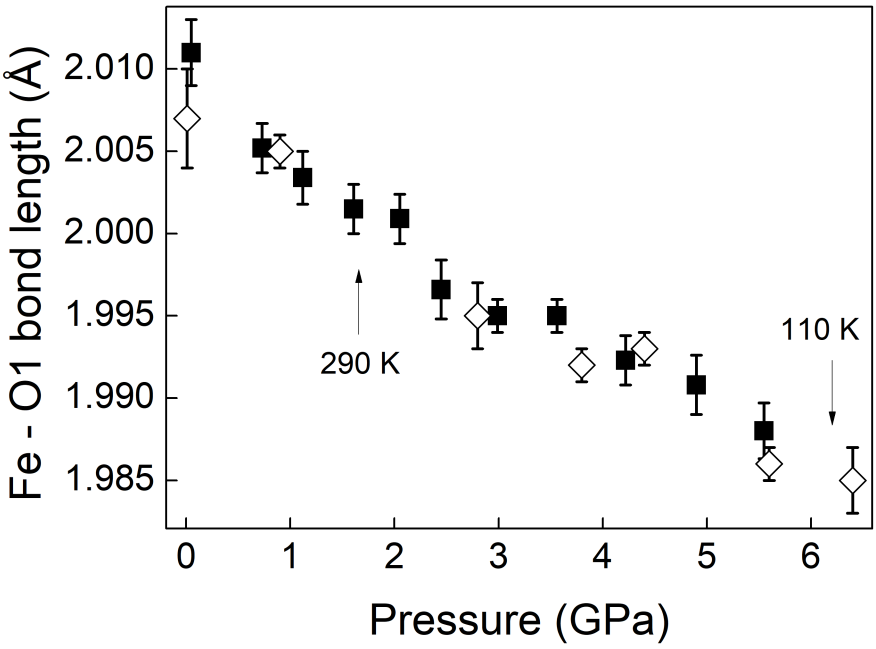

Figure 4.13 *Fe–O1 bond length of $LaFeO_3$ as a function of pressure at 110 (diamonds) and 290 K (squares). Error bars are also shown.*

octahedra. The equatorial Fe–O2–Fe angle increases in the pressure ranges investigated more than the Fe–O1–Fe angle, which remains nearly unchanged up to 6.5 GPa.

The ideal cubic perovskite is characterised by a twelve-coordinated A cation site, with twelve equidistant oxygen atoms. Orthorhombic perovskites, such as $LaFeO_3$, are usually described as eight-coordinated, with eight oxygen atoms first-nearest-neighbours and four second-nearest-neighbours. However, a previous single-crystal X-ray diffraction study of $LaFeO_3$ [225] proposes a higher coordination number of nine for the lanthanum in relation to the low distortion of the A-site compared to other orthorhombic ferrite-oxides. In $LaFeO_3$, the La–Oi bond distances vary over a wide range and a helpful method to monitor changes within the La site is by the distortion index σ, defined by equation: $\sigma = \frac{1}{n}\sum_i[(La - Oi) - < La - Oi >]$, where the sum is over the first-nearest-neighbours i. Its variation as a function of pressure at 290 K is shown in Figure 4.16.

While the distortion of the La site remains nearly unchanged at 110 K (values shown in Table B.2 in Appendix B), σ decreases in the 0–5.5 GPa pressure range at 290 K. The coordination number of nine for the La cations is confirmed in

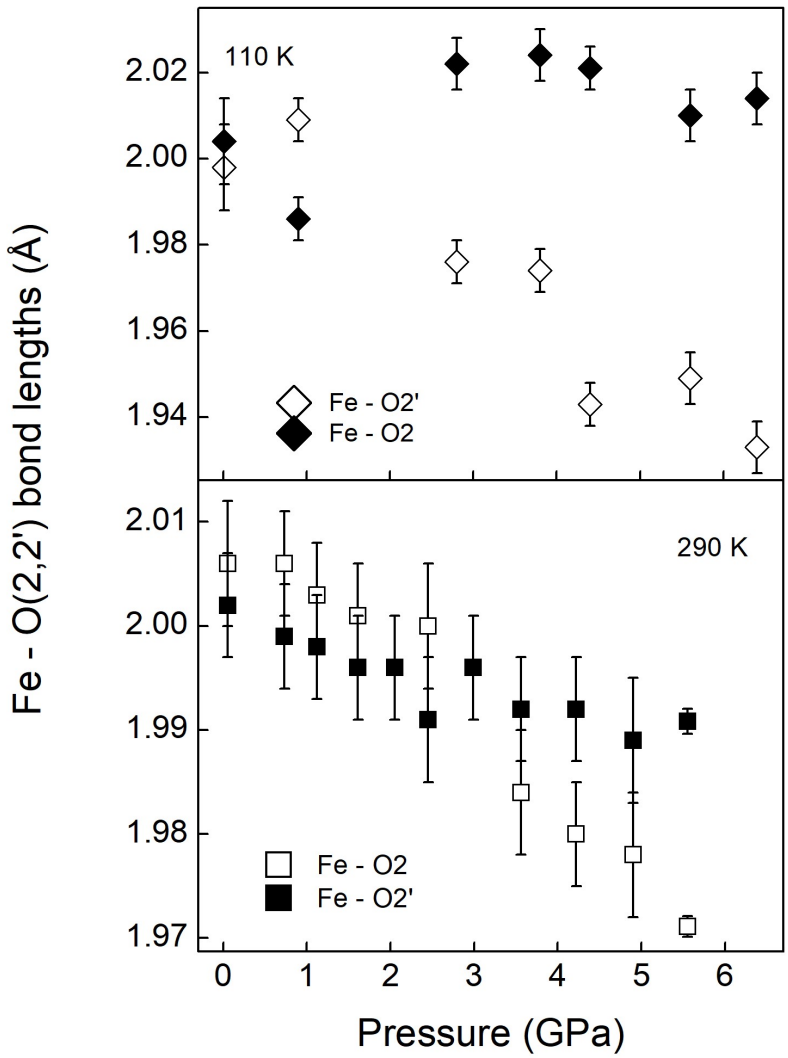

Figure 4.14 *Fe–O2,2′ bond distances variation of $LaFeO_3$ as a function of pressure at 110 (opened and filled diamonds) and 290 K (opened and filled squares). Error bars are also shown.*

the structural refinement carried out in this work at ambient pressure, in which nine La–Oi bond distances are observed for $LaFeO_3$. The application of pressure, which promotes a decrease of distortion of the La site, generates a tenth first-nearest-neighbour. Four non-degenerate La–O1 and three double-degenerate La–O2 are then refined by the Rietveld method. Determined structural parameters, fractional coordinates, bond distances and angles as a function of pressure are reported at each temperature in Tables B.1 and B.2 in Appendix B.

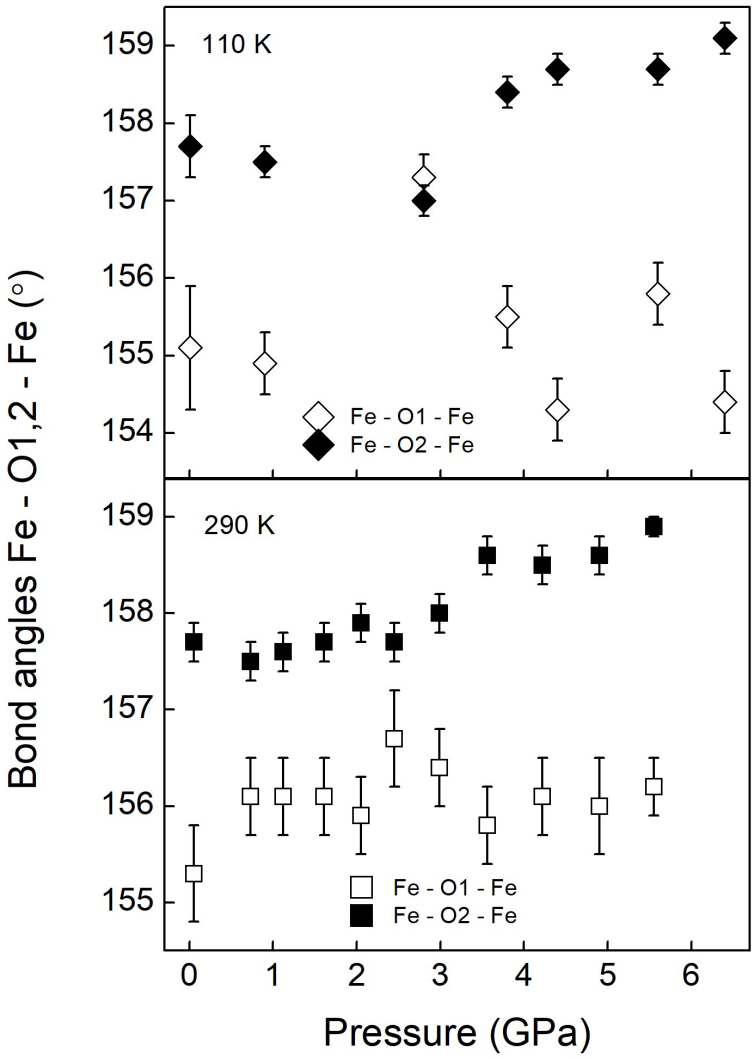

Figure 4.15 *Inter-octahedral angle Fe–O1,2–Fe variation as a function of pressure $LaFeO_3$ at 110 (diamonds) and 290 K (filled squares). Error bars are also shown.*

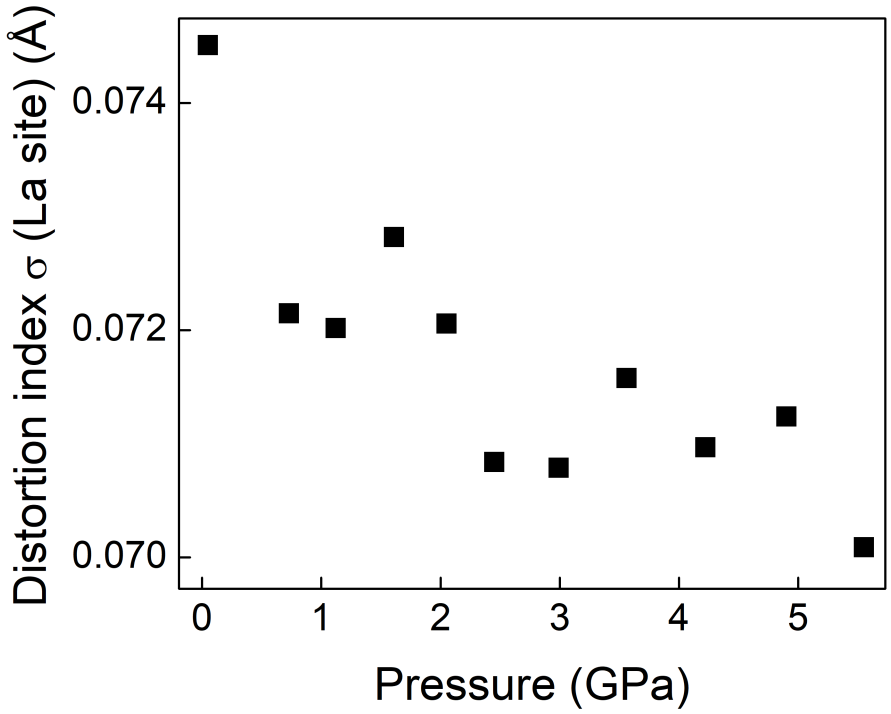

Figure 4.16 *Distortion index of La–Oi bond lengths of $LaFeO_3$ as a function of pressure at 290 K. See main text for definition.*

4.3.3 Tilting angles under high pressure

It is interesting to look at how the octahedral tilting distortion varies under the application of pressure and how this influences the structural changes. The in-phase and out-of-phase tilting angles, which describe the orthorhombic symmetry and shown in Figures 4.17a and 4.18a, were determined by the oxygen displacements from the ideal cubic structure positions according to Equations 1.4 and 1.5.

Ambient pressure and temperature values of 7.0(2)° and 12.2(1)° for the in-phase and out-of-phase tilting are in agreement with previous works [226, 229] and with values determined in this work of thesis from the higher resolution POLARIS data. The variation of ϕ_{in} and ϕ_{out} tilting angles as a function of pressure is shown in Figures 4.17b and 4.18b at 110 (diamonds) and 290 K (filled squares). While the tilting distortion around the cubic [110] diad axis (ϕ_{out}) is seen to remain nearly unchanged in the pressure range studied, the in-phase tilt of the octahedra around the *c*-axis decreases by more than 0.5° at ambient temperature and by nearly 1.5° at 110 K.

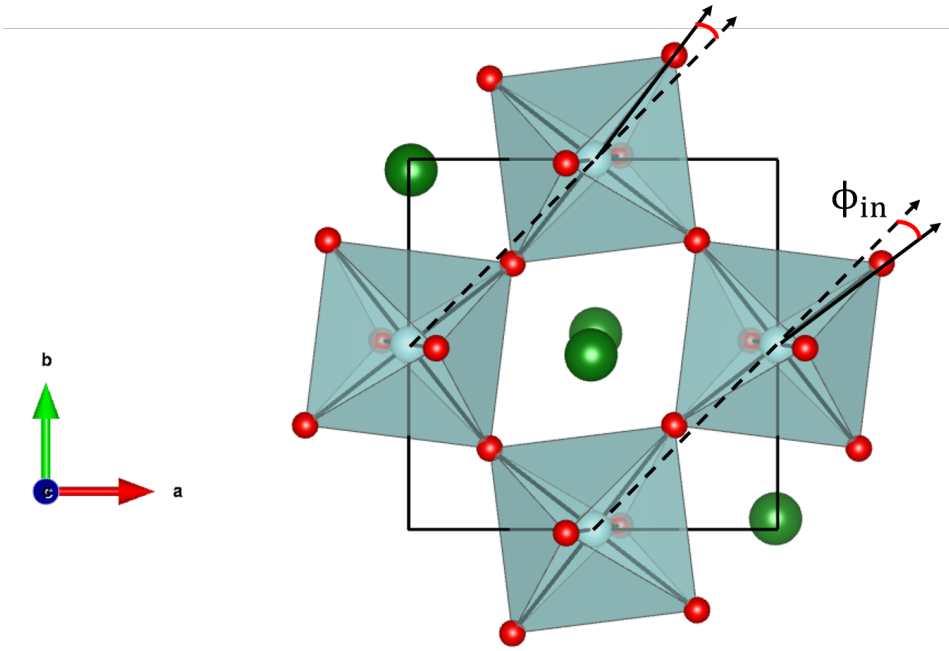

(a)

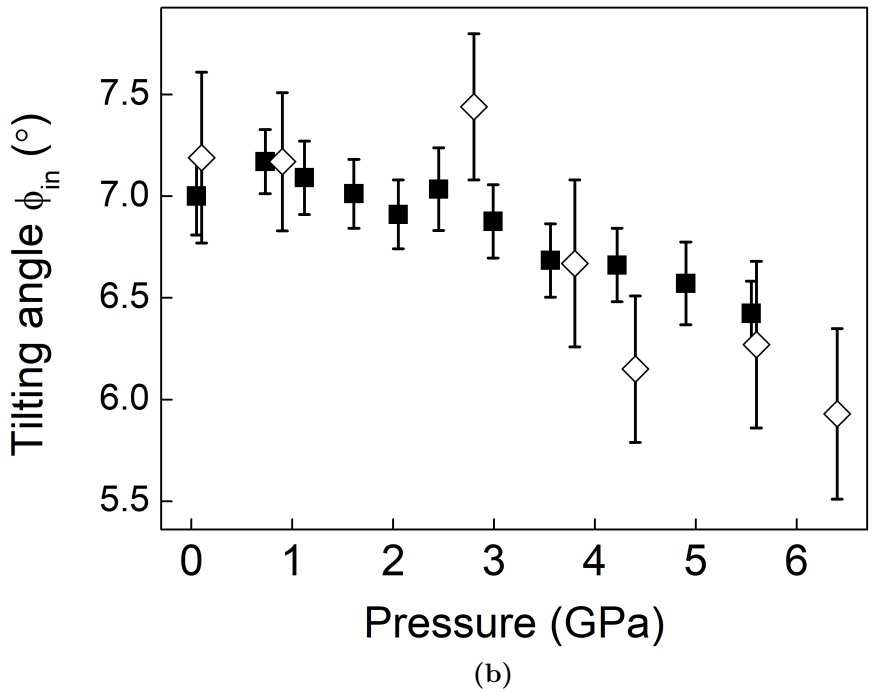

(b)

Figure 4.17 *4.17a Representation of the in-phase octahedral tilting angle of $LaFeO_3$ around the [001] cubic crystallographic direction. 4.17b Tilting angle variation of $LaFeO_3$ as a function of pressure at 110 (diamonds) and 290 K (filled squares). Error bars are also shown.*

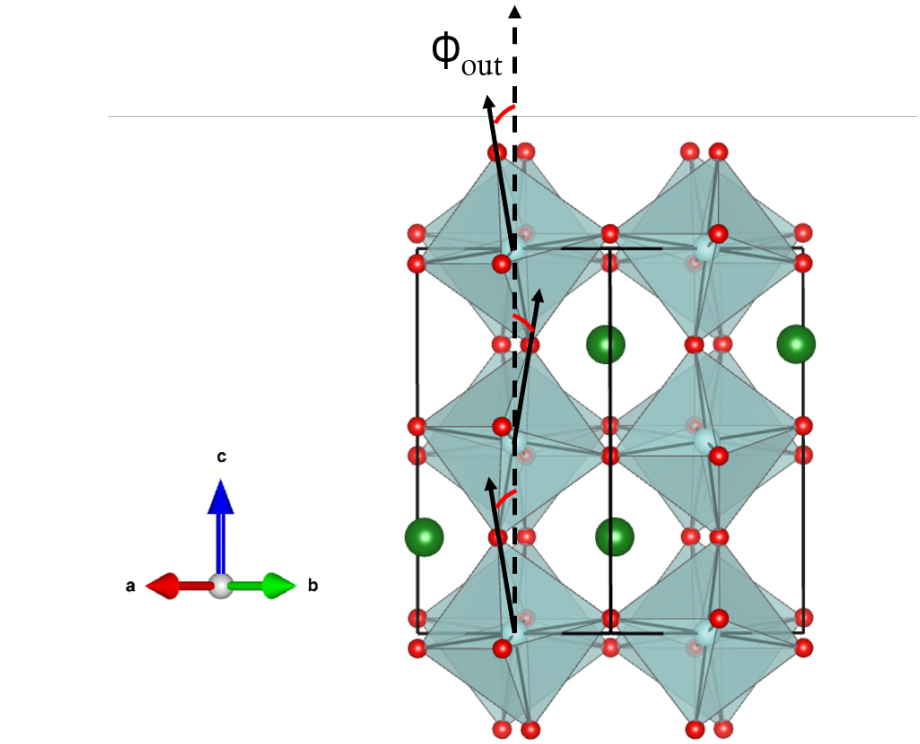

(a)

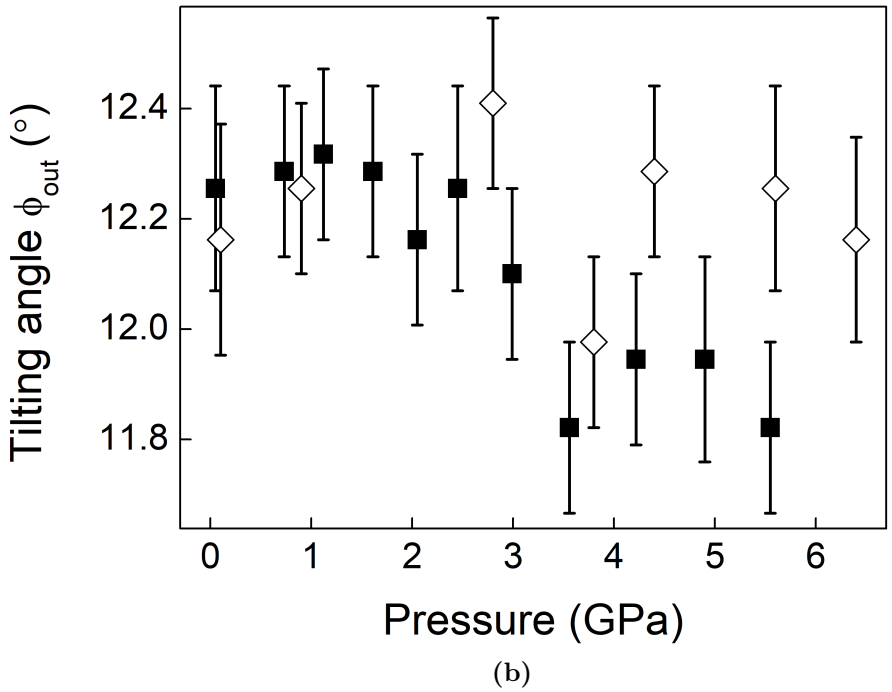

(b)

Figure 4.18 *4.18a Representation of the out-of-phase octahedral tilting angle of $LaFeO_3$ around the [110] cubic crystallographic direction. 4.18b Tilting angle variation of $LaFeO_3$ as a function of pressure at 110 (diamonds) and 290 K (filled squares). Error bars are also shown.*

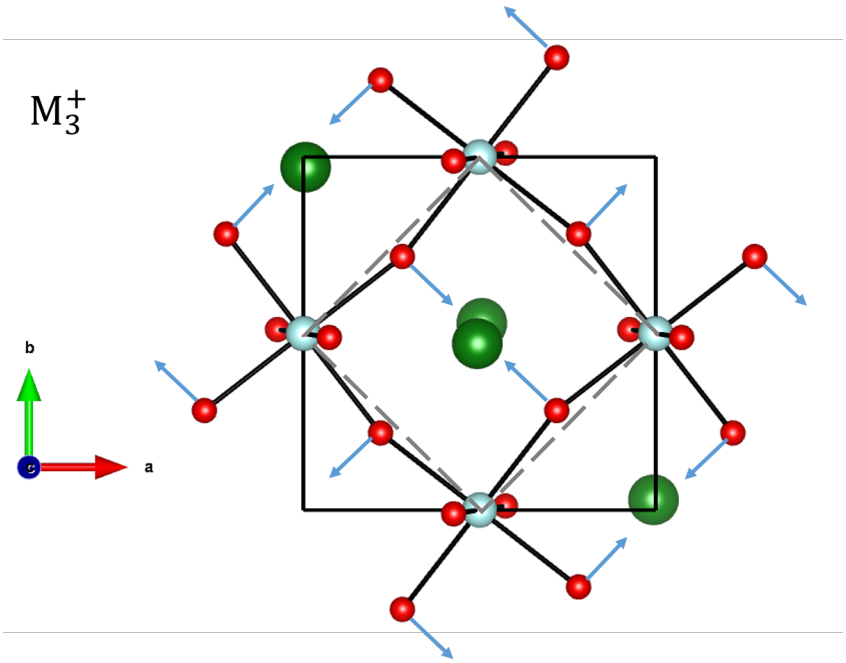

(a)

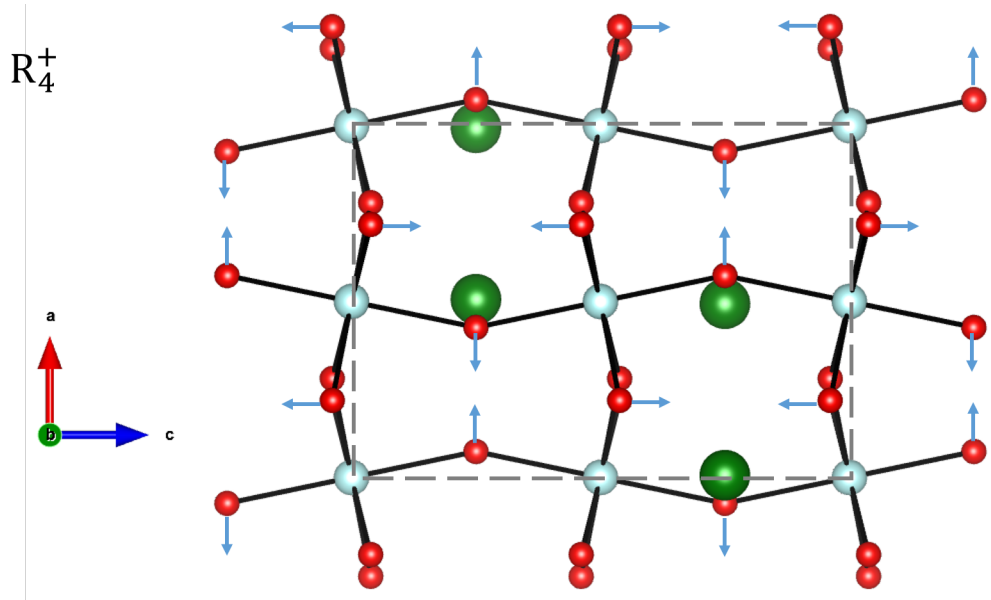

(b)

Figure 4.19 *Schematic representation of the M_3^+ (a) and R_4^+ (b) symmetry-adapted displacement modes. Blue arrows indicate the displacement from the ideal cubic positions, which lie along the dashed grey line. Green, light blue and red spheres show La, Fe and O atoms, respectively.*

There are two symmetry modes correspondent to the in-phase and out-of-phase tilting of the octahedra in the $a^-a^-c^+$ system: the out-of phase tilting mode, which transforms as R_4^+ and an additional displacement mode related to the in-phase tilting along the z axis referred to as M_3^+ [78, 102, 230]. Figure 4.19 shows a schematic representation of these two displacement modes.

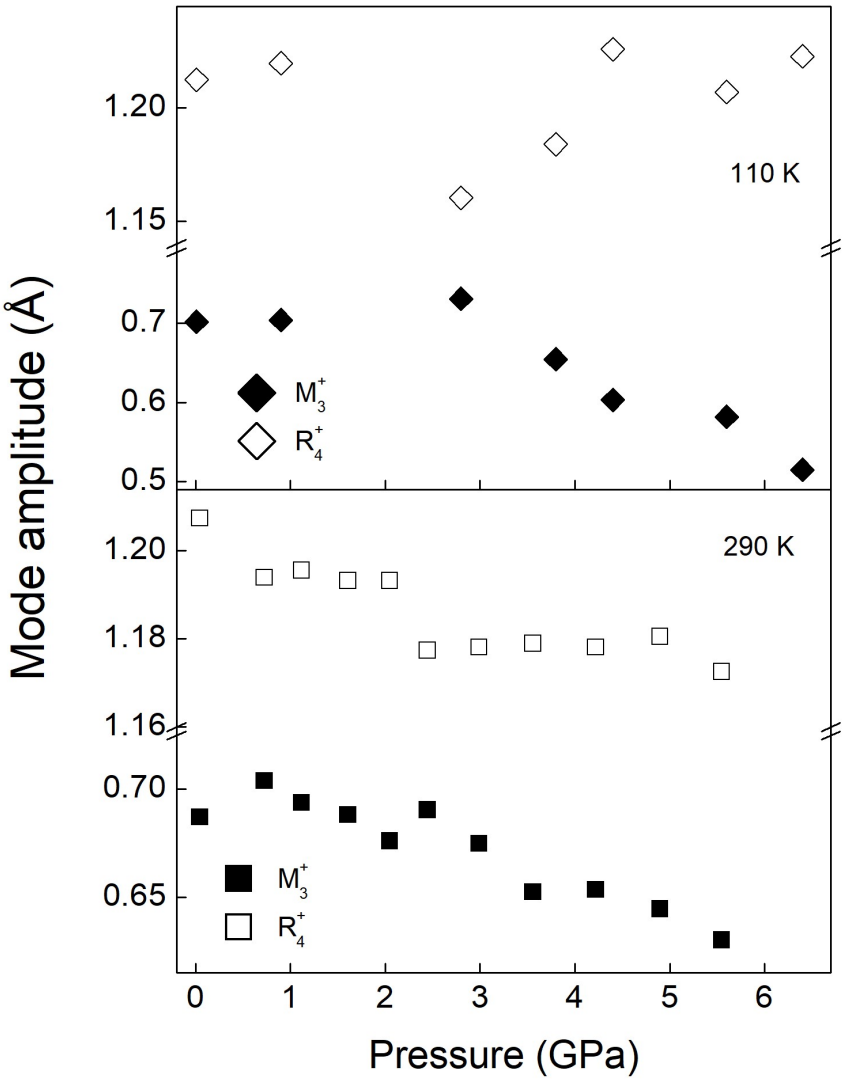

Figure 4.20 *R_4^+ (opens symbols) and M_3^+ (filled symbols) mode amplitude variation of $LaFeO_3$ as a function of pressure at 110 (diamonds) and 290 K (squares), as determined by the use of the ISODISTORT software [103].*

By the use of the software ISODISTORT [103] and the neutron-diffraction data as a function of pressure collected on PEARL the evolution of the

displacement amplitude modes have been analysed as a function of pressure at each temperature. Their amplitude variation as a function of pressure at each temperature is shown in Figure 4.20. The ambient pressure values are in agreement with values reported in the temperature-dependent neutron-diffraction study of $LaFeO_3$ [226]. The primary order parameters for a perovskite-structured compound with space group *Pbnm*, or for alternative space group settings, are associated with these modes, and these are both found to decrease as a function of pressure. However, the reduction of the M_3^+ displacement amplitude is much larger than the out-of-phase related mode. According to the approach of Howard and Stokes [78], when the M_3^+ mode tends to zero the structure must undergo a transition which will lead to an intermediate phase such as the *Ibmm* or $R\bar{3}c$, before adopting the cubic phase. The FeO_6 octahedra are also deformed from the cubic structure by modes X_5^+, M_2^+ and R_5^+ [102, 231, 232]. At each temperature the M_3^+ and R_4^+ tilting modes are much larger in magnitude than the octahedral deformation mode with *irrep* X_5^+, R_5^+, and M_2^+ in the pressure range studied, whose values fluctuate around zero. The displacements of the La cation along the orthorhombic *a* and *b*-axes, are each described by the sum of two basis-vectors of equal magnitude. These transform as the irreducible representations of the cubic aristotype phase, $R_5^+$and X_5^+ along the *a*-axis and *b*-axis respectively. However, their variation is negligible. Determined tilting angle values as a function of pressure are reported in Tables B.1 and B.2 in Appendix B.

4.3.4 Antiferromagnetic order in $LaFeO_3$ under high pressure

The antiferromagnetic character of $LaFeO_3$ is expressed in the neutron diffraction patterns by the appearance of extra Bragg reflections which are purely magnetic in nature. The Bragg reflection around $\sim$4.54 Å is observed in the neutron-diffraction patterns, whereas is not observed in the X-ray diffraction measurements. This reflection has nearly entirely magnetic contribution and arises from the (101) nuclear and the (011) magnetic Bragg reflections [216]. Its variation at ambient temperature in the 0–5.5 GPa pressure range is shown in Figure 4.21.

Neutron diffraction on powder samples, which can determine the Fe^{3+} moment direction from the intensities of magnetic Bragg peaks, becomes difficult for light rare-earth ortho-ferrites because some relevant reflections overlap due to the small orthorhombic distortion. However, the contribution of the (101) is negligible [216] and the variation of the intensity of this peak can give information on

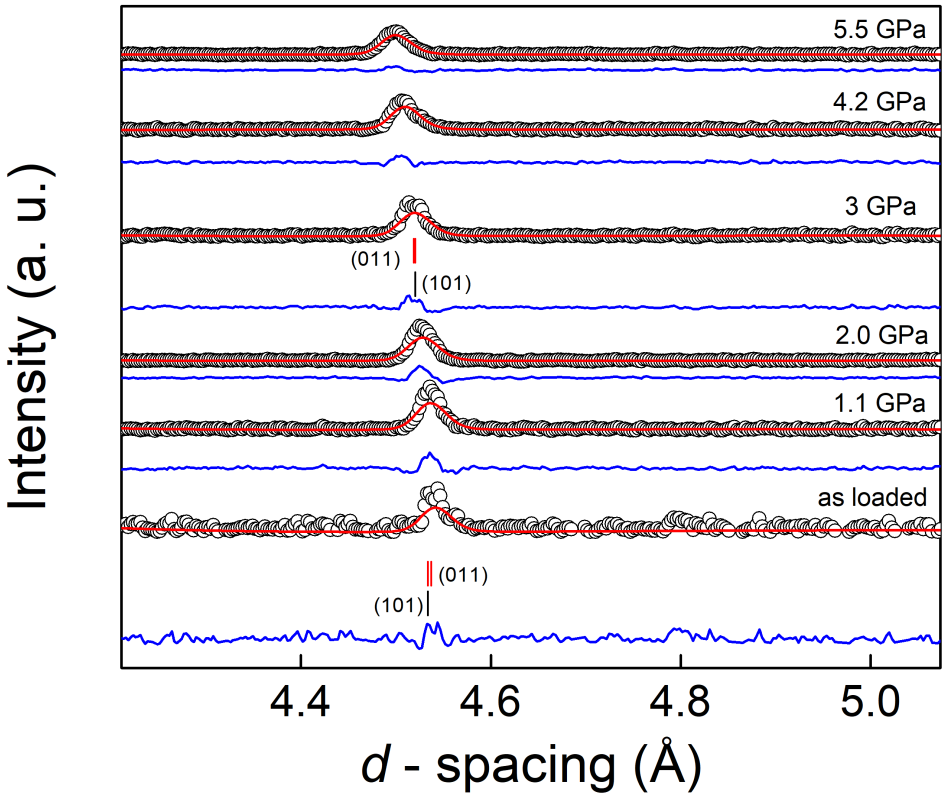

Figure 4.21 *$LaFeO_3$ long frame neutron diffraction data at ambient temperature in the 0–5.5 GPa pressure range (open circles). Red line shows Rietveld refinement of the data performed simultaneously to the short-frame diffraction data. Vertical tick marks show calculated reflections from the magnetic Pb'n'm (top, red) and nuclear Pbnm (black, bottom) phases. Note that the (101) and (011) reflections swap position after the lattice parameter cross-over at 2 GPa. Blue lines show residual of the Rietveld fits.*

the magnetic moment behaviour with pressure and temperature variation. The vanishing of such reflection would imply a transition from the antiferromagnetic order ($T_{\text{Nèel}}$ ~740 K) to a paramagnetic phase. Although the (011) magnetic reflection intensity decreases as function of applied pressure in this experiment, from the Rietveld fits of the neutron-diffraction data, the modulus of the magnetic moment was refined and found to remain unchanged over the pressure range investigated as shown in Figure 4.22.

The decreased intensity of the (011) reflection, which is observed by increasing pressure, is then ascribed to conventional loss of intensity of the neutron diffraction pattern. This is due to loss of signal during the compression of the

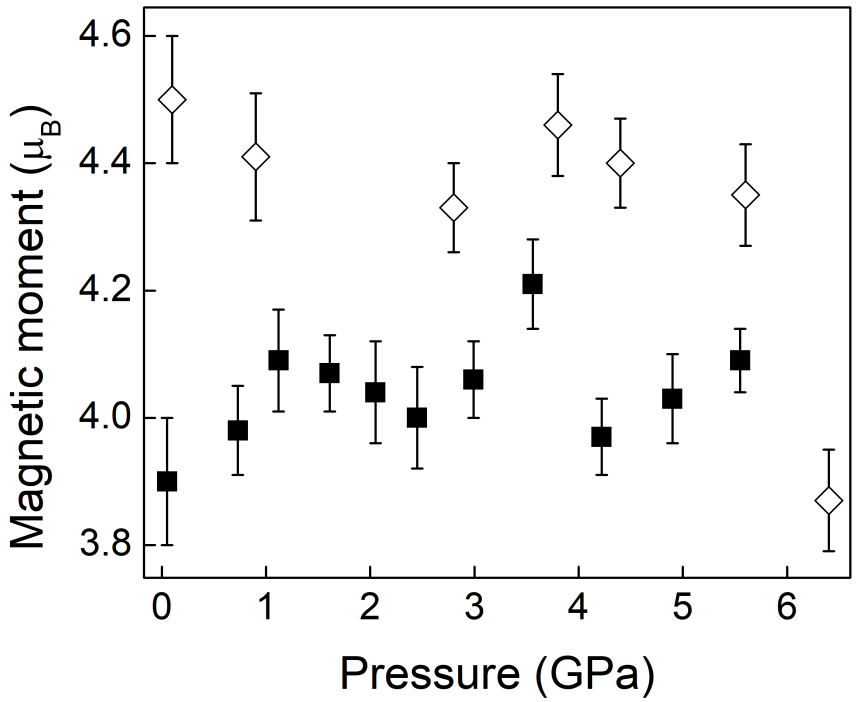

Figure 4.22 *$LaFeO_3$ magnetic moment variation as a function of pressure at 110 (diamonds) and 290 K (filled squares) as determined by Rietveld refinement by the use of the magnetic $Pb'n'm$ phase. Error bars are also shown.*

material and to the decrease of the solid angle of acceptance of the detectors, which depends on the angle of view of the anvils. This is in contrast to what is reported as a function of temperature, where not only the (011) reflection is seen to vanish at the transition temperature but also the modulus of the refined magnetic moment is found to gradually decrease to the value of zero [226]. Pressure seems not to affect the antiferromagnetic nature of $LaFeO_3$, which is found to be stable in the pressure range investigated. Refined magnetic moments as a function of pressure are reported in Tables B.1 and B.2 in Appendix B.

4.3.5 Evidence of structural transition in $LaFeO_3$

$LaFeO_3$ is suggested to undergo a second-order structural transition from orthorhombic *Pbnm* to body-centered *Ibmm* at a pressure around 20 GPa by a previous X-ray diffraction study [113]. Neutron-diffraction measurements were performed at ambient temperature at two higher pressure points 12.1 and

16.2 GPa in order to detect evidence of this transition in the structural changes. Experimental data are shown as open circles in Figures 4.23 and 4.24.

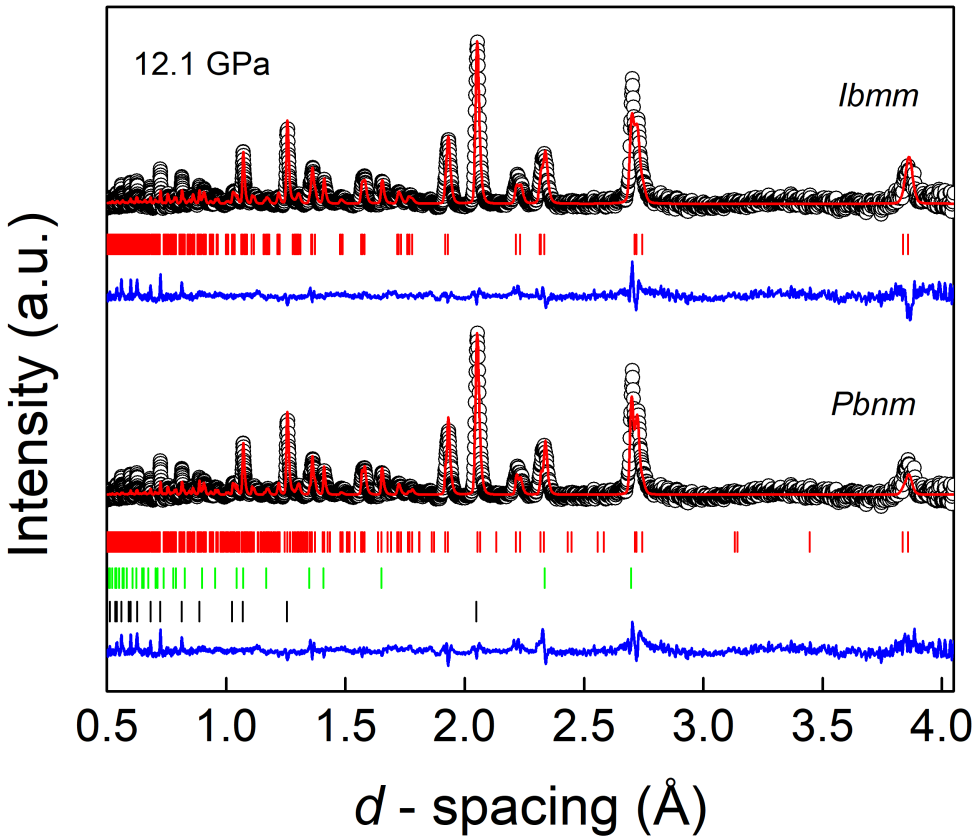

Figure 4.23 *Neutron diffraction patterns of $LaFeO_3$ collected at 290 K at 12.1 GPa. Experimental data are shown as open circles, while red solid lines show Rietveld refinement curves to the data adopting a Pbnm (bottom pattern) and Ibmm (top pattern) space group. Blue lines show residuals of the Rietveld fits. Vertical tick marks indicate calculated reflections from top to bottom: sample (Pbnm bottom pattern, Ibmm top pattern), cubic lead pressure marker, and diamond anvils. The Rietveld fits yielded wR_p values of (%) 6.74 (Pbnm) and 7.87 (Ibmm).*

Rietveld refinements of the neutron data, shown as red lines, were attempted adopting the primitive *Pbnm* and body-centred *Ibmm* space group for both pressure points. The atomic positions for La, Fe and O atoms in the *Ibmm* proposed structure are: La *4e* $\left(x, 0, \frac{1}{4}\right)$, Fe *4b* $\left(0, \frac{1}{2}, 0\right)$, O1 *4e* $\left(x, \frac{1}{2}, \frac{1}{4}\right)$ and O2 *8g* $\left(\frac{3}{4}, \frac{1}{4}, z\right)$. Red tick marks show the correspondent calculated reflections from the sample phases and give evidence of how systematic absences due to the body-centred lattice are observed in both neutron-diffraction patterns. Details of the

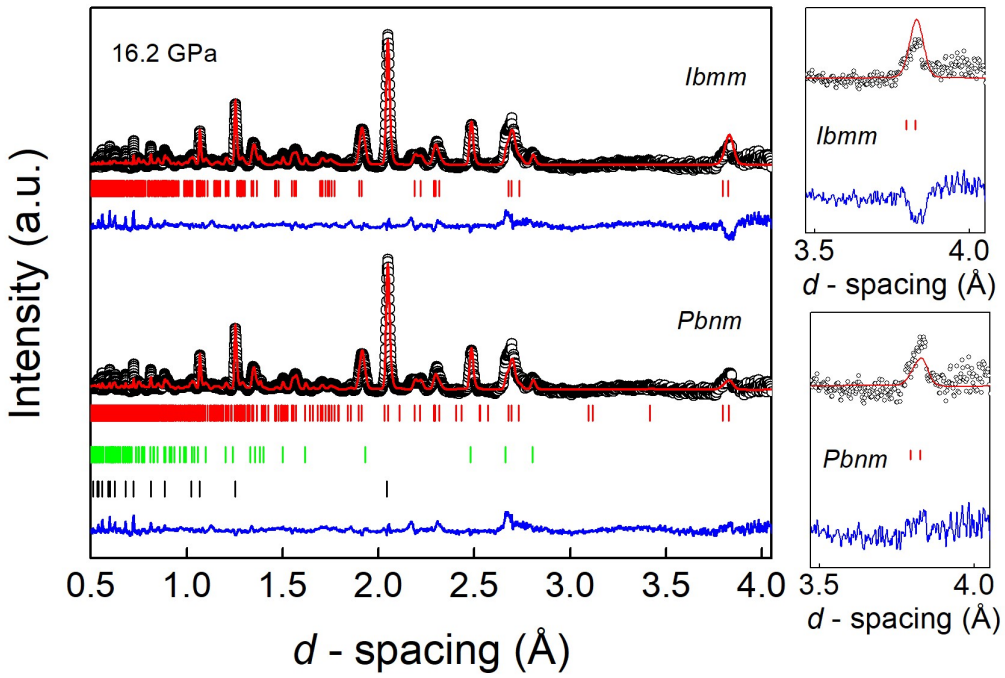

Figure 4.24 *Neutron diffraction patterns of $LaFeO_3$ collected at 290 K at 16.2 GPa. Experimental data are shown as open circles, while red solid lines show Rietveld refinement curves to the data adopting a Pbnm (bottom pattern) and Ibmm (top pattern) space group. Blue lines show residuals of the Rietveld fits. Vertical tick marks indicate calculated reflections from top to bottom: sample (Pbnm bottom pattern, Ibmm top pattern), h.c.p lead pressure marker, and diamond anvils. The Rietveld fits yielded wR_p values of (%) 6.46 (Pbnm) and 6.81 (Ibmm). Patterns on the right show a zoom in the 3.5–4.0 Å of the (002) and (110) Bragg reflections.*

Rietveld fits and refined fractional coordinates according to the two different structural models are reported in Table 4.5. Refined structural parameters and determined bond distances and angles are reported in Table B.3 in Appendicex B.

The transition from a primitive to a body-centred lattice is manifested by a systematic disappearance of selected Bragg reflections. Different symmetry operators are associated to the I-type lattice, which increase the combination of $\{h, k, l\}$ Miller planes giving disruptive interference. In the case of an *Ibmm* space group, the restriction on the (hkl)-indexed reflection is given by: $h + k + l = 2n$. Bragg reflections such as the (111) or the (201) are then forbidden and should disappear as the transition from *Pbnm* occurs. No clear visual evidence is found in the neutron patterns of Figures 4.23 and 4.24 of such structural transition.

Table 4.5 *Refined structural coordinates of $LaFeO_3$ according to the Pbnm and Ibmm space groups at pressures of 12.1 and 16.2 GPa as determined by Rietveld refinement. Fe cations are placed in special positions $(0, \frac{1}{2}, 0)$ The wR_p and χ^2 values of the Rietveld fits are also reported.*

12.1 GPa			
Space Group		*Pbnm*	*Ibmm*
	wR_p %	6.74	7.87
	χ^2	1.180	1.700
La	x	1.002(2)	1.006(3)
	y	0.020(2)	0
	z	0.25	0.25
O1	x	0.063(2)	0.066(2)
	y	0.491(4)	0.5
	z	0.25	0.25
O2	x	0.730(2)	0.75
	y	0.284(2)	0.25
	z	0.033(1)	0.035(1)
16.2 GPa			
Space group		*Pbnm*	*Ibmm*
	wR_p %	6.46	6.81
	χ^2	2.915	3.229
La	x	0.995(2)	0.991
	y	0.037(1)	0
	z	0.25	0.25
O1	x	0.068(2)	0.080(3)
	y	0.498(2)	0.5
	z	0.25	0.25
O2	x	0.730(2)	0.75
	y	0.275	0.25
	z	0.030(1)	0.031(1)

Although the primitive orthorhombic (111) reflection is not observed at both pressures, this cannot be interpreted in terms of an *Ibmm* lattice. The absence of this reflection is mostly ascribed to an increased attenuation of the integrated intensities caused by the use of sintered diamond anvils.

A further evidence of this structural transition may arise from the behaviour of the refined La(y) fractional coordinate in the *Pbnm* space group at 12.1 and 16.2 GPa, shown in Figure 4.25.

While in the low pressure range up to 5.5 GPa La(y) seems not affected by the application of pressure, at 12.1 and 16.2 GPa not only the refined values strongly diverge from previously refined coordinates, but are also in strong disagreement

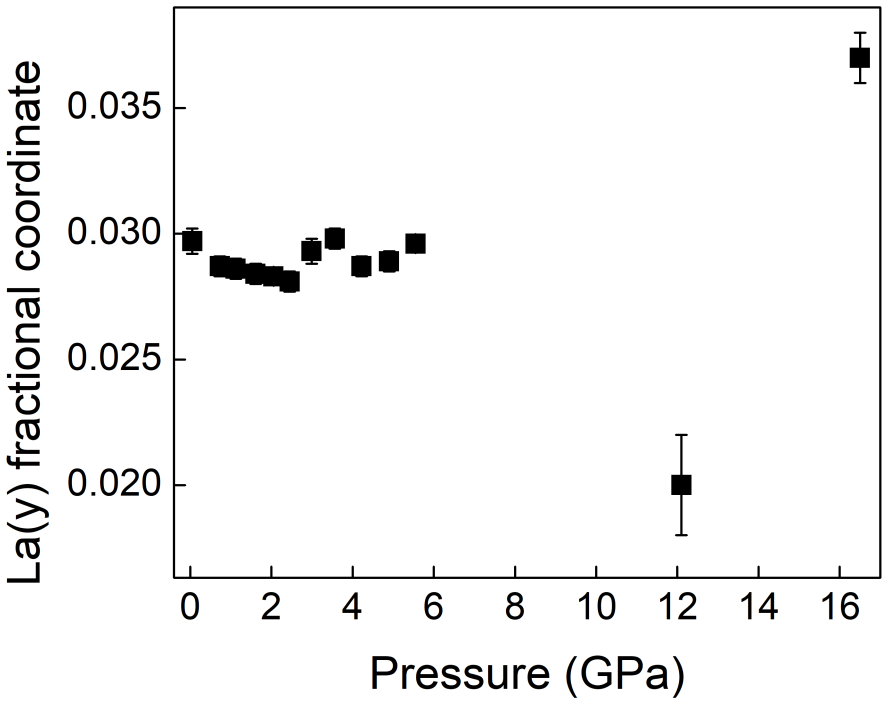

Figure 4.25 *Refined La(y) fractional coordinate of $LaFeO_3$ as a function of pressure adopting the Pbnm space group. The data show refined La(y) fractional coordinate from the two combined data sets: 0–5.5 GPa and 12.1/16.2 GPa.*

between each other. This may suggest that the *Pbnm* structural model is not appropriate at these selected pressures and a best structural fit is provided by the *Ibmm* space group. It is interesting to highlight the contrast between the high-pressure and high-temperature behaviour of the structural and magnetic properties of $LaFeO_3$. The oxide is reported to transform rhombohedral upon heating, whereas orthorhombic body-centred under hydrostatic pressure. Firstly, this is allowed by theory [78], which states that the vanishing of the M_3^+ symmetry adapted mode can promote either the rhombohedral $R\bar{3}c$ or the body-centred *Ibmm* space group. The origin of this different transition may rely in the different structural changes promoted by temperature and pressure on the structure. While temperature promotes an overall isotropic expansion of the crystal structure [104, 226], pressure drives a strongly anisotropic compression of bonds and lattice parameters.

Attempts to refine the ordered magnetic moment of the sample were performed. However, this led to unphysical values, higher than the theoretical limit of

$5(\mu_B)$ for high-spin Fe^{3+} ordered moments of $LaFeO_3$. Neutron-diffraction data at pressures higher than 10 GPa were performed with a different high-pressure equipment with respect to experimental data reported in the 0–6.5 GPa range. Sintered diamond anvils were used instead of the ZTA anvils. This allows us to generate higher pressures, but in the same time the use of sintered diamonds anvils causes an increased attenuation effect on the integrated intensity of neutron patterns. This is especially true for Bragg reflections at high d-spacing, as discussed for the (111) Bragg reflection, where the attenuation effect is mostly intense. Despite the data were reduced for sintered diamond attenuation, this may reflect the behaviours of parameters such as the modulus of the magnetic moment and the atomic coordinates.

4.3.6 Raman spectroscopy

Raman spectroscopy was also performed under high pressure on $LaFeO_3$. Spectroscopic investigations can complement the structural study performed by neutron diffraction and give insight in the local structural distortions of the material. The orthorhombic *Pbnm* symmetry is characterised by twenty-four Raman-active vibrational modes, which decompose into $\Gamma_{\text{Raman}} = 7A_g + 5B_{1g} + 7B_{2g} + 5B_{3g}$ [181]. Raman spectra were collected at ambient temperature in the 0–7.6 GPa pressure range and representative spectra are shown in Figure 4.26 in the $\sim$150–550 cm^{-1} Raman shift range.

Raman patterns are in agreement with ambient pressure and pressure dependent Raman spectra previously reported for ortho-ferrites and $LaFeO_3$ [201, 233–237]. Figure 4.27 shows a selected spectrum of $LaFeO_3$ in the 150–500 cm^{-1} acquired at 5.4 GPa.

Mode symmetries are assigned according to a previous ambient pressure study [235]. Raman peak positions were determined by Gaussian fits of the peak profiles. The associated uncertainty, which fell on the second decimal digits, are not reported.

The two Raman modes at 156 and 186 cm^{-1} are related to the lanthanum vibrational motion. However, because of the small volume of the La cage due to the small ionic radius of the lanthanum, these modes are also influenced by the FeO_6 octahedral rotations (around the [110] and [001] directions in *Pbnm*) and thereby the tilting angles.

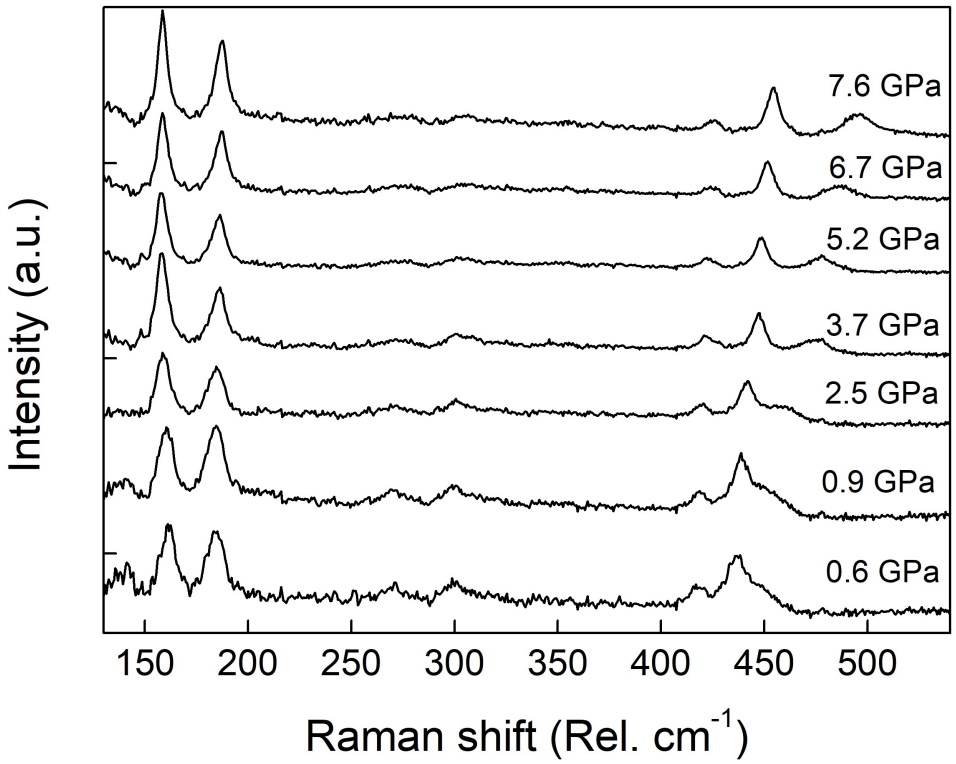

Figure 4.26 *Raman spectra of $LaFeO_3$ acquired in a Merrill-Basset diamond anvil cell in the 0–7.6 GPa pressure range. A diode laser (λ = 532.23 nm) was used with a laser power of 5 mW at the sample position, to avoid fluorescence from the sample, which occurs at higher laser powers.*

Figure 4.28 shows the variation in energy of these two modes as a function of pressure. While the fitted mode at 186 cm^{-1} stiffens as expected under high-pressure due to the decrease of the unit-cell lattice parameters, the mode at 158 cm^{-1} softens upon compression. This may be the initial indication of a structural phase transition in $LaFeO_3$ driven by the decrease of the in-phase octahedral distortion around the *c*-crystallographic axis. This mode transforms as the *irrep* M_3^+, whose amplitude decreases as a function of pressure as previously shown in Figure 4.20.

A high pressure Raman study on $LaFeO_3$ has been recently reported. In this work the structure has been investigated up to the structural transition pressure of 20 GPa, and it is suggested that the structure undergoes a structural transition in the investigated pressure range [237] because of the disappearance of the mode around 180 cm^{-1}, related to the in-phase tilting angle. Such mode is nearly

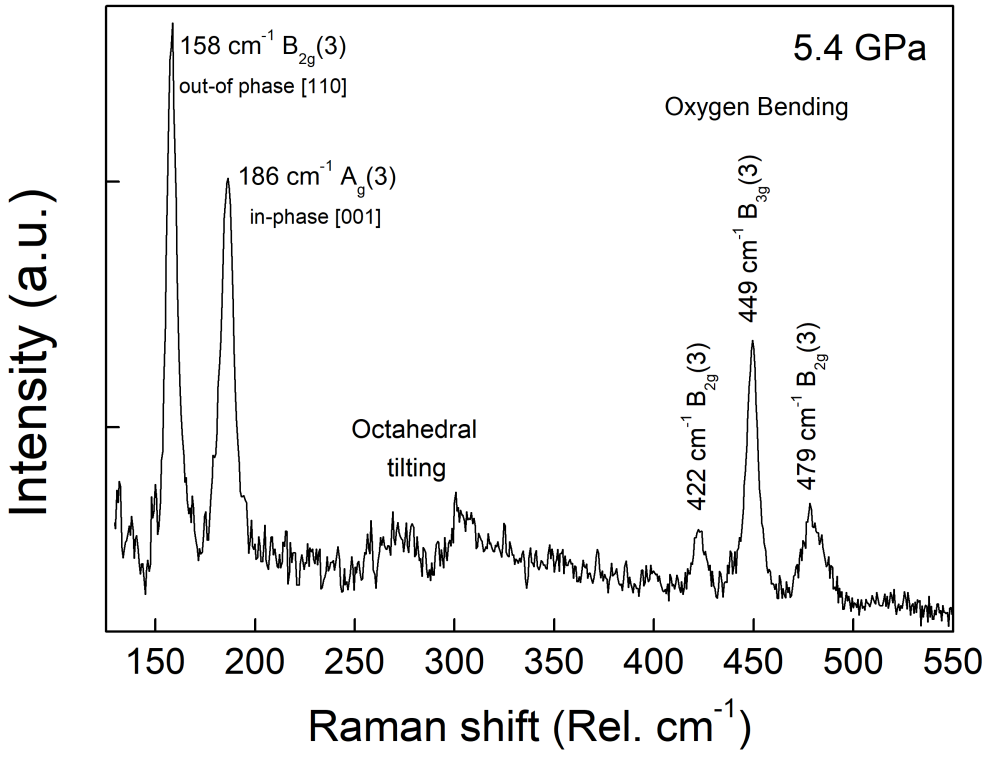

Figure 4.27 *Raman spectrum of $LaFeO_3$ collected at 5.4 GPa in the 100–550 cm^{-1} range using a Merrill-Bassett diamond anvil cell. Vibrational mode symmetries are assigned according to previous polarisation-dependent Raman study of $LaFeO_3$ [235].*

vanished at 15.6 GPa and totally vanished at a pressure of 19.4 GPa.

Raman modes associated to the oxygen displacements, hence tilting angle are also found in the 250–320 cm^{-1} range, while Raman vibrations related to oxygen bending modes are found in agreement with literature in the 400–500 cm^{-1} range. The oxygen bending modes are associated to different crystallographic directions and are seen to shift to higher energy in the pressure range investigated as shown in Figure 4.29, where their relative Raman shift is plotted as a function of the applied pressure. The B_{3g} mode is initially overlapping with the much more intense modes in the 400–500 cm^{-1} range. After 2 GPa such a mode is clearly distinguishable and hardens more strongly than the other octahedral bending mode vibrations.

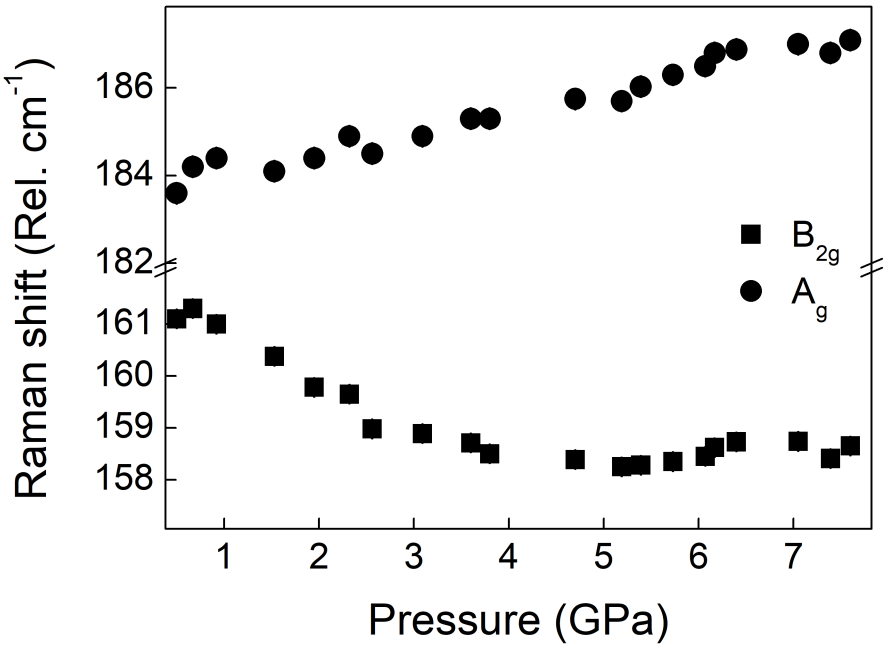

Figure 4.28 *Relative Raman shift variation as a function of pressure of the 156 and 180 cm^{-1} Raman modes of $LaFeO_3$ associated to both lanthanum vibrations and tilting of the FeO_6 octahedra.*

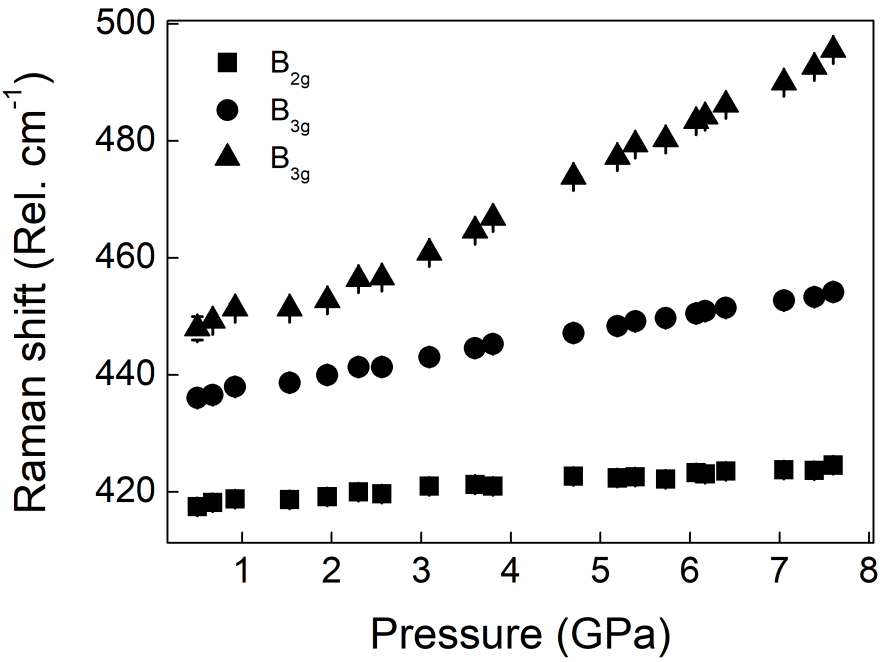

Figure 4.29 *Relative Raman shift as a function of pressure of the oxygen bending modes of $LaFeO_3$.*

4.4 Summary and conclusions

This study reports the structural and magnetic changes in the $LaFeO_3$ perovskite as a function of pressure and temperature. $LaFeO_3$ exhibits the orthorhombic *Pbnm* space group at temperatures of 110 and 290 K in the 0–6.5 GPa pressure range. The bulk modulus of $LaFeO_3$ was determined at each temperature and the compression behaviour analysed, which is observed to be strongly anisotropic. The G-type antiferromagnetism is also observed to be stable over the pressure ranges investigated and at each temperature, with a magnetic moment nearly unchanged by the application of pressure in the 0–6.5 GPa range. The a and b lattice parameter cross-over, previously reported as a function of temperature, was observed at 2 GPa at ambient temperature and at a slightly lower pressure of 1.7 GPa at 110 K. Accurate determination of the in-phase and out-of phase tilting angles was reported and a significant decrease of the in-phase tilting distortion is observed. The FeO_6 octahedra are found to be significantly deformed and it has not been possible to quantify the distortion parameters of $LaFeO_3$ by pure geometrical relations and a proper refinement of the atoms positions was necessary.

A transition from primitive *Pbnm* to body-centred *Ibmm* was previously reported around a pressure of 20 GPa. From the Rietveld refinement analysis shown in this work, no clear visual evidence of this structural transition is observed at the selected pressures of 12.1 and 16.2 GPa. Anomalies in the refined atomic coordinates adopting the *Pbnm* space group at each pressure point may indicate a loss of quality of a *Pbnm* fit. R-factors and χ^2 values of the Rietveld refinements are indeed comparable at both pressures, and no clear best-fit profile can be determined by Rietveld refinement. $LaFeO_3$ shows a strong difference in its temperature and pressure structural and magnetic behaviour. The crystal structure, which is reported to transform trigonal $R\bar{3}c$ at high temperature, transforms body-centred orthorhombic by application of hydrostatic pressure. Moreover, while temperature suppresses the magnetic moment of the sample, pressure is seen not to affect the antiferromagnetic interactions at ambient temperature in the 0–5.5 GPa pressure range.

Chapter 5

Effect of pressure in doped perovskite oxides: magnetic and structural study of $LaCo_{0.9}Mn_{0.1}O_3$.

This chapter studies the effect of pressure in the structural-physical properties of doped perovskites. The $LaCoO_3$ compound, extensively studied in Chapter 3, was selectively doped with a 0.1 relative fraction of manganese material on the B site. Changes in the high-pressure structural characteristics and physical properties are reported and discussed. High-pressure structural and magnetic characterisation was carried out on the $LaCo_{0.9}Mn_{0.1}O_3$ oxide. The bulk modulus of the sample was determined and accurate determination of the structural parameters and chemical bonds is reported. The neutron diffraction study is complemented with DC magnetometry measurements under high pressure, which are used to calculate the Curie temperature of the sample and its variation as a function pressure.

5.1 Background

$LaCo_{0.9}Mn_{0.1}O_3$ is a member of the $LaCo_xMn_{1-x}O_3$ perovskite series, on which has centred an intense research activity owing to remarkable changes in its electrical and magnetic properties in response to changes in chemical composition x or volume [31, 40, 121, 238, 239]. By selective doping divalent/trivalent/tetravalent cations can be introduced on the B-site of this family of compounds. Variations

in the oxidation state of the transition metal cations, Co and Mn, modifies the electronic structure of the materials and leads to a rich variety of electronic correlation phenomena, for example colossal magnetoresistance [28] or spin state transitions [240]. Low Mn doping in $LaCo_xMn_{1-x}O_3$, such as in $LaCo_{0.9}Mn_{0.1}O_3$, is found to create an efficient catalyst for particulate of exhausted substances in vehicles [43]. Understanding the structural-physical changes under high pressure of the structure is key to tune the catalytic properties of this compound and give insight on fundamental structural-physical correlated phenomena.

Members of the $LaCo_xMn_{1-x}O_3$ series exhibit different crystal symmetries and electronic configurations dependent on the composition x. The end member ($x = 1$), $LaCoO_3$, is a diamagnetic insulator which crystallises at ambient conditions into a trigonal structure with space group $R\bar{3}c$ [84]. At low T ($\sim 50\,\mathrm{K}$) $LaCoO_3$ is a non magnetic insulator with the Co^{3+} in the low-spin $S = 0$ state with electronic configuration $t_{2g}^6 e_g^0$. The change in spin-state configuration of Co^{3+} has been previously well documented [84, 123, 124, 241] and discussed in detail in Chapter 3. The opposite end member ($x = 0$), $LaMnO_3$, is an insulating, antiferromagnetic

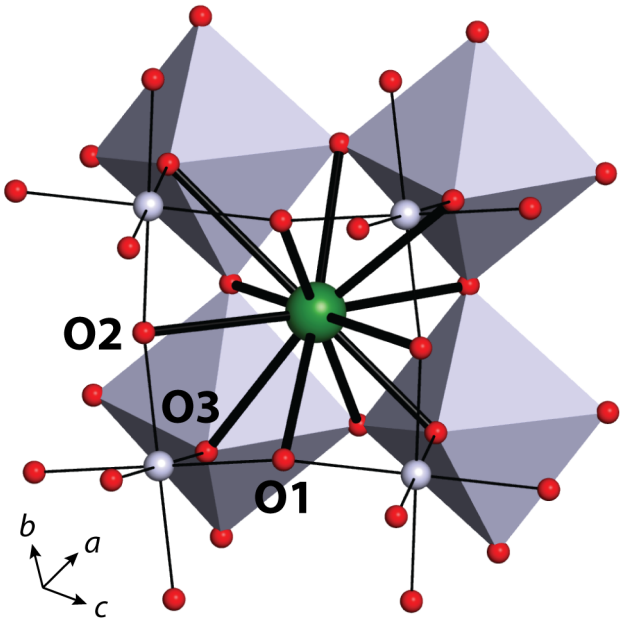

Figure 5.1 *Schematic representation of the crystal structure of $LaCo_{0.9}Mn_{0.1}O_3$. The crystal structure has trigonal symmetry $R\bar{3}c$ space group. The Co cation is placed on the Wyckoff site 2b $(0,0,0)$ coordinated by six oxygen atoms. The A-site cation, Wyckoff site 2a $\left(\frac{1}{4},\frac{1}{4},\frac{1}{4}\right)$, is placed in interstitial sites coordinated by twelve oxygen atoms, which are divided into three groups by different La-Oi (i = 1, 2, 3) bond lengths.*

material which crystallises in an orthorhombic structure with space group *Pbnm*. $LaMnO_3$ transforms to a ferromagnetic pseudo-cubic structure at ∼750 K. Across the composition range $0.1 < x < 0.9$ the crystal symmetry changes with x. At room temperature, members within $x = 0.1 - 0.4$ are orthorhombic with no ordering of the transition metal ions, whereas for $x = 0.5$ the material crystallises with monoclinic $P2_1/n$ symmetry and shows site ordering of the Co and Mn ions [92]. $LaCo_{0.9}Mn_{0.1}O_3$ and materials in the $x = 0.6 - 0.9$ range crystallise in the trigonal symmetry [31, 238] of which a schematic representation is reported in Figure 5.3 for the $LaCo_{0.9}Mn_{0.1}O_3$ sample. Within the $0.1 \leq x \leq 0.9$ range ferromagnetic ordering is predominant across the series with cobalt ions in diamagnetic low-spin state [240]. More recently, for the high cobalt compositions a highly non-uniform magnetic state of short-range ferromagnetic domains and ionically disordered spin-glass domains is suggested, in parallel to a dominance of antiferromagnetic interactions. This suggests a mixture of intermediate and high Co^{3+} states for the cobalt ion at high temperatures and a charge disproportionated Co^{2+}/Co^{4+} state [242].

A study of the structural and magnetic phase diagram of the series was recently reported by neutron diffraction and magnetisation measurements [238]. In this work, the composition $x = 0.9$ was studied by AC susceptibility measurements and a spin-glass-like behaviour was found at low temperature. A combination of Mn^{4+} ions and a mixed-valent cobalt in an intermediate spin state was proposed, stressing the difficulties to assign specific oxidation and spin states due to the disordered cation distribution across the structure.

5.2 Experimental

5.2.1 Synthesis

$LaCo_{0.9}Mn_{0.1}O_3$ was synthesized by the nitrate decomposition route, as previously reported in reference [186]. Details of the synthesis procedure are reported in Section 2.11. The degree of phase purity was verified by X-ray diffraction using a Rigaku MINIFLEX X-ray diffractometer, and further by neutron-diffraction characterisation on the POLARIS instrument, at the ISIS facility.

5.2.2 High-pressure neutron diffraction

High-pressure neutron-diffraction measurements were performed in the 0–6 GPa pressure range on the PEARL instrument, at the ISIS Neutron and Muon facility [158]. High pressure was applied by the use of a V3 variant Paris-Edinburgh press equipped with toroidal zirconia-toughened-alumina anvils [159]. The sample was loaded into a TiZr alloy encapsulated gasket [163]. Hydrostatic pressure conditions were obtained by the inclusion of a 4:1 ratio perdeuterated methanol-ethanol fluid. Lead was placed in the sample volume and used to determine the sample pressure. Neutron-diffraction data were collected in 5 tonnes steps up to a maximum of 65 tonnes. A beamline-developed correction for the wavelength and scattering-angle dependence of the neutron attenuation by the anvil (ZTA) and gasket (TiZr) materials was applied to the observed pattern [158]. The experimental patterns were normalised using in-house software MANTID [205] and Rietveld refinement of the data was performed using the GSAS package [146].

5.2.3 Magnetic characterisation

DC magnetisation measurements were performed using a MPMS-XL SQUID magnetometer at the Material Characterisation Laboratory, at the ISIS facility. The sample was loaded into a miniature Turn-buckle high pressure diamond anvil cell [185] specially designed for high-pressure magnetometry measurements and previously shown and described in Section 2.10.1. A CuBe gasket was used and a 4:1 ratio methanol-ethanol mixture was utilised as pressure transmitting medium. A ruby sphere, placed in the sample volume, was used to determine the pressure on the material by the ruby fluorescence technique [175]. The DAC was mounted into a plastic straw and aligned to the sample instrument position. Measurements of the temperature dependent DC magnetisation were carried out as a function of pressure from ambient to 4.1 GPa in an applied field of 100 Oe on both field-cooled (FC) and zero-field-cooled (ZFC) samples.

The mass of sample contained within the pressure cell is of the order $\sim$0.1 mg. In order to extract the weak magnetic signal from such a small volume of sample, careful background corrections are required. Measurements were first taken on an empty pressure cell, at ambient pressure, over the full temperature range investigated. Measurements of the pressure cell loaded with the sample were

performed in exactly the same conditions of mounting position, temperatures, fields, and cooling rates. To extract the sample contribution from the measured signal, an interpolated subtraction of the two moment-temperature curves was performed.

5.3 Results and discussions

5.3.1 High-pressure neutron diffraction

Neutron-diffraction data of $LaCo_{0.9}Mn_{0.1}O_3$ were collected at ambient temperature in the 0–6 GPa range. Experimental data are shown in Figure 5.2 as open circles. Representative neutron-diffraction patterns and Rietveld refinement details of $LaCo_{0.9}Mn_{0.1}O_3$ at pressures of 0.1 and 6.1 GPa are shown in Figure 5.3.

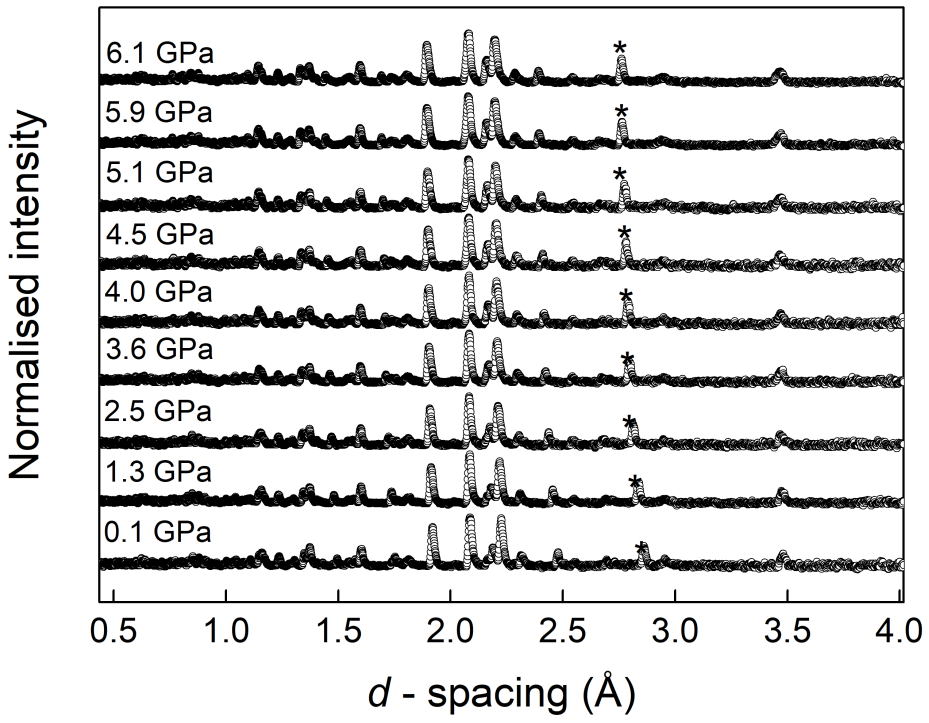

Figure 5.2 *Neutron diffraction data (open circles) of $LaCo_{0.9}Mn_{0.1}O_3$ collected on the PEARL instrument. Neutron diffraction intensities were focused by the used of the Mantid software [205]. Reflections marked as * indicate (111) Bragg reflections from the lead pressure marker.*

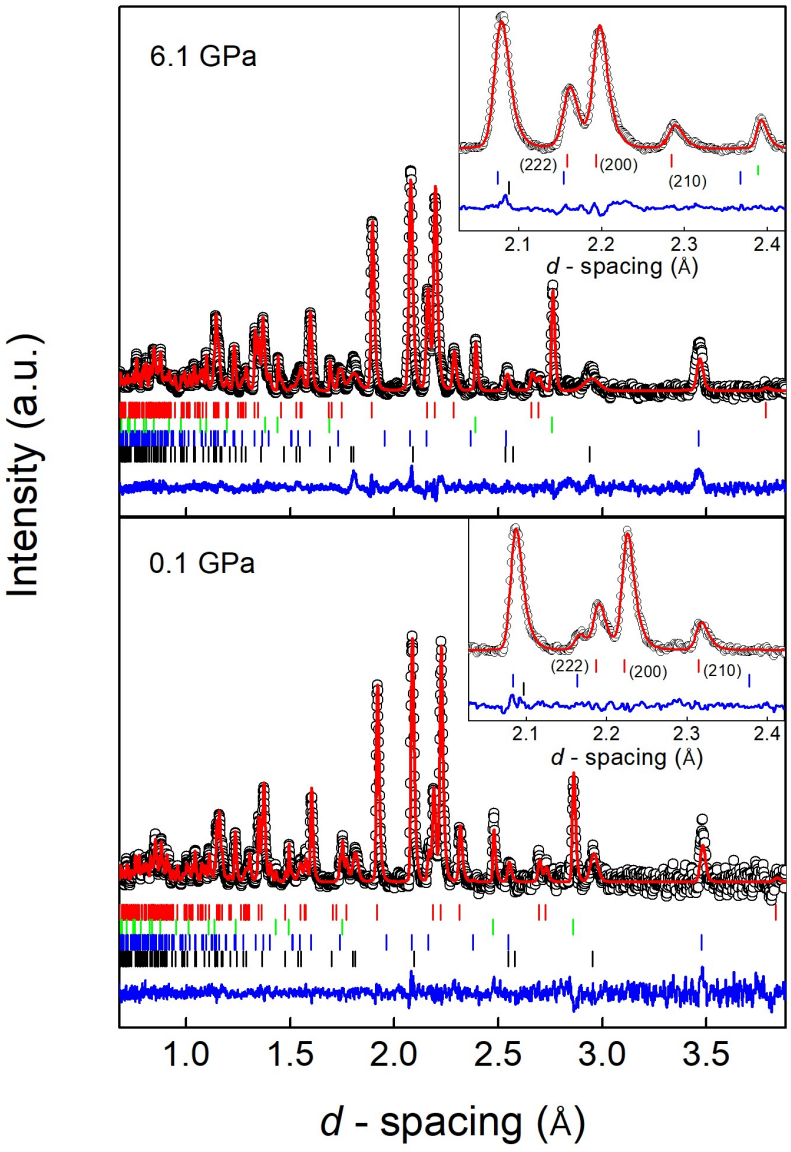

Figure 5.3 *Neutron diffraction pattern of $LaCo_{0.9}Mn_{0.1}O_3$ at a pressure of 0.1 and 6.1 GPa. Experimental data, depicted as open circles, were refined with an $R\bar{3}c$ rhombohedral model, which is shown as solid red line. Calculated reflections from sample, lead pressure marker, and anvils are also indicated as vertical tick marks: from top to bottom, sample, lead marker, alumina and zirconia. The bottom line shows the residual of the Rietveld refinement as difference between the experimental data and the calculated structure. Insets show a zoom in the 2–2.4 Å range of the (222), (200) and (210) trigonal reflections.*

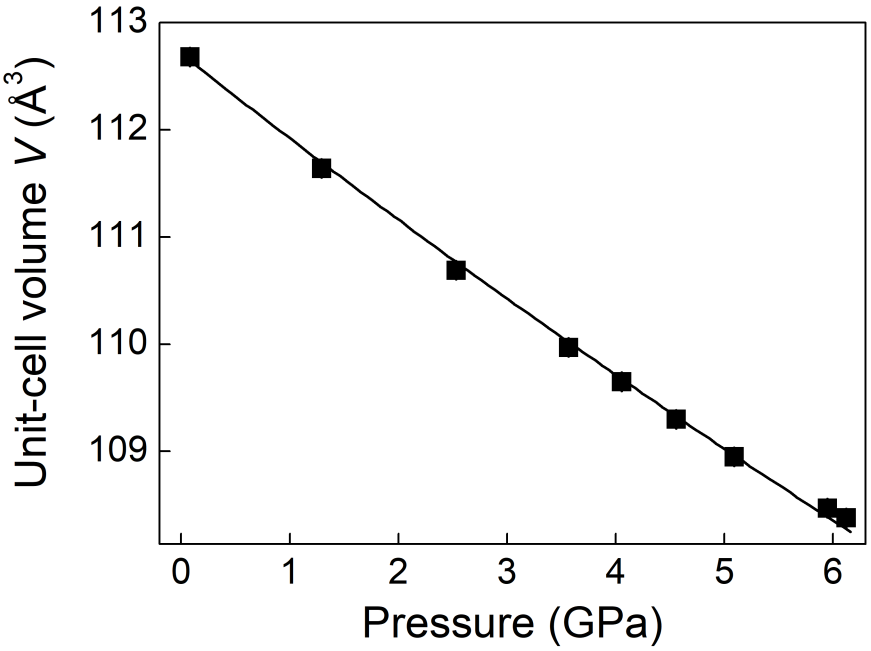

Figure 5.4 *$LaCo_{0.9}Mn_{0.1}O_3$ unit-cell volume (V) as a function of pressure. Solid line shows a second order ($B' = 4$) Birch-Murnaghan fitting equation. The fitted bulk modulus B_0 and volume V_0 parameters are B_0=140(11) GPa and V_0=112.7(2) Å^3. Error bars are also shown but smaller than symbols.*

Experimental data are shown as open circles, while solid red line represents the Rietveld refined curve. The data were fitted adopting the $R\bar{3}c$ space group, as reported previously for $LaCo_{0.9}Mn_{0.1}O_3$ [31, 238]. Refined structural parameters as a function of pressure are reported in Table 5.1 with details of the Rietveld fit. Neutron diffraction patterns show no evidence of symmetry lowering in the 0–6 GPa range and the rhombohedral phase is maintained in the pressure range studied. The absence of additional Bragg peaks of magnetic origin suggests no long-range magnetic order.

The unit-cell volume (V) as a function of pressure is shown in Figure 5.4. The compression is uniform in the pressure range studied, without any evidence of phase transition. The bulk modulus B_0 of the sample was calculated by means of the EoS-fitGUI software [206]. The volume compression data were fitted with a second-order ($B' = 4$) Birch-Murnaghan equation of state which yielded fitting values: V_0=112.7(2) Å^3 and B_0 = 140(11) GPa. The bulk modulus value is comparable to that determined for $LaCoO_3$ by X-Ray diffraction (150(2) GPa, [124]), but smaller than the 165(5) GPa determined by neutron diffraction [123],

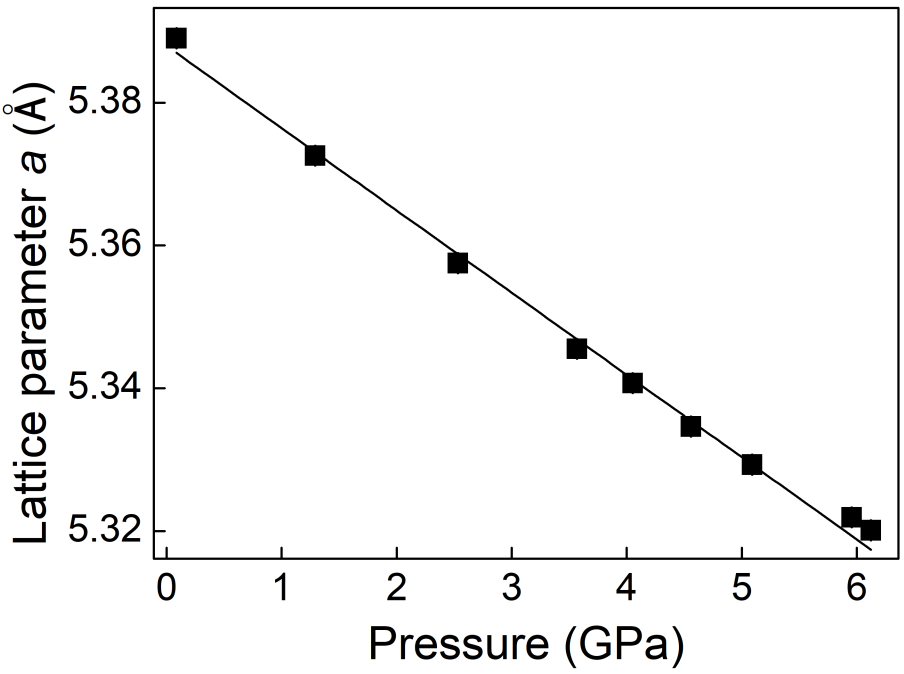

Figure 5.5 *Lattice parameter of $LaCo_{0.9}Mn_{0.1}O_3$ as a function of pressure. Solid line shows a linear fit to the data which yielded: $a_0 = 5.388(1)$Å and a compressibility rate $k_a = 0.0021(2)\,GPa^{-1}$. Error bars are also shown but smaller than symbols.*

both adopting a second order Birch-Murnaghan EoS. The fitted bulk modulus of $LaCo_{0.9}Mn_{0.1}O_3$ is very close within experimental error to the 135(2) GPa value determined in this thesis for the end member $LaCoO_3$ at ambient temperature, while the fitted ambient pressure unit-cell volume V_0 is lower that the 112.12(1) Å^3 reported from the same study of $LaCoO_3$ [1]. The introduction of manganese atoms drives the stabilisation of a larger unit-cell, but does not cause particular changes in the structural compression. Further evidence comes from the lattice parameter a as a function of pressure, which is shown in Figure 5.5.

The lattice constant linearly decreases in the 0–6 GPa range with a compressibility rate of 0.0021(2) GPa^{-1} in agreement with what reported for $LaCoO_3$ in Chapter 3. In contrast, the rhombohedral unit-cell angle α shown in Figure 5.6 does not show a significant variation under the application of pressure.

As with $LaCoO_3$, the $R\bar{3}c$ rhombohedral structure of $LaCo_{0.9}Mn_{0.1}O_3$ can be described as the result of anti-phase Co/MnO_6 octahedra cooperative rotations around the cubic-parent [111] crystallographic direction [65, 66]. The magnitude

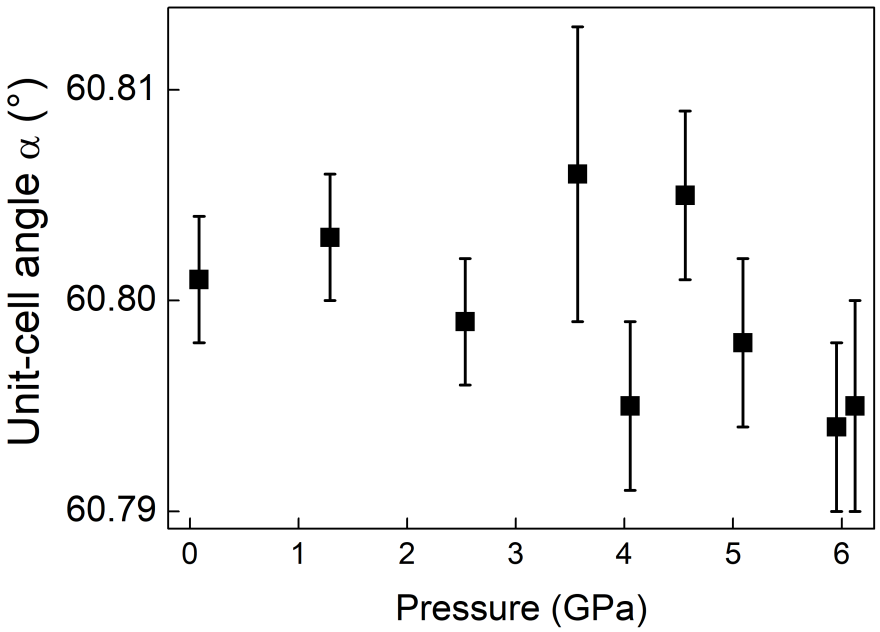

Figure 5.6 *Unit-cell angle α of $LaCo_{0.9}Mn_{0.1}O_3$ as a function of pressure. Error bars are also shown.*

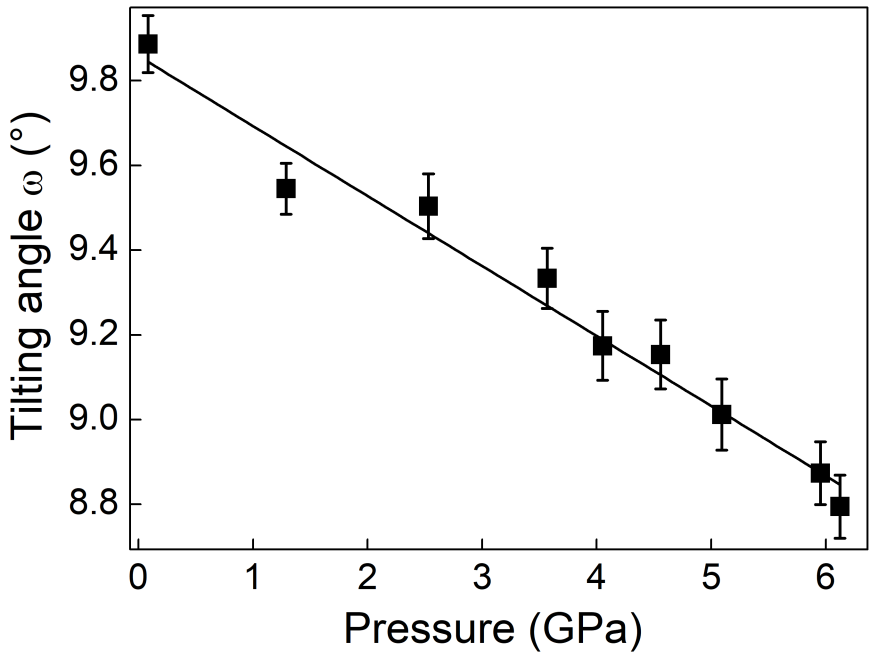

Figure 5.7 *Tilting angle (ω) of $LaCo_{0.9}Mn_{0.1}O_3$ as a function of pressure. Solid line shows a linear fit to the experimental data which yielded: $\omega_0 = 9.85(4)^\circ$ and $d\omega/dP = -0.16(1)\,10^{-3}\,^\circ/MPa$.*

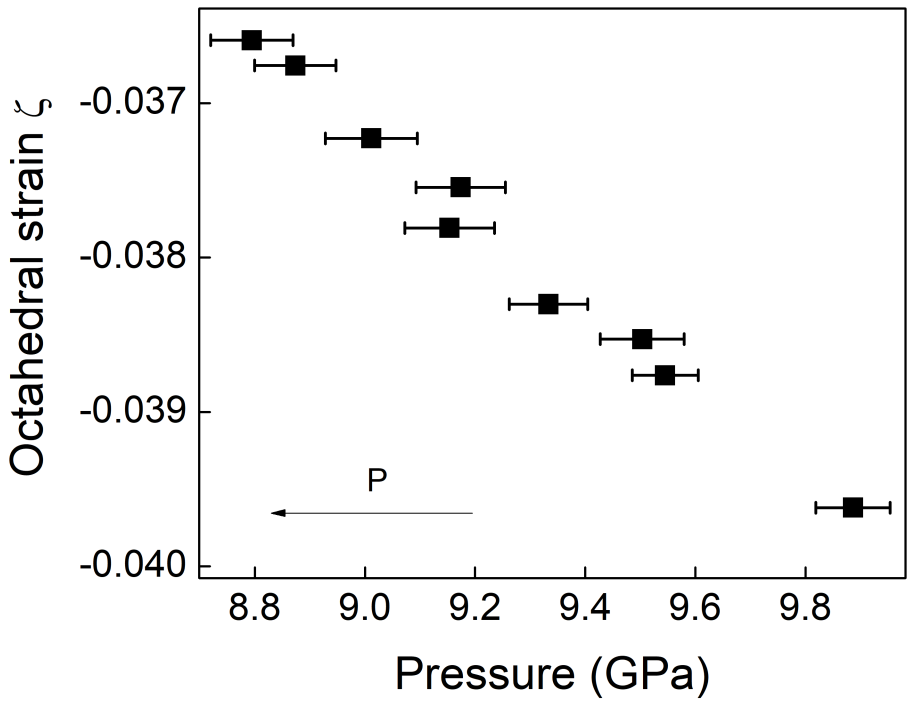

Figure 5.8 *Octahedral strain of $LaCo_{0.9}Mn_{0.1}O_3$ along the [111] cubic crystallographic direction as a function of the tilting angle parameter with increasing pressure. Error bars are also shown.*

of this distortion quantified by the tilting angle parameter ω as a response to hydrostatic pressure is shown in Figure 5.7.

The tilt angle ω decreases in the 0–6.1 GPa pressure range. The fitted ambient pressure value $\omega_0 = 9.85(4)^\circ$, determined by a linear fit to the data, is smaller than that of 10.3° reported for $LaCoO_3$ at ambient pressure and temperature [65, 187]. This suggests that the introduction of Mn cations reduces the tilting of the octahedra compared to that of undoped $LaCoO_3$. On further application of pressure, the tilt angle ω decreases as to tend to the ideal cubic value of $\omega = 0$. By linear extrapolation, it is calculated to become pseudo-cubic at a pressure of ∼61.5 GPa (assuming that the linear trend is maintained). Another distortion which characterises $LaCo_{0.9}Mn_{0.1}O_3$ is the homogeneous flattening or elongation of the Co/Mn–O_6 octahedra along the triad axis of the pseudo-cubic aristotype. The octahedral strain ζ is found to decrease linearly as a function of the tilt parameter ω and pressure, as shown in Figure 5.8. The extrapolated ambient pressure value of -0.0040 is lower than that of -0.0048 determined for $LaCoO_3$ [187]. As for the tilt angle ω, the introduction of Mn cations reduces the distortion

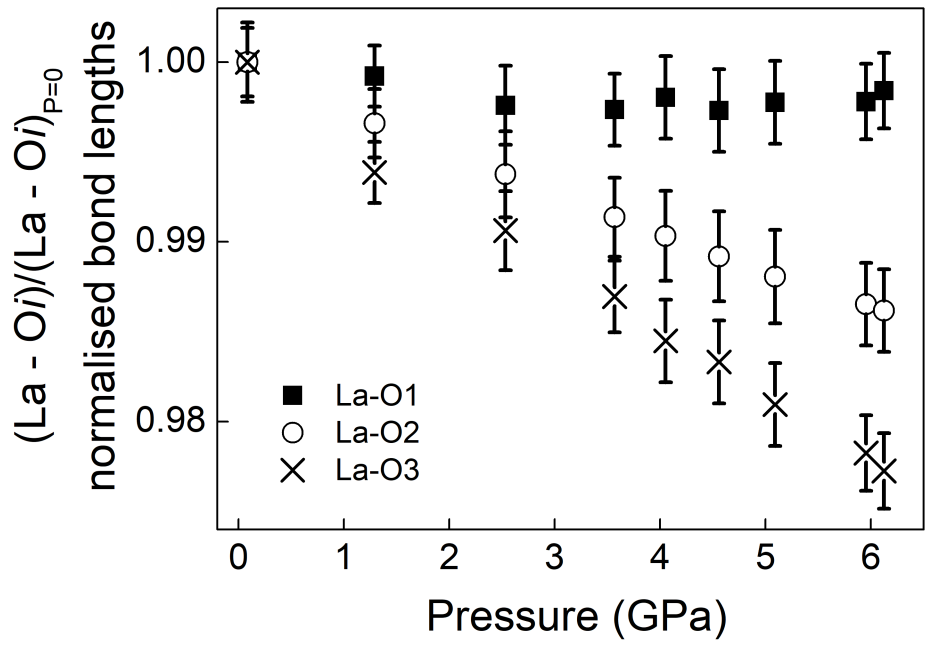

Figure 5.9 *Normalised La–Oi/(La–Oi)$_{P=0}$ bond distances (Figure 5.1) as a function of pressure. Note the small variation of the shortest La-O1 bond. Error bars are also shown.*

of the octahedra. As no significant variation is observed in the rhombohedral unit-cell angle α within the experimental error as shown in Figure 5.6, the overall reduction of the unit-cell volume appears to proceed via cooperative tilt and strain changes. Both strain and tilting angle distortions decrease under high pressure towards ideal values expected for a cubic structure. This suggests that application of pressure promotes a higher-symmetry structure in $LaCo_{0.9}Mn_{0.1}O_3$.

The variation of the La–Oi bond lengths under hydrostatic pressure was also investigated and their normalised values are shown as a function of pressure in Figure 5.9.

The shortest La–O1 bond length does not compress in the pressure range investigated, while the three/six-fold La–O2,3 bonds appear particularly sensitive to the applied pressure and linearly compress up to 6 GPa. The compressibility rates, calculated as $k = -L_0^{-1}(\mathrm{d}L/\mathrm{d}P)$, are $0.0036(1)\,\mathrm{GPa}^{-1}$ for La–O3 and $k = 0.0022(1)\,\mathrm{GPa}^{-1}$ for La–O2. The low compressibility reported for La–O1 respect to the other bonds may be due to the strong covalency of the shortest bond in the La-site caused by a larger overlap between the *2p* oxygen orbitals and the *4f* orbitals of the lanthanum.

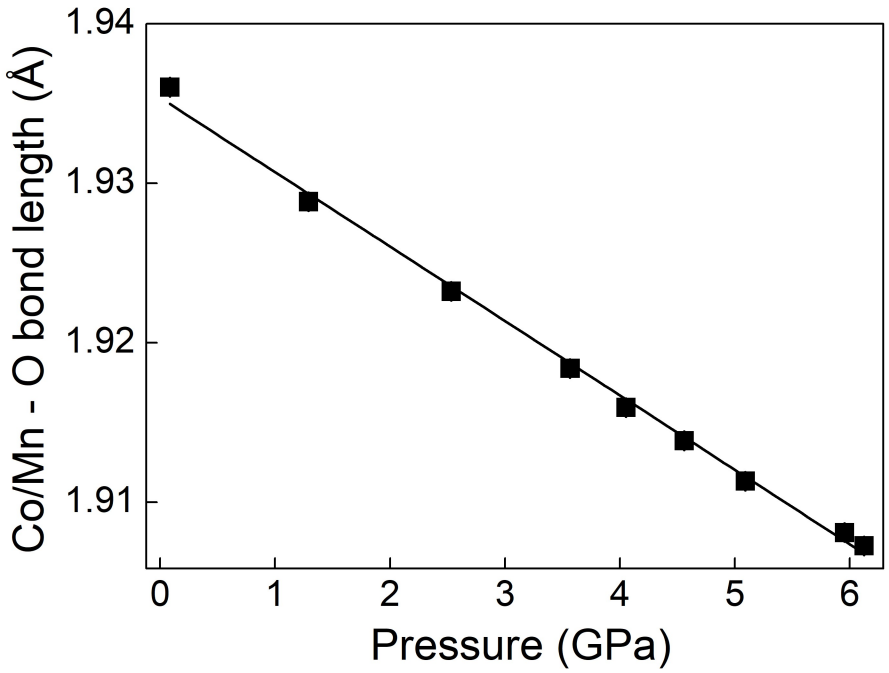

(a) **(b)**

Figure 5.10 *Average Co/Mn–O bond length as a function of pressure. Black solid line indicates a linear fit which yielded a compressibility rate of 0.0024(4) GPa^{-1}.*

Lastly, the evolution of the Co/Mn–O bond length and of the inter-octahedral Co/Mn–O–Co/Mn bond angle was analysed. As a result of the site disorder and the absence on average of the Jahn-Teller distortion effect, only the average Co/Mn–O bond distance and Co/Mn–O–Co/Mn bond angle can be determined by Rietveld refinement. From Figures 5.10a and 5.11, it can be seen that the Co/Mn–O bond length decreases as pressure increases, whilst the bond angle Co/Mn–O–Co/Mn increases with pressure, as observed in the pressure dependent neutron-diffraction study of $LaCoO_3$ by Kozlenko *et al* [123] for a smaller pressure range up to 4 GPa.

The calculated linear compressibility $k_{\text{Co/Mn–O}} = 0.0024(4)\,\text{GPa}^{-1}$ is in agreement with the $k_{\text{Co–O}} = 0.0024(3)\,\text{GPa}^{-1}$ compressibility reported by neutron diffraction [123] and with the compressibility rate determined in this work for $LaCoO_3$. It is also comparable to other rhombohedral perovskites such as $La_{0.7}Sr_{0.3}CoO_3$ [243] and $La_{0.7}Sr_{0.3}MnO_3$ rhombohedral manganite which shows a compressibility rate of $k_{\text{Mn–O}} = 0.0019(2)\,\text{GPa}^{-1}$, as determined by the Mn–O bond lengths data reported in reference [244]. The Mn doping is still too low to affect significantly

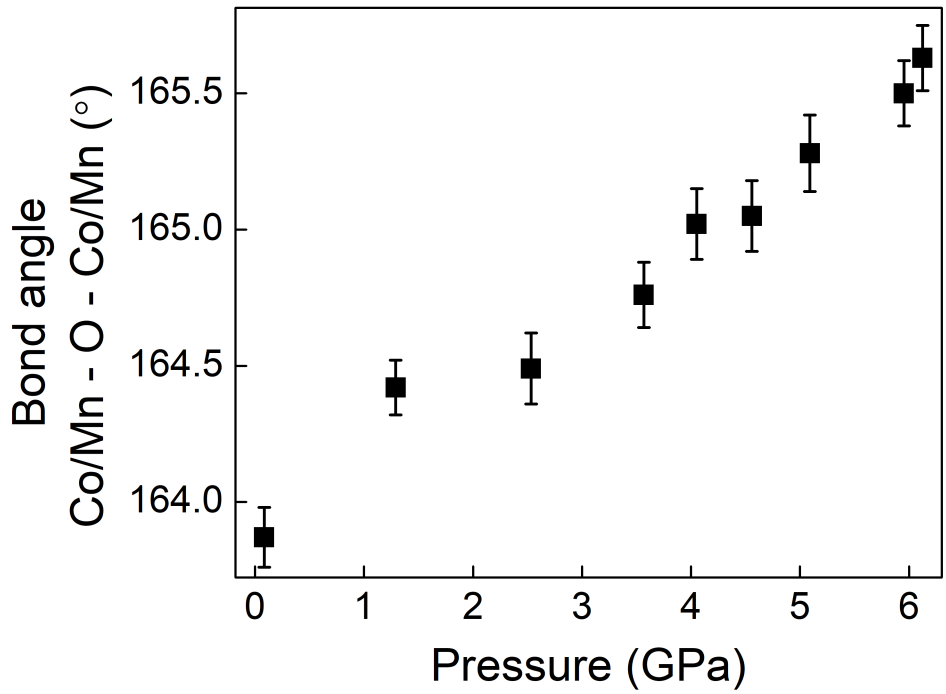

Figure 5.11 *Average Co/Mn–O–Co/Mn inter-octahedral bond angle as a function of pressure. Error bars are also shown.*

the compression rate, which seems dominated by the Co ions. Table 5.1 reports tilt angle, octahedral strain, the average Co/Mn–O bond distance, the Co/Mn–O–Co/Mn bond angle and the La-O bond distances values from ambient pressure to 6.1 GPa.

Table 5.1 *Structural parameters, tilting angle, octahedral strain, average Co/Mn–O bond distance, Co/Mn–O–Co/Mn bond angle, and La-O bond distances of $LaCo_{0.9}Mn_{0.1}O_3$ as a function of pressure, determined by Rietveld refinement. The atomic positions for La and Co/Mn cations in the proposed structure are: La $\left(\frac{1}{4},\frac{1}{4},\frac{1}{4}\right)$ and Co/Mn (0,0,0), on the Wyckoff sites 2a and 2b, respectively. The oxygen atoms are located on the 6e site $\left(-x,-x+\frac{1}{2},\frac{1}{4}\right)$, hence, the O_x positions are the only refinable parameters in the Rietveld procedure as well as the unit cell parameters. The R_p and wR_p values of the Rietveld fits are also reported.*

Pressure (GPa)	0.08(3)	1.29(3)	2.53(2)	3.56(3)	4.05(3)
V (Å^3)	112.669(6)	111.643(6)	110.697(8)	109.971(7)	109.649(8)
a (Å)	5.3890(2)	5.3726(2)	5.3575(2)	5.3455(2)	5.3407(2)
α (°)	60.801(3)	60.803(3)	60.799(3)	60.806(7)	60.795(4)
O_x	0.2002(3)	0.2019(3)	0.2021(3)	0.2029(3)	0.2037(4)
ω (°)	9.78(6)	9.45(6)	9.41(7)	9.25(7)	9.09(8)
ζ	−0.03962	−0.03876	−0.03853	−0.0383	−0.03755
Co/Mn–O (Å)	1.9360(3)	1.9322(3)	1.9288(2)	1.9183(3)	1.9159(3)
Co/Mn–O–Co/Mn (°)	163.87(11)	164.49(13)	164.42(10)	164.76(12)	165.02(13)
La–O1 (Å)	2.457(2)	2.455(2)	2.451(2)	2.451(3)	2.452(2)
La–O2 (Å)	2.708(2)	2.698(1)	2.691(2)	2.684(2)	2.682(2)
La–O3 (Å)	2.999(2)	2.980(2)	2.970(2)	2.959(2)	2.952(2)
R_p %	4.2	3.6	4.5	4.0	4.5
wR_p %	3.6	3.2	4.0	3.5	4.0

Pressure (GPa)	4.55(2)	5.09(3)	5.91(4)	6.12(3)
V (Å^3)	109.305(9)	108.956(9)	108.491(7)	108.389(8)
a (Å)	5.3346(2)	5.3293(3)	5.3219(2)	5.3201(3)
α (°)	60.805(4)	60.798(4)	60.793(3)	60.795(5)
O_x	0.2039(4)	0.2046(4)	0.2053(3)	0.2057(3)
ω (°)	9.07(8)	8.93(8)	8.87(7)	8.72(7)
ζ	−0.03781	−0.03723	−0.03676	−0.03659
Co/Mn–O (Å)	1.9138(3)	1.9113(3)	1.9084(2)	1.9072(3)
Co/Mn–O–Co/Mn (°)	165.05(13)	165.28(14)	165.33(11)	165.63(12)
La–O1 (Å)	2.450(2)	2.452(2)	2.449(2)	2.453(2)
La–O2 (Å)	2.678(2)	2.675(3)	2.6721(2)	2.670(2)
La–O3 (Å)	2.948(2)	2.942(2)	2.936(2)	2.930(2)
R_p %	4.5	3.4	3.4	3.0
wR_p %	4.0	4.0	3.4	2.9

5.3.2 Magnetic characterisation

Temperature-dependent bulk DC magnetisation measurements were performed from ambient pressure to 4.1 GPa in both zero-field-cooling and field-cooling routes. Figure 5.12 shows a representative example of ZFC (crosses) and FC (squares) magnetisation measurements performed at an applied pressure of 4.1 GPa in the 2–300 K range and at an applied magnetic field H of 100 Oe.

The magnetisation, M, is expressed in *emu*, because the mass of the sample (which was loaded inside a DAC during experiments) could not be measured. A large difference between the FC and ZFC magnetisation curves was found below T_C. This diversity arises from the presence of a highly non-uniform magnetic state of short-range-ordered ferromagnetic regions in a disordered spin-glass-like matrix, as previously reported at ambient pressure [31, 238, 242] and confirmed in our work up to 4.1 GPa. The ZFC magnetisation curve shows two main features one at

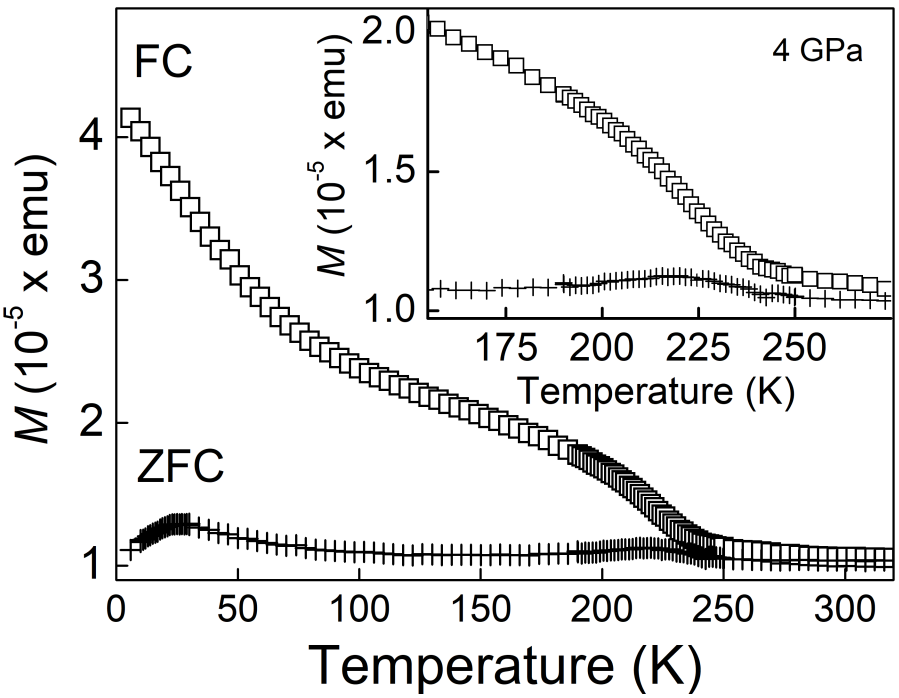

Figure 5.12 *Field-cooled (open squares) and zero-field-cooled (crosses) temperature-dependent DC magnetization measurements of $LaCo_{0.9}Mn_{0.1}O_3$ at an applied pressure of 4.1 GPa and applied magnetic field of 100 Oe. Inset shows an enlarged of the 150–275 K temperature range in proximity of the Curie temperature T_C. A low temperature peak is also found in the ZFC magnetisation curve (see text for details).*

Table 5.2 *Curie Temperature T_C and spin-glass-like transition temperature T_{sg} determined as a function of pressure from ambient pressure to 4.1 GPa. The corresponding tilting angle ω at each pressure point was extrapolated from the linear fit of the ω pressure evolution shown in Figure 5.7.*

Pressure (GPa)	0	0.66(1)	1.71(1)	2.55(1)	3.09(1)	3.56(1)	4.09(1)
ω (°)	9.85	9.75	9.57	9.44	9.34	9.28	9.18
T_C (K)	224.7	227.7	232.3	234.0	235.6	235.7	235.9
T_{sg} (K)	24.1	24.3	24.1	25.0	25.3	26.1	26.4

the Curie temperature T_C (∼236 K) and a second around 25 K, which arises from the spin-glass-like transition. T_C and the spin-glass-like transition temperature T_{sg} values are reported in Table 5.2 as a function of applied pressure and tilting angle ω.

Lack of consistency exists in the literature on the behaviour of the Curie temperature under the application of pressure. T_C shows both negative or positive pressure derivative, but has also been reported independent of pressure [245–249]. This unpredictable behaviour of T_C/dP depends on the complex combination of exchange interactions, such as direct exchange, superexchange, and double exchange, which take place in the perovskite structure and are responsible for its magnetic properties. The Curie temperature of $LaCo_{0.9}Mn_{0.1}O_3$ was determined as the minimum of the susceptibility first derivative in the ZFC measurements and its variation as a function of pressure and tilting angle ω is shown in Figure 5.13. The calculated ambient pressure value of 224.7 K is in agreement with that previously determined for $LaCo_{0.9}Mn_{0.1}O_3$ [238]. The Curie temperature of the doped sample is interestingly much higher than that determined for the parent compound $LaCoO_3$, which shows at ambient pressure a value of T_C ∼85 K as reported in previous work [192] and confirmed in this work of thesis by ambient pressure DC magnetometry measurements on $LaCoO_3$ (Chapter 3). As the tilting distortion decreases, the Curie temperature increases non-linearly in the pressure range studied to a value ∼ 236 K. At higher pressures T_C could stabilise around this value or decrease again after a maximum as can be seen by the trend in Figure 5.13.

Similar materials were studied under high-pressure such as the $La_{1-x}Sr_xMnO_3$ series [245]. In this series, the Curie temperature is reported to increase

as a function of pressure as a result of a pressure-enhanced double-exchange interaction, which is suggested to favour an increase of the electron mobility, hence increasing the Curie temperature. In $LaCo_{0.9}Mn_{0.1}O_3$ the initial trend of T_C indicates strengthening of the exchange interactions involved, but that must be interpreted under a more complicated view than a pure double-exchange model [31, 238, 242]. The initial positive shift of T_C under pressure may be attributed to a pressure-driven increase of the Co/Mn–O–Co/Mn bond angle and decrease of the tilting angle ω, which move towards ideal cubic values. The larger orbital overlap between ferromagnetic nearest neighbours is enhanced and the weak-short-range ferromagnetic interactions are reinforced [116, 188]. On further application of pressure, the Curie temperature shows decreasing pressure dependence. This may reflect the increase in octahedral crystal-field splitting between the t_{2g} and e_g orbitals in the transition-metals *3d*-shell caused by high pressure and reported for the end member $LaCoO_3$ [123]. Around 4 GPa $LaCoO_3$ is suggested to undergo an IS to LS state transition with all *3d* electrons in the t_{2g} orbitals, reducing the electron mobility within the structure.

The pressure behaviour of the spin-glass-like transition temperature T_{sg} as a

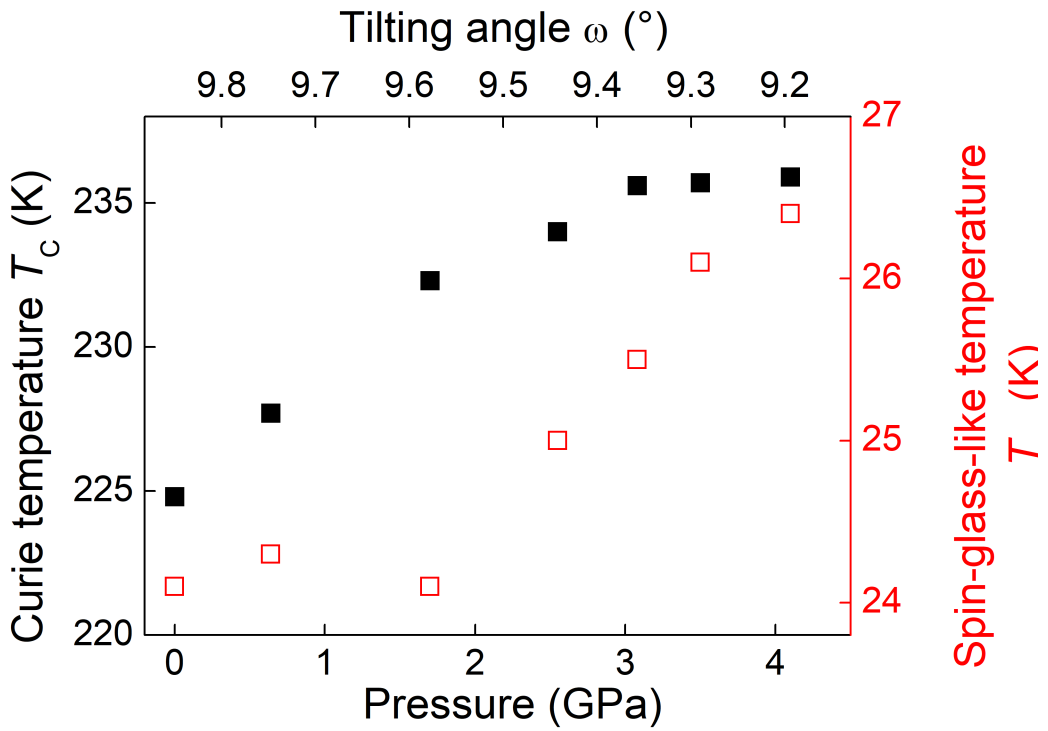

Figure 5.13 *Curie temperature T_C as a function of tilting angle ω (filled squares) and increasing pressure. Open squares show the spin-glass-like transition temperature T_{sg} variation as a function of pressure and tilting angle.*

function of pressure is also shown in Figure 5.13 as red open squares. In contrast with the Curie temperature, T_{sg} does not show an immediate response to the applied pressure. The spin-glass-like temperature oscillates within the experimental error around the ambient pressure of 24 K to a pressure of 2 GPa. Further application of pressure induces an increase of the temperature at which the material exhibits the glassy-like behaviour, which still persists at pressure up to 4.1 GPa.

5.4 Conclusions

Chemical doping is an efficient strategy to tune structural and physical properties of transition metal oxides. The $LaCoO_3$ parent compound was doped with a 0.1 manganese content and changes in its structural and magnetic properties were investigated. A high-pressure neutron-diffraction study of the structural behaviour of $LaCo_{0.9}Mn_{0.1}O_3$ was reported up to 6.1 GPa. The trigonal $R\bar{3}c$ crystal symmetry was found to be maintained over the pressure range investigated. The pressure dependence of the cell volume was fitted with a second order Birch-Murnaghan EoS and a bulk modulus of 140(11) GPa was determined for the sample. Interestingly, the rhombohedral unit-cell angle does not show any remarkable variation under the application of pressure, which appears not to affect the rhombohedral distortion of the lattice. The compression of the unit cell is found to depend on the tilting angle ω and octahedral strain ζ distortions, which are both found to decrease in the pressure range investigated. This suggests that the application of pressure favours a second-order transition to a higher symmetry structure, which has been estimated to occur around 61.5 GPa.

The Curie temperature of the doped sample was also determined and found to be significantly higher than that of the parent compound $LaCoO_3$. Even a low doping of 0.1 of manganese causes remarkable changes in the magnetic properties of this perovskite oxide. Finally, a non-linear increase of T_C and of the spin-glass-like transition temperature T_{sg} was observed under application of high-pressure, which appear to be controlled by the tilt angle ω and the Co/Mn–O–Co/Mn bond angle variation.

Chapter 6

Extending the accessible pressure range at the ISIS facility

This chapter describes the development of diamond anvil cells (DACs) for neutron diffraction on the PEARL diffractometer [158], at the ISIS Neutron and Muon Source. Diamond anvil cells were specially designed and adapted to the instrument layout and geometry of the scattering experiment. New sample-environment capabilities were developed and trial neutron-diffraction experiments were carried out to investigate the quality of collected data by the use of this new type of pressure cell. Among the work presented in this chapter, I have been responsible of the design and development of the ruby fluorescence and optical imaging setup, the cryogenic gas loading procedure, as well as to perform and analyse the trial high-pressure neutron-diffraction experiments with the use of the new diamond anvil cells.

6.1 Background

Extending the accessible pressure range is a historical challenge in high-pressure neutron-diffraction experiments. The low intensity of radiation fluxes at neutron sources generally requires the use of large sample volumes to obtain data of sufficient quality for structural refinement. This limits the pressure which can be applied on materials. Neutron diffraction is able nowadays to explore the multi-GPa pressure range after the development of opposed gem pressure cells [160, 250–

258]. This type of cell requires sample volumes of 3–4 order of magnitude lower than conventional sample sizes used on a neutron-diffraction experiment, for example with a Paris-Edinburgh press, hence enabling us to generate higher pressures. However, the impact of single-crystal diamond anvil cells in high-pressure neutron scattering has been very limited in the past. Natural single-crystal diamonds were very expensive with their cost exponentially rising with their dimension. Only small-culet diamonds were available and/or affordable, which prohibited loading of sample volumes large enough for use in neutron diffraction. Simultaneous improvements in diamond synthesis, such as in the chemical-vapour-deposition procedure [259], and pressure cell technology made available single-crystal large synthetic diamond anvils able to compress sample volumes as large as $1\,\mathrm{mm}^3$ [256, 257]. In parallel to anvil technology, progresses in neutron instrumentation also favoured the use of smaller sample volumes in a diffraction experiment at a neutron radiation source. For example, the application of focusing neutron optics provides an increased neutron radiation intensity on samples [254, 260]. Reducing the sample volume is the most efficient way to increase the pressure generated on samples, but this inevitably occurs at the expense of the signal to noise ratio. The loss of signal, however, is counteracted by a significantly reduced contaminating sample environment. Several neutron-diffraction measurements using DACs recently reported a much higher signal to noise ratio at fixed exposure time than other large volume cells such as the PE press [257]. Despite the compromise between sample volume and signal intensity, diamond anvil cells show a great potential in neutron-diffraction experiments and the choice of this type of cell has significantly grown.

Pioneering developments of gem anvil cells for neutron diffraction have been carried out since the 1980s at the Kurchatov Institute on the IR-8 continuous-reactor source [253, 261]. Scientists were able to develop diamond-opposed-anvil pressure tools to perform single-crystal neutron diffraction up to 31 GPa on a $0.01\,\mathrm{mm}^3$ deuterium sample and reported its equation of state [262]. Despite the high pressure achieved, the small sample volume constrained measurements that could be carried out. Experiments were limited to the collection of signals from a small number of strong peaks and only three reflections were observed at 31 GPa. Neutron-diffraction work at monochromatic reactor sources using gem (either diamonds or sapphires) anvil cells continued to develop with the work of Goncharenko, at the Saclay and ILL reactors in France. A new design of compact sapphire/diamond anvil cells [254, 255, 260, 263] achieved great impact results, such as the study of solid deuterium up to 38 GPa and low temperature [263].

Further work using both sapphire and diamond anvils reached an upper pressure limit of 43 GPa. This owed to the parallel progress in neutron instrumentation, such as the use of a focusing optic system and low-background conditions, which enabled the investigation of powder samples with volumes as small as 0.001 mm^3 [260]. At the ILL facility on the D9-diffractometer methods for single-crystal high-pressure diffraction have recently been developed [264] and measurements up to 10 GPa were obtained.

Diamond anvil cells for neutron experiments are also used in Laue diffraction at the Australian OPAL reactor at ANSTO on KOALA [265]. Mini-DAC based on the Merrill-Bassett design [173, 266] have been used and high-pressure neutron-diffraction has been performed up to 5 GPa in the 4–8 Å d-spacing range on single crystals of the size typically used in X-ray diffraction experiments.

In parallel with the work at reactor sources, high-pressure research is carried out at neutron spallation sources such as the ISIS facility, the SNS facility in Oak Ridge, Tennessee, USA and the Materials and Life Science Experimental Facility (MLS) at J-PARC, Tokai, Japan. At the SNS, Oak Ridge National Laboratory, great interest has been devoted to diamond anvil cells [267]. On the SNAP diffractometer the use of a new design of conically supported diamond anvil [256, 258], developed at the Geophysical Laboratory, DC, USA, provided the ability to load large sample volumes required for quantitative diffraction (0.1—0.2 mm^3 for strongly scattering systems). By the use of these new compact large diamond anvils, high-pressure data up to 94 GPa have been reported on a D_2O powder sample [258] and structural refinement has been reported up to 43 GPa [268].

At the ISIS facility high-pressure experiments are routinely performed. Different devices have been developed to perform high-pressure research on small sample volumes. Techniques for high-pressure single-crystal neutron diffraction have been developed [269] and single crystals of size ∼0.5–1 mm^3 of $D_2C_4O_4$ have been studied up to 10 GPa. By the use of spherical sapphire anvils in a VX-type PE press [160] single-crystal high-pressure neutron diffraction has been performed and neutron-diffraction patterns have been successfully collected on a crystal of D_2O ice VI of 0.5 mm^3 volume [270]. The PEARL diffractometer can already study samples up to 28 GPa, but a lot of attention is dedicated to the development of new pressure tools which will enhance the instrument performance. The installation of specially designed diamond anvil cells will open up the study of small volumes of either single-crystal (0.5–1 mm^3 volume range)

or polycrystalline (0.01–0.1 mm^3) samples with the aim of reaching pressures as high as 50 GPa.

6.2 High-pressure neutron-diffraction on PEARL: capabilities and developments

PEARL [158] is the diffractometer dedicated to perform high-pressure research at the ISIS Neutron and Muon Source, and is classified as a medium-resolution, high-flux instrument. A schematic layout of the diffractometer is shown in Figure 6.1.

After leaving the moderator, the polychromatic neutron radiation is collimated by a pair of movable B_4C jaws, which define the beam size at the sample position. The pressure cells are placed at the centre of the instrument and their position controlled by a motorised system, which ensures the sample is situated at the defined instrument centre. The diffractometer can operate in the transverse

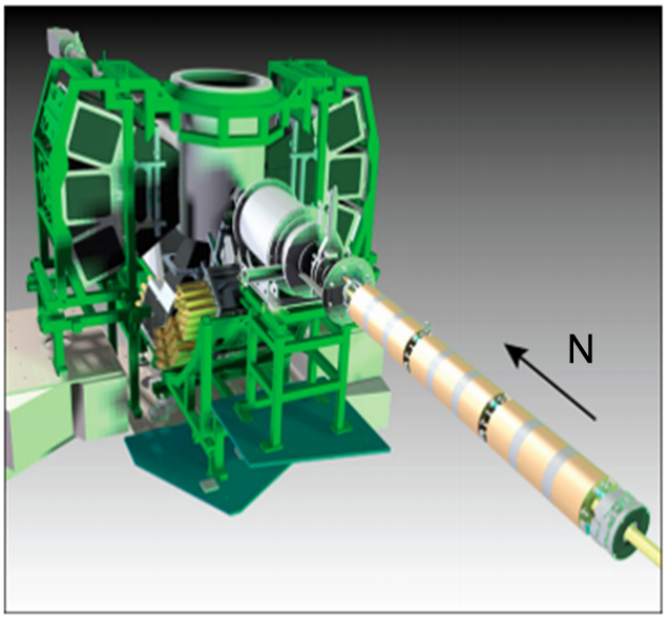

Figure 6.1 *Schematic representation of the PEARL instrument [158]. The incident neutron beam arrives from the moderator along the direction of the arrow. The beam passes through the beam pipe, the jaw sets, monitors, and scrapers before scattering into the sample located at the centre of the instrument. Transverse detector banks are located perpendicular to the beam. At the bottom of the figure, a part of the low-angle banks is also shown.*

Table 6.1 *PEARL diffractometer technical capabilities [158].*

Instrument Parameter	Value
ToF (ms)	1.5–20
d - spacing range (Å)	0.4 – 4.1 (transv.) 12.5 (longit.)
2θ range - transverse (°)	81.2 – 98.8
2θ range - longitudinal (°)	20 – 60 100 – 160
Wavelength range (Å)	0.4 – 5.8
Moderator to sample distance (m)	12.8
Sample to transverse detector distance (m)	0.8
Transverse average resolution (%)	~ 0.64
Sample range (mm^3)	33 – 100
Pressure range (GPa)	0.5 – 28
Temperature range (K)	80 – 1400

scattering geometry as schematically shown in Figure 6.1. The incident neutron beam (black arrow) hits the sample, and fixed detector banks collect the neutrons diffracted at 90°. The pressure cell can be rotated by 90° to acquire access to the longitudinal banks. Table 6.1 summarises main parameters of the PEARL instrument capabilities.

High-pressure experiments have been performed on PEARL for nearly thirty years. Early pressure tools, such as piston cylinder and gas cells [161, 271], were used before the development in the 1990s of the Paris-Edinburgh press [159]. This hydraulic-type cell boosted high-pressure neutron-diffraction experiments at the ISIS facility and is described in detail in Section 2.7.1. The usable sample volume ranges from 33 to 1000 mm^3 and provides the ability to perform powder structural refinement in the 1–28 GPa pressure range [159, 272]. Pressures as high as 28 GPa can be reached using double-toroidal sintered diamond anvils. Unfortunately, the anvils frequently break reaching 28 GPa, making this type of experimental setup very expensive. Developing new pressure tools and enhancing the instrument capabilities is therefore a priority on PEARL.

6.2.1 DAC installation: technical needs

To extend the accessible pressure range at the ISIS facility specially designed diamond anvil cells have begun to be tested on the PEARL instrument. The geometry and the functional mechanism of DACs are different from the PE-

press. New cell environment capabilities had to be designed and developed, in order to adapt the diamond anvil cell to the geometry and layout of the PEARL diffractometer and the ISIS neutron beam.

To perform an experiment on PEARL, the pressure cell is held by a mounting flange, which is moved into the instrument by means of an overhead crane. An alignment camera provides optical access to the cell, and motorised translation motors align the press flange to the instrument sample position. A similar mounting flange system needs to be developed to support and place diamond anvil cells in the diffractometer. The mounting flange must also be equipped with remote-controlled moving stages to move the cell and align it to the instrument sample position. A further technical requirement is to adapt the incoming neutron beam to the entrance of the diamond anvil cell. During diffraction experiments by PE presses, a hexagonal borum nitride (BN) collimator of typical inner diameter of 5 mm is placed at the entrance of the press. This element is essential to collimate the incoming radiation into the sample and reduce the scattering of neutrons from the press and its components, which would affect the collected pattern. Diamond anvil cells are characterised by a much smaller sample entrance typically $\sim$800 μm. A new collimation system has to be designed to collimate the neutron beam and avoid extra contribution to the diffraction pattern from the sample environment.

The PEARL instrument operates in the transverse scattering geometry with fixed detectors and a polychromatic neutron incoming radiation. This comes with a disadvantage: the polychromatic beam has to cross nearly 6 mm of anvil material using the PE press and is strongly distorted by the wavelength dependent absorption effect, which needs proper correction operations to obtain reliable intensity in the collected data. Diamond anvils also attenuate the incoming neutron beam [273–275]. The integrated intensities of measured Bragg reflections in a neutron-diffraction experiment are found to be significantly reduced when the diamond anvils diffract simultaneously at the same setting as the sample, with an intensity loss which may be as high as the 50% [274]. This phenomenon is also strongly pressure dependent and the degree of attenuation increases with pressure [274]. Attenuation correction methods must be developed for a correct reduction of the intensity of collected data. Reducing the sample volume inevitably affects the counting statistics. The low neutron radiation intensity available in a neutron experiment and the absence of focusing neutron optics on PEARL impose lengthy collection times in order to achieve good data quality for structural refinement

with smaller samples. Typical collection times in the order of 2–3 h provide a good data quality by the use of the PE-press and accurate structural refinement is possible depending on the type of sample. Typical sample volumes loaded in DAC are of the order of 0.01–0.1 mm^3 and much longer collection times are required to overcome the weak neutron flux and increase the signal to noise ratio $\sim$10 h.

Below, two further technical requirements are described: the choice of suitable pressure transmitting media and the determination of applied pressure to samples.

6.2.2 In situ determination of pressure on samples

The pressure applied to a sample in the PE press is typically determined by including a pressure marker in the sample volume with well-known equation of state. Anvils generally used on PEARL, such as the ZTA or sintered diamond anvils, are opaque to visible light and do not permit the use of alternative optical techniques. Materials typically used as pressure markers in neutron-diffraction are Pb, MgO or NaCl.

Diamond anvil cells are made of polished single-crystal diamonds, which are transparent to light. This enables us to use optical systems to obtain optical access to the loaded sample and to measure the pressure *in situ* by ruby fluorescence measurements [175–177], as is routinely done in X-ray diffraction or Raman spectroscopy high-pressure experiments. This work of thesis has aimed at designing and developing this kind of equipment on the PEARL instrument. The main aim was to create a setup able to operate during experiments, without the necessity to open the PEARL instrument and have direct access to the optics. In this case a great advantage is given by the geometry of the diffractometer. PEARL offers a more than sufficient space to host a fixed optical setup, which could be shielded, craned down into the instrument and operate in a remote way during the diffraction experiment.

6.2.3 Hydrostatic compression beyond 10 GPa

Compression in hydrostatic or quasi-hydrostatic conditions of samples is essential in high-pressure research. Although materials found inside earth or planetary bodies are not at pure hydrostatic conditions, hydrostatic pressure is the

thermodynamic variable comparable to theory and must be maintained during experiments.

The sample is immersed in an inert fluid, which acts as a pressure transmitting medium. The function is to ensure that the pressure applied is homogeneous and to avoid effects such as uni-axial or shear stress on the compressed material. This would lead to a decreased experimental quality with collected patterns affected by the appearance of anomalies, such as in high-pressure diffraction experiments an inhomogeneous d-spacing displacement of Bragg reflections or peak broadening [276]. The choice of the right pressure transmitting medium (PTM) is critical and must be made according to the kind of sample and geometry of the experiment [277].

In neutron diffraction it is desirable to use fluids with a small neutron cross-section, in particular no materials containing hydrogen atoms due to its high incoherent scattering cross-section. Further requirements are a low compressibility to avoid large volume changes and chemical inertness to the sample to avoid reactions during experiments. Even if the pressure transmitting fluid does not contain hydrogen, its neutron scattering power is typically of the same order of magnitude as the sample. A diffraction pattern will therefore contain the signal of the sample superimposed over broad oscillations, which are produced by the fluid or glassy PTM. The most common pressure transmitting media used in neutron-diffraction high-pressure experiments are silicon oil, perdeuterated 4:1 methanol-ethanol fluid, fluorinert liquids, and noble gases at very high pressures [278, 279]. The perdeuterated 4:1 methanol-ethanol solution is the most widely used PTM and is characterised by a hydrostatic limit of 10.5 GPa [163, 277, 278, 280]. Above such pressure point, solidification of the fluid will take place, and non-hydrostatic condition will inevitably occur.

The DAC project aims at reaching pressures much higher than 10 GPa, and an alternative candidate as pressure transmitting fluid to guarantee the accuracy of the collected data at higher pressures is to be used. Noble gases represent an excellent choice providing stable hydrostatic conditions over a wider pressure range [277, 278, 281–283]. Such gases are also chemically inert to samples, optically transparent and good thermal insulators, which are qualities of extreme importance in a good PTM. This work has also focused on deploying a cryogenic gas loading technique for diamond anvil cells, which is adopted on PEARL when pressures over 10 GPa are required.

6.2.4 Advantages and motivations

PEARL is a diffractometer specially designed for high-pressure investigations and its design and geometry favour the development of new pressure tools. The time-of-flight technique at the ISIS spallation source is advantageous for high-pressure experiments. The Q-dependence of the scattered signal is related to the incoming neutron wavelengths by the time-of-flight and can be mapped at fixed scattering angles. Measurements can be performed in transverse scattering geometry with fixed detector banks. Optimisation of shielding from the cell is possible and hence a minimised background scattering from the sample environment arising from the instrument itself, the pressure cell or from intrinsic noise such as electronic noise or high energy gamma rays. A low background from the sample environment is fundamental in a high-pressure measurement and becomes essential when a sample volume of the order of $0.1\,\mathrm{mm}^3$ is placed in the relatively weak flux of a neutron beam.

The diamond anvil cell is already successfully used as main pressure tool for spectroscopic investigations or diffraction by X-ray synchrotron radiation. The high flux available at a synchrotron source permits the use of small sample volumes and very high pressures can be easily generated. However, the X-ray radiation scatters with the electron cloud of atoms and, differently from neutrons, the scattering cross-section is Z dependent. X-ray diffraction is not sensitive either to light atoms, such as hydrogen or deuterium, or to atoms with similar atomic number in the same compound. Neutrons show a complex dependence on Z of the scattering process which enables us to distinguish either light atoms, such as hydrogen or deuterium, or compounds made of elements with similar Z. Perovskite structures, such as samples investigated in this thesis [1, 2], generally comprise two heavy cations and a much lighter anion, such as oxygen atoms, and these conditions favour neutron diffraction as the technique of choice. The light anion scattering signal would be totally masked in an X-ray diffraction experiment by the heavier atoms signal (typically rare-earth or transition metal elements), hence a proper quantitative analysis is less robust than in a neutron-diffraction experiment. The introduction of DACs on PEARL will provide the ability to study these types of materials (and many more) at pressures beyond those reported to-date, providing a higher level of accuracy in determining structural parameters than in an X-ray diffraction experiment.

In addition, the ability to study sample volumes of the order of the $0.1\,\mathrm{mm}^3$ will

pave the way to study on PEARL samples synthesised by high-pressure/high-temperature methods, which rarely produce sample quantities sufficient for a neutron-diffraction experiment by means of a PE-press [284].

6.3 Results and discussion

As discussed in previous sections, the PEARL diffractometer is an instrument optimised to the use of PE presses and special capabilities had to be designed and developed to adapt the diamond anvil cell to the ISIS diffractometer. In this section the new instrument developments on PEARL will be discussed in detail. In parallel to that, trial neutron-diffraction measurements using the diamond anvil cell have been performed and first attempts of data analysis have been carried out and reported below.

The first interest was to create the supporting flange for the DAC, which can be raised and craned into the instrument. Figure 6.2 shows a side view of the diamond anvil cell attached to the specially-designed flange. The flange is characterised by two levels. The upper level hosts the optical setup integrated to perform *in situ* ruby fluorescence measurement and to acquire optical access to the gasket. The diamond anvil cell is placed in the lower level supported by remote-controlled moving stages, which can translate and rotate the cell. Preliminary variable Z, Y, X and θ cell coordinate scans of the upstream and downstream PEARL detector integrated intensity are performed to find the maximal measured neutron intensity. This corresponds to the cell centred position to be used during the diffraction experiment. A further moving stage placed on the lower panel at the right entrance of the DAC supports the new collimation system designed and developed at the ISIS facility. A side view of a specially designed DAC used on PEARL is shown in Figure 6.3a with its technical design 6.3b.

The cell is characterised by single-crystal diamond anvils with flat parallel surfaces (culets). The culet diameter covers a wide range, typically from 0.7 to 2 mm, and loading of sample volumes up to 0.1 mm^3 are possible. The small culet dimension permits us to generate very high pressures with a relatively small load. The four screws placed at the top of the cell mechanically transmit the force onto an upper piston which drives the upper anvil towards the bottom fixed diamond. The 4-screw cap is used to apply a sealing load to the DAC and relatively low pressures. Higher forces are generated by a specially designed steel membrane

(not shown), whose expansion driven by gas pressure allows us to control the applied force and achieve a nearly linear load generation. Figure 6.4 shows an optical image of a 1.3 mm diameter diamond anvil culet used on PEARL. The sample material is placed between the two anvils inside a drilled metallic disk (gasket). The gasket is made of a foil pre-shaped on the diamond anvil culet by the use of a manual hydraulic press (pre-indented). The metallic foil is typically

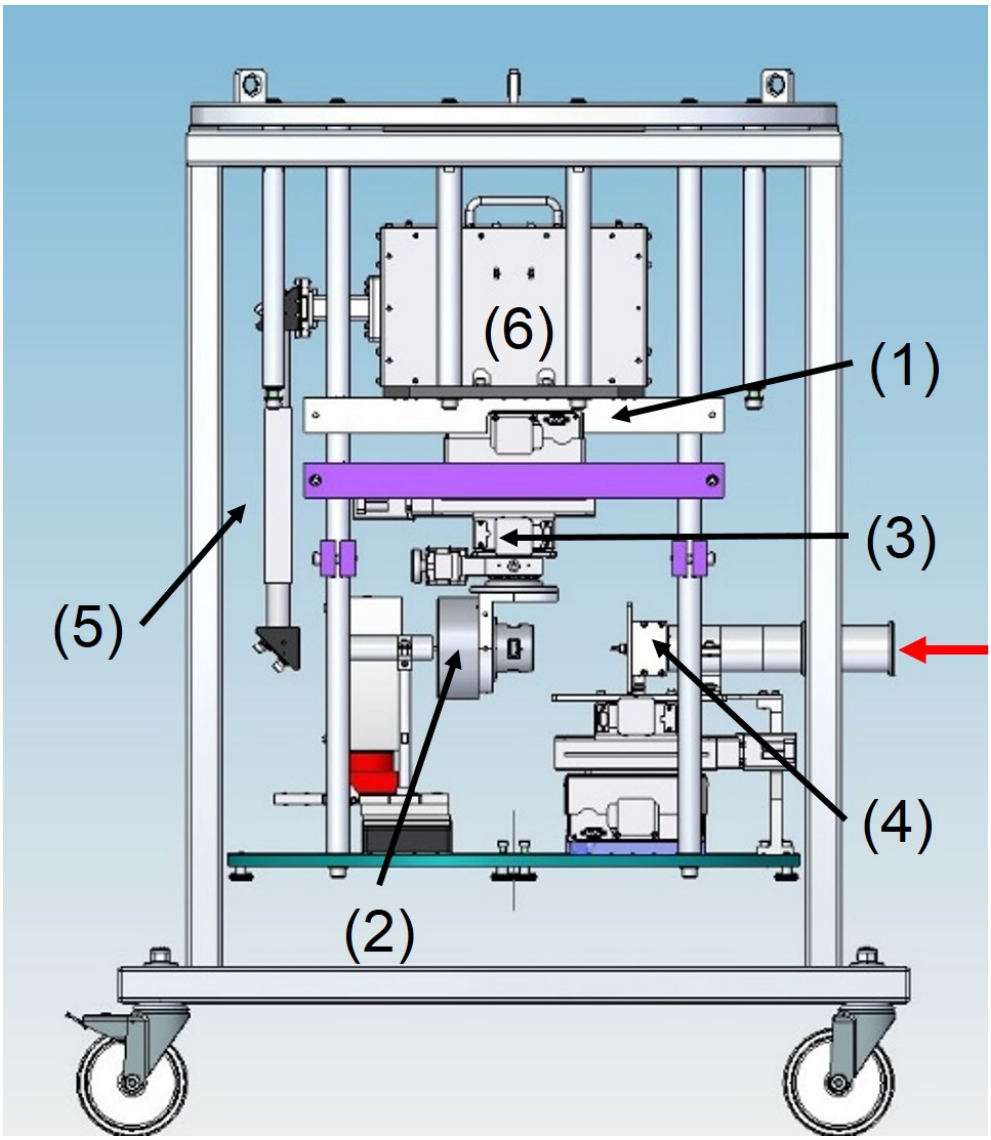

Figure 6.2 *Side view of the diamond anvil cell mounting flange (1) developed on the PEARL instrument. 2) DAC. 3) Remote-controlled motorised stages. 4) Hexagonal borum nitride collimation set. Cadmium shielding is also present to reduce background scattering contribution. 5) Periscope connecting the DAC sample location to 6) black box hosting the optical setup for ruby fluorescence measurements (see section 6.3.2 for details). Red arrow indicates the incoming neutron radiation direction.*

(a)

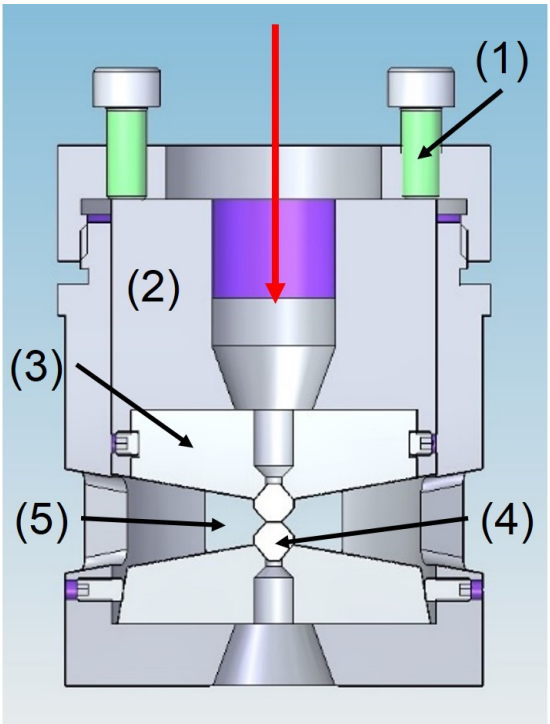

(b)

Figure 6.3 *6.3a Side view of a specially designed DAC used on PEARL. The sample is located between the two diamond anvils inside a drilled gasket, which can be seen through the cell window. The DAC is closed by a 4-screw cap, which is used to apply a sealing load and very low pressures. 6.3b Schematic representation of the DAC section: (1) screw; (2) piston; (3) anvil seats; (4) diamond anvils and (5) cell window. Red arrow indicates the incoming neutron beam direction.*

pre-indented from a thickness of 500 μm to $\sim$200 μm. A hole typically in the 500–800 μm diameter range is drilled at the centre of the gasket indentation. The powder sample is packed inside the drilled hole with a pressure marker material, a ruby chip in the case of diamond anvil cells. The gasket is essential for the transmission of pressure onto the sample. As the load is applied onto the DAC, the gasket contracts inwards and transmits the generated force onto the sample. The choice of the gasket material is thus extremely important to optimise the pressure transmission. The most widely used gaskets are made of aluminium, niobium, copper, copper-nickel, steel or copper-beryllium, which are also adopted for neutron-diffraction experiments.

Neutron-diffraction patterns are collected in transverse geometry. The neutron beam is scattered at 90° after passing through the diamond anvil, thereby careful diamond attenuation corrections are required on the raw data, and Bragg peaks from the diamond phase will affect collected patterns [274, 275]. To-date, neutron-diffraction data collected on PEARL by the use of DACs are focused using current available scripts and standard vanadium normalisation. The development of a specific diamond attenuation correction script is still a work in progress on PEARL. The transverse scattering geometry requires the neutron beam to pass also through the metallic gasket before being collected by the detector banks, hence affecting the neutron-diffraction pattern with further reflections from the

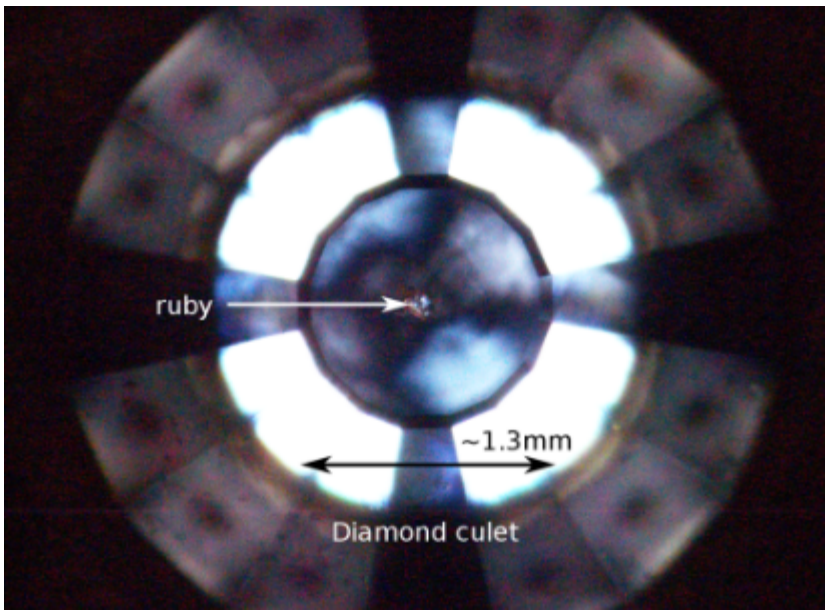

Figure 6.4 *Optical image of the diamond culet (d = 1.3 mm). The gasket hole is the outer metallic ring, which surrounds the ruby chip, loaded to act as pressure marker.*

gasket material.

6.3.1 Beam control

Background scattering from the sample environment, such as the pressure cell and the metallic gasket, inevitably affects measured neutron-diffraction patterns. To reduce the undesirable background scattering this work aimed at designing a specific collimation system for the diamond anvil cell. Figure 6.5 shows a detailed design of the hexagonal boron nitride (BN) collimation set integrated in the PEARL flange and placed as shown in Figure 6.2.

The collimation system consists in the insertion of different BN elements along the incoming neutron beam at the entrance of the pressure cell to reduce the incoming neutron radiation section to the dimension of the DAC sample entrance. Upper left panel of Figure 6.6a shows the full beam size on PEARL acquired by a neutron camera located at the instrument sample position. The dark triangle shape is a cadmium (Cd) marker[1] with a top side of 5.5 mm length, which is used to calibrate

[1]Cadmium is commonly used in neutron sources as thermal neutron absorber. The Cd material is exploited not only for its very high absorption cross-section but also for its cut-off energy effect: only neutrons with kinetic energy below the cut-off, $\sim 0.5\,\text{eV}$ for the ^{113}Cd isotope, are absorbed.

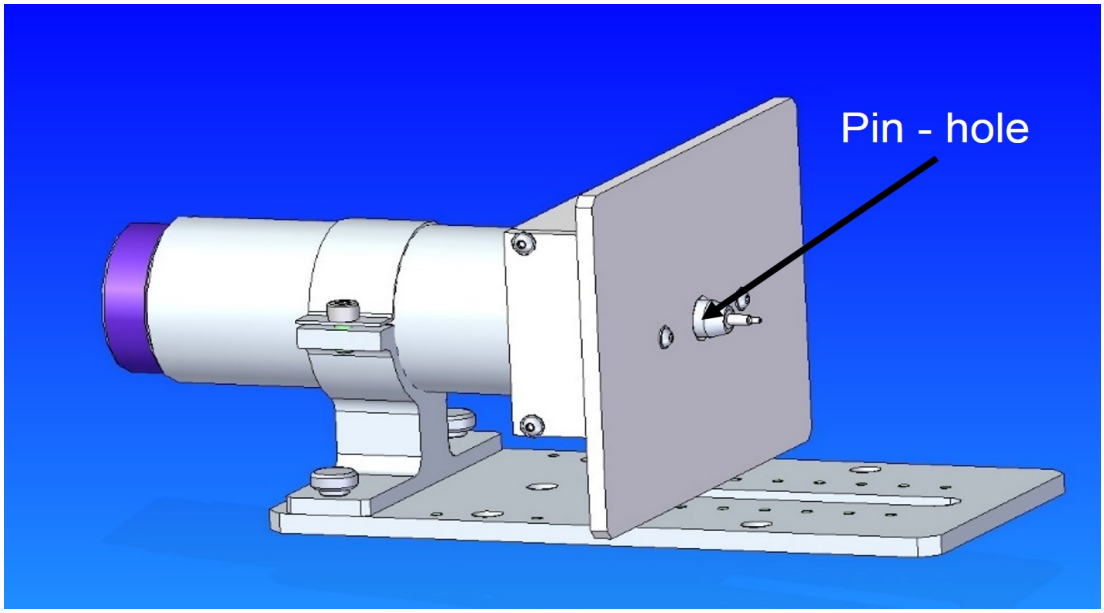

Figure 6.5 *Borum nitride neutron collimation set for diamond anvil cells. The final pin-hole has a typical inner diameter ranging from 400 to 800 μm.*

the pixel size of the neutron images. The full beam size has thus a diameter of about 2.3 cm. The bottom right panel of Figure 6.6a shows the reduced neutron

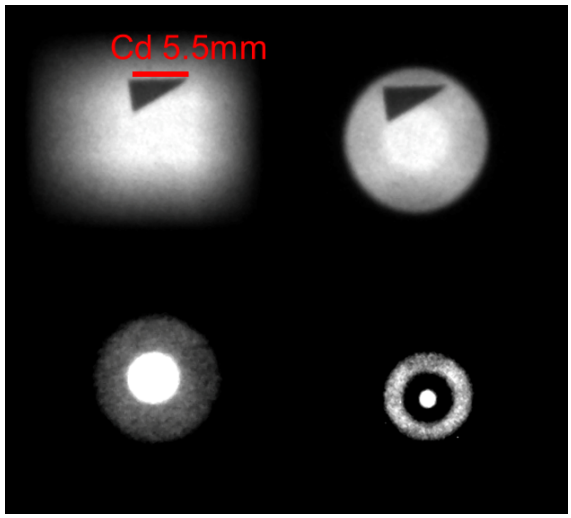

(a)

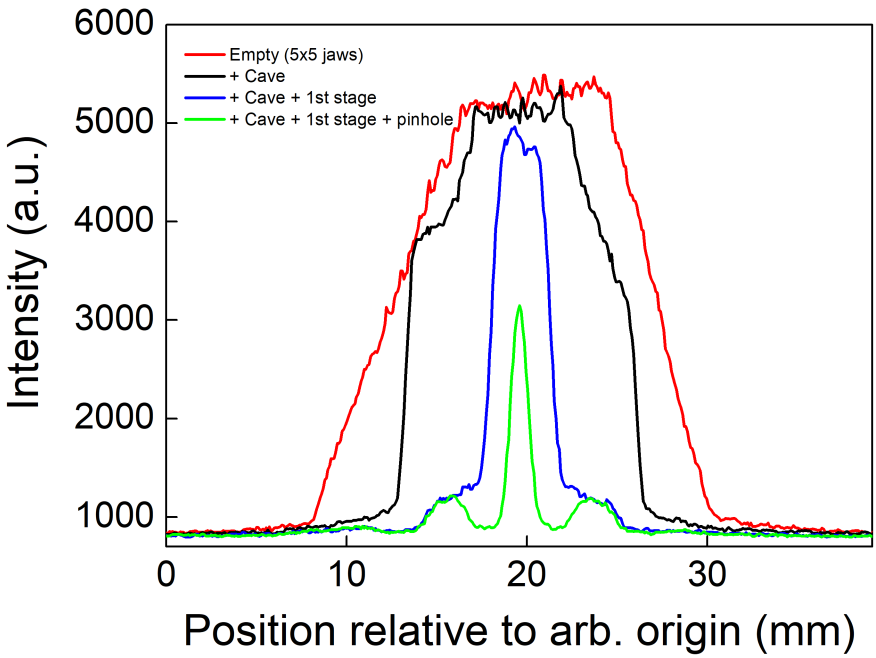

(b)

Figure 6.6 *6.6a Neutron-camera images of the neutron beam section as different collimation elements are integrated at the DAC entrance. The beam was imaged at the instrument sample position. The black triangle shows a cadmium sheet of known dimensions applied to the cell to calibrate the camera pixels. 6.6b Transmitted beam intensity at the application of different collimation elements: cave; cave and stage; cave, stage and pinhole.*

beam spot down to 1.2 mm after the integration of a final 3D-printed BN pin-hole (Figure 6.5). The inner pin-hole aperture typically ranges from 400 to 800 μm. The correspondent neutron beam intensity as a function of the integration of the diverse BN collimation elements was analysed and shown in Figure 6.6b. The two low energy shoulders in the curve associated to the completed BN collimation set correspond to the outer ring still visible in the neutron beam image in right lower panel of Figure 6.6a. A possible cause may be found in high energy neutrons, which are not absorbed by the collimation set and detected by the neutron camera and PEARL detectors. Nevertheless, the intensity is moderated enough to give a negligible contribution to the neutron-diffraction pattern.

6.3.2 The Ruby fluorescence setup

The remarkable advantage provided by diamond anvils is their transparency to visible light. Optical systems can be used to acquire optical access to the loaded sample and to have live control of the gasket behaviour during the application of load. In addition, pressure on samples can be determined *in situ* by the ruby fluorescence method [175–177]. An optical setup for ruby fluorescence measurements and optical live access to the sample has been built and integrated on the PEARL instrument. A schematic representation of the setup is shown in Figure 6.7.

The setup is designed and built to fit the geometry of the DAC flange and of the PEARL instrument. The main optical components are placed on the upper board of the flange inside an interlocked box as shown in Figure 6.2. The sample is loaded in the DAC placed underneath the optical bench at the instrument sample position. The upper plane is optically connected to the cell entrance by means of a periscope. The periscope is mounted on a remote-controlled moving stage, which aligns and moves the cell entrance off the incoming optical path from the upper level. The setup enables optical access to the sample and the acquisition of ruby fluorescence spectra. The two operations are optically independent and can be individually performed. As shown in Figure 6.7, the visible light is sent through a focusing lens and is reflected from the upper optical plane into the periscope by a plate beam-splitter aligned to the periscope entrance. At the exit of the periscope, the light is focused into the cell by a plano-convex lens (f = 150 mm) placed at the end of the optical path on the lower level. The scattered light is then collected in backscattering by a CCD camera placed on the upper

level. The CCD camera is equipped with a modular magnifying lens system, which provides different magnification powers. The ability to optically access the gasket is fundamental for detecting any change in the gasket behaviour during the application of pressure. The optical setup is also equipped with a diode laser ($\lambda = 532\,\text{nm}$) to perform fluorescence measurements. The laser, after passing through a collimation system, is sent into the periscope by means of a cube beam-splitter. The laser is then focused into the sample through the same plano-convex lens as the visible light. The fluorescence signal is collected in backscattering by means of a spectrometer fibre optic connected to the setup.

An example of ruby fluorescence spectrum acquired from a diamond anvil cell placed as in Figure 6.7 is shown in Figure 6.8. The limited space available on the upper optical plane and the necessity to connect the two different levels posed several constraints on the setup layout. First of all, the fixed periscope entrance

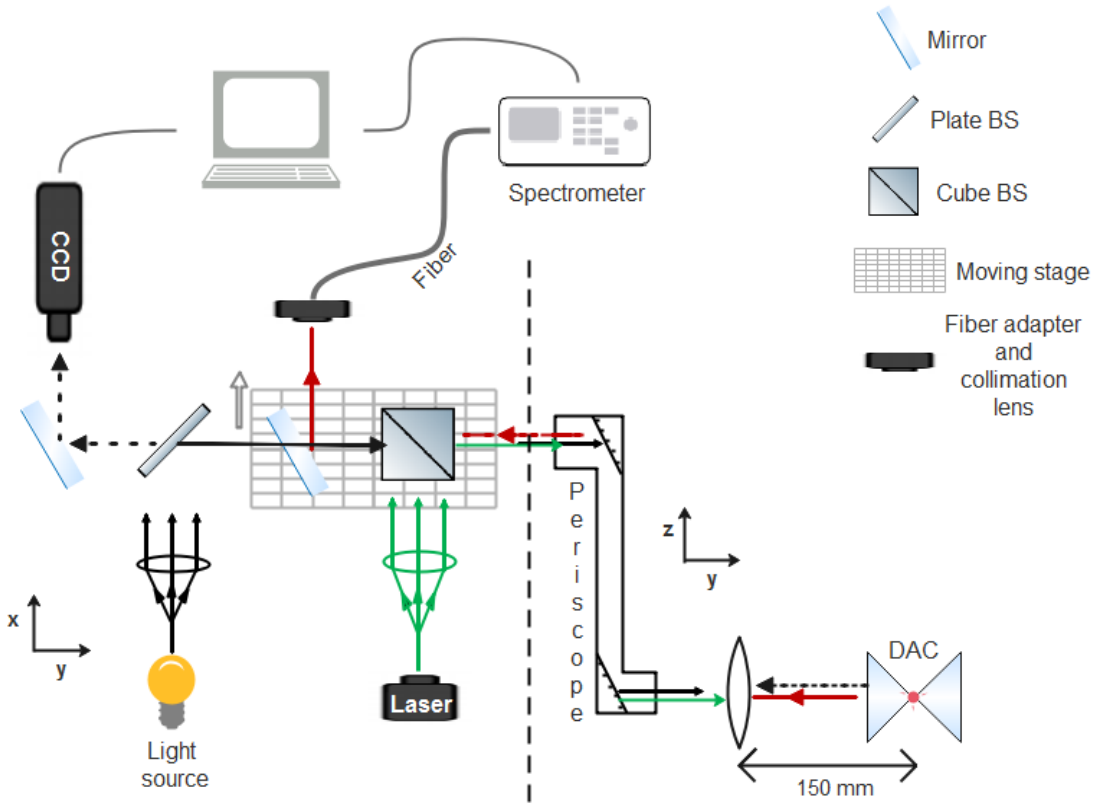

Figure 6.7 *Schematic ruby fluorescence and image acquisition optical setup details. Panel at the left of dashed line depicts optical components located on top bench of the DAC flange, as shown in Figure 6.2. Right panel depicts optical components at the bottom of the same DAC flange consisting of the periscope exit and the focusing plano-convex lens (focal length $f = 150\,\text{mm}$). See main text for details.*

on the upper plane required both light and laser to be directed to the centre of the periscope. As shown in Figure 6.7, the plate beam-splitter, which reflects the incoming light and is crossed in backscattering before the light is collected by the CCD camera, is aligned to the mirror and beam-splitter directing the laser into the cell and into the fibre entrance. To clear up the light source optical path, the cube beam-splitter and the mirror are placed on a remote-controlled moving stage, depicted as a gray grid in Figure 6.7. By moving the stage off the aligned light source position to the periscope entrance (along the arrow direction), it is possible to switch from the optical image to the ruby spectrum acquisition. The whole setup is fixed to the DAC flange, craned down into the instrument with the loaded pressure cell and remote-controlled from the PEARL instrument cabin. This enables us to switch from the ruby/video to neutron-diffraction acquisition without needing manual access to the optics.

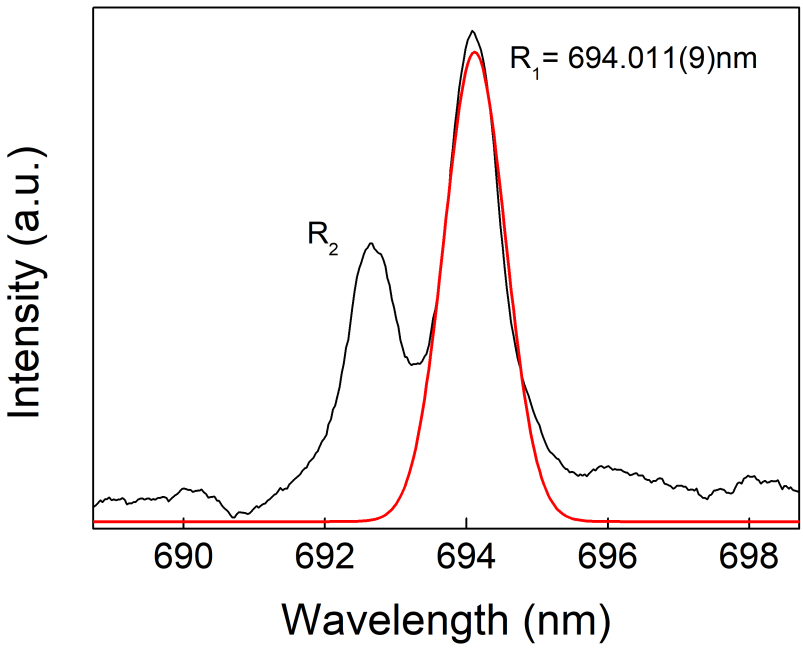

Figure 6.8 *Ruby fluorescence signal (black line) acquired with the ruby fluorescence setup developed on PEARL. Red line shows a gaussian fit to the R_1 line of the fluorescence doublet, which yielded: $\lambda_{R_1} = 694.011(9)\,nm$.*

6.3.3 Cryogenic Argon loading

Among several good candidates as transmitting fluids, which provide quasi-hydrostatic condition at high pressure, the noble gas argon represents a good choice. This is related to its qualities of small pressure gradient at high pressures, low neutron absorption and incoherent-scattering cross-section, ease of loading and low price. Despite its low solidification point at ambient temperature, around 1.4 GPa at 300 K [282] and a hydrostatic limit around 10–12 GPa, the pressure gradient is maintained below 2% up to 20 GPa [277], making it a good and cost-effective candidate for quasi-hydrostatic high-pressure studies above 10 GPa.

In order to adopt the noble gas argon as pressure transmitting fluid a specially designed cryogenic gas-loading system has been developed. Two different methods can be used to load gas in diamond anvil cells: either by loading the liquefied gas by cryogenic techniques [285] or by loading the condensed gas at room temperature by high-pressure techniques [286]. Both methods are successfully used, but the cryogenic technique is simpler and less expensive for DAC technology and it is the method developed on PEARL.

The specially designed cryoloader for the PEARL instrument is shown in Figure 6.9a. It is characterised by a deep outer ring (outer jacket) and a concentric shallower inner ring (inner jacket). The inner jacket hosts the diamond anvil cell and is designed to tightly fit the DAC to keep the cell still during the loading procedure. The DAC is placed into the inner jacket not completely sealed, but a space of less than ∼1 mm is left between the anvils as to allow the PTM to flow inside the cell. The outer jacket is filled with liquid nitrogen, which cools down the DAC-cryoloader system. When the cell is at the thermal equilibrium with the liquid nitrogen bath, a copper coil attached to an Ar gas cylinder is placed in the cryoloader around the inner jacket. The gas cylinder is then opened and an Ar flow at a pressure of ∼2 bar is released. In the cooled coil, the flowing argon condenses and the liquid Ar is directed into the inner jacket where the DAC is placed. After the inner jacket is nearly filled up with the liquid PTM, a sealing load is applied to the DAC by the 4-screw mechanism. The loading procedure can be summarised as:

1. The cell is placed into the inner jacket of the cryoloader.
2. Liquid nitrogen is placed into the outer jacket of the cryoloader as shown in Figure 6.9a.

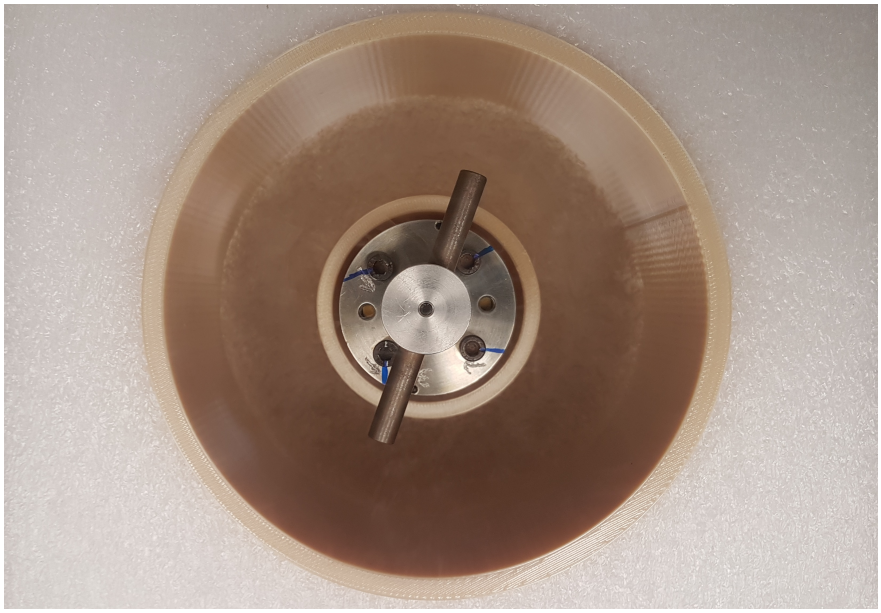

(a)

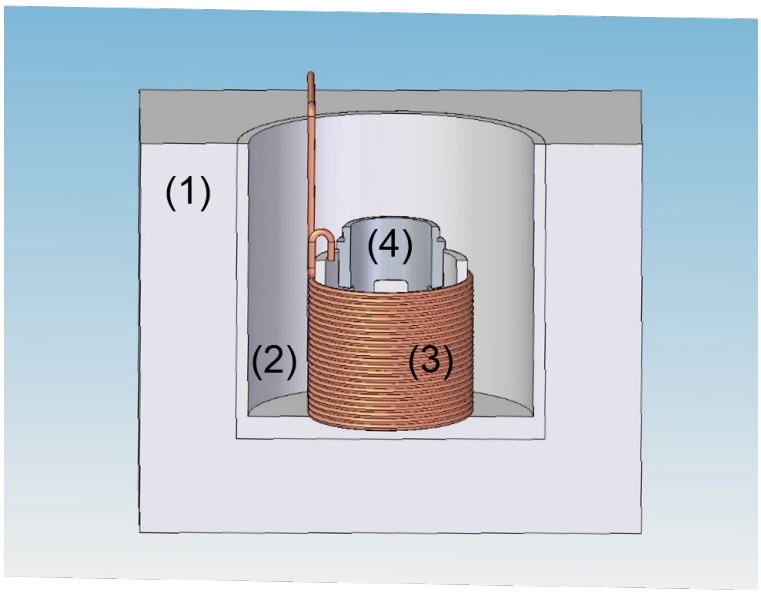

(b)

Figure 6.9 *6.9a Specially designed cryoloader for cryogenic gas loading. 6.9b Sketch of the Ar loading apparatus. The cryoloader (1) outer jacket (2) is topped up with liquid nitrogen. The DAC is placed into the inner jacket (4), which is filled up with liquid Ar by the surrounding copper coil (3) attached to the Ar gas cylinder (not shown).*

3. When the DAC is in thermal equilibrium with the liquid N_2, a copper coil, connected to an Ar cylinder, is immersed into the N_2-filled outer jacket.

4. The argon gas flows inside the coil cooled in liquid nitrogen (Ar has a boiling temperature of 84 K), and the liquid gas will condense into the inner jacket where the cell is placed.

5. After sufficient Ar has filled the inner jacket, the coil is removed and the DAC is sealed as required by the four-screw system.

6. The cell is finally removed from the cryoloader and left to warm up naturally.

A sketch of the Ar cryogenic setup is shown in figure 6.9b for clarity. Despite the apparent simplicity of the loading procedure, several issues have arisen from the development of this technique. A delicate step is to finely tune the distance between the two anvils, as to compromise the necessity to let Ar flow in and avoid the loaded sample to be washed out by the liquefied gas flow. Furthermore, accurate calibration of the four sealing screws is fundamental to apply an initial homogeneous load to the piston and hence to the loaded argon. Heating up of the system is also liable to happen, and liquid N_2 evaporates from the outer jacket. It is fundamental to be certain that the entire cell body is in thermal equilibrium with the liquid nitrogen. Pre-cooling of the DAC may be needed to achieve and maintain a stable temperature, and the nitrogen level in the outer jacket must be monitored during the loading procedure and filled up if necessary.

6.4 Neutron-diffraction data of $\leq$0.1mm^3 sample volume

After developing the instrument capabilities mentioned above, testing the diamond anvil cells was performed with trial neutron diffraction measurements on different types of compounds. The main interest is to test the quality of the neutron-diffraction pattern collected by DAC on such a small amount of sample, and consequently to test the quality of the collected data to obtain an accurate and reliable quantitative structural refinement.

A first test measurement was carried out on a germanium sample. The choice to load germanium powder arises from its high coherent neutron scattering cross-section ($b = 8.185$ fm) and its small incoherent scattering contribution to the

diffraction pattern. These properties make germanium a good neutron scatterer, which facilitates the pattern acquisition of a small sample volume. A 0.1 mm^3 of Ge powder was loaded in DAC inside a steel-gasket hole of about 500 μm in diameter, as shown in Figure 6.10a. A 4:1 perdeuterated methanol-ethanol

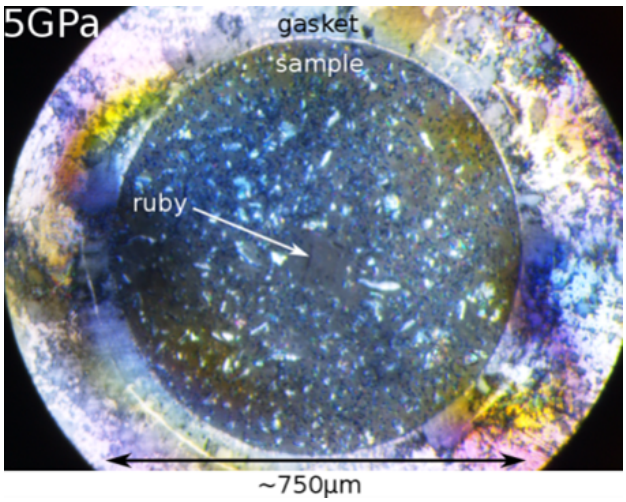

(a)

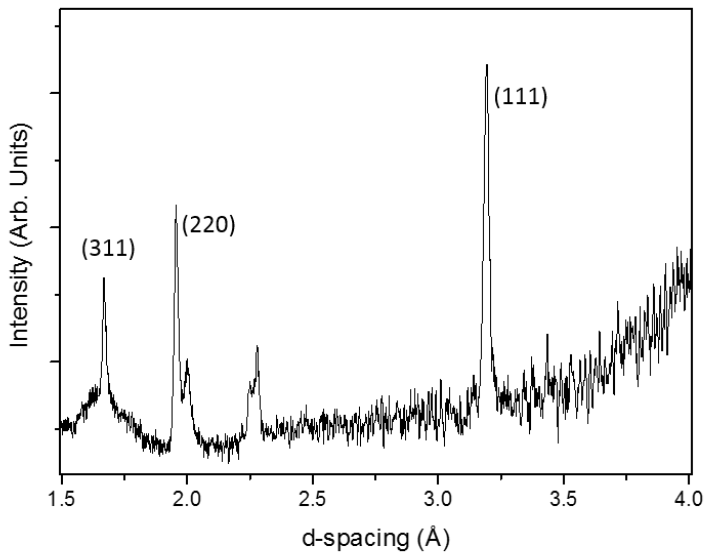

(b)

Figure 6.10 *6.10a Optical image of the germanium powder sample loaded in DAC within a stainless-steel gasket. The sample is packed with a ruby chip placed at the centre of the diamond culet. 6.10b Neutron-diffraction pattern of germanium collected on PEARL at a pressure of 5 GPa. Peaks from the diamond anvils are also present in the neutron pattern, but the (111), (220) and (311) Ge reflections can clearly be seen over the all background.*

solution was used as pressure transmitting medium. A pressure of 5 GPa was applied on the sample and the pressure value determined by ruby fluorescence. The neutron diffraction pattern of the Ge sample collected on PEARL is shown in Figure 6.10b in the 1.5–4 Å d-spacing range. The pattern was collected over a ∼20 h collection time to compensate the low-intense neutron flux. The (111), (220) and (311) reflections from the Ge phase are marked and clearly distinguished in the neutron pattern over the background and the extra Bragg reflections from the diamond anvils. This first result confirms the possibility to obtain neutron diffraction patterns by means of diamond anvil cells on such a small sample volume at the ISIS facility. However, germanium is a very good scatterer and is characterised by a simple crystal structure. A more complex crystallographic sample has to be tested on PEARL to provide a more reliable proof of the quality of the collected signal.

6.4.1 Neutron diffraction data beyond 10 GPa

A second experiment was carried out on a D_2O ice VII sample aimed at testing the performance of pressure generation of this design of diamond anvil cell. The high-pressure phases of solid water depending on temperature are referred to as ice VII and VIII. At 300 K the ice VII phase ($Pn\bar{3}m$) is stable in the 2–∼70 GPa range, while for temperatures below 270 K down to 0 K the ice VIII phase ($I4_1/amd$) stabilises. These two phases have already been extensively studied [268, 287–291]. The crystal structure of D_2O ice VII at 13.1 GPa is shown in Figure 6.11. The presented structure was depicted by the use of the Vesta software [292] from neutron-diffraction data collected in the current work by diamond anvil cells. The oxygen atoms lie on average sites that form a bcc lattice with each oxygen surrounded by eight equidistant neighbours. Each O atom forms hydrogen bonds with four of these neighbours (with two accepted and two donated bonds) to create a tetrahedrally coordinated network.

Pure D_2O (99.9% deuterated) was loaded and sealed in a diamond anvil cell. Load was increased rapidly using a hydraulic press, and then locked in using the four-screw mechanism. The sample pressure was initially measured, by ruby fluorescence spectroscopy, to be 13.1 GPa. Higher pressures were generated by a gas-membrane driven system increasing the external load up to 70 bar in 10 bar steps. A BN pin-hole of both 600 and 700μm diameter was placed in front of the diamond anvil cell entrance. Further pressure points were determined by applying

previously reported equation of states of ice VII [290]. An example of neutron diffraction pattern of D_2O ice VII collected on PEARL is shown in Figure 6.12 (open circles). Rietveld refinement of the data (red curves) where possible was performed using as starting positions: O at $\left(\frac{1}{4}, \frac{1}{4}, \frac{1}{4}\right)$ and D at (0.41,0.41,0.41) with a 0.5 of occupancy.

The only (110) Bragg reflection is observed in the neutron diffraction pattern, while the other characteristic (111) and (220) reflections are not detected, but completely covered by the background as shown in inset of Figure 6.12. The pressure value was verified by the use of a Birch-Murnaghan EoS adopting fitted parameters reported by Klotz *et al* determined by neutron-diffraction of volume $V_0 = 42.25\,\text{Å}^3$, bulk modulus $B_0 = 13.8(2)\,\text{GPa}$ and $B' = 5.9(1)$ [290]. The pressure so determined yielded a value of 11.9 GPa. A pressure loss of ∼1 GPa occurred from the sample loading to the diffraction experiment. This divergence

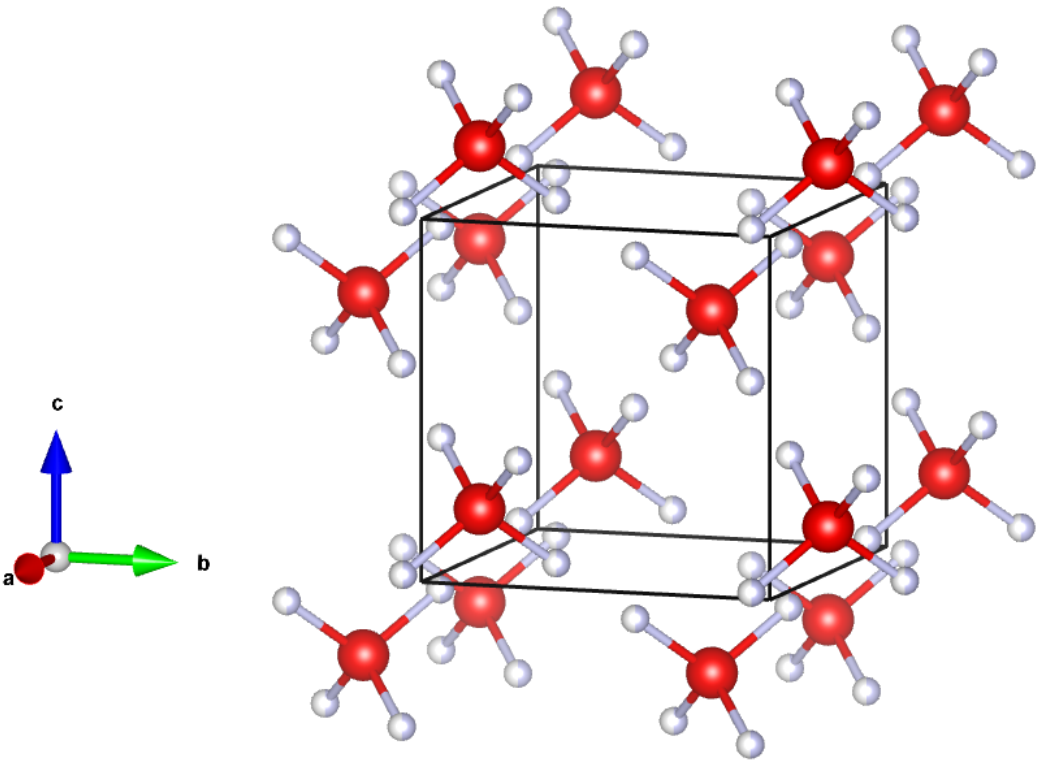

Figure 6.11 *D_2O ice VII crystal structure at 13.1 GPa. Fractional coordinates in the proposed structure are: O 2b $\left(\frac{1}{4}, \frac{1}{4}, \frac{1}{4}\right)$ and D 8e (x, y, z). Red spheres show oxygen atoms, grey smaller spheres are deuterium atoms and bi-color lines represent D–O bond lengths. The presented structure represents the temporal and spacial averaged structure that is mapped by the diffraction intensities and calculated by Rietveld refinement.*

is due both to error in the pressure determination with the equation of state and to a slight offset of the DAC respect to the instrument sample position. The main interest of this test is to verify the signal to noise ratio and to develop a good quality of counting statistics with increasing pressure. The diffraction pattern shown in Figure 6.12 was collected for only ∼50 min and an increased collection time may increase the signal to noise ratio.

By increasing pressure the patterns lose quality and intensity. This was later found to be a result of the diamond anvils embedded on seats which were too soft. This made the diamonds sink into the seats and reduced the angular aperture for diffraction. Higher pressure points were also measured at 14.9, 19.8, 30.0 and 36.0 GPa. Figure 6.13 shows representative full diffraction patterns at the

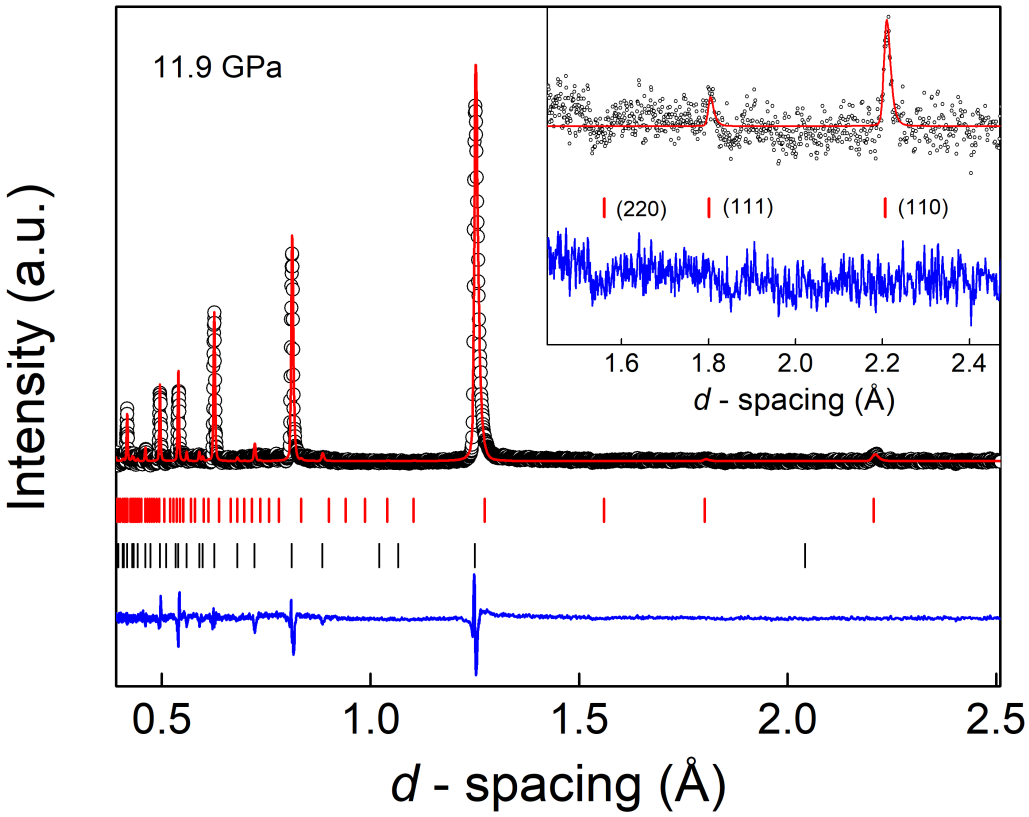

Figure 6.12 *Neutron-diffraction pattern of D_2O ice VII at 11.9 GPa. Data are shown as open circles. Red line shows either Rietveld refinement of the neutron pattern or Le Bail extraction of the structure. Vertical tick marks indicate from top to bottom: sample, single-crystal diamond anvils. Inset shows details of the Rietveld refinement of the (110) Bragg reflection of ice VII. Blue lines show residual of the fits.*

selected pressures of 19.8 and 36 GPa. Right panels show a zoom in the 1.8–2.4 Å range, given as evidence of the Rietveld refinement performed on the (110) Bragg reflection used to determine the lattice parameter and hence the pressure on the D_2O sample.

The difference in quality of the data between 19.8 and 36 GPa depends on the acquisition time. The highest pressure point has a data collection time of ∼13 h, whereas less than 2 h of collection were used at 19.8 GPa. Table 6.2 reports refined volume, structural parameters and pressure values of D_2O ice VII. Pressure values were again determined by the use of a Birch-Murnaghan EoS adopting parameters determined by neutron diffraction of $V_0 = 42.25$ Å^3, bulk modulus $B_0 = 13.8(2)$ GPa and $B' = 5.9(1)$.

Despite the increase of the acquisition time at the last pressure point, the (110) reflection is hardly detectable and significantly broadened. The pressure point was determined by isolating the weak (110) reflection and by fitting the position

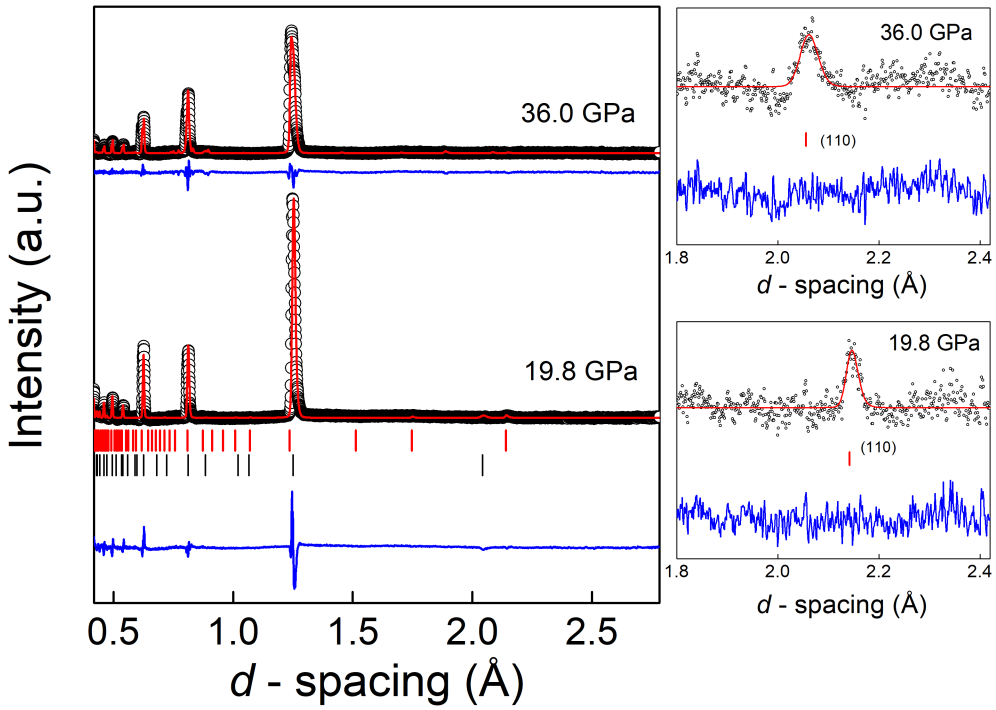

Figure 6.13 *D_2O neutron diffraction data collected at 19.8 and 36.0 GPa (open circles). Red lines show a Le Bail fit to the data. Right panels show a zoom in the 1.8–2.4 d-spacing range. Red lines show Rietveld refinements of the (110) Bragg reflection of ice VII. Blue lines indicate residual of the fits.*

Table 6.2 *Refined volume and structural parameters of $Pn\bar{3}m$ D_2O ice VII as a function pressure. Reported pressure values are determined using the D_2O equation of state determined by previous neutron diffraction work [290].*

Unit-cell volume (Å)	Pressure (GPa)	Lattice Parameter (Å)
30.38(2)	11.9	3.1206(6)
29.77(3)	13.4	3.099(1)
27.71(2)	19.8	3.0262(7)
25.53(4)	30.0	2.944(1)
24.57(6)	36.0	2.907(1)

with the cubic space group of ice VII.

Figure 6.14 shows a plot of the generated pressure on D_2O as a function of the applied pressure by the gas membrane system. The trend reflects a standard pressure as a function of load performance curve, which is satisfactory for the current experiment. The diamond anvil cell has reached 36 GPa on the D_2O sample, and the pressure values could be determined monitoring the (110) Bragg reflection despite the low signal to noise ratio. A major issue during the refinement

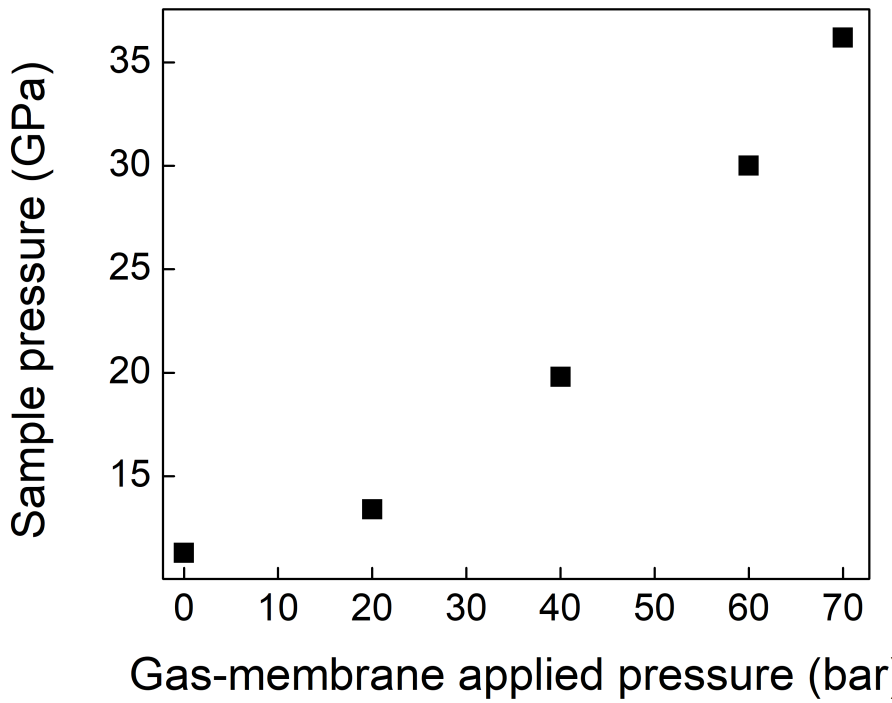

Figure 6.14 *Determined pressure on the D_2O sample as a function of the applied pressure generated by the gas membrane system.*

of the structure comes from strong Bragg peaks from the single-crystal diamond anvils. The diamond phase was introduced in the Rietveld powder diffractogram refinement as an additional phase, but this strongly affects the ability to obtain a good refinement of the overall d-spacing range. In addition, by increasing loading a strong peak broadening of the sample reflections occurred. This is found to be an effect of the diamond-anvil attenuation on the sample Bragg intensities, which increases with increasing pressure [268, 274, 275, 291]. Diamond attenuation correction is extremely important for D_2O ice VII, where the (111) Bragg reflection lies inside the largest dip in transmission through the diamond. No attenuation correction was applied to this data set with a consequent loss of intensity and peak broadening, which is seen to worsen with increasing pressure.

6.4.2 $LaCoO_3$ beyond 10 GPa

A further test was carried out on the $LaCoO_3$ perovskite material previously study by PE-press [1]. $LaCoO_3$ is a perovskite compound exhibiting the $R\bar{3}c$ space group. The crystal structure is more complex than the diamond-like $Fd\bar{3}m$ germanium and can ideally represent the standard type of material investigated on PEARL. Furthermore, the recent study by PE-press, shown in Chapter 3, offers a straightforward comparison to the DAC measurements in terms of collected patterns and quantitative structural analysis. About 0.1 mm^3 of the $LaCoO_3$ powder sample was loaded in DAC in a stainless-steel gasket pre-indented to 210 μm of thickness in a drilled hole of 800 μm in diameter. Argon was loaded as PTM following the Ar cryogenic loading method previously described, as the aim of this second test was not only to verify the quality of the neutron patterns but also to apply a pressure higher than 10 GPa onto the sample. The small amount of perovskite sample was successfully measured and Figure 6.15 shows neutron-diffraction patterns acquired on PEARL at pressures of 2.6, 5.3 and 15.3 GPa of the $LaCoO_3$ sample in the 1.5–2.6 Å d-spacing range.

Pressure values were determined *in situ* by ruby fluorescence measurements. Raw data are shown as open circles, while the red line represents the Rietveld refinement to the data. Tick marks from the sample phase are shown and the Bragg reflection from the steel gasket is marked as *. The diffraction patterns at 2.6 and 5.3 GPa were collected over 20 h while the last pressure point at 15.3 GPa was collected over 9 h, in order to compare the different statistics associated to the collected data. The main reflections from the sample are clearly

visible over the background and the choice of this shortened d-spacing range is due to the presence of the high intense single-crystal diamond Bragg peaks at lower d-spacing, which would affect the quality of the Rietveld refinement. After successfully measuring the $LaCoO_3$ material, Rietveld refinement of the diffraction patterns were performed using the GSAS package [146]. The main interest is to verify the quality of the data collected by DAC, that is how accurate a quantitative structural analysis is by the refinement of the DAC-neutron-powder-diffraction patterns. Refined structural parameters such as the volume, the Co–O bond distance and the oxygen fractional coordinate were compared to values reported in the previous study on $LaCoO_3$ by PE-press [1]. Table 6.3 reports selected refined and calculated parameters from the DAC and PE-press neutron-

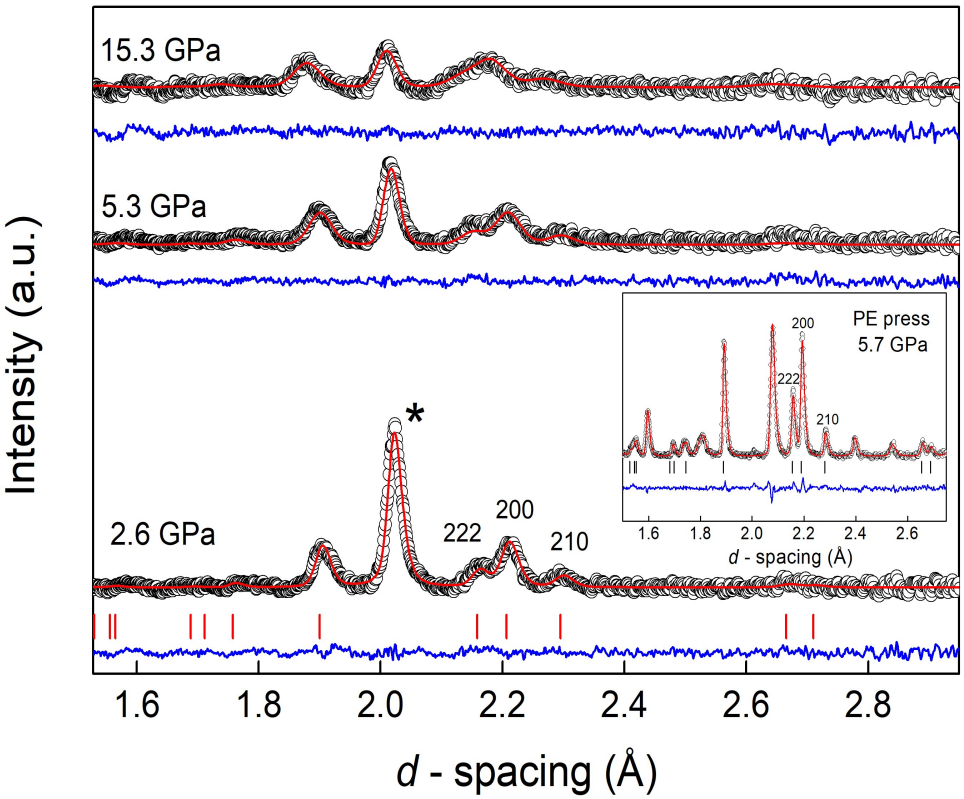

Figure 6.15 *Neutron diffraction patterns of $LaCoO_3$ collected on PEARL at applied pressures of 2.6, 5.3 and 15.3 GPa. Data are shown as open circles, while red lines represent the Rietveld refinement to the data. Tick marks indicate calculated reflection from the sample phase. Reflection arising from the steel gasket is marked as "*". Bottom blue line shows the residual of the refinement calculated as difference between observed and calculated intensity. Inset shows the $LaCoO_3$ diffraction pattern acquired using the PE press.*

Table 6.3 *Refined and determined structural parameters of $LaCoO_3$ by DAC and PE-press neutron-diffraction data obtained by Rietveld refinement using the GSAS package.*

Parameter	Diamond anvil cell		Paris-Edinburgh press [1]	
P (GPa)	2.6	5.3	2.5	5.6
O_x	0.202(1)	0.201(1)	0.2044(3)	0.2055(4)
V (Å^3)	109.84(3)	108.91(4)	110.114(4)	107.892(6)
a (Å)	5.332(1)	5.309(1)	5.3476(1)	5.3476(1)
α (°)	61.09(1)	61.28(1)	60.810(2)	60.821(3)
Co–O (Å)	1.9180(9)	1.9135(11)	1.9182(2)	1.9045(3)
Co–O–Co (°)	164.7(4)	164.3(4)	164.70(9)	165.07(10)
La–O1 (Å)	2.454(7)	2.445(7)	2.4598(18)	2.455(2)
La–O2 (Å)	2.6783(8)	2.6677(10)	2.68518(18)	2.6699(2)
La–O3 (Å)	2.966(7)	2.968(7)	2.9532(18)	2.930(2)

diffraction data at pressures of $\sim$ 2.5 and 5.5 GPa. A direct comparison between the calculated volumes and Co–O bond distances as a function of pressure can be seen in Figures 6.16a and 6.16b, where the values determined by neutron-diffraction measurements using the DAC are plotted against previously reported PE-press data [1].

Although there is clear correlation between the two pressure cells at the lowest pressure point of collection around 2.5 GPa, the structural parameters start to diverge with increasing pressure. The parameter offsets are still very low at the pressure value around 5.5 GPa with a divergence of only 0.9 % for the volume and 0.5 % for the Co–O bond distance. This low divergence reassures on the quality and consistency of our measurements and probable causes may be found either in non-hydrostatic conditions during the DAC measurements (a non-successful Ar loading) or in the cell position, not aligned to the sample instrument position.

A great advantage in a neutron diffraction experiment compared to an X-ray one is to exploit the complex dependence on the atomic number Z of the scattering cross section. As a consequence, elements such as oxygen atoms are accurately visible by neutrons even in presence of heavier atoms such as lanthanum or cobalt. This implies a better accuracy compared to X-ray diffraction in the refined oxygen positions and hence in the structural parameters such as bond distances and angles or tilting angles directly related to them [65]. In the light of this, the major interest is to test the DAC-data sensitivity to the refined oxygen fractional coordinate in order to verify the reliability of the refined values by Rietveld refinement. A straightforward way to pursue this verification is to displace the O_x

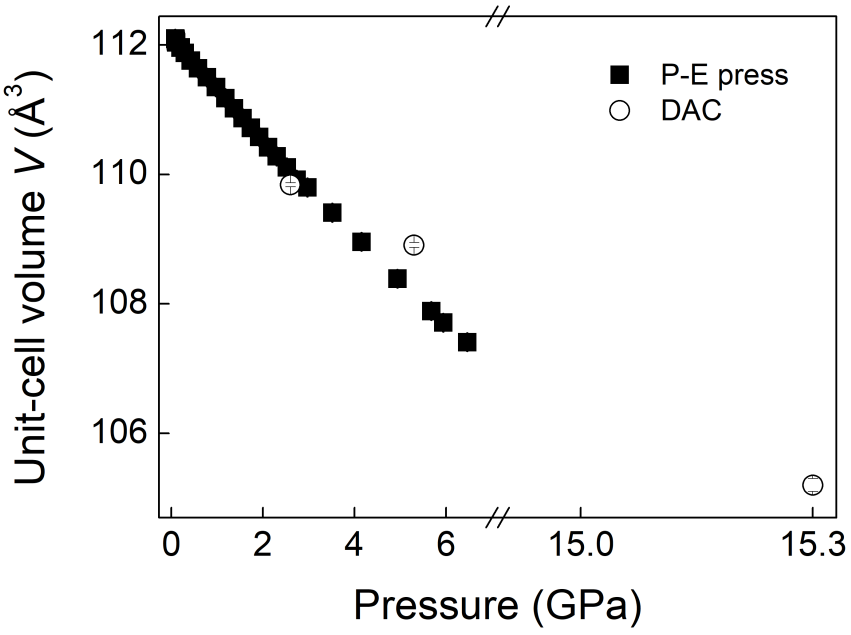

(a)

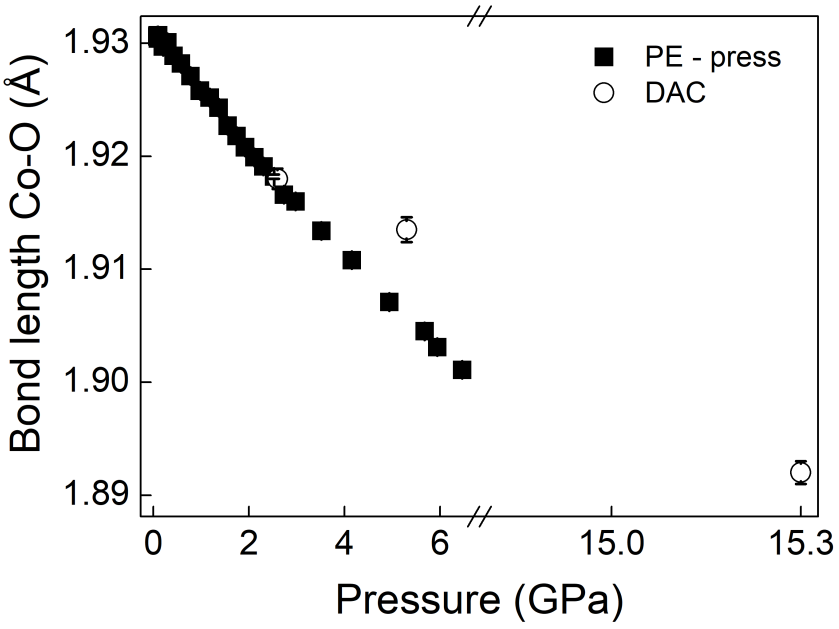

(b)

Figure 6.16 *6.16a $LaCoO_3$ unit-cell volume as a function of pressure determined from DAC neutron-diffraction data (open circles) and PE-press data (filled squares). 6.16b Co–O pressure dependence determined from DAC and PE-press neutron-diffraction data with consistency of symbols. Error bars are also shown.*

(in $R\bar{3}c$ the only O_x coordinate is refined by symmetry) fractional coordinate from the refined position and monitor how the quality of the refinement is affected, that is to monitor the χ^2 behaviour. Figure 6.17 shows the variation of the χ^2 associated to the Rietveld refinement as a function of the oxygen displacement from the refined position.

The DAC refinement shown as open circles was performed on the data set at 5.3 GPa, while filled squares show the PE press χ^2 at the pressure value of 5.6 GPa as reported in [1]. Despite the different variation range for the two pressure cells, the χ^2_{DAC} minimum at the refined position is clearly defined as the O_x is arbitrary moved off. This result proves the reliability of the oxygen coordinate obtained by means of the DAC-neutron-diffraction pattern and hence the possibility to perform structural refinement from the collected data despite the lower sensitivity due to the reduced sample volume. A slight offset can be seen between the two minima, but this is found to reflect an offset between the DAC position during experiments and the instrument calibrated sample position.

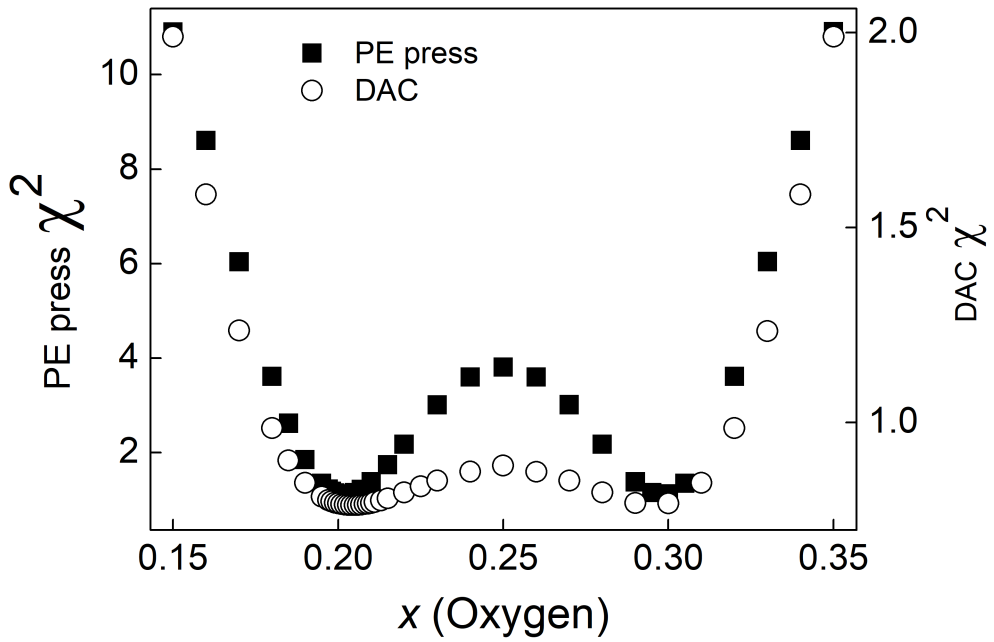

Figure 6.17 *$LaCoO_3$ Rietveld refinement χ^2 variation as function of the O_x fractional coordinate displacement from the refined value for both the DAC (open circles) and PE press (filled squares) measurements.*

6.5 Summary and conclusions

The development of diamond anvil cells on the PEARL instrument is a project aimed at extending the accessible pressure range on the ISIS diffractometer. Special sample environment capabilities had to be developed to adapt the DAC to the geometry of the instrument and to the ISIS neutron beam. A special mounting flange equipped with a moving stage system was designed in order to align the cell accurately from a remote location. A specific BN collimation system was also developed to tune the PEARL neutron radiation to the small entrance of diamond anvil cells to avoid contribution from the sample environment to the scattering signal. The transparency of the diamond anvils was exploited to use ruby fluorescence measurements to determine *in situ* the pressure generated on samples, and to create optical-live access during experiments. The development of a cryogenic gas loading procedure for diamond anvil cells was also carried out to use argon as PTM and maintain quasi-hydrostatic pressure conditions above 10 GPa.

After developing the required instrument capabilities, trial neutron-diffraction measurements were performed on different kind of samples. On an ice VII D_2O sample PEARL reached its maximal generated pressure with a value of ∼36 GPa. Powder samples such as germanium were also investigated by means of DACs and neutron-diffraction patterns of a sample volume in the order of $\sim 0.1\,mm^3$ was successfully measured at the ISIS facility. The $LaCoO_3$ oxide has also been measured on PEARL and neutron diffraction patterns were collected up to ∼15 GPa. The structural analysis carried out on the perovskite sample showed that the data collected by means of the DAC are characterised by a good sensitivity to the structural parameters. This result is extremely promising with the aim of using the diamond anvil cell to perform a quantitative structural analysis of samples under investigation. Despite these positive results, it is important to highlight that no diamond attenuation correction was performed on the current work, and this inevitably affects the reliability of the overall results.

To-date the DAC is routinely tested on PEARL. Improvements in the collimation system and shielding to reduce the background scattering from the pressure cell and its components are fundamental to enhance the signal quality. A perfect alignment of the cell to the instrument sample position is also fundamental to the reliability of the collected data. Future work will aim to develop a diamond attenuation correction procedure, to take into account the important effect of

intensity loss due to scattering from the diamond anvils. Further testing of the DAC performance in signal quality and pressure generation will also be performed, with the final goal to make diamond anvil cells an alternative choice as pressure tool at the ISIS facility.

Chapter 7

Conclusions

The present work explored the effects of hydrostatic pressure on structural properties of perovskite materials and how physical properties are altered by changes within the crystal structure. Physical and structural properties are strongly correlated in perovskite oxides and the ability to induce subtle variations on the crystal structure by application of pressure (and/or temperature) enables us to tune in a controlled way electrical, mechanical and magnetic properties, with great advantages in technological applications. In parallel, the present work extended the PEARL instrument capabilities through the deployment of diamond anvil cells for neutron diffraction. Diamond anvil cells provide an extended accessible pressure range during experiments and in particular enable measurements of samples synthesised by high-pressure techniques, which typically do not produce sample quantity enough for a PE press.

However, it is still challenging to combine high-pressure experiments with neutron diffraction techniques. Neutron radiation fluxes are relatively low and require large sample volumes to obtain good quality data. Such large sample volumes limit the pressure which can be generated. Although the technical challenge may discourage the use of neutron diffraction for high-pressure experiments, it is worthwhile because this technique provides a unique signature of a material crystal structure and its magnetic properties which cannot be obtained with other diffraction techniques such as X-ray diffraction.

Firstly, this work has shown empirical findings on perovskite oxides, focusing on structural-physical property relationships and how these are correlated by the application of pressure. In chapter *High-pressure studies of* $LaCoO_3$, high-

pressure/temperature dependent experiments on the $LaCoO_3$ oxide are reported. This material is characterised by electronic spin-state transitions, which are strongly temperature and pressure dependent. However, there is a strong literature controversy on the structural-physical properties of $LaCoO_3$, which promote these electronic transitions. In the current thesis, unique information has been obtained on this material by the use of neutron diffraction. Structural parameters, tilting angles, bond distances and angles have been determined with a higher accuracy than previously obtainable, and the structural behaviour observed is found to be in contrast with previous X-ray work on $LaCoO_3$. The chapter *High pressure study of $LaFeO_3$* reports a similar study on $LaFeO_3$. In this case, the interest has been to detect possible pressure-induced phase transitions of the structure, and measurements have been collected up to 16 GPa. This work is the first high-pressure neutron-diffraction characterisation of this material at such high pressures. As for $LaCoO_3$, structural parameters, tilting angles, bond distances and angles have been determined with an excellent accuracy. In addition, neutrons can be used to map the magnetic structure of materials, and the magnetic moment of the long-range antiferromagnetic $LaFeO_3$ has been investigated as a function of pressure. This work has also investigated the effect of chemical doping on these materials and how their structural and physical properties are affected under high-pressure. In chapter *Effect of pressure in doped perovskite oxides: magnetic and structural study of $LaCo_{0.9}Mn_{0.1}O_3$* the $LaCo_{0.9}Mn_{0.1}O_3$ oxide has been studied at ambient temperature in the 0–6 GPa range. Again, full structural refinement has revealed how the structure changes under the application of pressure. A very interesting result has been obtained on the magnetic behaviour of this sample. By DC magnetometry measurement, the Curie temperature evolution has been studied. A non-linear increase as a function of pressure has been reported and related to the tilting distortion of the octahedra, which are found to control the Curie temperature behaviour. These chapters have focused on the structural-physical properties of oxides. The main interest has been to determine the tilting angles distortion parameters, and how they vary with pressure, because the tilting of the octahedra is known to be responsible for most electronic, magnetic and optical properties of perovskites. This work of thesis has determined such fundamental parameters for all the investigated samples by the use of neutron-diffraction, which has a high sensitivity to all the single constituents of the crystal structure, obtaining values of very high accuracy.

In the last of the results chapters *Extending accessible pressure range at the ISIS facility* this thesis describes the work carried out to deploy new pressure cells

on the PEARL instrument. Specially designed diamond anvil cells have been implemented on PEARL, and fundamental instrument capabilities, such as the ruby fluorescence optical setup, cryogenic gas loading for pressure transmitting media and a specially designed collimation set have been developed. The signal quality of these cells has been tested with various types of materials with very promising results. Neutron-diffraction data has been successfully collected on the PEARL instrument for the first time on samples in the order of $\sim$0.01 mm^3. Data collected on $LaCoO_3$ has provided a sufficient data quality to perform Rietveld refinement of the crystal structure. In addition, a pressure value of $\sim$36 GPa has been obtained on an ice VII D_2O sample, which is the highest pressure value ever obtained on PEARL.

The diamond cells have shown a great potential for high-pressure experiments despite the technical challenges mainly related to the combination of small sample volumes and low neutron fluxes. Future work will aim firstly to develop a diamond attenuation correction method for these specially designed cells, which will improve the quality of the collected data by enabling subtle corrections of the collected signal intensity. Furthermore, additional tests will explore the pressure performance of these cells with the goal to go beyond the 36 GPa pressure value obtained on PEARL. Lastly, further measurements are needed to improve the signal to noise ratio and accuracy of data, by testing different collimation sets or by enhancing shielding of background scattering. Such improvements will enable the study of perovskite-oxides investigated in this work of thesis at pressures higher than those reported so far. Future work will aim at reviewing these samples, and many more, with this new type of cell with the final goal to explore part of the phase diagram which have rarely been reached by neutron-diffraction.

Despite the technical challenges of combining high-pressure experiments with neutron diffraction, this is an experimental technique which provides unique information on materials. This is especially true for perovskite-oxide materials and their structural-physical property relationships. Neutrons are capable of helping us to map the structure with an accuracy not achievable by other diffraction techniques, and also provide information on physical properties. The well-established PE-press as pressure tool for neutron diffraction has led in the past and is still leading high-pressure research and impact results can be obtained. In parallel to that continuous effort is made in enhancing high-pressure neutron-diffraction capabilities such as the DAC deployment at the ISIS facility. The DAC project has already overcome many technical challenges and is yielding valuable

results. With further refinement it will surely become an even more robust and reliable method for high-pressure studies on a wide variety of materials.

Appendix A

Refined and determined structural parameters of $LaCoO_3$ as a function of pressure and temperature.

Neutron-diffraction data of $LaCoO_3$ were collected on the PEARL instrument as a function of pressure and temperature. $LaCoO_3$ was measured at 120 K in the 0–4.1 GPa pressure range; at 290 K (ambient temperature) in the 0–6.4 GPa range; and at 480 K in the 0–5.5 GPa pressure range. Refined and determined structural parameters of complete collected data sets are reported as a function of pressure in Table A.1 for measurements at 120 K, Table A.2 for measurements at 290 K and Table A.3 for measurements at 480 K.

The structure was refined with a trigonal $R\bar{3}c$ space group in rhombohedral setting. The atomic positions used in the proposed structure at each temperature and pressure are: La $\left(\frac{1}{4}, \frac{1}{4}, \frac{1}{4}\right)$, Co $(0, 0, 0)$ and O $\left(x, -x + \frac{1}{2}, \frac{1}{4}\right)$, on the Wyckoff sites *2a*, *2b* and *6e*, respectively. The O_x crystallographic positions are the only parameters refined by the Rietveld procedure, as well as the unit-cell parameters. Tilting angle (ω) and octahedral strain parameters (ζ) were calculated using Equations 1.6 and 1.7, as defined in Section 1.4.3 for the $R\bar{3}c$ space group. The R_p and wR_p values of the Rietveld refinements are also reported.

Table A.1 *Structural parameters, O_x fractional coordinate, tilting angle ω, strain ζ, La–Oi bond distances, Co–O bond distances and Co–O–Co bond angles of $LaCoO_3$ as a function of pressure at 120 K determined by Rietveld refinement.*

P (GPa)	0.06(7)	0.21(7)	0.34(7)	0.69(7)	0.91(7)
V (Å^3)	111.02(1)	110.87(1)	110.73(1)	110.44(1)	110.25(1)
a (Å)	5.3584(1)	5.3555(1)	5.3538(2)	5.3485(2)	5.3453(2)
α (°)	60.907(2)	60.922(2)	60.910(3)	60.924(2)	60.928(2)
O_x	0.1997(3)	0.1998(3)	0.2006(3)	0.1999(3)	0.2006(3)
ω (°)	9.80(5)	9.87(5)	9.70(7)	9.84(5)	9.71(6)
ζ	-0.0432	-0.0436	-0.0428	-0.0436	-0.0434
Co–O (Å)	1.9300(2)	1.9260(3)	1.9246(2)	1.9235(2)	1.9218(2)
Co–O–Co (°)	164.4(1)	163.7(1)	164.0(1)	163.7(1)	163.9(1)
La–O1(Å)	2.4425(16)	2.4423(17)	2.446(2)	2.4399(16)	2.4423(17)
La–O2(Å)	2.69314(17)	2.6916(2)	2.6903(2)	2.6880(2)	2.6860(2)
La–O3(Å)	2.9893(16)	2.9877(17)	2.981(2)	2.9832(16)	2.9778(17)
wR_p (%)	6.2	6.46	7.88	6.11	6.4
R_p (%)	6.27	6.34	7.94	6.15	6.51
P (GPa)	1.0(7)	1.69(7)	1.75(7)	1.83(7)	1.96(8)
V (Å^3)	110.18(1)	109.63(1)	109.57(1)	109.54(1)	109.41(1)
a (Å)	5.3442(2)	5.3348(1)	5.3339(2)	5.3333(2)	5.3313(2)
α (°)	60.929(2)	60.939(2)	60.940(2)	60.942(2)	60.940(3)
O_x	0.2000(2)	0.2010(3)	0.2008(3)	0.2006(3)	0.2015(3)
ω (°)	9.82(6)	9.62(4)	9.66(6)	9.71(6)	9.53(7)
ζ	-0.0437	-0.0435	-0.0436	-0.0438	-0.0433
Co–O (Å)	1.9219(2)	1.9179(2)	1.9177(3)	1.9177(3)	1.9163(3)
Co–O–Co (°)	163.8(1)	164.1(1)	164.0(1)	163.9(1)	164.2(1)
La–O1 (Å)	2.4387(18)	2.4404(13)	2.4388(18)	2.4373(18)	2.441(2)
La–O2 (Å)	2.6858(2)	2.68053(14)	2.6801(2)	2.6799(2)	2.6785(2)
La–O3 (Å)	2.980(2)	2.9701(13)	2.971(2)	2.972(2)	2.965(2)
wR_p (%)	7.38	4.71	6.53	6.61	7.35
R_p (%)	9.52	4.95	7.04	6.87	7.85
P (GPa)	2.09(8)	2.31(8)	2.59(8)	2.80(8)	3(8)
V (Å^3)	109.28(1)	109.14(1)	108.90(1)	108.73(1)	108.51(2)
a (Å)	5.3288(2)	5.3264(2)	5.3219(2)	5.3191(2)	5.3165(2)
α (°)	60.951(3)	60.952(3)	60.967(3)	60.967(3)	60.974(3)
O_x	0.2004(3)	0.2002(3)	0.2004(4)	0.2017(4)	0.2014(4)
ω (°)	9.75(6)	9.78(6)	9.74(7)	9.49(7)	9.56(6)
ζ	-0.0442	-0.0443	-0.0447	-0.0440	-0.0444
Co–O (Å)	1.9164(2)	1.9156(3)	1.9141(3)	1.9121(3)	1.9116(3)
Co–O–Co (°)	163.9(1)	163.8(1)	163.9(1)	164.3(1)	164.2(1)
La–O1 (Å)	2.4344(17)	2.4326(18)	2.432(2)	2.437(2)	2.435(2)
La–O2 (Å)	2.67786(2)	2.6767(2)	2.6744(2)	2.6723(2)	2.6711(2)
La–O3 (Å)	2.971(2)	2.970(2)	2.967(2)	2.958(2)	2.959(2)
wR_p (%)	6.25	6.61	6.94	6.83	6.57
R_p (%)	6.44	6.9	6.83	6.81	6.51

P (GPa)	3.30(9)	3.95(9)	4.04(9)	4.15(9)
V (Å^3)	108.38(2)	108.04(2)	108.00(2)	107.93(2)
a (Å)	5.3130(2)	5.3061(3)	5.3053(2)	5.3042(3)
α (°)	60.980(3)	61.013(4)	61.016(3)	61.014(4)
O_x	0.2015(4)	0.2024(4)	0.2011(3)	0.2019(4)
ω (°)	9.53(7)	9.37(7)	9.60(6)	9.46(7)
ζ	-0.0444	-0.0451	-0.0458	-0.0454
Co–O (Å)	1.9103(3)	1.9077(3)	1.9083(3)	1.9073(3)
Co–O–Co [°]	164.2(1)	164.5(1)	164.1(1)	164.3(1)
La–O1 (Å)	2.434(2)	2.437(2)	2.430(2)	2.433(2)
La–O2 (Å)	2.6693(2)	2.6654(2)	2.6656(2)	2.6647(2)
La–O3 (Å)	2.957(2)	2.950(2)	2.956(2)	2.951(2)
wR_p (%)	6.72	6.93	5.67	6.87
R_p (%)	6.73	7.02	5.49	6.90

Table A.2 *Structural parameters, O_x fractional coordinate, tilting angle ω, strain ζ, La–Oi bond distances, Co–O bond distances and Co–O–Co bond angles of $LaCoO_3$ as a function of pressure at 290 K, determined by Rietveld refinement. The R_p and wR_p values of the Rietveld fits are also reported.*

P (GPa)	0.08(7)	0.10(8)	0.09(6)	0.09(6)	0.20(6)	0.29(7)	0.42(6)
V (Å^3)	112.10(1)	112.04(1)	112.08(1)	112.05(1)	111.95(1)	111.88(1)	111.76(1)
a (Å)	5.3802(1)	5.3790(1)	5.3799(1)	5.3792(1)	5.3777(1)	5.3766(1)	5.3746(1)
α (°)	60.795(2)	60.801(2)	60.795(2)	60.803(2)	60.800(2)	60.798(2)	60.800(2)
O_x	0.2030(3)	0.2024(3)	0.2028(3)	0.2029(3)	0.2031(3)	0.2020(3)	0.2028(2)
ω (°)	9.50(5)	9.67(5)	9.60(5)	9.57(5)	9.54(5)	9.70(5)	9.58(5)
ζ	-0.0387	-0.0394	-0.0390	-0.0392	-0.0390	-0.0394	-0.0391
Co–O (Å)	1.9307(2)	1.9307(2)	1.9307(2)	1.9305(2)	1.9298(2)	1.9301(2)	1.9289(2)
Co–O–Co (°)	164.34(8)	164.05(9)	164.17(7)	164.22(8)	164.28(7)	164.00(8)	164.22(7)
La–O1 (Å)	2.4665(16)	2.4631(18)	2.4654(14)	2.4659(15)	2.4662(14)	2.4595(16)	2.4628(14)
La–O2 (Å)	2.70225(16)	2.70196(18)	2.70223(14)	2.70177(15)	2.70095(15)	2.70096(16)	2.69958(14)
La–O3 (Å)	2.9783(16)	2.9810(18)	2.9791(14)	2.9785(15)	2.9765(14)	2.9818(16)	2.9766(14)
wR_p (%)	3.57	4.60	3.56	3.82	3.59	3.95	3.51
R_p (%)	3.82	5.27	3.62	4.08	3.46	4.13	3.38
P (GPa)	0.58(6)	0.77(6)	0.97(2)	1.18(8)	1.36(7)	1.55(7)	1.74(7)
V (Å^3)	111.64(1)	111.50(1)	111.34(1)	111.18(1)	111.02(1)	110.87(1)	110.72(1)
a (Å)	5.3728(1)	5.3703(1)	5.3677(1)	5.3652(1)	5.3623(1)	5.3599(1)	5.3574(1)
α (°)	60.799(2)	60.803(2)	60.805(2)	60.803(2)	60.808(2)	60.808(2)	60.809(2)
O_x	0.2027(3)	0.2032(3)	0.2037(3)	0.2032(3)	0.2031(3)	0.2042(3)	0.2043(3)
ω (°)	9.61(5)	9.49(5)	9.40(5)	9.44(5)	9.45(5)	9.31(5)	9.31(5)
ζ	-0.0392	-0.0390	-0.0388	-0.0389	-0.0391	-0.0387	-0.0388
Co–O (Å)	1.9282(2)	1.9271(2)	1.9258(2)	1.9252(2)	1.9243(2)	1.9227(2)	1.9218(2)
Co–O–Co (°)	164.15(8)	164.36(8)	164.51(8)	164.44(8)	164.42(8)	164.66(8)	164.65(8)
La–O1 (Å)	2.4617(15)	2.4631(16)	2.4652(17)	2.4612(17)	2.4596(17)	2.4644(18)	2.4636(17)
La–O2 (Å)	2.69866(16)	2.69721(17)	2.69561(17)	2.69457(18)	2.69321(17)	2.69144(18)	2.69017(18)
La–O3 (Å)	2.9758(15)	2.9723(16)	2.9677(17)	2.9690(17)	2.9681(17)	2.9609(18)	2.9593(17)
wR_p (%)	3.88	4.03	4.13	4.19	4.21	4.28	4.28
R_p (%)	4.20	4.58	4.66	4.97	4.69	4.89	5.04
P (GPa)	1.91(8)	2.11(8)	2.30(8)	2.52(8)	2.73(8)	2.97(7)	3.51(8)
V (Å^3)	110.57(1)	110.41(1)	110.27(1)	110.11(1)	109.92(1)	109.79(1)	109.40(1)
a (Å)	5.3551(1)	5.3525(1)	5.3504(1)	5.3476(1)	5.3444(1)	5.3425(1)	5.3357(1)
α (°)	60.811(2)	60.813(2)	60.807(2)	60.810(2)	60.815(2)	60.811(2)	60.821(2)
O_x	0.2045(3)	0.2044(3)	0.2045(3)	0.2044(3)	0.2052(3)	0.2049(3)	0.2055(3)
ω (°)	9.24(5)	9.35(5)	9.29(5)	9.28(5)	9.22(5)	9.25(5)	9.25(5)
ζ	-0.0386	-0.0389	-0.0386	-0.0387	-0.0386	-0.0386	-0.0389
Co–O (Å)	1.9208(2)	1.9199(2)	1.9191(2)	1.9182(2)	1.9166(2)	1.9160(2)	1.9134(2)
Co–O–Co (°)	164.78(8)	164.59(8)	164.70(9)	164.70(9)	164.81(9)	164.75(9)	164.76(9)
La–O1 (Å)	2.4638(18)	2.4623(18)	2.4616(18)	2.4598(18)	2.463(2)	2.460(2)	2.460(2)
La–O2[(Å)	2.68889(18)	2.68760(18)	2.68651(18)	2.68518(18)	2.68318(18)	2.68236(18)	2.67870(18)
La–O3 (Å)	2.9568(18)	2.9558(18)	2.9540(18)	2.9532(18)	2.9475(19)	2.9475(18)	2.9414(18)
wR_p (%)	4.38	4.38	4.38	4.30	4.35	4.33	4.25
R_p (%)	5.81	5.10	5.30	5.15	5.16	5.00	4.91

P (GPa)	4.15(1)	4.93(1)	5.67(1)	5.93(1)	6.46(1)
V (Å^3)	108.96(1)	108.38(1)	107.89(2)	107.71(2)	107.41(2)
a (Å)	5.3288(1)	5.3188(2)	5.3110(2)	5.3079(2)	5.3032(2)
α (°)	60.814(2)	60.828(3)	60.821(3)	60.826(3)	60.818(3)
O_x	0.2054(3)	0.2059(4)	0.2055(4)	0.2059(4)	0.2063(4)
ω (°)	9.27(5)	9.12(6)	9.06(6)	9.04(6)	9.02(6)
ζ	-0.0388	-0.0387	-0.0383	-0.0384	-0.0383
Co–O (Å)	1.9108(2)	1.9071(3)	1.9045(3)	1.9032(3)	1.9011(3)
Co–O–Co (°)	164.73(9)	164.9(1)	165.0(1)	165.0(1)	165.1(1)
La–O1 (Å)	2.456(2)	2.455(2)	2.449(2)	2.450(2)	2.449(2)
La–O2 (Å)	2.67526(18)	2.6699(2)	2.6663(2)	2.6645(2)	2.6620(2)
La–O3 (Å)	2.9378(19)	2.930(2)	2.928(2)	2.924(2)	2.919(2)
wR_p (%)	4.36	5.25	5.17	5.49	5.29
R_p (%)	5.06	6.93	6.85	7.06	6.88

Table A.3 *Structural parameters, O_x fractional coordinate, tilting angle ω, strain ζ, La–Oi bond distances, Co–O bond distances and Co–O–Co bond angles of $LaCoO_3$ as a function of pressure at 480 K determined by Rietveld refinement. The R_p and wR_p values of the Rietveld fits are also reported.*

P (GPa)	0.11(2)	0.15(2)	0.22(2)	0.39(2)	0.56(2)	0.69(2)	0.85(2)
V (Å^3)	113.23(1)	113.20(1)	113.16(1)	112.99(1)	112.85(1)	112.71(1)	112.60(1)
a (Å)	5.4026(2)	5.4020(1)	5.4010(2)	5.3985(2)	5.3963(2)	5.3939(2)	5.3923(2)
α (°)	60.688(2)	60.691(3)	60.699(3)	60.694(3)	60.693(3)	60.697(3)	60.693(3)
Ox	0.2031(4)	0.2041(4)	0.2041(4)	0.2051(4)	0.2051(4)	0.2046(4)	0.2051(5)
ω (°)	9.07(7)	9.03(7)	9.03(7)	8.84(7)	8.84(8)	8.93(8)	8.84(9)
ζ	-0.0319	-0.0313	-0.0315	-0.0273	-0.0272	-0.0295	-0.0272
Co–O (Å)	1.9364(3)	1.9361(3)	1.9359(3)	1.9342(3)	1.9334(3)	1.9330(3)	1.9319(3)
Co–O–Co (°)	165.07(12)	165.14(12)	165.14(13)	165.46(13)	165.48(15)	165.29(15)	165.47(16)
La–O1 (Å)	2.478(2)	2.479(2)	2.479(2)	2.483(2)	2.482(2)	2.478(2)	2.480(3)
La–O2 (Å)	2.7130(2)	2.7126(2)	2.7121(2)	2.7103(2)	2.7092(2)	2.7083(2)	2.7072(3)
La–O3 (Å)	2.981(2)	2.980(2)	2.979(2)	2.972(2)	2.971(2)	2.973(2)	2.969(3)
wR_{p} (%)	3.84	4.11	4.15	4.05	4.31	4.35	4.55
R_{p} (%)	4.10	4.61	4.54	4.41	4.65	4.49	4.87

P (GPa)	1.01(2)	1.16(2)	1.34(2)	1.55(2)	1.77(2)	1.99(3)	2.24(3)
V (Å^3)	112.43(1)	112.30(1)	112.14(1)	111.95(1)	111.79(1)	111.62(1)	111.41(1)
a (Å)	5.3893(2)	5.3874(2)	5.3849(3)	5.3815(3)	5.3790(3)	5.3759(3)	5.3728(2)
α (°)	60.701(3)	60.696(3)	60.694(3)	60.702(3)	60.703(4)	60.709(4)	60.705(4)
O_x	0.2053(5)	0.2053(5)	0.2059(5)	0.2049(5)	0.2057(5)	0.2055(6)	0.2066(6)
ω (°)	8.80(9)	8.80(9)	8.68(9)	8.88(9)	8.72(9)	8.7(1)	8.5(1)
ζ	-0.0265	-0.0264	-0.0236	-0.0284	-0.0247	-0.0258	-0.0205
Co–O (Å)	1.9309(3)	1.9302(3)	1.9288(4)	1.9284(4)	1.9270(4)	1.9261(4)	1.9242(4)
Co–O–Co (°)	165.52(15)	165.52(16)	165.72(16)	165.40(17)	165.64(18)	165.59(19)	165.93(2)
La–O_1 (Å)	2.480(3)	2.479(3)	2.481(3)	2.474(3)	2.477(3)	2.475(3)	2.479(3)
La–O_2 (Å)	2.7056(3)	2.7047(3)	2.7031(3)	2.7019(3)	2.7003(3)	2.6988(3)	2.6967(3)
La–O_3 (Å)	2.966(3)	2.965(3)	2.960(3)	2.964(3)	2.959(3)	2.958(3)	2.951(3)
wR_{p} (%)	4.57	4.52	4.59	4.61	4.74	4.65	4.68
R_{p} (%)	4.89 2	4.88	4.80	4.91	5.03	5.0	4.98

P (GPa)	2.53(2)	3.01(3)	3.09(2)	3.38(3)	3.70(3)	3.99(2)	4.30(2)
V (Å^3)	111.16(1)	110.95(1)	110.73(1)	110.49(1)	110.26(1)	110.04(1)	109.81(1)
a (Å)	5.3685(4)	5.3652(4)	5.3607(4)	5.3572(4)	5.3530(4)	5.3498(4)	5.3459(4)
α (°)	60.711(5)	60.707(5)	60.731(5)	60.725(5)	60.738(6)	60.727(6)	60.729(6)
O_x	0.2063(6)	0.2063(7)	0.2058(7)	0.2060(7)	0.2070(7)	0.2082(8)	0.2071(8)
ω (°)	8.6(1)	8.6(1)	8.7(1)	8.6(1)	8.5(1)	8.2(1)	8.4(1)
ζ	-0.0220	-0.0219	-0.0249	-0.0238	-0.0193	-0.0144	-0.0187
Co–O (Å)	1.9229(4)	1.9217(5)	1.9208(5)	1.9193(5)	1.9173(5)	1.9152(5)	1.9146(5)
Co–O–Co (°)	165.8(2)	165.8(2)	165.7(2)	165.7(2)	166.0(2)	166.4(2)	166.1(2)
La–O1 (Å)	2.476(3)	2.475(4)	2.470(4)	2.470(4)	2.473(4)	2.478(4)	2.471(4)
La–O2 (Å)	2.6947(3)	2.6930(4)	2.6910(4)	2.6892(4)	2.6866(4)	2.6845(4)	2.6830(4)
La–O3 (Å)	2.950(3)	2.948(4)	2.949(4)	2.946(4)	2.939(4)	2.930(4)	2.934(4)
wR_{p} (%)	4.64	4.69	4.91	4.89	4.91	4.92	4.93
R_{p} (%)	5.09	5.18	5.27	5.40	5.30	5.22	5.36

P (GPa)	4.93(2)	5.51(2)
V (Å^3)	109.35(2)	109.05(2)
a (Å)	5.3387(5)	5.3330(5)
α (°)	60.725(6)	60.742(6)
O_x	0.2073(8)	0.2094(8)
ω (°)	8.4(1)	8.0(1)
ζ	-0.0177	-0.0112
Co–O (Å)	1.9118(5)	1.9086(5)
Co–O–Co (°)	166.1(2)	166.8(3)
La–O1 (Å)	2.468(4)	2.478(5)
La–O2 (Å)	2.6793(4)	2.6755(4)
La–O3 (Å)	2.929(4)	2.915(5)
wR_{p} (%)	4.93	4.61
R_{p} (%)	5.27	4.28

Appendix B

Refined and determined structural parameters of $LaFeO_3$ as a function of pressure and temperature.

Neutron-diffraction data of $LaFeO_3$ were collected on PEARL as a function of pressure and temperature. $LaFeO_3$ was measured at 110 K in the 0–6.5 GPa pressure range, and at 290 K (ambient temperature) in the 0–5.5 GPa range. Refined and determined structural parameters are reported in Table B.2 for measurements at 110 K, and in Table B.1 for measurements at 290 K.

In-phase and out-of-phase tilting angles (ϕ_{in} and ϕ_{out}) were calculated by Equations 1.4 and 1.5, as defined in Section 1.4.2 for the orthorhombic symmetry. The magnetic moment (μ) is also reported as a function of pressure as determined by Rietveld refinement with a magnetic *Pb'n'm* space group. The atomic positions for La, Fe and O atoms in the proposed structure are: La *4c* $\left(x, y, \frac{1}{4}\right)$; Fe *4b* $(0, \frac{1}{2}, 0)$; O1 *4c* $\left(x, y, \frac{1}{4}\right)$ and O2 *8d* (x, y, z). The wR_p values of the Rietveld fits are also shown.

Table B.1 *Structural parameters, fractional coordinates, tilt angles, La/Fe–Oi bond distances, Fe–Oi–Fe bond angles, and magnetic moment of $LaFeO_3$ as a function of pressure at 290 K, as determined by Rietveld refinement (see main text for details). The wR_p values of the Rietveld fits are also reported.*

Pressure (GPa)	0.05(1)	0.73(1)	1.12(1)	1.61(1)	2.05(1)	2.45(2)
V (Å^3)	243.148(8)	242.136(6)	241.580(7)	240.885(6)	240.347(6)	239.832(8)
a (Å)	5.5581(5)	5.5525(4)	5.5489(4)	5.545(4)	5.5418(4)	5.5386(6)
b (Å)	5.5663(5)	5.5577(4)	5.5528(4)	5.5465(4)	5.5412(4)	5.5362(5)
c (Å)	7.8591(7)	7.8464(5)	7.8404(5)	7.8321(5)	7.8266(5)	7.8214(7)
La (x)	0.991(3)	0.993(3)	0.993(2)	0.992(3)	0.993(3)	0.993(2)
La (y)	0.0297(5)	0.0287(4)	0.0286(4)	0.0284(4)	0.0283(3)	0.0281(4)
$O1$ (x)	0.075(1)	0.074(1)	0.073(1)	0.073(1)	0.074(1)	0.072(1)
$O1$ (y)	0.454(1)	0.488(1)	0.489(1)	0.487(1)	0.488(1)	0.490(1)
$O2$ (x)	0.7203(8)	0.7190(7)	0.7192(8)	0.7196(7)	0.7197(7)	0.7198(9)
$O2$ (y)	0.2817(9)	0.2819(7)	0.2814(8)	0.2811(8)	0.2803(8)	0.2815(9)
$O2$ (z)	0.0384(6)	0.0385(5)	0.0386(5)	0.0385(5)	0.0381(5)	0.0384(6)
Fe–O1 (Å)	2.011(2)	2.005(1)	2.003(1)	2.001(1)	2.000(1)	1.996(2)
Fe–O2' (Å)	2.006(6)	2.006(5)	2.003(5)	2.001(5)	1.996(5)	2.000(6)
Fe–O2 (Å)	2.002(5)	1.999(5)	1.998(5)	1.996(5)	1.996(5)	1.991(6)
Fe–O1–Fe (°)	155.3(5)	156.1(4)	156.1(4)	156.1(4)	155.9(4)	156.7(5)
Fe–O2–Fe (°)	157.7(2)	157.5(2)	157.6(2)	157.7(2)	157.9(2)	157.7(2)
σ (La site)	0.07451	0.07215	0.07202	0.07282	0.07206	0.07084
ϕ_{in} (°)	7.0(2)	7.1(1)	7.0(2)	7.0(1)	6.9(1)	7.0(2)
ϕ_{out} (°)	12.2(1)	12.3(1)	12.3(1)	12.3(1)	12.1(1)	12.2(2)
μ (μ_B)	3.9(1)	3.98(7)	4.09(8)	4.07(6)	4.04(8)	4.00(8)
wR_p %	4.3	3.9	4.1	4.9	3.9	4.6

Pressure (GPa)	2.99(2)	3.56(3)	4.22(9)	4.9(1)	5.5(1)
V (Å^3)	239.081(7)	238.316(7)	237.557(7)	236.843	236.086(7)
a (Å)	5.5337(5)	5.5293(6)	5.5245(5)	5.5192(6)	5.5149(5)
b (Å)	5.5295(4)	5.5214(4)	5.5152(3)	5.5086(4)	5.5015(3)
c (Å)	7.8132(6)	7.8059(7)	7.7965(6)	7.7900(8)	7.7810(7)
La(x)	0.9917(9)	0.9897(7)	0.9923(9)	0.992(1)	0.9894(4)
La(y)	0.0293(5)	0.0298(4)	0.0287(4)	0.0289(4)	0.0296(3)
$O1$ (x)	0.073(1)	0.074(1)	0.074(1)	0.074(1)	0.074(1)
$O1$ (y)	0.461(1)	0.490(1)	0.491(1)	0.491(1)	0.494(1)
$O2$ (x)	0.7194(8)	0.7202(8)	0.7201(8)	0.7205(9)	0.7206(7)
$O2$ (y)	0.2797(8)	0.2788(8)	0.2785(8)	0.2781(9)	0.2769(7)
$O2$ (z)	0.0379(5)	0.0370(5)	0.0374(5)	0.0374(6)	0.0370(5)
Fe–O1(Å)	1.995(1)	1.995(1)	1.992(1)	1.990(2)	1.988(1)
Fe–O2' (Å)	1.996(5)	1.984(6)	1.980(5)	1.978(6)	1.971(1)
Fe–O2 (Å)	1.996(5)	1.992(5)	1.992(5)	1.989(6)	1.990(1)
Fe–O1–Fe (°)	156.4(4)	155.8(4)	156.1(4)	156.0(5)	156.2(3)
Fe–O2–Fe (°)	158.0(2)	158.6(2)	158.5(2)	158.6(2)	158.9(2)
σ (La site)	0.07079	0.07158	0.07097	0.07124	0.07009
ϕ_{in} (°)	6.8(2)	6.6(1)	6.6(1)	6.5(2)	6.4(1)
ϕ_{out} (°)	12.1(1)	11.8(1)	11.9(1)	11.9(2)	11.8(1)
μ (μ_B)	4.06(6)	4.21(7)	3.97(6)	4.03(7)	4.09(5)
wR_p %	4.2	4.4	4.4	4.6	3.9

Table B.2 *Structural parameters, fractional coordinates, tilt angles, La/Fe–Oi bond distances, Fe–Oi–Fe bond angles, and magnetic moment of $LaFeO_3$ as a function of pressure at 110 K, as determined by Rietveld refinement (see main text for details). The wR_p values of the Rietveld fits are also reported.*

Pressure (GPa)	0.15(4)	0.91(4)	2.82(4)	3.83(4)
V (Å^3)	241.74(1)	240.50(1)	238.11(1)	236.99(1)
a (Å)	5.5487(8)	5.5390(5)	5.5280(9)	5.523(1)
b (Å)	5.5560(9)	5.5458(5)	5.5250(7)	5.5108(8)
c (Å)	7.840(1)	7.8292(7)	7.795(1)	7.785(1)
La (x)	0.991(1)	0.9883(9)	0.9916(9)	0.990(1)
La (y)	0.031(1)	0.0306(4)	0.0320(5)	0.0341(5)
*O*1 (x)	0.077(1)	0.077(1)	0.068(1)	0.074(1)
*O*1 (y)	0.487(1)	0.486(1)	0.483(1)	0.482(1)
*O*2 (x)	0.719(1)	0.7170(7)	0.7223(8)	0.7259(9)
*O*2 (y)	0.281(1)	0.2799(8)	0.2876(8)	0.2844(9)
*O*2 (z)	0.0381(1)	0.0384(5)	0.0389(5)	0.0375(5)
Fe–O1(Å)	2.007(3)	2.005(1)	1.995(2)	1.992(1)
Fe–O2'(Å)	1.99(1)	2.009(5)	1.976(5)	1.974(5)
Fe–O2(Å)	2.00(1)	1.986(5)	2.022(6)	2.024(6)
Fe–O1–Fe (°)	155.1(8)	154.9(4)	157.3(3)	155.5(4)
Fe–O2–Fe (°)	157.7(4)	157.5(2)	157.0(2)	158.4(2)
σ (La site)	0.07411	0.07568	0.07322	0.07707
ϕ_{in} (°)	7.2(4)	7.1(3)	7.4(3)	6.6(4)
ϕ_{out} (°)	12.1(2)	12.2(1)	12.4(1)	11.9(1)
μ (μ_B)	4.5(1)	4.41(8)	4.33(7)	4.46(8)
wR_{p} %	7.9	3.5	4.1	3.9

Pressure (GPa)	4.47(4)	5.61(5)	6.42(5)
V (Å^3)	236.07(1)	234.52(1)	233.38(2)
a (Å)	5.518(1)	5.509(1)	5.507(1)
b (Å)	5.5025(8)	5.4847(8)	5.4717(9)
c (Å)	7.774(1)	7.760(1)	7.744(1)
La (x)	0.994(1)	0.994(1)	0.996(1)
La (y)	0.0326(5)	0.0346(6)	0.0350(5)
*O*1 (x)	0.077(1)	0.074(1)	0.078(1)
*O*1 (y)	0.481(1)	0.486(1)	0.484(1)
*O*2 (x)	0.7282(8)	0.726(1)	0.729(1)
*O*2 (y)	0.2821(8)	0.281(1)	0.281(1)
*O*2 (z)	0.0385(5)	0.0384(6)	0.0381(6)
Fe–O1(Å)	1.993(1)	1.986(1)	1.985(2)
Fe–O2'(Å)	1.943(5)	1.949(6)	1.933(6)
Fe–O2(Å)	2.021(5)	2.010(6)	2.014(6)
Fe–O1–Fe (°)	154.3(4)	155.8(4)	154.4(4)
Fe–O2–Fe (°)	158.7(2)	158.7(2)	159.1(2)
σ (La site)	0.08043	0.07651	0.06264
ϕ_{in} (°)	6.1(3)	6.2(4)	5.9(4)
ϕ_{out} (°)	12.2(1)	12.2(1)	12.1(2)
μ (μ_B)	4.40(7)	4.35(8)	3.87(8)
wR_{p} %	2.9	4.1	3.4

B.1 Refined and determined structural parameter of $LaFeO_3$ above 10 GPa.

Table B.3 reports structural parameters of $LaFeO_3$ determined by neutron-diffraction at ambient temperature at pressures of 12.1 and 16.2 GPa. Neutron-diffraction data were refined adopting both primitive *Pbnm* and body-centred *Ibmm* orthorhombic symmetries. The atomic positions for La, Fe and O atoms in the *Ibmm* structure are: La *4e* $\left(x, 0, \frac{1}{4}\right)$, Fe *4b* $\left(0, \frac{1}{2}, 0\right)$, O1 *4e* $\left(x, \frac{1}{2}, \frac{1}{4}\right)$ and O2 *8g* $\left(\frac{3}{4}, \frac{1}{4}, z\right)$.

Table B.3 *Structural parameters, tilt angles, Fe–Oi bond distances, Fe–Oi–Fe bond angles, and magnetic moment of $LaFeO_3$ at 12.1 and 16.2 GPa, as determined by Rietveld refinement adopting the Pbnm and Ibmm space groups. The wR_p and χ^2 values of the Rietveld fits are also reported.*

Space Group	*Pbnm*		*Ibmm*	
Pressure (GPa)	12.1	16.2	12.1	16.2
V (Å^3)	228.34(3)	222.16(5)	228.37(4)	222.18(6)
a (Å)	5.4875(7)	5.463(1)	5.4884(9)	5.465(1)
b (Å)	5.4237(7)	5.353(1)	5.4221(8)	5.348(1)
c (Å)	7.6721(8)	7.595(1)	7.673(1)	7.599(2)
Fe–O1 (Å)	1.949(2)	1.935(3)	1.952(3)	1.950(4)
Fe–O2 (Å)	1.904(13)	1.913(13)	1.948(1)	1.926(1)
Fe–O2' (Å)	2.011(13)	1.954(12)	1.948(1)	1.926(1)
Fe–O1–Fe (°)	159.5(8)	157.6(9)	158.5(9)	154.1(1)
Fe–O2–Fe (°)	160.3(5)	162.9(6)	163.7(6)	165.7(7)
ϕ_{in} (°)	6.1(3)	5.1(3)	0	0
ϕ_{out} (°)	10.8(4)	9.6(3)	11.3(3)	9.9(3)
wR_{p} %	6.74	6.46	7.87	6.81
χ^2	1.180	2.915	1.700	3.229

Bibliography

[1] M. Capone, C. J. Ridley, N. P. Funnell, M. Guthrie, and C. L. Bull. *Phys. Status Solidi A*, 216(6):1800736, 2019.

[2] M. Capone, C. J. Ridley, N. P. Funnell, G. B. G. Stenning, J. S. Loveday, M. Guthrie, and C. L. Bull. *J. Phys. Condens. Matter*, 30(3):035402, 2017.

[3] C. J. Ball, B. D. Begg, D. J. Cookson, G. J. Thorogood, and E. R. Vance. *J. Solid State Chem.*, 139(2):238, 1998.

[4] A. Kojima, K. Teshima, Y. Shirai, and T. Miyasaka. *J. Am. Chem. Soc.*, 131(17):6050, 2009.

[5] K. Kuhar, A. Crovetto, M. Pandey, K. S. Thygesen, B. Seger, P. C. K. Vesborg, O. Hansen, I. Chorkendorff, and K. W. Jacobsen. *Energy Environ. Sci.*, 10:2579, 2017.

[6] M. Trzebiatowska, A. Gagor, L. Macalik, P. Peksa, and A. Sieradzki. *Dalton Trans.*, 48:15830, 2019.

[7] B. L. Chamberland. *Mater. Res. Bull.*, 6(5):311, 1971.

[8] S. J. Clarke, B. P. Guinot, C. W. Michie, M. J. C. Calmont, and M. J. Rosseinsky. *Chem. Mater.*, 14:288, 2002.

[9] E. Knittle and R. Jeanloz. *Science*, 235(4789):668, 1987.

[10] R. J. Hemley and R. E. Cohen. *Annu. Rev. Earth Planet. Sci.*, 20, 1992.

[11] Y. Wang, D. J. Weidner, R. C. Liebermann, and Y. Zhao. *Phys. Earth Planet. Inter.*, 83(1):13, 1994.

[12] C. Meade, H.-K. Mao, and J. Hu. *Science*, 268(5218):1743, 1995.

[13] K. Hirose, S. Kei, R. Sinmyo, and J. Hernlund. *Science*, 358(6364):734, 2017.

[14] S.-H. Shim, T. S. Duffy, and G. Shen. *Science*, 293(5539):2437, 2001.

[15] L. Zhang, Y. Meng, W. Yang, L. Wang, W. L. Mao, Q.-S. Zeng, J. S. Jeong, A. J. Wagner, K. A. Mkhoyan, W. Liu, R. Xu, and H-K. Mao. *Science*, 344 (6186):877, 2014.

[16] H. F. Kay and P. Vousden. *Philos. Mag.*, 40(309):1019, 1949.

[17] D. Popovici, M. Okuyama, and J. Akedo. Barium titanate-based materials – a window of application opportunities. *Ferroelectrics*, 2011.

[18] N. Nuraje and K. Su. *Nanoscale*, 5:8752, 2013.

[19] N. A. Benedek and C. J. Fennie. *J. Phys. Chem. C*, 117:13339, 2013.

[20] H. Ye, Y. Tang, P. Li, W. Liao, J. Gao, X. Hua, H. Cai, P. Shi, Y. You, and R. Xiong. *Science*, 361(6398):151, 2018.

[21] Y. Bai, T. Siponkoski, J. Peräntie, H. Jantunen, and J. Juuti. *Appl. Phys. Lett.*, 110(6):063903, 2017.

[22] M. Acosta, N. Novak, V. Rojas, S. Patel, R. Vaish, J. Koruza, G. A. Rossetti, and J. Rödel. *Appl. Phys. Rev.*, 4(4):041305, 2017.

[23] R. von Helmolt, J. Wecker, B. Holzapfel, L. Schultz, and K. Samwer. *Phys. Rev. Lett.*, 71:2331, 1993.

[24] Y. Tokura, A. Urushibara, Y. Moritomo, T. Arima, A. Asamitsu, G. Kido, and N. Furukawa. *J. Phys. Soc. Jpn.*, 63(11):3931, 1994.

[25] S. Jin, T. H. Tiefel, M. McCormack, R. A. Fastnacht, R. Ramesh, and L. H. Chen. *Science*, 264(5157):413, 1994.

[26] A. Urushibara, Y. Moritomo, T. Arima, A. Asamitsu, G. Kido, and Y. Tokura. *Phys. Rev. B*, 51:14103, 1995.

[27] C. N. R. Rao, A. K. Cheetham, and R. Mahesh. *Chem. Mater.*, 8(10):2421, 1996.

[28] A. P. Ramirez. *J. Phys. Condens. Matter*, 9:8171, 1997.

[29] B. Raveau, A. Maignan, C. Martin, and M. Hervieu. *Chem. Mater.*, 10(10): 2641, 1998.

[30] W. Prellier, Ph. Lecoeur, and B. Mercey. *J. Phys. Condens. Matter*, 13 (48):R915, 2001.

[31] C. Autret, J. Hejtmánek, K. Knížek, M. Maryško, Z. Jirák, M. Dlouhá, and S. Vratislav. *J. Phys. Condens. Matter*, 17(10):1601, 2005.

[32] Y. Guo, L. Shi, S. Zhou, J. Zhao, and W. Liu. *Appl. Phys. Lett.*, 102(22): 222401, 2013.

[33] G. Gou, N. Charles, J. Shi, and J. M. Rondinelli. *Inorg. Chem.*, 56(19): 11854, 2017.

[34] S. Yamada, N. Abe, H. Sagayama, K. Ogawa, T. Yamagami, and T. Arima. *Phys. Rev. Lett.*, 123:126602, 2019.

[35] Y. Noda, H. Kimura, M. Fukunaga, S. Kobayashi, I. Kagomiya, and K. Kohn. *J. Phys. Condens. Matter*, 20(43):434206, 2008.

[36] J. Lu, A. Günther, F. Schrettle, F. Mayr, S. Krohns, P. Lunkenheimer, A. Pimenov, V. D. Travkin, A. A. Mukhin, and A. Loidl. *EPJ B*, 75(4): 451, 2010.

[37] J.-G. Park, M. D. Le, J. Jeong, and S. Lee. *J. Phys. Condens. Matter*, 26 (43):433202, 2014.

[38] M. A. Pena and J. L. G. Fierro. *Chem. Rev*, 101:1981, 2001.

[39] J. Suntivich, K. J. May, H. A. Gasteiger, J. B. Goodenough, and Y. Shao-Horn. *Science*, 334:1383, 2011.

[40] S. Wang, G. Xue, and J. Lian J. Meng. *J. Rare Earths*, 32(9):855, 2014.

[41] H. Zhu, P. Zhan, and S. Dai. *ACS Catal.*, 5(11):6370, 2015.

[42] J. Hu, L. Wang, L. Shi, and H. Huang. *Electrochim. Acta*, 161(S3-2):115, 2015.

[43] H. Liang, Y. Hong, C. Zhu, S. Li, Y. Chen, Z. Liu, and D. Ye. *Catal. Today*, 201:98, 2013.

[44] M. K. Wu, J. R. Ashburn, C. J. Torng, P. H. Hor, R. L. Meng, L. Gao, Z. J. Huang, Y. Q. Wang, and C. W. Chu. *Phys. Rev. Lett.*, 58:908, 1987.

[45] S. Hikami and Y. Matsuda. *Jpn. J. Appl. Phys.*, 26(S3-2):1027, 1987.

[46] R. J. Cava. *Science*, 247(4943):656, 1990.

[47] D. Shi, V. Adinolfi, R. Comin, M. Yuan, E. Alarousu, A. Buin, Y. Chen, S. Hoogland, A. Rothenberger, K. Katsiev, Y. Losovyj, X. Zhang, P. A. Dowben, O. F. Mohammed, E. H. Sargent, and O. M. Bakr. *Science*, 347 (6221):519, 2015.

[48] L. Protesescu, S. Yakunin, M. I. Bodnarchuk, F. Krieg, R. Caputo, C. H. Hendon, R. X. Yang, A. Walsh, and M. V. Kovalenko. *Nano Lett.*, 15(6): 3692, 2015.

[49] W. Nie, H. Tsai, R. Asadpour, J.-C. Blancon, A. J. Neukirch, G. Gupta, J. J. Crochet, M. Chhowalla, S. Tretiak, M. A. Alam, H.-L. Wang, and A. D. Mohite. *Science*, 347(6221):522, 2015.

[50] Q. Liu, Y. Wang, N. Sui, Y. Wang, X. Chi, Q. Wang, Y. Chen, W. Ji, L. Zou, and H. Zhang. *Sci. Rep.*, 6(5):29442, 2016.

[51] M. Saliba, T. Matsui, K. Domanski, J. Y. Seo, A. Ummadisingu, S. M. Zakeeruddin, J. P. Correa-Baena, W. R. Tress, A. Abate, A. Hagfeldt, and M. Grätzel. *Science*, 354(6309):206, 2016.

[52] G. R. Yettapu, D. Talukdar, S. Sarkar, A. Swarnkar, A. Nag, P. Ghosh, and P. Mandal. *Nano Lett.*, 16(8):4838, 2016.

[53] J. He, A. S. Vasenko, R. Long, and O. V. Prezhdo. *J. Phys. Chem. Lett.*, 9(8):1872, 2018.

[54] J. Hu, C. Zhao, S. He, W. Ti, C. Hao, and J. Shengye. *Chin. Chem. Lett.*, 29(5):699, 2018.

[55] S. S. Shin, S. J. Lee, and S. I. Seok. *APL Mater.*, 7(2):022401, 2019.

[56] A. Pérez-Tomas, H. Xie, Z. Wang, H. Kim, I. Shirley, S. Turren-Cruz, A. Morales-Melgares, B. Saliba, D. Tanenbaum, M. Saliba, S. M. Zakeeruddin, M. Grätzel, A. Hagfeldt, and M. Lira-Cantu. *Sustain. Energy Fuels*, 3:382, 2019.

[57] A. K. Jena, A. Kulkarni, and T. Miyasaka. *Chem. Rev.*, 119(5):3036, 2019.

[58] W. Rittisut, J. Padchasri, P. Kidkhunthod, S. Rujirawat, and R. Yimnirun. *Integr. Ferroelectr.*, 195(1):19, 2019.

[59] H. Fujishita, Y. Shiozaki, and E. Sawaguchi. *J. Phys. Soc. Jpn.*, 46(2):581, 1979.

[60] I. G. Wood, K. S. Knight, G. D. Price, and J. A. Stuart. *J. Appl. Crystallogr.*, 35(3):291, 2002.

[61] V. M. Goldschmidt. *Naturwissenschaften*, 14(21):477, 1926.

[62] C. Li, K. C. Kwan Soh, and P. Wu. *J. Alloys and Compd.*, 372(1):40, 2004.

[63] B. A. Wechsler and C. T. Prewitt. *Am. Mineral.*, 69(1-2):176, 1984.

[64] R. D. Shannon. *Acta Crystallogr. A*, 32(5):751, 1976.

[65] H. Megaw and C. Darlington. *Acta Crystallogr. A*, 31:161, 1975.

[66] P. M. Woodward. *Acta Crystallogr. B*, 53:32, 1997.

[67] Y. S. Zhao, D. J. Weidner, J. Ko, K. Leinenweber, X. Liu, B. Li, Y. Meng, R. E. G. Pacalo, M. T. Vaughan, Y. Wang, and A. Yeganeh-Haeri. *J. Geophys. Res. Solid Earth*, 99(B2):2871, 1994.

[68] P. G. Radaelli and S. W. Cheong. *Phys. Rev. B*, 66:094408, 2002.

[69] K. Knížek, P. Novák, and Z. Jirák. *Phys. Rev. B*, 71:054420, 2005.

[70] H.-Z. Liu, J. Chen, J. Hu, C. D. Martin, D. J. Weidner, D. Häusermann, and H.-K. Mao. *Geophys. Res. Lett.*, 32(4):L04304, 2005.

[71] Y. Lee and B. N. Harmon. *J. Appl. Phys.*, 113(17):17E145, 2013.

[72] C. N. W. Darlington, W. I. F. David, and K. S. Knight. *Phase Transit.*, 48 (4):217, 1994.

[73] U. D. Venkateswaran, V. M. Naik, and R. Naik. *Phys. Rev. B*, 58:14256, 1998.

[74] A. Okazaki and Y. Suemune. *J. Phys. Soc. Jpn.*, 16(2):176, 1961.

[75] F. Aguado, F. Rodríguez, S. Hirai, J. N. Walsh, A. Lennie, and S. A. T. Redfern. *High Press. Res.*, 28(4):539, 2008.

[76] J.-S. Zhou, J. A. Alonso, J. T. Han, M. T. Fernández-Díaz, J.-G. Cheng, and J .B. Goodenough. *J. Fluor. Chem.*, 132(12):1117, 2011.

[77] A. M. Glazer. *Acta Crystallogr. B*, 28:3384, 1972.

[78] C. Howard and H. Stokes. *Acta Crystallogr. B*, 54:782, 1998.

[79] J.-S. Zhou, J.-Q. Yan, and J. B. Goodenough. *Phys. Rev. B*, 71:220103, 2005.

[80] Y. S. Zhao, D . J. Weidner, J. B. Parise, and D. E. Cox. *Phys. Earth Planet. Inter*, 76:1, 1993.

[81] Y. S. Zhao, D . J. Weidner, J. B. Parise, and D. E. Cox. *Phys. Earth Planet. Inter.*, 76:17, 1993.

[82] S. Geller and E. A. Wood. *Acta Crystallogr.*, 9(7):563, 1956.

[83] J. Rodríguez-Carvajal, S. Rosenkranz, M. Medarde, P. Lacorre, M. T. Fernandez-Díaz, F. Fauth, and V. Trounov. *Phys. Rev. B*, 57:456, 1998.

[84] G. Thornton, B. C. Tofield, and A. W. Hewat. *J. Solid State Chem.*, 61(3): 301, 1986.

[85] J. L. García-Muñoz, J. Rodríguez-Carvajal, P. Lacorre, and J. B. Torrance. *Phys. Rev. B*, 46:4414, 1992.

[86] A. N. Petrov, V. I. Voronin, T. Norby, and P. Kofstad. *J. Solid State Chem.*, 143(1):52, 1999.

[87] X. Luo and B. Wang. *J. Appl. Phys.*, 104(5):053503, 2008.

[88] S. C. Abrahams, J. M. Reddy, and J. L. Bernstein. *J. Phys. Chem. Solids*, 27(6):997, 1966.

[89] C. H. Lei, J. G. Wen, M. J. Sardela, I. Bareño, S.-H. Kang Petrov, and D. P. Abraham. *J. Mater. Sci.*, 44:5579, 2009.

[90] S. M. Moussa, B. J. Kennedy, and T. Vogt. *Solid State Commun.*, 119(8): 54, 2001.

[91] S. Hanif, M. Hassan, S. Riaz, S. Atiq, S. S. Hussain, S. Naseem, and G. Murtaza. *Results Phys.*, 7:3190, 2017.

[92] C. L. Bull, D. Gleeson, and K. S. Knight. *J. Phys. Condens. Matter*, 15 (29):4927, 2003.

[93] A. J. Barón-González, C. Frontera, J. L. García-Muñoz, J. Blasco, and C. Ritter. *J. Phys. Conf. Ser.*, 325:012007, 2011.

[94] N. Tsukuda and A. Okazaki. *J. Phys. Soc. Jpn.*, 33(4):1088, 1972.

[95] A. Hassini, M. Gervais, J. Coulon, V. Ta Phuoc, and F. Gervais. *Mat. Sci. Eng. B*, 87(2):164, 2001.

[96] L. F. Schneemeyer, J. K. Thomas, T. Siegrist, B. Batlogg, and L. W. Rupp. *Nature*, 335:421, 1988.

[97] B. J. Kennedy, C. J. Howard, and B. C. Chakoumakos. *Phys. Rev. B*, 59: 4023, 1999.

[98] K. Leinenweber and J. Parise. *J. Solid State Chem.*, 114(1):277, 1995.

[99] W. Hönle, G. Miller, and A. Simon. *J. Solid State Chem.*, 75(1):147, 1988.

[100] R. Diehl, G. Brandt, and E. Salje. *Acta Crystallogr. B*, 34(4):1105, 1978.

[101] P. M. Woodward, A. W. Sleight, and T. Vogt. *J. Solid State Chem.*, 131 (1):9, 1997.

[102] K. S. Knight. *Can. Mineral.*, 49(3):793, 2011.

[103] B. J. Campbell, H. T. Stokes, D. E. Tanner, and D. M. Hatch. *J. Appl. Crystallogr.*, 39:607, 2006.

[104] S. M. Selbach, J. R. Tolchard, A. Fossdal, and T. Grande. *J. Solid State Chem.*, 196:249, 2012.

[105] S. A. Hayward, F. D. Morrison, S. A. T. Redfern, E. K. H. Salje, J. F. Scott, K. S. Knight, S. Tarantino, A. M. Glazer, V. Shuvaeva, P. Daniel, M. Zhang, and M. A. Carpenter. *Phys. Rev. B*, 72:054110, 2005.

[106] M. Medarde, J. Mesot, S. Rosenkranz, P. Lacorre, W. Marshall, S. Klotz, J. S. Loveday, G. Hamel, S. Hull, and P. Radaelli. *Physica B Condens. Matter*, 234-236:15, 1997.

[107] R. J. Angel, J. Zhao, and N. L. Ross. *Phys. Rev. Lett.*, 95:025503, 2005.

[108] R. J. Angel, J. Zhao, N. L. Ross, C. V. Jakeways, S. A. T. Redfern, and M. Berkowski. *J. Solid State Chem.*, 180(12):3408, 2007.

[109] J. Zhao, N. L. Ross, and R. J. Angel. *Acta Crystallogr. B*, 62(3):431, 2006.

[110] C. Lin, Y. Zhang, J. Liu, X. Li, Y. Li, L. Tang, and L. Xiong. *J. Phys. Condens. Matter*, 24(11):115402, 2012.

[111] J.-G. Cheng, K. E. Kweon, J.-S. Zhou, J. A. Alonso, P.-P. Kong, Y. Liu, C. Jin, J. Wu, J.-F. Lin, S. A. Larregola, W. Yang, G. Shen, A. H. MacDonald, A. Manthiram, G. S. Hwang, and J. B. Goodenough. *PNAS*, 110(50):20003, 2013.

[112] B. J. Kennedy, T. Vogt, C. D. Martin, J. B. Parise, and J. A. Hriljac. *J. Phys. Condens. Matter*, 13(48):L925, 2001.

[113] M. Etter, M. Müller, M. Hanfland, and R. E. Dinnebier. *Acta Crystallogr. B*, 70(3):452, 2014.

[114] S. Åsbrink and A. Waśkowska. *Phys. Rev. B*, 53:12, 1996.

[115] J. B. Goodenough. *Phys. Rev.*, 100:564, 1955.

[116] J. Kanamori. *J. Phys. Chem. Solids*, 10:87, 1959.

[117] P. W. Anderson. *in Magnetism, Academic Press, New York*, pages 25–83, 1963.

[118] K. Asai, P. Gehring, H. Chou, and G. Shirane. *Phys. Rev. B*, 40:10982, 1989.

[119] K. Asai, A. Yoneda, O. Yokokura, J. M. Tranquada, G. Shirane, and K. Kohn. *J. Phys. Soc. Jpn.*, 67(1):290, 1998.

[120] K. Asai, O. Yokokura, M. Suzuki, T. Naka, T. Matsumoto, H. Takahashi, N. Môri, and K. Kohn. *J. Phys. Soc. Jpn.*, 66(4):967, 1997.

[121] M. Sikora, K. Knizek, Cz. Kapusta, and P. Glatzel. *J. Appl. Phys.*, 103: 07C907, 2008.

[122] C. Zobel, M. Kriener, D. Bruns, J. Baier, M. Grüninger, T. Lorenz, P. Reutler, and A. Revcolevschi. *Phys. Rev. B*, 66:020402, 2002.

[123] D. P. Kozlenko, N. O. Golosova, Z. Jirák, L. S. Dubrovinsky, B. N. Savenko, M. G. Tucker, Y. Le Godec, and V. P. Glazkov. *Phys. Rev. B*, 75:064422, 2007.

[124] T. Vogt, J. A. Hriljac, N. C. Hyatt, and P. Woodward. *Phys. Rev. B*, 67: 140401, 2003.

[125] S. Lee, M. T. Fernandez-Diaz, H. Kimura, Y. Noda, D. T. Adroja, S. Lee, J. Park, V. Kiryukhin, S.-W. Cheong, M. Mostovoy, and J.-G. Park. *Phys. Rev. B*, 88:060103, 2013.

[126] J. M. Moreau, C. Michel, R. Gerson, and W. J. James. *J. Phys. Chem. Solids*, 32(6):1315, 1971.

[127] W. Kaczmarek, M. Polomska, and Z. Pajak. *Phys. Lett. A*, 47(3):227, 1974.

[128] T. Atou, H. Chiba, K. Ohoyama, Y. Yamaguchi, and Y. Syono. *J. Solid State Chem.*, 145(2):639, 1999.

[129] B. W. Lee, P. S. Yoo, V. B. Nam, K. R. N. Toreh, and C. U. Jung. *Nanoscale Res. Lett.*, 10(1):47, 2015.

[130] A. Moreira dos Santos, S. Parashar, A. R. Raju, Y. S. Zhao, A. K. Cheetham, and C. N. R. Rao. *Solid State Commun.*, 122(1):49, 2002.

[131] R. Seshadri and N. A. Hill. *Chem. Mater.*, 13(9):2892, 2001.

[132] P. G. de Gennes. *Phys. Rev.*, 118:141, 1960.

[133] J.-H. Lee, N. C. Bristowe, J. H. Lee, S.-H. Lee, P. D. Bristowe, A. K. Cheetham, and H. M. Jang. *Chem. Mater.*, 28(12), 2016.

[134] R. Prasanna, A. Gold-Parker, T. Leijtens, B. Conings, A. Babayigit, H. G Boyen, M. F. Toney, and M. D. McGehe. *J. Am. Chem. Soc.*, 139(32): 11117, 2017.

[135] J. Mizusaki, K. Arai, and K. Fueki. *Solid State Ion.*, 11(3):203, 1983.

[136] J. P. Attfield. *Chem. Mater.*, 9:3239, 1998.

[137] H. Hayashi, H. Inaba, M. Matsuyama, N. G. Lan, M. Dokiya, and H. Tagawa. *Solid State Ion.*, 122:1, 1999.

[138] T. Mayeshiba and D. Morgan. *Phys. Chem. Chem. Phys.*, 17:2715, 2015.

[139] R. Gao, A. C. P. Jain, S. Pandya, Y. Dong, Y. Yuan, H. Zhou, L. R. Dedon, V. Thoréton, S. Saremi, R. Xu, A. Luo, T. Chen, V. Gopalan, E. Ertekin, J. Kilner, T. Ishihara, N. H. Perry, D. R. Trinkle, and L. W. Martin. *Adv. Mater.*, page 1905178, 2019.

[140] D. S. Sivia. *Oxford, Oxford University Press*, 2011.

[141] W. H. Bragg. *Proc. R. Soc. Lond. A*, 89:246, 1913.

[142] L. R. B. Elton and D. F. Jackson. *Am. J. Phys.*, 34(11):1036, 1966.

[143] P. P. Ewald. *Acta Crystallogr. A*, 25(1):103, 1969.

[144] G. E. Bacon. *Clarendon Press, Oxford*, 1955.

[145] G. Taylor. *Acta Crystallogr. D*, 59(11):1881, 2003.

[146] A. C. Larson and R. B. Von Dreele. *Los Alamos National Laboratory Report LAUR*, page 86, 2000.

[147] H. M. Rietveld. *J. Appl. Crystallogr.*, 2(2):65, 1969.

[148] R. B. Von Dreele, J. D. Jorgensen, and C. G. Windsor. *J. Appl. Crystallogr.*, 15(6):581, 1982.

[149] W. I. F. David. *J. Res. Natl. Inst. Stand. Technol.*, 109:107, 2004.

[150] J. S. Loveday, R. J. Nelmes, C. L. Bull, H. E. Maynard-Casely, and M. Guthrie. *High Press. Res.*, 29(3):396, 2009.

[151] A. D. Fortes, I. G. Wood, L. Vočadlo, K. S. Knight, W. G. Marshall, M. G. Tucker, and F. Fernandez-Alonso. *J. Appl. Crystallogr.*, 42(5):846, 2009.

[152] H. E. Maynard-Casely, C. L. Bull, M. Guthrie, I. Loa, M. I. McMahon, E. Gregoryanz, R. J. Nelmes, and J. S. Loveday. *J. Chem. Phys.*, 133(6): 064504, 2010.

[153] F.D. Murnaghan. *Am. J. Math.*, 59:235, 21937.

[154] F. Birch. *Phys. Rev.*, 71:809, 1947.

[155] F. Birch. *J. Geophys. Res. Solid Earth*, 83(B3):1257, 1978.

[156] J. Sun, Q. Wu, L.-C Cai, and F.-Q Jing. *Chin. J. High Press. Phys.*, 18: 109, 2004.

[157] T. Katsura and Y. Tange. *Minerals*, 9(12), 2019.

[158] C. L. Bull, N. P. Funnell, M. G. Tucker, S. Hull, D. J. Francis, and W. G. Marshall. *High Press. Res.*, 36(4):493, 2016.

[159] J. M. Besson, R. J. Nelmes, G. Hamel, J. S. Loveday, G. Weill, and S. Hull. *Physica B*, 180:907, 1992.

[160] S. Klotz, G. Hamel, and J. Frelat. *High Press. Res.*, 24(1):219, 2004.

[161] S. Klotz. Techniques in high pressure neutron scattering. *Boca Raton, FL: CRC Press, Taylor and Francis*, 2013.

[162] L. G. Khovstantsev. *High Temp. High Press.*, 16:165, 1984.

[163] W. G. Marshall and D. J. Francis. *J. Appl. Crystallogr.*, 35:122, 2002.

[164] Th. Strässle, S. Klotz, K. Kunc, V. Pomjakushin, and J. S. White. *Phys. Rev. B*, 90:014101, 2014.

[165] D. Martíinez-García, Y. Le Godec, M. Mézouar, G. Syfosse, J. P. Itié, and J. M. Besson. *High Pressure Research*, 18:339, 2000.

[166] D. L. Decker. *J. Appl. Phys.*, 36(1):157, 1965.

[167] H.-K. Mao, X.-J. Chen, Y. Ding, B. Li, and L. Wang. *Rev. Mod. Phys.*, 90: 015007, 2018.

[168] C. E. Weir, E. R. Lippincott, A. Van Valkenburg, and E. N. Bunting. *J. Res. Natl. Inst. Stand.*, 1:55, 1959.

[169] C. E. Weir, A. Van Valkenburg, and E. R. Lippincott. *Buttenworth Inc. Washington D. C.*, page 51, 1962.

[170] N. N. Patel, M. Sunder, and S. M. Sharma. *Indian J. Phys.*, 92:1259, 2018.

[171] T. Fedotenko, L. Dubrovinsky, G. Aprilis, E. Koemets, A. Snigirev, I. Snigireva, A. Barannikov, P. Ershov, F. Cova, M. Hanfland, and N. Dubrovinskaia. *Rev. Sci. Instrum.*, 90(10):104501, 2019.

[172] A. Van Valkenburg. *Rev. Sci. Instrum.*, 33:1462, 1962.

[173] L. Merrill and W. A. Bassett. *Rev. Sci. Instrum.*, 45:290, 1974.

[174] R. A. Forman, G. J. Piermarini, J. D. Barnett, , and S. Block. *Science*, 176:284, 1972.

[175] K. Syassen. *High Press. Res.*, 28(2):75, 1972.

[176] G. J. Piermarini, S. Block, J. D. Barnett, and R. A. Forman. *J. Appl. Phys.*, 46:2774, 1975.

[177] H. K. Mao, J. Xu, and P. M. Bell. *J. Geophys. Res. B*, 91:4673, 1986.

[178] L. Liu, Y. Bi, and J.-A. Xu. *Chin. Phys. B*, 22(5):056201, 2013.

[179] M. N. Iliev, M. V. Abrashev, H.-G. Lee, V. N. Popov, Y. Y. Sun, C. Thomsen, R. L. Meng, and C. W. Chu. *Phys. Rev. B*, 57:2872, 1998.

[180] M. Abrashev, J. Bäckström, L. Börjesson, V. Popov, R. Chakalov, N. Kolev, R.-L Meng, and M. Iliev. *Phys. Rev. B*, 65:184301, 2002.

[181] E. Kroumova, M. Aroyo, J. Perez-Mato, A. Kirov, C. Capillas, S. Ivantchev, and H. Wondratschek. *Phase Transit.*, 76:155, 2003.

[182] M. A. Islam, J. M Rondinelli, and J. E. Spanier. *J. Phys. Condens. Matter*, 25(17):175902, 2013.

[183] P. Marcon and K. Ostanina. *Prog. Electromagn. Res.*, 2012.

[184] M. Buchner, K. Höfler, B. Henne, V. Ney, and A. Ney. *J. Appl. Phys.*, 124 (16):161101, 2018.

[185] G. Giriat, W. Wang, P. J. Attfield, A. D. Huxley, and K. V. Kamenev. *Rev. Sci. Instrum.*, 81:073905, 2010.

[186] R. Mortimer, J. Powell, and N. Vasanthacharaya. *J. Phys. Condens. Matter*, 9:11209, 1997.

[187] C. L. Bull and K. S. Knight. *Solid State Sci.*, 57:38, 2016.

[188] J. B. Goodenough. *J. Phys. Chem. Solids*, 6(2):287, 1958.

[189] S. Yamaguchi, Y. Okimoto, and Y. Tokura. *Phys. Rev. B*, 55:R8666, 1997.

[190] T. Saitoh, T. Mizokawa, A. Fujimori, M. Abbate, Y. Takeda, and M. Takano. *Phys. Rev. B*, 55:4257, 1997.

[191] M. A. Korotin, S. Yu. Ezhov, I. V. Solovyev, V. I. Anisimov, D. I. Khomskii, and G. A. Sawatzky. *Phys. Rev. B*, 54:5309, 1996.

[192] J.-Q. Yan, J.-S. Zhou, and J. B. Goodenough. *Phys. Rev. B*, 69:134409, 2004.

[193] A. S. Panfilov, G. E. Grechnev, I. P. Zhuravleva, A. A. Lyogenkaya, V. A. Pashchenko, B. N. Savenko, D. Novoselov, D. Prabhakaran, and I. O. Troyanchuk. *Low Temp. Phys.*, 44(4):328, 2018.

[194] P. M. Raccah and J. B. Goodenough. *Phys. Rev.*, 155:932, 1967.

[195] K. Knížek, Z. Jirák, J. Hejtmánek, P. Henry, and G. André. *J. Appl. Phys.*, 103(7):07B703, 2008.

[196] G. Vankó, J. P. Rueff, A. Mattila, Z. Németh, and A. Shukla. *Phys. Rev. B*, 73:024424, 2006.

[197] A. M. Durand, D. P. Belanger, C. H. Booth, F. Ye, S. Chi, J. A. Fernandez-Baca, and M. Bhat. *J. Phys.: Condens. Matter*, 25(38):382203, 2013.

[198] B. Pimentel, R.J. Caraballo-Vivas, N.R. Checca, D.L. Rocco, and M.S. Reis. *J. Alloys Cpd.*, 796:331, 2019.

[199] A. Ishikawa, J. Nohara, and S. Sugai. *Phys. Rev. Lett.*, 93:136401, 2004.

[200] E. Granado, N. O. Moreno, A. Garcia, J. A. Sanjurjo, C. Rettori, I. Torriani, S. B. Oseroff, J. J. Neumeier, K. J. McClellan, S. W. Cheong, and Y. Tokura. *Phys. Rev. B*, 58:11435, 1998.

[201] M. Popa, J. Frantti, and M. Kakihana. *Solid State Ion.*, 154:135, 2002.

[202] V. P. Gnezdilov, A. V. Yeremenko, Yu. G. Pashkevich, P. Lemmens, G. Güntherodt, S. V. Shiryaev, G. L. Bychkov, and S. N. Barilo. *Low Temp. Phys.*, 29(11):963, 2003.

[203] M. Popa, L. V. Hong, and M. Kakihana. *Physica B Condens. Matter*, 327 (2):233, 2003.

[204] N. Orlovskaya, D. Steinmetz, S. Yarmolenko, D. Pai, J. Sankar, and J. B. Goodenough. *Phys. Rev. B*, 72:014122, 2005.

[205] O. Arnold, J. C. Bilheux, J. M. Borreguero, A. Buts, S. I. Campbell, L. Chapon, M. Doucet, N. Draper, R. Ferraz Leal, M. A. Gigg, V. E. Lynch, A. Markvardsen, D. J. Mikkelson, R. L. Mikkelson, R. Miller, K. Palmen, P. Parker, G. Passos, T. G. Perring, P. F. Peterson, S. Ren, M. A. Reuter, A. T. Savici, J. W. Taylor, R. J. Taylor, R. Tolchenov, W. Zhou, and J. Zikovski. *Nucl. Instrum. Meth. Phys. Res. A*, 764:156, 2014.

[206] J. Gonzalez-Platas, M. Alvaro, F. Nestola, and R. J. Angel. *J. Appl. Crystallogr.*, 49:1377, 2016.

[207] R. Lengsdorf, M. Ait-Tahar, S. S. Saxena, M. Ellerby, D. I. Khomskii, H. Micklitz, T. Lorenz, and M. M. Abd-Elmeguid. *Phys. Rev. B*, 69:140403, 2004.

[208] R. L. White. *J. Appl. Phys.*, 40(3):1061, 1969.

[209] P. Ciambelli, S. Cimino, L. Lisi, M. Faticanti, G. Minelli, I. Pettiti, and P. Porta. *Appl. Catal. B*, 33(3):193, 2001.

[210] G. Martinelli, M. C. Carotta, M. Ferroni, Y. Sadaoka, and E. Traversa. *Sens. Actuators B Chem.*, 55(2):99, 1999.

[211] Y. Nishihata, J. Mizuki, T. Akao, H. Tanaka, M. Uenishi, M. Kimura, T. Okamoto, and N. Hamada. *Nature*, 418:164, 2002.

[212] P. V. Hendriksen, P. H. Larsen, M. Mogensen, F. W. Poulsen, and K. Wiik. *Catal. Today*, 56(1):283, 2000.

[213] S. Acharya, J. Mondal, S. Ghosh, S. K. Roy, and P. K. Chakrabarti. *Mater. Lett.*, 64(3):415, 2010.

[214] J. Faye, A. Baylet, M. Trentesaux, S. Royer, F. Dumeignil, D. Duprez, S. Valange, and J.-M. Tatibouët. *Appl. Catal. B*, 126:134, 2012.

[215] M. Sukumar, L. J. Kennedy, J. J. Vijaya, B. Al-Najar, and M. Bououdina. *Mater. Sci. Semicond. Process.*, 100:225, 2019.

[216] T. Peterlin-Neumaier and E. Steichele. *J. Magn. Magn. Mater.*, 59(3):351, 1986.

[217] D. D. Sarma, N. Shanthi, S. R. Barman, N. Hamada, H. Sawada, and K. Terakura. *Phys. Rev. Lett.*, 75:1126, 1995.

[218] S. C. Parida, S. K. Rakshit, and Z. Singh. *J. Solid State Chem.*, 181(1): 101, 2008.

[219] J. W. Seo, E. E. Fullerton, F. Nolting, A. Scholl, J. Fompeyrine, and J-P. Locquet. *J. Phys. Condens. Matter*, 20(26):264014, 2008.

[220] S. A. Ivanov, R. Tellgren, F. Porcher, T. Ericsson, A. Mosunov, P. Beran, S. K. Korchagina, P. A. Kumar, R. Mathieu, and P. Nordblad. *Mat. Res. Bull.*, 47(11):3253, 2012.

[221] C. C. dos Santos, J. P. Barbosa, M. A. B. dos Santos, F. A. M. Lira, F. J. B. Cardoso, J. C. Pinheiro, O. Treu Filho, and R. T. Kondo. *Comput. Mater. Sci.*, 39(3):713, 2007.

[222] T. Wang, C. Wu, J. Xing, J. Wu, B. Li-Chen, X. Xu, K. Wang, and J. Zhu. *J. Am. Ceram. Soc.*, 102(10):6126, 2019.

[223] M. Idrees, M. Nadeem, M. Atif, M. Siddique, M. Mehmood, and M. Hassan. *Acta Mater.*, 59:1338, 2011.

[224] A. S. Mahapatra, A. Mitra, A. Mallick, A. Shaw, J. M. Greneche, and P. K. Chakrabarti. *J. Alloys Compd.*, 743:274, 2018.

[225] M. Marezio and P. D. Dernier. *Mater. Res. Bull.*, 6(1):23, 1971.

[226] C. A. L. Dixon, C. M. Kavanagh, K. S. Knight, W. Kockelmann, F. D. Morrison, and P. Lightfoot. *J. Solid State Chem.*, 230:337, 2015.

[227] J.-S. Zhou and J. B. Goodenough. *Phys. Rev. Lett.*, 94:065501, 2005.

[228] P. M. Woodward, T. Vogt, D. E. Cox, A. Arulraj, C. N. R. Rao, P. Karen, and A. K. Cheetham. *Chem. Mater.*, 10(11):3652, 1998.

[229] F. Zaza, V. Pallozzi, E. Serra, and M. Pasquali. *AIP Conf. Proc.*, 1667(1): 020003, 2015.

[230] K. S. Knight. *Can. Mineral.*, 47(2):381, 2009.

[231] W. Cochran and A. Zia. *Phys. Status Solidi B*, 25(1):273, 1968.

[232] C. N. W. Darlington. *Acta Crystallogr. A*, 58(1):66, 2002.

[233] H. C. Gupta, M. K. Singh, and L. M. Tiwari. *J. Raman Spectrosc.*, 33(1): 67, 2002.

[234] M. Romero, R. W. Gómez, V. Marquina, J. L. Pérez-Mazariego, and R. Escamilla. *Physica B Condens. Matter*, 443:90, 2014.

[235] M. C. Weber, M. Guennou, H. J. Zhao, J. Íñiguez, R. Vilarinho, A. Almeida, J. A. Moreira, and J. Kreisel. *Phys. Rev. B*, 94:214103, 2016.

[236] P. V. Coutinho, F. Cunha, and P. Barrozo. *Solid State Commun.*, 252:59, 2017.

[237] D. Triyono and H. Laysandra. *IOP Conf. Ser. Mater. Sci. Eng.*, 496:012045, 2019.

[238] C. L. Bull, H. Y. Playford, K. S. Knight, G. B. G. Stenning, and M. G. Tucker. *Phys. Rev. B*, 94:014102, 2016.

[239] C. L. Bull, H. Y. Playford, K. S. Knight, W. G. Marshall, G. B. G. Stenning, R. I. Smith, and Z. Hart. *J. Phys. Condens. Matter*, 27:165401, 2015.

[240] J. B. Goodenough, A. Wold, R. J. Arnold, and N. Menyuk. *Phys. Rev.*, 124:373, 1961.

[241] S. Yamaguchi, Y. Okimoto, H. Taniguchi, and Y. Tokura. *Phys. Rev. B*, 53:R2926, 1996.

[242] I. O. Troyanchuk, L. S. Lobanovky, D. D. Khalyavin, S. N. Pastushonok, and H. Szymczak. *J. Magn. Magn. Mater.*, 210:63, 2000.

[243] N. O. Golosova, D. P. Kozlenko, V. I. Voronin, V. P. Glazkov, and B. N. Savenko. *Phys. Solid State*, 48:96, 2006.

[244] D. P. Kozlenko, I. N. Goncharenko, B. N. Savenko, and V. I. Voronin. *J. Phys. Condens. Matter*, 16:6755, 2004.

[245] Y. Moritomo, A. Asamitsu, and Y. Tokura. *Phys. Rev. B*, 51:16491, 1995.

[246] L. Patrick. *Phys. Rev.*, 93:384, 1954.

[247] Y.-M. Zhou, W.-T. Geng, and D.-S. Wang. *Phys. Rev. B*, 57:5029, 1998.

[248] G. A. Samara and A. A. Giardini. *Phys. Rev.*, 186:577, 1969.

[249] S. K. Bose, J. Kudrnovský, V. Drchal, and I. Turek. *Phys. Rev. B*, 84: 174422, 2011.

[250] P. M. Bell, H.-K. Mao, and K. Goettel. *Science*, 226:542, 1984.

[251] J. A. Xu, H.-K. Mao, and P. M. Bell. *Science*, 232:1404, 1986.

[252] J. A. Xu, H. K. Mao, R. J. Hamley, and E. Hines. *J. Phys. Condens. Matter*, 14:11543, 2002.

[253] S. P. Besedin, I. N. Makarenko, S. M. Stishov, V. P. Glazkov, N. Goncharenko, and V. A. Somenkov. *High Press. Res.*, 14:193, 1995.

[254] I. N. Goncharenko. *High Press. Res.*, 24(1):193, 2004.

[255] I. N. Goncharenko. *High Press. Res.*, 27:183, 2007.

[256] R. Boehler and K. De Hantsetters. *High Press. Res.*, 24(3):391, 2004.

[257] R. Boehler, J. J. Molaison, and B. Haberl. *Rev. Scient. Instrum.*, 88(8): 083905, 2017.

[258] R. Boehler, M. Guthrie, J. J. Molesan, A. M. dos Santos, S. Sinogeikin, S. Machida, N. Pradhan, and C. A. Tulk. *High Press. Res.*, 33(3):546, 2013.

[259] J. Gracio, Q. Fan, and J. Mendes. *J. Phys. D Appl. Phys.*, 43:374017, 2010.

[260] I. N. Goncharenko, I. Mirebeau, and A. Ochiai. *Hyperfine Interact.*, 128: 225, 2000.

[261] V. P. Glazkov, A. V. Irodova, S. M. Somenkova, S. Sh. Shilstein, and S. P. Besedin. *J. Less-Common Met.*, 129:165, 1987.

[262] S. P. Besedin, I. N. Makarenko, S. M. Stishov, V. P. Glazkov, I. N. Goncharenko, A. V. Irodova, V. A. Somenkov, and S. Sh. Shilstein. *High Press. Res.*, 4:447, 1990.

[263] I. N. Goncharenko and P. Loubeyre. *Nature*, 435:1206, 2005.

[264] C. L. Bull, M. Guthrie, J. Archer, M. T. Fernandez-Diaz, J. S. Loveday, K. Komatsu, H. Hamidov, and R. J. Nelmes. *J. Appl. Crystallogr.*, 44(4): 831, 2011.

[265] J. B. Binns, K. V. Kamenev, G. J. McIntyre, S. A. Moggach, and S. Parsons. *IUCrJ*, 3:168, 2016.

[266] S. A. Moggach, D. R. Allan, S. Parsons, and J. E. Warrenc. *J. Appl. Crystallogr.*, 41:249, 2008.

[267] M. Guthrie. *J. Phys. Condens. Matter*, 27:153201, 2015.

[268] M. Guthrie, R. Boehler, C. A. Tulk, J. J. Molaison, A. M. dos Santos, K. Li, and R. J Hemley. *Proc. Natl. Acad. Sci.*, (110):10552, 2013.

[269] C. L. Bull, M. Guthrie, R. J. Nelmes, J. S. Loveday, K. Komatsu, H. Hamidov, and M. J. Gutmann. *High Press. Res.*, 29(4):780, 2009.

[270] C. L. Bull, M. Guthrie, R. J. Nelmes, J. S. Loveday, H. Hamidov, and M. J. Gutmann. *High Press. Res.*, 29(4):644, 2009.

[271] D. B. Mc Whan, D. Bloch, and G. Parisot. *Rev. Sci. Instrum.*, 45:643, 1974.

[272] S. Klotz, J. M. Besson, G. Hamel, R. J. Nelmes, J. S. Loveday, W. G. Marshall, and R. M. Wilson. *Appl. Phys. Lett.*, 66:1735, 1995.

[273] R. M. Wilson, J. S. Loveday, R. J. Nelmes, S. Klotz, and W. G. Marshall. *Nucl. Instr. Met. Phys. Res. A*, 354(1):145, 1995.

[274] J. S. Loveday, M. I. McMahon, and R. J. Nelmes. *J. Appl. Crystallogr.*, 23 (5):392, 1990.

[275] M. Guthrie, C. G. Pruteanu, M. E. Donnelly, J. J. Molaison, A. M. dos Santos, J. S. Loveday, R. Boehler, and C. A. Tulk. *J. Appl. Crystallogr.*, 50(1):76, 2017.

[276] K. Takemura. *J. Phys. Soc. Jpn. A*, 76:202, 2007.

[277] S. Klotz, J. C. Chervin, P. Munsch, and G. Le Marchand. *J. Phys. D Appl. Phys.*, 42:075413, 2009.

[278] R. J. Angel, M. Bujak, J. Zhao, G. D. Gatta, and S. D. Jacobsen. *J. Appl. Crystallogr.*, 40:26, 2007.

[279] S. Klotz, Th. Strässle, G. Rousse, G. Hamel, and V. Pomjakushin. *Appl. Phys. Lett.*, 86:031917, 2005.

[280] G. J. Piermarini, S. Block, and J. D. Barnett. *J. Appl. Phys.*, 44(12):5377, 1973.

[281] P. M. Bell and H.-K. Mao. *Year b.-Carnegie Inst. Wash*, 80:404, 1981.

[282] C. S. Zha, R. Boehler, D. A. Young, and M. Ross. *J. Chem. Phys.*, 85:1034, 1986.

[283] K. Takemura and A. Dewaele. *Phys. Rev. B*, 78:104119, 2008.

[284] C. J. Ridley, K. S. Knight, C. W. Wilson, R. I. Smith, and C. L. Bull. *J. Phys. Condens. Matter*, 31(39):395402, 2019.

[285] M. Sekar, N. R. Sanjay Kumara, P. Ch. Sahu, N. V. Chandra Shekar, and N. Subramanian. *Rev. Sci. Instrum.*, 79:076103, 2008.

[286] T. Kenichi and P. Ch. Sahu. *Rev. Sci. Instrum.*, 72:3873, 2001.

[287] R. J. Hemley, A. P. Jephcoat, H. K. Mao, C. S. Zha, L. W. Finger, and D. E. Cox. *Nature*, 330:737, 1987.

[288] R. J. Nelmes, J. S. Loveday, W. G. Marshall, J. M. Besson, S. Klotz, and G. Hamel. *Rev. High Pres. Sci. Tech.*, 7:1138, 1998.

[289] J. S. Loveday, G. Hamel, R. J. Nelmes, S. Klotz, M. Guthrie, and J. M. Besson. *High Press. Res.*, 17(3):149, 2000.

[290] S. Klotz, K. Komatsu, H. Kagi, K. Kunc, A. Sano-Furukawa, S. Machida, and T. Hattori. *Phys. Rev. B*, 95:174111, 2017.

[291] M. Guthrie, R. Boehler, J. J. Molaison, B. Haberl, A. M. dos Santos, and C. Tulk. *Phys. Rev. B*, 99:184112, 2019.

[292] K. Momma and F. Izumi. *J. Appl. Crystallogr.*, 41(3):653, 2008.